UNIVERSITY OF SOUTHAMPTON

FACULTY OF PHYSICAL SCIENCES AND ENGINEERING

Electronics and computer science

Volume 1 of 1

Development of a multi-parameter *in vivo* sensing platform for intrauterine studies and subfertility diagnostics

by

Roeland H.G. Mingels

Thesis for the degree of Doctor of Philosophy

May 2018

Supervisors: Prof. H.Morgan

Prof. Y.Cheong

UNIVERSITY OF SOUTHAMPTON

ABSTRACT

FACULTY OF PHYSICAL SCIENCES AND ENGINEERING

Faculty of Electronics and Computer Science

Thesis for the degree of Doctor of Phylosophy

Development of a multi-parameter *in vivo* sensing platform for intrauterine studies and subfertility diagnostics

By Roeland H.G. Mingels

Couples in the developed world are increasingly being confronted with subfertility issues. In over 18% of the cases no clear reason can be identified. It is suspected that abnormalities in the physiological parameters of the uterine environment have a significant influence on embryo implantation and development. However, data from human patients is highly limited and has not been revisited for decades. Empirical studies on *in vitro* fertilisation (IVF) have already confirmed that levels of pH and dissolved oxygen (DO) can inhibit embryo development and decrease implantation success rates. As the current success rate for IVF remains stagnant at 33%, information on the intrauterine environment can be of great importance. Hitherto, diagnostic capabilities to assess these parameters *in vivo* are still lacking.

This thesis describes the development of a system to monitor levels of pH and DO in utero. A pH and DO sensor together with a miniature reference electrode (RE) are incorporated onto a single, double sided sensor die sized 2.3 x 4.3 mm. The performance of the reference electrode and the individual sensors has been assessed to determine their applicability in an implantable system with power constraints, measuring unobtrusively for a period of 30 days. It is key that the biological relevancy is not compromised by sensor characteristics such as accuracy, precision and long-term drift.

Both pH and DO sensors used a miniature silver-silver chloride (Ag-AgCl) reference electrode, formed through the electrochemical deposition of Silver onto Platinum electrodes. Excellent performance has been observed over a 40 day period with a yield of 90% by employing a two day preliminary test. The use of an internal biocompatible electrolyte has been investigated, developed and tested. Although no added advantage was noted the described theory, simulation and results have led to an integrated sensor package developed in parallel with the sensors.

The sensing of DO levels within the biologically relevant range of 0.26 – 2.27 mg L^{-1} has been investigated. Arrays of disk-shaped microelectrodes inside a recess were fabricated and tested. By employing microelectrodes, the power requirements for the implantable system were kept to a minimum; this was further enhanced by measuring at short times using chrono-amperometric detection. A conditioning procedure has been developed and incorporated into the measurement scheme to ensure a reproducible signal of the transient response. A comparison between the performance of the DO sensor and the theory was given, based on simulated and measured data. An error of 0.5 mg L^{-1} has been observed for the final version of the DO sensors over the course of long-term experiments. The cause for the error has been shown to be delamination of the photoresist surrounding the electrodes, something which could only be observed during the long-term measurements. A lower limit of 1 mg L^{-1} was determined. This is within the biologically relevant range.

A pH sensor has been developed based on metal-metal oxide films of Iridium oxide (IrO_x). Two deposition methods have been investigated: Thermal Iridium oxide Films (TIROF) and Electrodeposited Iridium oxide Films (EIROF). The sensors have been characterised based on their short- and long-term performance. Drift values for the TIROF sensors showed good performance during long-term operation. Drift values were <0.02 pH day^{-1} with an accuracy of 0.24 pH. The pH sensors formed by electrochemical deposition have been investigated in a similar manner. Although the sample size was smaller compared to TIROF, a typical drift of 0.02 pH day^{-1} has been observed with high accuracy. To enhance the pH sensors performance during long-term measurements a method for an on-chip calibration has been developed and tested. Based on simulation models, locally generated pH gradients have been used to obtain the current status of the pH sensors. Findings during the experiments have resulted in an unconventional and novel approach to this method of self-calibration, relying on a preconditioning cycle rather than a differential change in pH.

All of the individual sensor components have been assessed for their biocompatibility. Human endometrial epithelium cells were cultured and exposed to the different components as per *ISO19033*. Cytotoxicity was not observed in any of the materials. Integration of the separate sensors into a single package, capable of housing all the components has been performed and is currently being manufactured by external parties. The integrated sensor head has opened up a new diagnostic tool for intrauterine studies. For the first time clinicians can offer a means to assess the critical parameters *in utero* and aid couples in achieving their dream.

Academic Thesis: Declaration Of Authorship

I, Roeland H.G. Mingels

declare that this thesis entitled

"Development of a multi-parameter in vivo sensing platform for intrauterine studies and subfertility diagnostics"

and the work presented in it are my own and has been generated by me as the result of my own original research.

I confirm that:

1. This work was done wholly or mainly while in candidature for a research degree at this University;
2. Where any part of this thesis has previously been submitted for a degree or any other qualification at this University or any other institution, this has been clearly stated;
3. Where I have consulted the published work of others, this is always clearly attributed;
4. Where I have quoted from the work of others, the source is always given. With the exception of such quotations, this thesis is entirely my own work;
5. I have acknowledged all main sources of help;
6. Where the thesis is based on work done by myself jointly with others, I have made clear exactly what was done by others and what I have contributed myself;
7. Parts of this work have been published as:

> Ng, K.Y.B., Mingels, R., Morgan, H., et al., *In vivo oxygen, temperature and pH dynamics in the female reproductive tract and their importance in human conception: a systematic review.* Human Reproduction Update, 2018. 24(1): p. 15-34.

Signed: .....

Date: .....

Table of contents

Nomenclature

APS	Ammonium persulfate
ART	Artificial reproductive techniques
BDD	Boron doped diamond
CCS	Cupper-Cupper sulfate
CE	Counter electrode
CMOS	Complementary metal oxide semiconductor
CP	Conditioning procedure
CS	Chitosan
CV	Cyclic voltammetry / cyclic voltammogram
DI	Deionised
DO	Dissolved oxygen
DOC	Dissolved oxygen concentration
EIROF	Electrodeposited Iridium oxide film
FBS	Fetal bovine serum
FET	Field effect transistor
FNA	Fuming nitric acid
GI	Gastrointestinal
Gp	Genipin
HCD	High current density
HEC-1A	Human endometrial cell line (1A)
HFEA	Human Fertilisation Embryo Authority
HER	Hydrogen evolution reaction
IrO_x	Iridium oxide
ISFET	Ion sensitive field effect transistor
IUD	Intrauterine device
IUSD	Intrauterine sensor device
IV	Intravenous
IVF	*in vitro* fertilisation
LCD	Low current density

LOQ	Limit of quantification
LSV	Linear sweep voltammetry
M	Metal
MEMs	Mechanical-Electrical Microsystems
MO	Metal oxide
NICE	National Institute for Healthcare Excellence
OCP	Open circuit potential
ORP	Oxidation reduction potential
ORR	Oxygen reduction reaction
pAm	Polyacrylamide
PBS	Phosphate buffered saline
PDMS	Polydimethylsiloxane
PECVD	Plasma enhanced chemical vapour deposition
PhD	Doctor of Philosophy
PMMA	Polymethylmethacrylate
POC	Point of care
PVC	Polyvynil chloride
RE	Reference electrode
RIE	Reactive ion etch
SCE	Saturated calomel electrode
SHE	Standard hydrogen electrode
TIROF	Thermal Iridium oxide film
UoS	University of Southampton
WE	Working electrode

Acknowledgements

I would like to say thanks to all the people who have helped me achieve this work. Firstly, Prof. Hywel Morgan and Prof. Ying Cheong. I am grateful to have been guided by you throughout this PhD. Without your knowledge, advice and resources this work would not have been possible. I have truely enjoyed this project and the lab environment and am thankful that I can still continue the work today. I would also like to thank all the colleagues who helped me with the clean-room fabrication in particular Ying Tran and Dr. Sumit Kalsi. I would also like to thank Bonnie Ng. as a fellow author on the publication and Kri Muller for her help with the cytotoxicity assays.

A warm thank you goes out to the Vivoplex team, which I have considered myself part of, and have watched grow during the course of my PhD. In particular Dr. Tania Read for her help with the optimisation of the protocols. Special thanks to Dr. Shilong Lu who has been my Vivoplex colleague form the beginning, when it was just the two of us. I would like to thank you for all your guidance and practical know-how. You are the most optimistic and driven person I have ever seen, and I consider you a great example.

A thank you is in place for all the friends I have made here in Southampton: Marios Stravou, Carlos Honrado, Kai Chang, Yuetao Li. A special thank you to Josh Robertson, for his Scottish roots. Riccardo Real for his kitchen talk. Josip Ivica for his irreplaceable craziness. Anna Desalvo, as a neighbour and master chef. Till we meet again.

I would like to end with a few words to my dearest family:

Paul en Carla, Rietje en Laurent, Astrid; Iech wel uuch hartelek daanke veur al wat geer veur miech gedoon hob door de jaore heen. Oeteraard ouch veur Bompa en Bomma, tante Lieske en Ome Jos. Iech hoop dat geer wet dat oondaanks dat iech altied wied eweg bin gewees, mien thoes nog altied in Mesteech ligk. Kri, veer zien al hiel lang saame en iech wel d'ch bedaanke veur alle steun, zorg, holp en leefde door de jaore.

Chapter 1 -Introduction

Technological developments in the field of medical diagnostics have shown an increasing trend towards low cost, accurate and reliable devices (1-3). The necessity to limit healthcare costs has pushed the development of point of care (POC) diagnostic. These are patient friendly devices, capable of obtaining data during a day-to-day routine (4-6). New technologies, obtained through research in nano-technology and micro-electronics, have created a vast database of research topics and market opportunities including, micro electro mechanical systems (MEMS), microfluidic devices, bio- and electrochemical sensors (3, 7, 8). The compatibility of these technologies with conventional complementary metal oxide semiconductor (CMOS) fabrication processes, has enabled their use in newly developed diagnostic tools.

Of particular interest is the application of these systems in an *in vivo* environment. The benefits of an *in vivo* sensing platform can easily be understood. Not only does it provide accurate and direct readings at the site of implantation, but it also provides more comfort. A well-designed implanted sensor system is able to operate from the patient's home, increasing comfort, and providing accurate data during their day-to-day routine, resulting in a realistic health profile. As a comparison, invasive sensors, such as intravenous (IV) probes require hospitalisation and are considered less comfortable for patients. Furthermore, the current generation of wearable sensors only provides data limited to superficial organs i.e. the skin, and blood vessels. Their inability to measure deep inside the human body limits their field of application (5, 9-12)

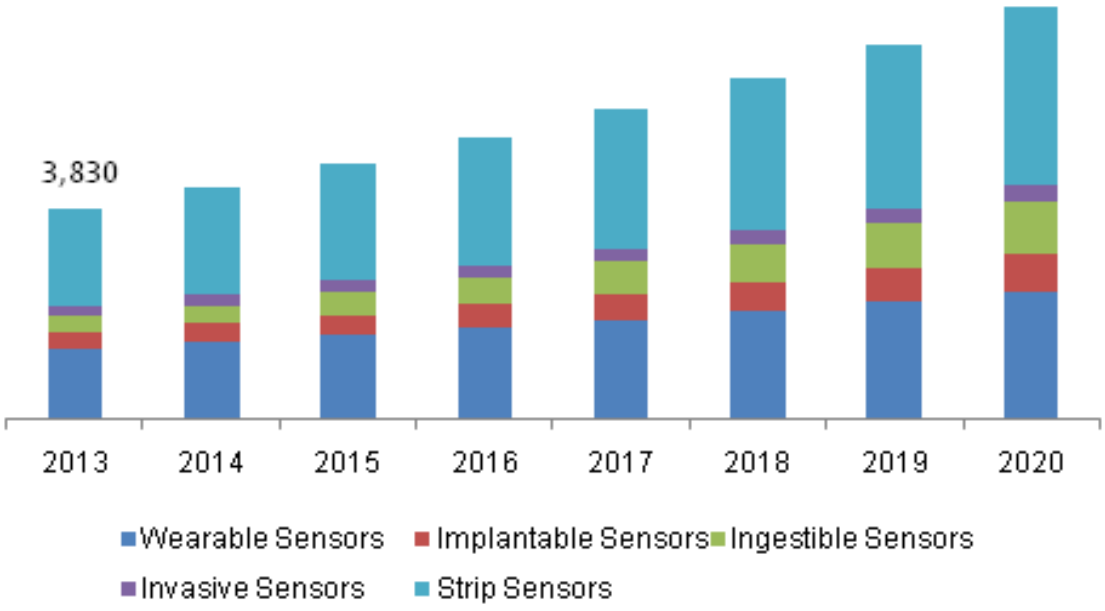

Figure 1.1 - Disposable, medical sensors market trend as researched by Grand View Research. Y-axis) Market value in billions of united states Dollars; x- axis) time in years (1).

The main drive behind the development of a sensor system for diagnostics remains the commercial and healthcare need for a specific system (3). As is shown in Figure 1.1, a steady increase in market value is expected to 2020 in all sectors (1). A distinction should be made between *ex vivo* and *in vivo* sensing devices. Regarding the first: the increase in wearable sensor technology can be contributed to its relatively easy development and variety of application including sports and workplace health monitoring. Strip sensors, are cheap, disposable and can be used by the patient to provide preliminary results on health status. Regarding *in vivo* sensing: ingestible sensors such as the endoscopic capsules are seeing increased usage due to accurate and patient friendly imaging of the intestinal tract (13). Invasive sensors are increasingly being incorporated in IV and needle based devices to monitor physiological parameters, including oxygen and glucose concentrations (12, 14).

In vivo sensing using implantable devices is one of the most researched fields to date. However, difficulties have to be overcome before a successful system is developed, as the internal environment of the human body poses a challenge for their stability, life-time and ability to communicate. First, issues with biofouling result in inaccurate readings and influence sample delivery to the sensing site. Second, sensor degradation and rejection, caused by the foreign body immune response, demand well designed sensors which are resilient and biocompatible (15). Third, long-term monitoring is limited by power consumption of the complete system (16). Fourth, data transmission through the body puts strict limitations on the carrier wave frequency (17). Fifth, size limitations require miniature sensors and electronics. Lastly, the strict rules and regulations regarding the materials used, demand extensive testing and trials. All of the fore mentioned issues make the application of implantable devices highly specific and only viable when there is a large market demand. A market of interest for the application of such a system, which has seen an increase in growth, is the human reproduction and fertility market (18).

This thesis describes the development of a multi-parameter implantable sensor for use in an implantable platform for studies *in utero* and subfertility diagnostics; specifically targeting dissolved oxygen (DO) and pH. Hitherto, no tool exists to monitor the intrauterine physiology *in vivo*, and thus a ‘black-box’ exists for clinicians. The platform used for implementation of the sensors was developed in a previous PhD project at the University of Southampton (UoS), and consists of a miniaturised electronics, data-communication and wireless power transfer links (19). An introduction to the subject matter and biological background to the project is given in this chapter. The following chapters discuss the different aspects of the sensor development process together with the results and discussion.

1.1 The need for intrauterine sensing

Before discussing the necessity for intra-uterine studies and subfertility diagnostics, it is important to determine what defines sub- and infertility. The National Institute for Health and Care Excellence (NICE) state that a person is considered to be sub-fertile when:

"A woman of reproductive age has not conceived after 1 year of unprotected vaginal sexual intercourse, in the absence of any known cause of infertility."

If after two to three years the couple is still unable to conceive they are considered to be infertile. Figures from the 2013 report from the Human Fertilisation and Embryology Authority (HFEA) further show that 16% of the couples fail to conceive within the first year and 8% in the second year (20, 21).

Couples in the developed world are increasingly being confronted with fertility issues. It is estimated that currently one in six couples have difficulty conceiving (21, 22). A rise in fertility treatments and artificial reproduction techniques (ART) has been observed over the past few years. Partly, this can be attributed to the later age at which women in the developing world start to conceive. It has been shown that as the age of the female increases, the chance of successful conception decreases (23). The consequences for patients diagnosed with infertility exceed the general inability to conceive offspring. Studies have shown that the inability to procreate causes distress in couples, and results in feelings of anger, anxiety, worthlessness and marital stress (24, 25). Especially when no underlying cause is identified, these feelings are amplified. Hence, as more people are looking for help when confronted with sub- and infertility, the necessity to accurately determine the cause becomes of great importance.

According to NICE the main causes for infertility in females include ovulary disorders, tubal damage (tubo-peritoneal) and cervical abnormalities. Charted data for main causes of infertility are shown in Figure 1.2. In 18% of the cases no explanation for the infertility can be given and this percentage is expected to increase to over 25% (20, 26, 27). It is expected that the intrauterine environment could have an influence on the lack of conception in the unidentified cases. However, to-date only little is known about its physiology, and there are no means available to accurately assess the parameters that influence the development of the embryo within the womb, which include pH and DO.

Intravaginal sensors have been developed and include temperature sensors for ovulation monitoring and pressure sensing for intra-vaginal muscle recordings (28, 29). Vaginal pH monitoring through the use of swab sample analysis is also common practice (30). *Au contraire,* obtaining intrauterine readings is still uncommon. Limited *in vivo* measurements have been performed and are limited to blood-gas analysers which incorporate needle based sample devices and require hospitalisation. Furthermore, their focus is on the health of a developing foetus rather than investigating the lack

conception (31, 32). Hitherto, autonomous sensor platforms for continuous monitoring are still lacking, and as such is the focus of this work.

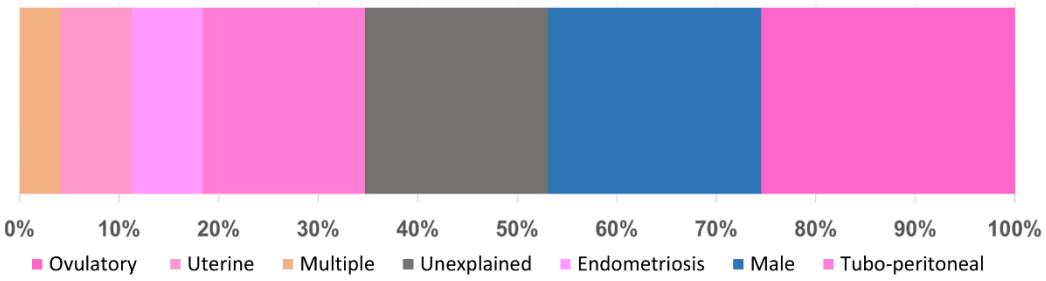

Figure 1.2 - Charted data on the main causes for infertility as defined by Evers et al., NICE, and the Complete Fertility Centre Southampton; Note the large share belonging to unexplained infertility, together with uterine related infertility (20, 26, 33).

1.2 The role of the uterus

Conception in humans is a complex process controlled on the molecular scale. As studies provide more insight into the factors influencing conception and embryo implantation, it is clear that the uterus, and the endometrium within, plays a vital role (34). Figure 1.3 shows a schematic representation of the human female reproductive system. Indicated is the endometrium; the inner lining of the uterus. Research has shown that implantation is a process in which there is tightly regulated cross-talk between embryo and endometrium (34, 35).

During the monthly cycle there is a short window during which the endometrium is receptive to the embryo. Here, the endometrium experiences decidualisation under the influence of progesterone and estrogen (36). Defects in the endometrium, including a too thin lining, altered expression of adhesive molecules and endometriosis can be determining factors in the success rate of implantation. Therefore, a thorough understanding of the endometrium and its signalling pathways is of great importance (34). In addition, the thickness of the endometrium has been shown to be of great influence on the implantation success rate and the survivability of the embryo.

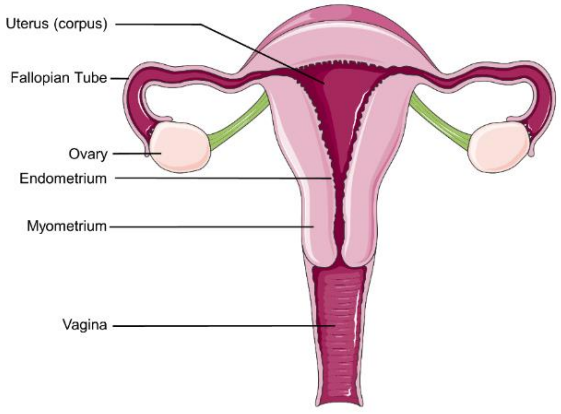

Figure 1.3 – Illustration of the female reproductive system. Indicated is the endometrium which plays a vital role in the reception of the embryo.

In humans and primates the cyclical change of the uterus is referred to as the uterine cycle. Here, three phases can be distinguished: menses, proliferative phase and secretory phase. A typical human menstrual cycle lasts twenty-eight days. The cycle starts with the menses and is recognised by the shedding of the uterine lining, also referred to as menstruation, and lasts approximately seven days. During the proliferative phase a follicle within the ovaries starts to develop and initiates the thickening of the endometrium. Prior to ovulation the endometrium has reached a thickness of 3-4 mm (37). The proliferation phase lasts seven days, after which ovulation occurs. During the early secretory phase the endometrium continues to prepare for a pregnancy and is receptive to the embryo for around fourteen days. This time period is known as the implantation window. It is here that blood vessels start to develop within the endometrium to facilitate the oxygenation of the endometrium to facilitate the developing embryo. If no conception has occurred within this period, menstruation is initiated and a new cycle begins.

For non-primates the cyclical change of the uterus is known as the estrous cycle. Here four stages are distinguished: proestrous, estrus, metestrus and diestrus, respectively. Implantation occurs during the estrus stage of the cycle (38). In the proestrous stage the follicle starts to develop within the ovaries; during the estrous phase the uterus is receptive to the embryo; during the metestrous and diestrous phase the uterine lining either starts to grow or is resorbed depending on whether or not implantation has occurred. Note that the duration, occurrence and activity of these phases is species dependent. Presented here is a general overview of the stages that are expected to occur in all said species discussed next.

1.3 Dissolved oxygen within the female reproductive tract

As is the case throughout the human body, the oxygen levels within tissue are controlled by the partial pressure differences between the arteries and the surrounding tissue. As the bloodstream, saturated with haemoglobin bound oxygen reaches the reproductive tract, the partial pressure difference in oxygen (pO_2) causes a diffusional flux from the arteries into the tissue (39).

$$C = \alpha\, pO_2 \qquad (eq.\,1.1)$$

Unlike pO_2, dissolved oxygen is a measure of concentration (C) rather than pressure relating to the amount of oxygen dissolved in a liquid under a given pressure and at a set temperature and salinity. The two are related to each other by Henry's constant (α) which describes the solubility of the species of interest within a certain media, as shown in equation 1.1. Here, pO_2 represents the partial pressure of oxygen within the atmosphere in mmHg and α solubility of oxygen within a liquid. For a 13% atmospheric pO_2 i.e. 100 mmHg as present within the lungs alveoli, the DO value can be estimated as 1.77 mg L^{-1} with Henry's constant for blood set equal to 0.0031 mL/mmHg/dL. The change over time for the species dissolved within said liquid is described by Fick's laws, as shown in equation

1.2. Fick's first law describes the diffusional flux for a concentration *C* across a distance *x*. Where *D* is the diffusion coefficient and equals 2.1 10^{-9} m^2 s^{-1} for oxygen in water[1]. Fick's second law, shown in equation 1.3, describes the change in concentration, $\delta C\ \delta t^{-1}$, over time and its relationship to distance, *x*. Both equations describe the case for one-dimensional diffusion.

$$J = -D\frac{dC}{dx} \qquad (eq.1.2)$$

$$\frac{\delta C}{\delta t} = D\frac{\delta^2 C}{\delta x^2} \qquad (eq.1.3)$$

Because the diffusional flux is related to distance, tissue that lies further away from the arteries is less oxygenated. Within the uterus the endometrial tissue contains the blood vessels and thus the supply of oxygen to the surrounding cells. As illustrated in Figure 1.4, Oxygen diffuses from the spiral arteries, through the endometrium towards the epithelium. From here, it can be expected that the oxygen level established *in utero* is directly related to the concentration gradient across the endometrial epithelium. It has been shown by *Isaacs* and discussed by *Nejat et al.* that a thin endometrial lining is related to implantation failure. A negative effect on the implantation success rate was found in patients with a uterine lining of 3.7 mm, most likely due to higher level of oxygenation (40, 41).

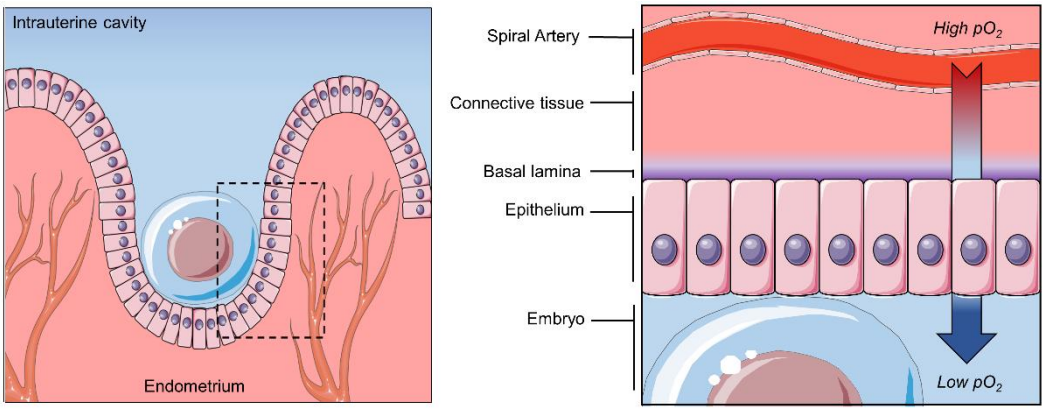

Figure 1.4 - Representation of the diffusional flux of DO from the endometrium into the uterine cavity. The high pO_2 around the spiral arteries causes a flux of dissolved oxygen across the epithelium into the intrauterine cavity providing the embryo with oxygen (38).

Because menstruation is a cyclical event, the resulting intrauterine dissolved oxygen concentration (DOC) is of a cyclical nature. Increased oxygenation of the growing endometrium through the arterial growth within the underlying tissue is enhanced to facilitate the developing embryo. It has been postulated by *Casper et al.*, that a thin lining exposes the embryo to high oxygen levels from the spiral arteries surrounding the uterus. This increase in oxygen tension between the embryo and

[1] Note: this value will be used as the diffusion coefficient for dissolved oxygen throughout this work.

endometrium causes embryo implantation and development to fail (42). Assessment of the endometrial thickness can be performed by ultrasound and is common practice to determine uterine receptivity (43).

Figure 1.5.a shows the measured pO_2 within the uterus of Guinea pigs, rats and hamsters as performed during animal trials by *Garris*, *Mitchell*, *Yedwab* and *Kaufman* (44-47). From the figure it is clear that there is a variation based on the cyclical nature of the uterine lining. In all studies a drop in pO_2 occurs during the estrus phase, indicating that the uterine lining has thickened. This in contrast to the proestrus phase in which the uterine lining is thin. From these studies, the range for the intrauterine pO_2 can be determined as lying between 6 - 50 mmHg i.e. 0.26 - 2.27 mg L^{-1}.

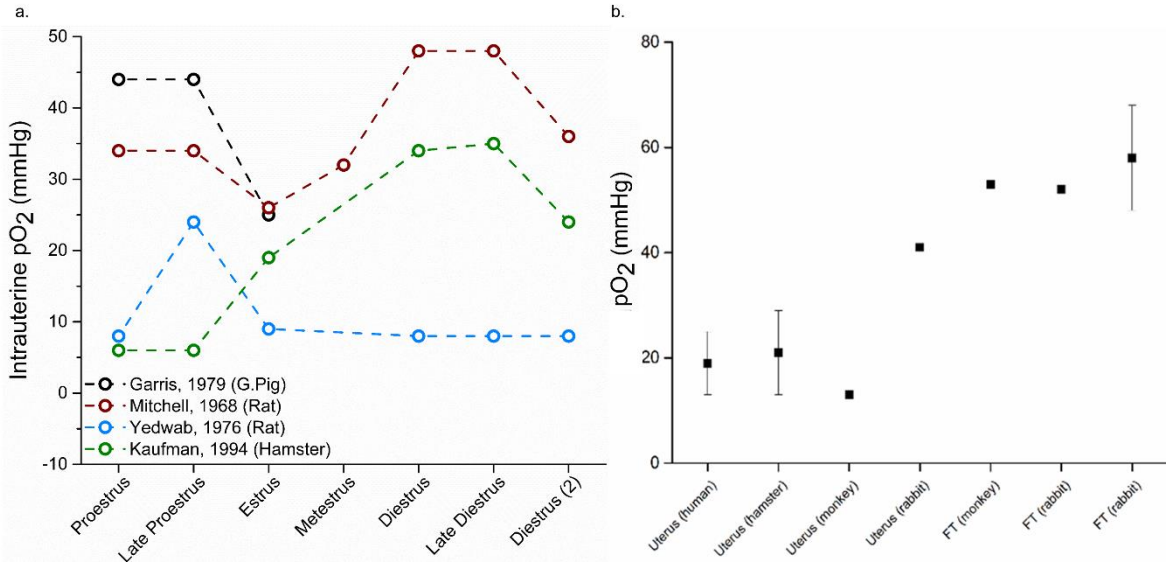

Figure 1.5 - a) Results of four intrauterine *pO2* studies on animals during the estrus cycle. The variation in *pO2* throughout the cycle is confirmed in all studies and showing a reduction of intrauterine *pO2* in the estrus phase. b) Oxygenation within the uterus and fallopian tubes in humans, rabbits, hamsters and monkeys. The study shows that there is an oxygen gradient within the female reproductive tract with high oxygenation in the fallopian tubes compared to lower *pO2* in-utero (38).

Figure 1.5.b shows a summary of the results from studies on pO_2 within the uterus and fallopian tubes for animals and humans (stage not specified). It can be seen that there is an oxygen gradient within the reproductive tract ranging from high oxygenation in the upper regions, to lower oxygenation in the lower regions (47-50). Part of the variation between the studies can be attributed to the measurement techniques. In most cases electrochemical Clark-type devices are surgically inserted into the tissue of interest (a detailed description of the Clark-electrode and its limitations is given chapter 4).

Failed to report in many instances, is the degree of tissue damage that occurs during this implantation. As the Clark sensor relies on the partial pressure between the external environment and the internal electrolyte, histological effects can have an effect on the outcomes as tissue oxygenation is increased. Furthermore, between the studies there is a large difference in measurement times. Ranging from twenty minutes by *Mitchell* to only a few minutes by *Fischer* (46, 50). However, *Ottosen et al.*

showed that, the variation of the pO_2 for humans varies greatly with means between 6.4 - 32 mmHg; measured using optical DO sensing (51). This opens up room for questioning the accuracy of this type of surgical assessment under the influence of general anaesthetics and uncontrolled conditions.

Kaufmann and *Mitchell* have in addition performed interesting studies on the amplitude and frequency of change during the different stages of the estrus cycle; a summary of the results is shown in Figure 1.6. The pulsating nature of blood to many of the organs could be part of their observed pulsed oxygenation. The amplitude lies well within the set range found in the outlined studies; a peak frequencies of 26 and 19 mHz were determined (46, 47). The latter can be used to set a biologically relevant sampling rate, which shows that there is a peak almost every minute.

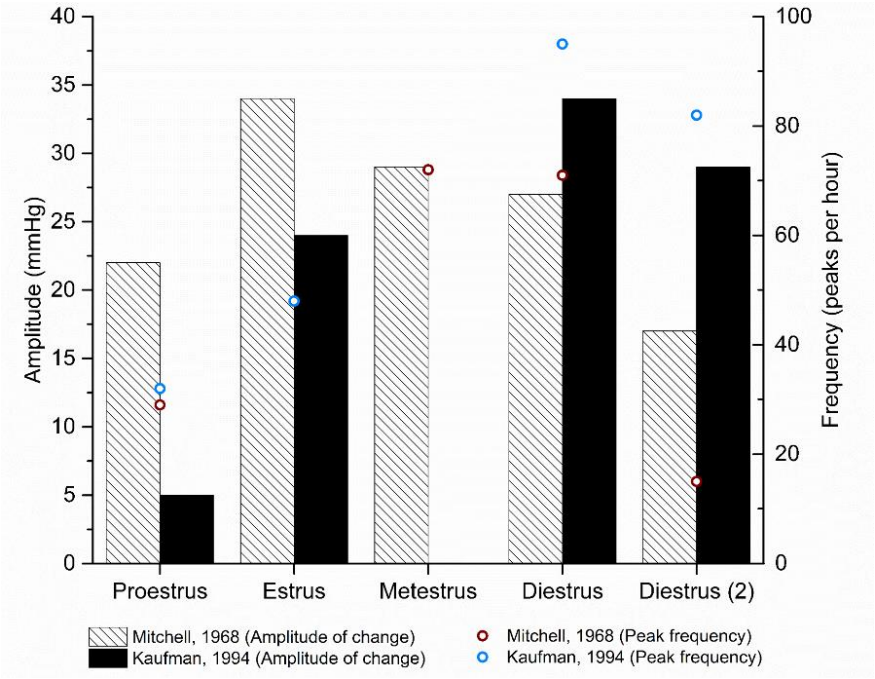

Figure 1.6 – Summary of the studies on the pulsating nature of the intrauterine pO_2. Shown is the amplitude and the frequency for the pO_2 variation (38).

1.4 pH within the female reproductive tract

The regulation of pH within the human body is critical for living organisms. The human physiology employs buffers to maintain the pH on the intra- and extracellular levels. A buffer system consists of a weak acid in combination with its conjugate base. Its function is to compensate changes when acids and basis are added. According to Le Chattelier's principle: the chemical equilibrium within a system will re-establish itself based on the changing factor. As proposed by *Arrhenius* in 1884, an acid can be defined as a substance which produces a hydronium ion (H^+) when in aqueous solutions. A base on the other hand produces a hydroxide (OH^-) anion under the same condition (52). For acids the equilibrium reaction as shown in equation 1.4 occurs. Here, *HA* denotes the acid and A^- the base.

As described by *Henderson* and improved upon by *Hasselbalch*, the pH of the acid-base equilibrium reaction can be determined using the equally named Henderson-Hasselbalch equation, which for acids is shown in equation 1.5 and 1.6.

$$HA + H_2O \rightleftarrows A^- + H^+ \qquad (eq.1.4)$$

$$pH = pK_a + log_{10}\left(\frac{[A^-]}{[HA]}\right) \qquad (eq.1.5)$$

$$pK_a = -log_{10}(K_a) = -log_{10}\left(\frac{[H^+][A^-]}{[HA]}\right) \qquad (eq.1.6)$$

Thus, for any given concentration of weak acid and conjugate base the pH can be determined. The relationship between the pH, acid ionisation constant (K_a) and the concentrations of the products is shown in equation 1.6. A buffered system is able to compensate for small changes in the concentration of hydronium or hydroxide by changing into its counterpart through dissociation. The buffer capacity is determined by the concentration of the weak acid and conjugated base within the solution i.e. the more is present, the more can be buffered.

Three main buffer systems exist within the human body: bicarbonate, phosphate and protein. The first is used for cell respiration. Carbon dioxide (CO_2) in liquid forms carbonic acid which, when buffered, dissociates into hydronium and bicarbonate resulting in acidification. To prevent a high degree of acidification the CO_2 is expelled by the lungs; the phosphate buffer system controls the intracellular pH by buffering incoming hydroxides and hydronium ions using dihydrogen- or hydrogen-phosphate; proteins contribute by interacting with the acids accepting or donating protons (39, 52).

Within the female reproductive tract different pH levels are maintained, as illustrated in Figure 1.7. The pH within the vagina is low compared to the *corpus* and fallopian tubes. The vaginal pH serves a protective role and is lethal for sperm and bacteria. In contrast, the pH within the *corpus* has an embracing role, creating an optimal environment for embryo implantation and development. Little is known about the regulation of the intrauterine pH but it can be expected that a diffusion based mechanism controls the pH in the uterine fluid giving rise to a gradient extending from the extracellular pH near the epithelium, controlled by all the aforementioned buffer systems.

As shown in Figure 1.7 the intrauterine pH varies between pH 5.4 in the cervix to pH 7.94 in the fallopian tubes (53-61). The pH range of interest can therefore be set as pH 6 to pH 8. It can clearly be seen that there is a niche on the intrauterine pH levels, as none of the studies have been performed on human subjects. Variations of the pH within the female reproductive tract are controversial.

As determined in the studies by *Mather et al.* and *McLachlan et al.* a difference during the estrus cycle has been observed, with a variation of 0.4 to 0.1 pH, respectively (53, 61). It can therefore be concluded that a variation within this range has to be distinguishable.

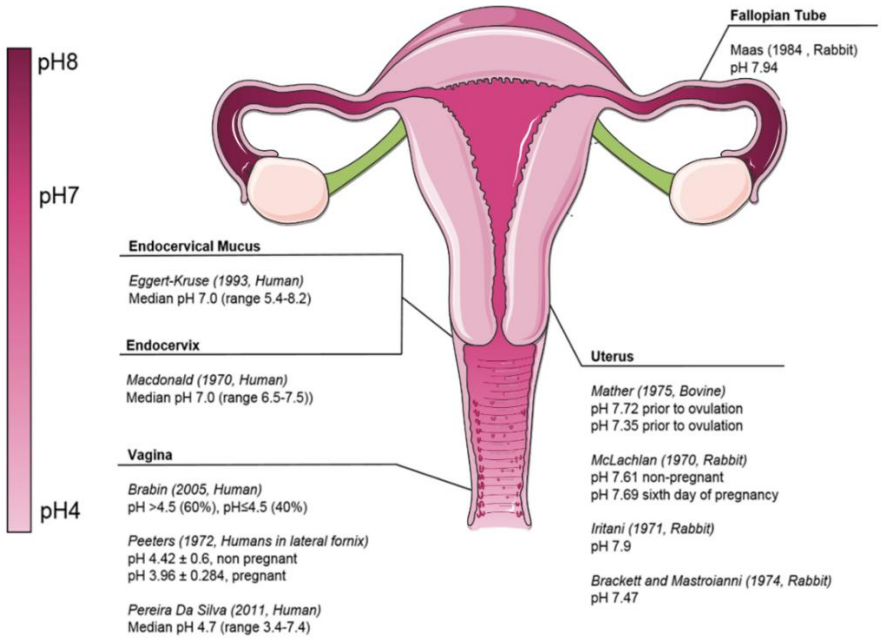

Figure 1.7 – Summary of studies investigating the pH within the female reproductive tract. The colour gradient indicates the change in pH from acidic in the vagina to more alkaline in the fallopian tubes. Note that intrauterine data has solely been obtained through animal studies (38).

1.5 The role of *in vitro* fertilisation

For couples confronted with unknown subfertility, the only treatment available is artificial reproduction. An increase in ART is noted in the current figures on the *in vitro* fertilisation (IVF) market value. The market was valued at $ 9.2 billion in 2012 and is expected to grow to $ 21.6 billion by 2020 (18). This expected rise has led to an increasing amount of research on successful development and implantation of human embryos (21, 62). Unfortunately success by means of IVF cannot be guaranteed. In fact, success rates of IVF have been stagnant over the past decade with one-in-three odds (20, 21). Regardless of the discomfort, costs, stress and poor odds, couples confronted with unexplained subfertility see IVF as their only means to successfully conceive.

In general, a typical IVF cycle consists of the following steps: boosting of the follicle and oocyte retrieval, insemination, culturing and incubation, embryo implantation. A schematic representation is shown in Figure 1.8. Of particular interest is the fertilisation and culturing step. Here the retrieved oocyte is fertilised using the partner's sperm. Followed by the embryonic development, in lab conditions, using culture media. It has been found that the success of IVF remains compromised by the culture conditions, resulting in implantation failure and retarded intrauterine growth (63-65). Therefore, optimisation of the culture media is an important step in IVF development.

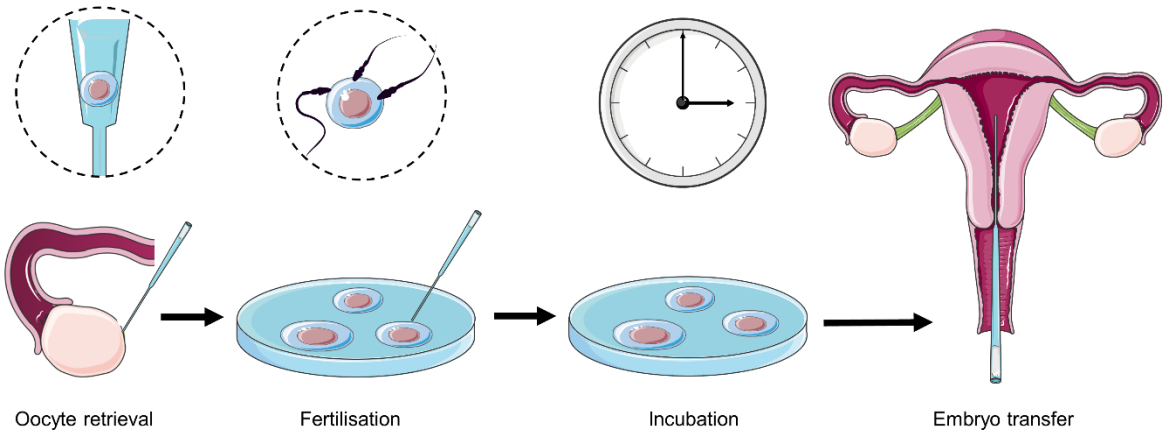

Figure 1.8 - Representation of an IVF cycle; starting from bottom left with egg retrieval, insemination with male subjects sperm, culturing and incubation of the oocyst and implantation of the developed embryo.

A logical step towards enhancement of the success rate would be aimed at mimicking the intrauterine environment for culture conditions. However, current developments have been based on empirical work. The key parameters of DO and pH are regulated by the conditions inside the incubator through the control of temperature, oxygen, and carbon dioxide levels. According to *Gardner et al.*, embryo development at concentrations of 5% atmospheric oxygen (1.77 mg L^{-1}) are optimal. In contrast, a higher concentration, 20% atmospheric oxygen, has shown to inhibit the growth of the embryo. The first is considered to resemble the intrauterine oxygen level more closely (66, 67). The influence of pH on embryonic development has also been assessed. Optimized pH is considered to be between pH 6.4 and pH 7.4; at higher levels, blastocyst development and gene expression was found to be negatively affected (67, 68).

1.6 Implications of the intrauterine knowledge

The results from the discussed studies show that there is a lack of data from human patients on both pH and DO *in utero*. Most of the research papers that have been assessing the parameters are from past decades, showing a lack of progress in the field. This can be partly attributed to the fact that no means exist to perform minimally invasive measurements of the intrauterine physiology. Important to note as well is that the measurements are not performed on a continuous basis. It has been shown that, all events occurring within the uterus are cyclical and of a varying nature. Furthermore the variations between studies indicate that absolute determination of DOC and pH might not be valid. Rather, variations from subject to subject and large fluctuations might be more indicative of subfertility. The knowledge obtained with embryo cultures is therefore empirical in nature. Thus, intrauterine data, especially during the course of a complete menstrual cycle, will greatly benefit ART research and development, if only to confirm the empirical knowledge already gained. It is therefore reasonable to assume that elucidation of the uterine environment can boost success rates helping couples achieve their dream through personalised health plans.

1.7 Implantable devices and multi-parameter sensing systems

Intrauterine sensing is a novel method for fertility diagnostics. Hitherto, no system exist that performs this task in an autonomous manner from the patient's home. To gain insight into the aspects that comprise the development of this new type of intrauterine sensing device (IUSD) an outline of existing devices is given. From an application perspective conventional intrauterine devices (IUDs) most closely resemble said system; from a functionality perspective blood-gas analysers and endoscopic capsules show closest resemblance.

1.7.1 Intra-uterine devices and fertility monitoring

Hitherto, a variety of intrauterine devices exist. Most common are the contraceptive devices under their trade names: *ParaGard* and *Mirena*® (69, 70). The contraceptive IUDs are implanted by a clinician and remain within the uterus; implantation times can last for years depending on the brand. As illustrated in Figure 1.9, an IUD consists of a plastic body made out of medical grade low density polyethylene. The lower end contains a coil which can contain either Cupper (Cu) or hormones. In both cases, the gradual release of the components prevent fertilisation by killing and immobilising sperm, respectively. The IUD is inserted via an insertion tool operated by the clinician. The IUD sits inside the tool which is inserted into the uterus. A push mechanism deploys the IUD which unfolds the wings, preventing it from dropping out during everyday activities. The chord at the end is used to retrieve the device.

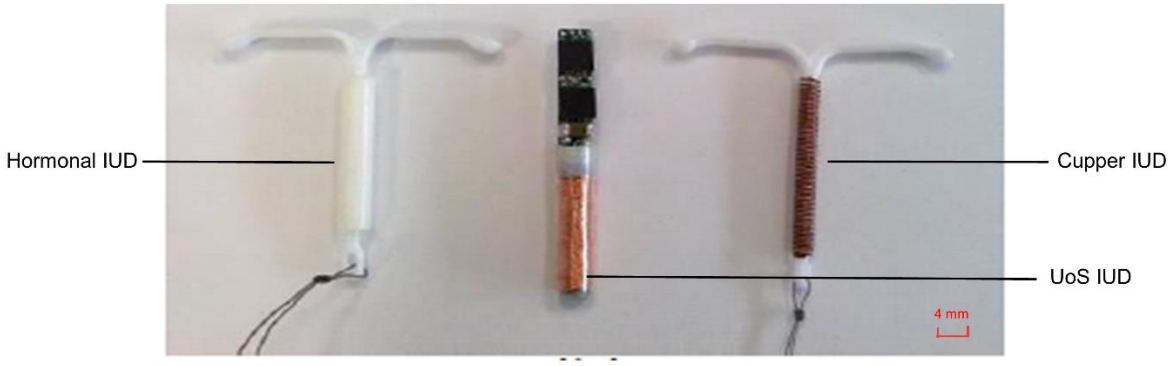

Figure 1.9 – Size reference for three types of IUD. Left to right) Hormonal IUD (*Mirena*®), UoS implantable IUSD, Cupper IUD (*ParaGard*) (19).

IUDs come in a variety of sizes to compensate for differences in physique between patients. The IUSD developed in previous work at the UoS mimics the shape of the conventional devices. As can be denoted from Figure 1.9, the size constraint for the sensor is approximately 4 mm. The platform consists of a coil for data and power transfer, a radio frequency identification processor, a microcontroller unit and a temperature sensor. A communications link between the IUSD and an externally worn receiver belt is continuously maintained. Successful laboratory tests and animal trials

have been performed with the system. This platform is used for the implementation of the sensors developed in this work and is part of *Vivoplex* (19).

Fertility monitoring devices are available for purchase to give prospective parents insight into their fertility. In all of the fertility monitoring products, the aim is to predict the implantation window. Most basic are temperature devices which use basal body temperature readings to determine the phase of the menstrual cycle (71). More advanced methods relate optimal implantation time to hormone levels. An example is the *OvaCue* which uses measurements of the electrolyte concentration within the saliva and cervical mucus under the influence of estrogen (72). The *Clearblue* fertility monitor bases its predictions on the hormone levels found within urine samples. As hormone levels can directly be related to the menstrual cycle, high accuracy regarding the days of the implantation window can be achieved (73, 74). However, measurements are point based and rely on the user taking readings within the time-frame, lacking the continuous monitoring throughout the day. In none of the cases the critical parameters for embryo development are monitored. Thus, even if fertilisation is successful implantation can still fail without any underlying cause.

1.7.2 Blood-gas analysers

Blood-gas analysers are common in hospital settings and are employed to directly determine a wide variety of parameters within a patient's sample. Parameters commonly assessed are pH, DO, lactate, glucose, carbon dioxide and potassium. Devices such as the *iStat* and *EasyStat* rely on delivery of the sample through extraction and insertion of blood from the patient (75, 76). In contrast more complex in-line analysers such as the *Proxima* can extract samples bed-side and thus provide a monitoring apparatus for continuous sampling (77).

The blood-gas analysers consist of a sample delivery system and disposable sensor chips which measure the species of interest. More details on the functionality of the sensors related to this work are given in the relevant chapters. The systems have a small footprint by the use of the latest in CMOS technology, employing miniature Clark-electrodes, conductivity sensors and ion-sensitive field effect transistors (ISFETs). Shown in Table 1.1 is an overview of the performance of a selection of these devices focussed on pH and DO. It should be noted that only the performance of the *iStat* has been independently verified in a study by *Harter et al.*

The blood-gas analysers have one mayor advantage compared to the implantable sensors presented in this work: they can be recalibrated on a regular basis. All sensors on the analysers are designed in a way that calibration prior to use is possible and in most cases this includes individual reading at set time points. As an example, a patented method, such as that of the *iStat,* calibrates the sensors using a solution of known concentration of the species of interest prior to the introduction of the sample (78). In-line devices incorporate known storage solutions between measurements, allowing for drift-

correction and recalibration. This form of recalibration means that continuous sampling is only partially true.

Table 1.1 – Overview of the performance of blood-gas analysers for DO and pH.

	DO		pH	
	Type	**Error**	**Type**	**Error**
iStat[1]	Clark	1.46 mg L^{-1}	Potentiometric	± 0.1 pH
EasyStat[2]	Clark	0.23 mg L^{-1}	Potentiometric	± 0.02 pH
Proxima[3]	Clark	0.04 mg L^{-1}	ISFET	± 0.01 pH

1 As per validation study by *Harter et al.*(79-81); 2 unverified study from FDA (82); According to brochure from *Sphere Medical Ltd* (77).

1.7.3 Endoscopic capsules

A critical aspect of the IUSD presented here is its capability to measure continuously over long time periods, and the ability to assess physiological parameters unobtrusively *in vivo*. Implantable devices which most closely resemble this type of system are of the capsule sort (83, 84). These capsules are employed to monitor and assess parameters in the gastrointestinal (GI) tract. Besides integrated camera systems, advances have been made regarding the incorporation of impedance sensors and electrochemical pH sensors, to monitor physiological changes along the tract (85-87). Types of pH sensors include: ISFETS and metal oxide sensors. Of particular interest is the latter, as discussed in chapter 5 (13, 88, 89) . Wireless data and power transmission is employed in all cases. In contrast to the system in this work, endoscopic capsules typically measure for a short duration (1-2 days), i.e. the time it takes for the capsule to pass through the gastrointestinal tract (88, 89). This is illustrative of the subjective nature of the term: 'long-term'. In GI applications a one to two day measurement period is long-term whereas for an IUSD the same term implies thirty days.

1.8 Research outline

This thesis describes the design, fabrication and testing of a multi-parameter sensing platform for intrauterine sensing of DO and pH. A system capable of performing this task, on a real-time basis, will aid researchers and clinicians alike in the proper diagnosis of subfertility for female individuals. The success rate of embryo implantation can be increased by elucidating the 'black box' that is the intrauterine environment. It is expected that: a system capable of assessing the key parameters *in utero*, will open a wider field of research on embryo implantation and human reproduction. Optimal treatment plans could be delivered by clinicians that employ such a system in their practice. Furthermore, the technology could confirm or disprove the results obtained with IVF.

The development of a long-term implantable system is challenging. History has shown that the promising prospects of everlasting implants have been difficult to achieve in practice. Limitations on implantation time, patient comfort, biocompatibility and sensor performance have all shown extreme complexity (16). The requirements for the *in vivo* sensors to be incorporated into an IUSD can be listed based on the following key aspects: size, accuracy and precision, stability, power consumption and biocompatibility.

First, the size of the IUSD is limited by the size of the uterus. Variations from person to person are common. The best criteria for size, is the size of conventional IUDs such as the *Mirena*®. As discussed in section 1.7, the size of a *Mirena*® is typically 4.3 mm in diameter, excluding the wings. Because this size constraint applies to the entirety of the implantable platform including the parts developed previously at the UoS, the sensor die size has to be smaller if it is to be implemented into the existing platform. In the previous work on an intrauterine platform a device size of 4.3 mm in diameter was achieved (19). Here, an arbitrary value of 2.3 mm width for the sensor is chosen, leaving an additional 2 mm for the packaging and encapsulation, or future miniaturisation.

Second, accuracy and precision are key parameters in sensors performance. To illustrate the difference between these characteristics, Figure 1.10 shows them in the form of targets. As can be seen, accuracy relates to the actual value that is to be determined i.e. the degree of error between a reference value based on a calibrant or calculation. In a linear calibration, this can be seen as the error with respect to the linear regression fit also referred to as the standard error. The precision and reproducibility relates to how well these values are repeated for individual and replicate sensor devices. In general, the precision of a single experiment can be said to be equal to the standard deviation; In contrast, the precision between experiments is the sum of the standard deviations divided by the square root of the data set. In an ideal case a sensor would be both accurate and precise. However, inaccuracy is easier to compensate in an implantable device that measures unobtrusively as it is most likely to be related to a systematic error and a post-implantation calibration can be performed. As long as the sensor maintains its precision changes in physiological parameters can still be determined.

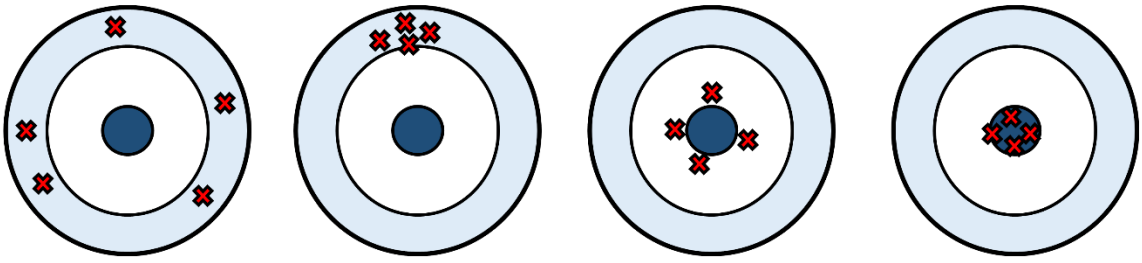

Figure 1.10 – Illustration showing the meaning of accuracy and precision using targets. left to right) Low accuracy and low precision; low accuracy and high precision; high accuracy and low precision; high accuracy and high precision.

Third, stability or drift relates specifically to the long-term performance of the sensors. Any sensor measuring unobtrusively is expected to drift over time. If the drift can be determined prior to the actual measurement, a correction factor can be implemented into the signal processing scheme, thereby improving the accuracy and precision of a given system over time. Drift is a particular problem in long-term *in vivo* applications as it is not possible to recalibrate to compensate its effect and highly dependent on the measurement environment.

It should also be noted that the long-term performance with respect to drift is a highly subjective term and more often than not, misused in literature. It only takes a quick search to find unsubstantiated claims on this performance characteristic. The characteristic is often extrapolated to without any scientific evidence in the form of measurement data over the stated time period. In contrast, this work aims to gives an estimate of expected drift values, i.e. an assessment of the precision of the drift, over a period of thirty days, measured unobtrusively with a high sample rate and compares these differences with the performance of macroscale, commercial devices to properly assess the confidence of the obtained measurements.

Fourth, of particular importance for a future application is the power requirement. In the previous work on an intrauterine device, a battery-less system was used, relying on energy harvesting techniques to power the implant. This sets the power consumption of the system within the µW range. It should be noted that this is a key aspect in the design and measurement methodologies of the sensor devices in this work. Wherever possible, power consumption is kept to a minimum.

Lastly, biocompatibility of the fabricated sensors is critical. Any implantable device has to be tested extensively for biocompatibility. In the case of electrochemical sensors, an interface exists between the sensors and the human body. Throughout this work materials which comply with biocompatibility legislation have been chosen. Biocompatibility tests have also been conducted and are discussed in Chapter 6.

1.8.1 Research hypotheses

For the development of the sensors the research question that is to be answered is two-fold and relates to sensor implementation and performance. The two questions are:

1. Can a miniaturised DO and pH sensor be developed which meets the power constraints set by an IUSD reliant on wireless-energy transfer, and integrated into a device which meets the size constrains posed by the human uterus?

2. Can the performance of this device be predicted within a tolerable accuracy and stability during the course of long-term measurements up to 30 days, without impairing the biological relevancy of the measured results?

Looking specifically at the IUSD discussed in this work and the key physiological criteria based on the literature study in this chapter, a summary of parameters is given in Table 1.2. The biological relevancy of the data is still up for debate. Not solely because there is a large variation between studies on intrauterine pH and DO. Rather, it is likely that differential values i.e. the variations and trend over time play a key role. It should also be stressed that, the fact that no means of measuring *in utero* exist to this date. As such, any data has a significant novelty in the biomedical field, elucidating the intrauterine environment.

Table 1.2 – Overview of the required performance for the DO and pH sensor.

	DO sensor[2]	**pH sensor**
Range	0.26 – 2.27 mg L^{-1}	pH 6 – 8
Accuracy	0.4 mg L^{-1}	0.2
Precision	0.2 mg L^{-1}	0.1
Quantifiable limit	0.1 – 0.4 mg L^{-1}	0.1-0.3 pH
Sample rate	Minutes	unknown

1.8.2 Structure of the thesis

An overview of the interrelation between the different aspects of the sensor development process is shown in Figure 1.11. For both sensors a reference electrode (RE) is required which provides the reference potential for the DO and pH measurements, as explained in detail in Chapter 3. The performance of both sensors is in part determined by this RE. A secondary aim within this research is to create a RE which can function in an intrauterine environment. In brief, this means that the potential stability has to be maintained or drifts in a predictable manner.

This thesis first discusses the sensor designs. A wide variety of designs have been developed, manufactured and tested. Hence, it is key to first give an overview and visual reference of the differences in designs to appreciate the evolution into a single sensor chip with dual functionality. The designs used are outlined in chronological order and named by type and will be referred to as such in the following chapters. The development of the individual sensors is discussed next. Each chapter discusses the theory and state-of-the-art of the sensors, followed by the materials and methods used to achieve the results.

[2] As per figure 1.5 and 1.6; values converted from mmHg to mg L^{-1}, assuming blood at 1 atm.

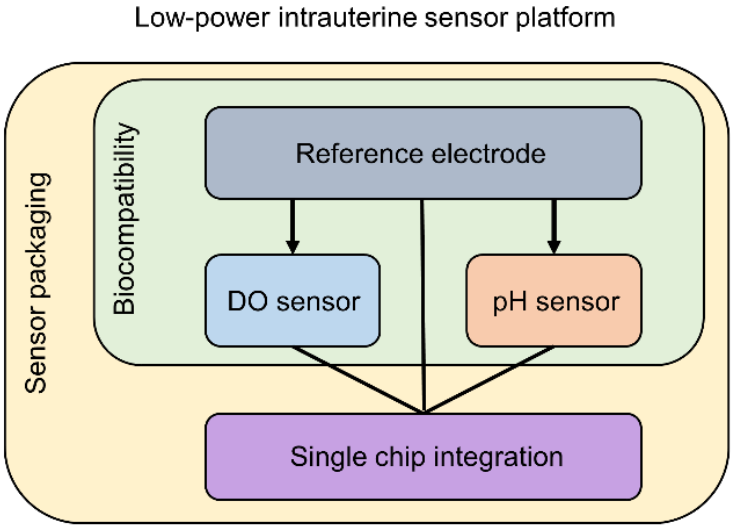

Figure 1.11 - Overview of the components within the project showing how the development of the DO and pH sensor is governed by the reference electrode. All three are integrated into a single chip. Sensor packaging and biocompatibility have played a key role throughout the project influencing material choices and design geometries.

Comparisons to theory are made and a comparative discussion based on literature and theory is given. Each chapter on the sensor development contains an overview and estimate of the yield to illustrate the reproducibility and viability of the sensor system. To further enhance accuracy during implantation, a novel on-chip calibration method has been devised (patent pending). By employing the knowledge gained in the development of the sensors an integrated self-calibrating sensor is proposed. The results of these tests are presented in Chapter 6.

The biocompatibility of the sensors is critical for the application and a biocompatibility study has been performed on the components of the sensor device. The biocompatibility testing has been performed as per *ISO10993:5*. In parallel to the sensor development a sensor package, to be used for implementation into the IUSD, has been developed. The results from the biocompatibility experiments and the package designs, followed by the final sensor package are discussed in Chapter 6. Throughout the course of this work interesting research aspects are highlighted based on discoveries made. A proposal for future investigations is presented in the future work, outlined in chapter 7.

1.9 Summary

This chapter discussed the need for and lack of a novel intrauterine sensor device. With an increased number of cases of unexplained subfertility and stagnant IVF success rates, the intrauterine environment has to be re-evaluated. The key parameters which influence embryo development and implantation include DO and pH. However, no means to assess these parameters *in vivo* are available and data obtained from patients is lacking. This work aims to develop a low-power DO and pH sensor which can assess the parameters unobtrusively over the course of one menstrual cycle, without impairing the biological relevancy of the data.

Chapter 2 - Sensor fabrication and design

The sensors are based on micro fabricated electrodes made on a glass wafer. Throughout the course of the work a wide variety and designs were tested for their quality as a pH sensor, DO sensor and RE. Modification and optimisation of the sensor lay-out and fabrication has been a continuous process. In order to give a clear view on the data, the fabrication of the sensor dies and the differences in their designs with respect to geometry and lay-out are discussed in this chapter.

2.1 Materials and methods

2.1.1 Platinum patterning

The Platinum (Pt) electrodes were formed though metal sputtering followed by a photolithographic pattern and etch process performed under clean-room conditions. An overview of the process is depicted in Figure 2.1. First, a glass wafer is cleaned using fuming nitric acid (FNA) followed by a dehydration overnight at 110 ^{0}C. The wafer was rinsed with nitrogen gas to remove any loose particulates from the surface. Second, Pt was deposited using a sputter deposition. The machine first performed a ten second plasma clean, followed by the deposition of a 25 nm Titanium (Ti) as an adhesion layer; next 200 nm of Pt was deposited. A FNA clean was performed after deposition, followed by a dehydration overnight at 110 ^{0}C.

The Pt pattern was defined using photo-lithography. First, the wafer was cleaned using nitrogen gas to remove loose particulates. Second, positive tone photoresists (S1813), filtered and at room temperature, was deposited via spin-coating. The wafer was transferred to a hot-plate for a soft-bake at 90 ^{0}C for one minute.

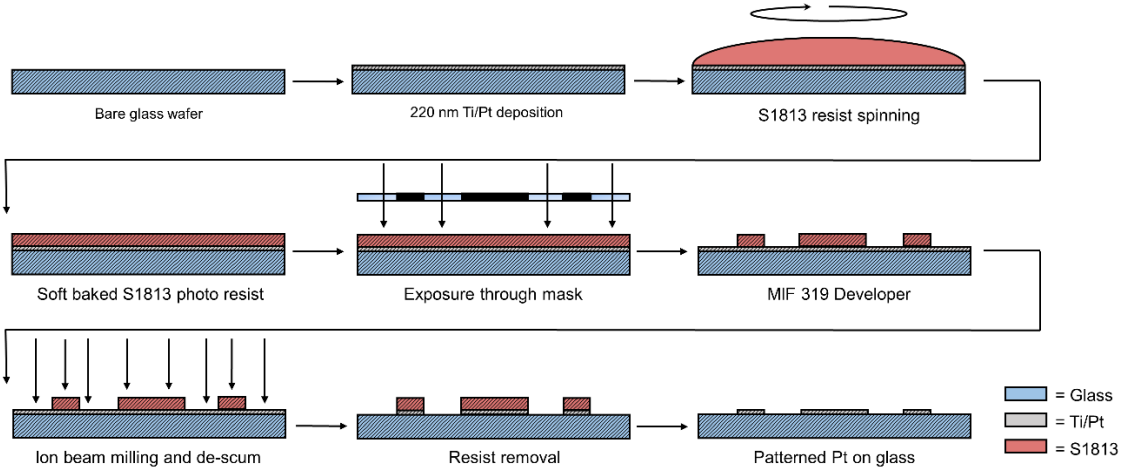

Figure 2.1 - Platinum patterning process overview. Titanium (20 nm) is sputtered on a glass substrate followed by 200 nm of Pt. Positive S1813 photoresist is spin coated, soft-baked and patterned. The patterned resist is developed in MIF 319 developer solution and rinsed with deionised water. Reactive ion milling is performed to remove the exposed Pt and Titanium. The protective layer of photoresist is stripped. The resulting patterned Pt can be used for further processing into sensor dies.

Acetate masks, printed and provided by *Photo-Litho UK*, with a minimal feature resolution down to 5 µm, were cut to size and taped to a 5 inch glass carrier slide using scotch tape. Prior to use the mask was inspected for any dirt or resist residues and cleaned if necessary. An EVG620 mask aligner was used for exposure. The mask aligner is calibrated on a regular basis and the exposure time calculated based on the calibration value.

Development of the photoresist was performed using MF340 developer solution, by immersing the wafer under continuous manual agitation; a rinse with deionised (DI) water completes the process. The developed features were checked on a surface profiler. A hard-bake at 120 ^{0}C for twenty minutes completed the process. Patterning was performed using an *Oxford instruments IonFab 300Plus*. The wafer was transferred and loaded into the ion beam mill. The process removed the Pt left uncovered by the photoresist. After the ion mill process, the resist was stripped. The wafer was now ready for the second patterning which defined the DO sensor and passivated the electrode tracks.

2.1.2 Silicon dioxide adhesion patterning

During the later stages of this research an intermediate layer of Silicon dioxide (SiO_2) was deposited before patterning of the feature defining photoresist layer for the DO sensors. The addition of this intermediate layer promoted adhesion between the resist and the wafer. Briefly, SiO_2 was deposited using plasma enhanced chemical vapour deposition (PECVD) at 350 ^{0}C. A resist-layer, negative lift-off 2070, was deposited and soft-baked at 110 ^{0}C on a hotplate. The resist was exposed on the EVG620T mask aligner to pattern the DO sensor structures. The resist was developed using AZ726 developer followed by a rinse with DI water. The exposed SiO_2 was dry-etched using fluoromethane (CH_3F) by reactive ion etching (RIE). The photoresist layer across the SiO_2 features was removed using which completed the SiO2 process. An overview of the process is depicted in Figure 2.2.

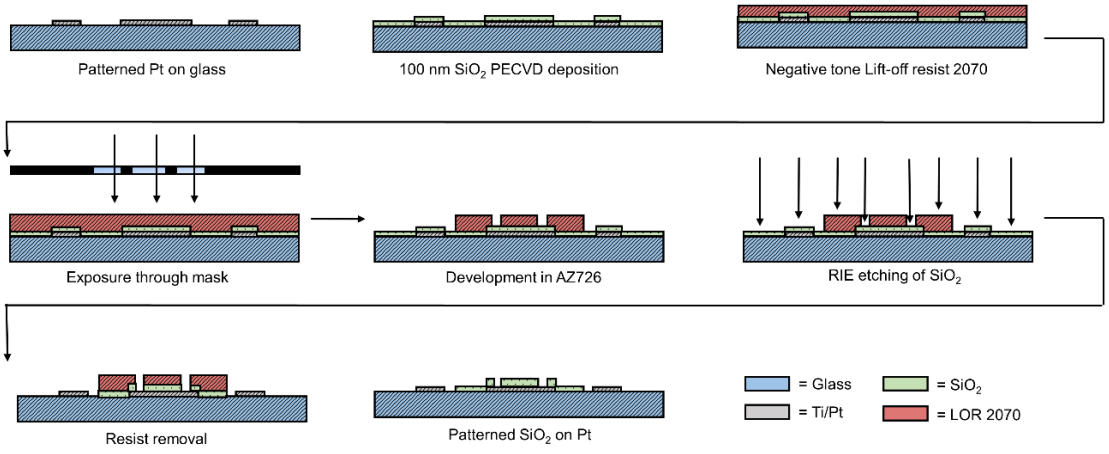

Figure 2.2 – Silicon dioxide deposition and patterning process to promote adhesion of the resist structures used in DO sensing. Deposition is performed using PECVD. A negative-tone lift-off resist is patterned using a mask aligner. The exposed resist is developed using AZ726 developer, followed by a rinse in DI water. The exposed SiO_2 is etched using CH_3F. The resist is stripped and the resulting SiO_2 on Pt can be used for further processing.

2.1.3 Sensor patterning

The pattern defining the DO sensor has been achieved using two types of photoresist: TMMF (tradename) and SU-8, respectively. The SU-8 was deposited via spin-coating. The resist was patterned using the same process as described in section 2.1.1. The alterations are: SU-8 was deposited, EC developer solution was used; no milling was performed. An overview of the TMMF deposition is depicted in Figure 2.3. TMMF is a dry-film, epoxy based, photoresist which has to be laminated onto the surface of the wafer. First, the Pt patterned wafer was removed from the dehydration oven and cleaned using nitrogen gas.

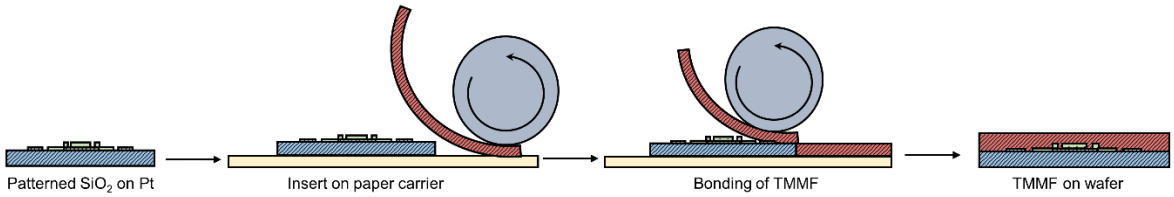

Figure 2.3 - Lamination of dry-film photoresist. The patterned Pt wafer with or without SiO_2 is placed on a paper carrier sheet. The carrier sheet is pushed into the rollers of the laminator which are heated to 85 ^{0}C. The rollers pull the paper and wafer through. The dry-film TMMF resist is laid across and pulled tight once taken by the rollers. As the paper, wafer and resist move through, the resist is bonded. The resulting TMMF on Pt can now be processed further.

A laminator was heated to 85 ^{0}C with a low rotation of the rollers. A sheet of TMMF-55 or TMMF-25 (number indicating the thickness of the photosensitive layer in micrometres) at room temperature was cut to size and the inner film removed. The wafer was placed on a sheet of paper and pushed into the rollers which gradually pulled the paper and wafer through. Meanwhile, the resist was laid across and pulled tight once taken by the rollers. As the wafer and resist progressed through the rollers, the resist was bonded. The process can be repeated until the desired thickness is achieved; a stacked layer of TMMF is then present. A similar process as for the Pt patterning was followed to define the DO sensor in TMMF. Once the patterning of either SU-8 or TMMF had been completed the wafer was ready to be scribed into the individual sensor dies used for testing.

2.2 Sensor designs

Three main types of sensor configurations were developed and used for pH and DO sensing. Each is discussed based on key aspects which are: sensor lay-out, DO sensor critical parameters, fabrication method. For the DO sensor, a disk microelectrode recessed in a well was developed, more details on the motivation behind this choice is given Chapter 4. An overview of the critical dimensions is shown in Figure 2.4. Henceforth, in this chapter, the term DO sensor relates to this type of geometry. The DO sensor consists of an array of Pt disk microelectrodes with size N. The critical radius r_0, ensures microelectrode behaviour is maintained and is typically below 25 µm (90). The inter-electrode spacing d, was varied and ensured the diffusion boundaries would not overlap. Finally, the height of the recess H, varied throughout the designs.

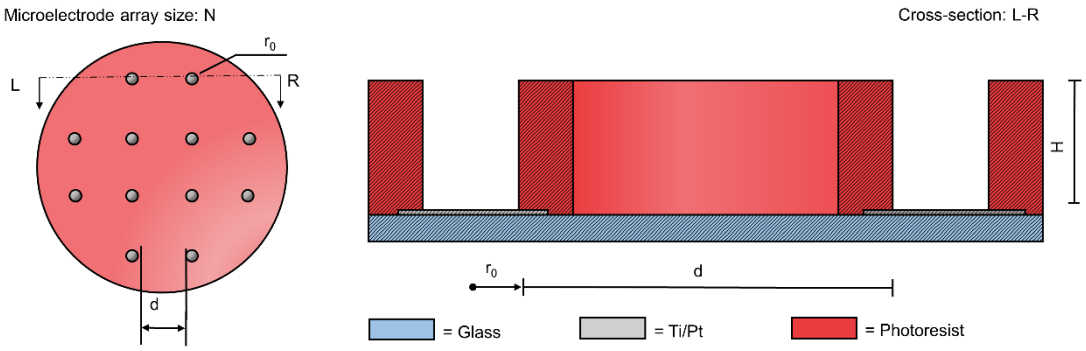

Figure 2.4 - Illustration of the DO sensor. The DO sensor consists of a well recessed disk microelectrode array with size *N*; critical radius r_0; inter-electrode spacing *d*; recess height *H*.

2.2.1 Sensor Type-A

Figure 2.5 shows the diagram of the design for sensor Type-A. The design was previously developed at the UoS and has a footprint of 4 x 7 mm. The sensor consists of three electrodes which function as the counter electrode (CE), reference electrode and working electrode (WE) for the DO sensor. The design employs a channel structure which defines the sensing electrodes. The channel is defined in a multi-layer stack of TMMF with a total height of 220 µm or 55 µm. The design has been used in this work solely to create the first REs and all of the thermally formed pH sensors. It was found during pH sensor development that the TMMF is ideally suited for lift-off during the deposition and thermal formation of Iridium oxide (IrO_x), as discussed in Chapter 5. Here the channel defines the pH sensor and constricts it to a size of 2000 x 300 µm.

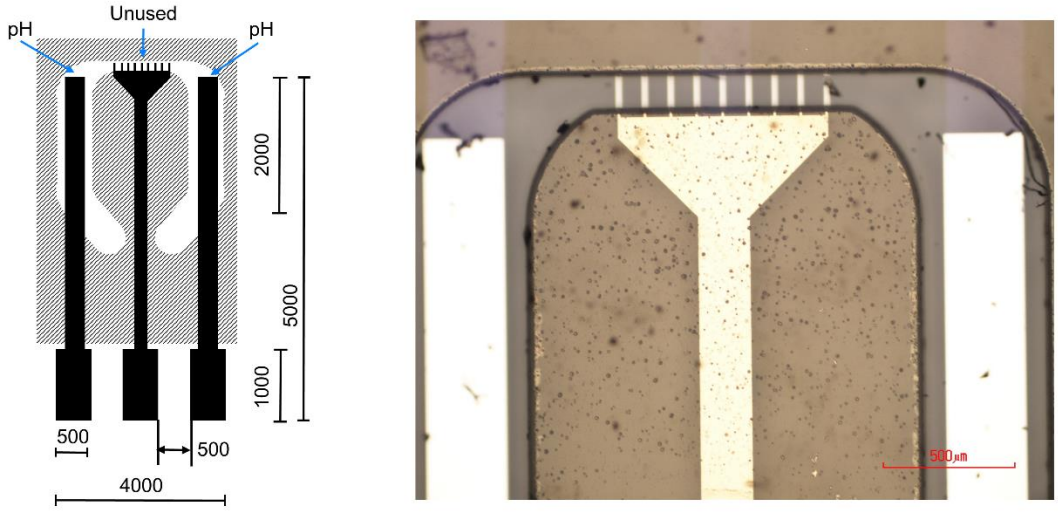

Figure 2.5 - Sensor Type-A consisting of two Pt band electrodes and a micro-band electrode array. Only the two outer electrodes have been used in this work. The patterned resist layer was made using stacked TMMF (50 – 220 µm and used a lift-off resist layer for Iridium oxide deposition. Size in µm.

2.2.2 Sensor Type-B

Figure 2.6 depicts an overview of sensor Type-B. The three electrodes function as the CE, WE and RE. Considered in the design are the following criteria: large surface area for the CE; large surface area for the RE; varying radius for the disk microelectrodes; circular configuration for optimal current distribution. The recess height has been defined within 55 or 25 µm TMMF. The tracks running from the contacts were passivated in the process. A variety of array sizes has been implemented in the mask design and have been compared in the experiments discussed in Chapter 4. Sensors of Type-B have been used for DO and RE experiments. The array sizes were either 5, 6 or 8 disks, each with a critical radius designed to be 11 µm.

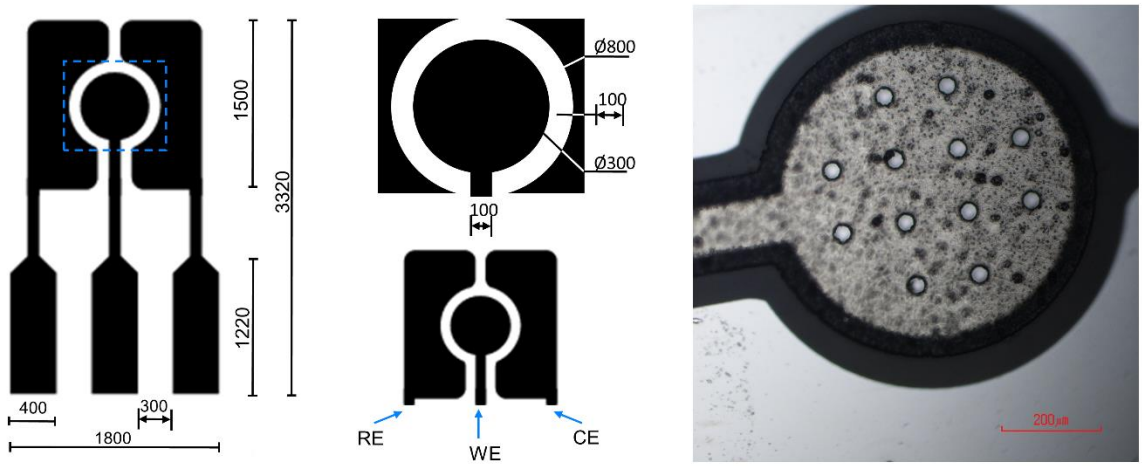

Figure 2.6 - Sensor Type-B consisting of a large Pt CE, a large RE and a patterned WE defined within the photoresist. The working electrode is an array of disk microelectrodes recessed within 25 – 55 µm TMMF photoresist. Size in µm.

2.2.3 Sensor Type-C

Figure 2.7 shows an overview of sensor Type-C. Here, a circular lay-out was chosen, aimed to integrating the two sensors onto a single sensor die with a footprint of 2.3 x 4.3 mm. A double-sided sensor design was developed which contains the pH and DO sensors on the top, and the CE and RE on the bottom. The current density was optimised by the circular shape of the electrodes. The diameter of the individual disk microelectrodes was designed to be 22 µm. The DO sensor has been defined with either TMMF, SU-8 or SiO_2. The inter-electrode spacing has been set equal for all designs as at least twenty times the radius. This results in two array sizes with *N* equal to 6 and 8. The open structure in the centre of the die is envisioned to be used as a through hole via, to create a junction for ionic contact between the top and bottom of the sensor die. Additionally it serves as a diffusional flux limiting channel for the internal electrolyte of the RE; more details are discussed in Chapter 3 and Chapter 7.

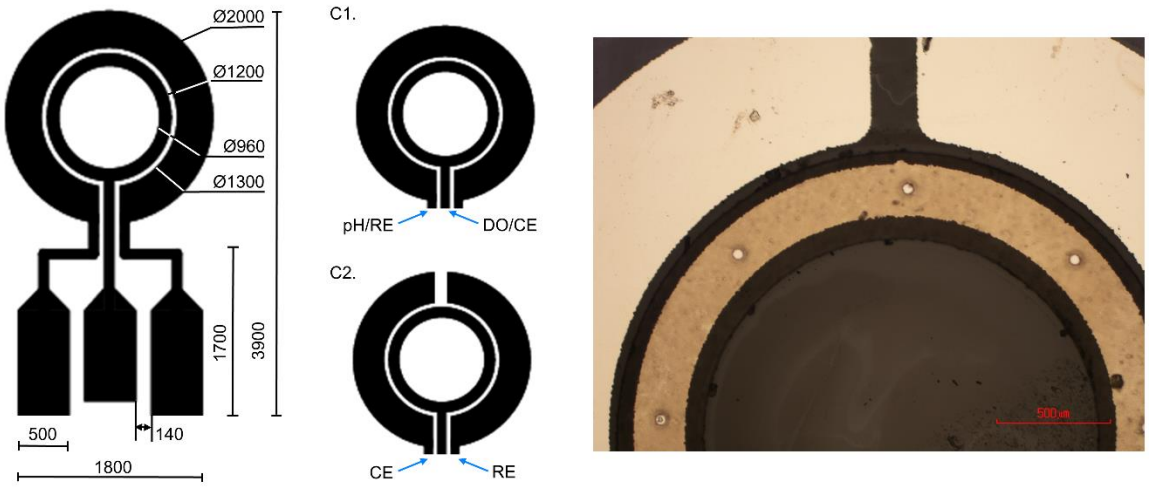

Figure 2.7 - Sensor Type-C2 consisting of circular Pt electrodes for a double-sided sensor die. Designs for top and bottom is equal to C1. The pH sensor and WE are position on the top side. The CE and RE are positioned on the bottom side of the sensor die. The open area in the middle of the die is aimed at creating a connecting junction from the bottom to the top side of the die. Design C, in which the ring has been split is used for silver plating experiments. Size in µm.

2.3 Summary

This chapter discussed the fabrication and design for the sensors used in this work. Platinum electrodes on a glass substrate were formed using a micro-lithographic pattern and etch process performed in a clean-room. The electrodes used for the CE and RE consist of large Pt electrodes. The DO sensor consists of a micro disk array recessed within a well created within the photoresist. The height of the recess has been varied in the different designs to be used for a comparative, experimental study. Three main designs have been fabricated throughout the course of this work. Sensor Type-A has been used as a pH sensor; sensor Type-B and Type-C for DO sensing. Each of the design iterations are discussed in the next chapters.

Chapter 3 -Reference electrode development

An on-chip, miniaturised RE is required for both pH and DO sensing. Its main purpose is to provide a stable reference potential for the potentio- and amperometric measurements involved with pH and DO sensing, respectively (91, 92). This is achieved by the fact that it has a fixed, quantifiable, potential within a solution, compared to the changing potential at the working electrode (WE) (93). In macro-scale environments a variety of RE types exist including standard hydrogen electrode (SHE), saturated calomel electrode (SCE), silver-silver chloride (Ag-AgCl), copper-copper(II) sulphate (CCS); each of which has its own potential. By convention, the SHE potential is set at 0 V and all others are referenced against the SHE at normal temperature and pressure.

Depending on the field of application, preference is given to one or the other. For biological applications the most important aspect is biocompatibility (94, 95). Hence, the use of toxic heavy metals, like mercury in the SCE, is not preferred. Furthermore, scalability, cost and ease of fabrication are of importance; these criteria are met by the Ag-AgCl reference electrode. To-date, the fabrication of a stable and long lasting miniaturised Ag-AgCl RE remains challenging. This chapter discusses the development of such a RE for applications *in utero*. First, the background and theory are discussed; followed by the materials and methods, then the results and discussion.

3.1 Background and theory

The equilibrium reaction for the Ag-AgCl system is shown in equation 3.1. As can be denoted, the surface potential of the Ag-AgCl electrode arises from the redox equilibrium between silver (Ag) and its salt (AgCl). As shown in equation 3.1, the RE surface interacts with the surrounding chloride anion. Here, an equilibrium reaction exists where AgCl is continuously re-dissolved and formed.

$$AgCl\,(s) + e^{-} \rightleftarrows Ag(s) + Cl^{-}(aq) \qquad (eq.3.1)$$

In its simplest form, the electrode consists of a silver wire with its interfacing surface converted into AgCl. When immersed in a chloride (Cl^-) containing electrolyte a potential is established. The potential of the electrode is given by the Nernst equation shown in equation 3.2. Here, E^0 is the standard potential for the Ag-AgCl reaction, R is the molar gas constant, F is the Faraday constant, n the number of electrons, T the absolute temperature and $[Cl^-]$ the concentration of the chloride ion. Thus, a decade change in the concentration alters the potential by a Nernst factor of approximately -59 mV (T = 297 K), with a standard potential for the reaction equal to +0.222 V vs. SHE; as summarised in the table available in appendix A1. Therefore, in a pseudo-type setup, in which the Ag-AgCl electrode is immersed directly into an analyte, the concentration of the chloride has to be known and constant to prevent fluctuation of the RE potential (93, 95-97).

The underlying principle discussed here shows the first challenge in constructing a miniature reference electrode: as the size of the electrode decreases, less Ag, and consequently, less AgCl is available for the equilibrium. Consequently, any loss of AgCl in the bulk solution causes fluctuations in its potential.

$$E = E^0 - 2.303\left(\frac{RT}{nF}\right)\log[Cl^-] \qquad (eq. 3.2)$$

Commercial Ag-AgCl REs are kept in an environment containing sufficient amounts of Cl^- i.e. saturated electrolyte, most commonly potassium chloride (KCl). This separates the electrode from the analyte using a liquid barrier across a porous junction. It also ensures that enough Cl^- is present to maintain the equilibrium reaction, even when effusion occurs (91, 93, 95). An image and illustration of a commercial RE and its components are shown in Figure 3.1. It is only in this situation that the potential of the RE is fully stable, albeit only if the effusion of Cl^- is sufficiently limited.

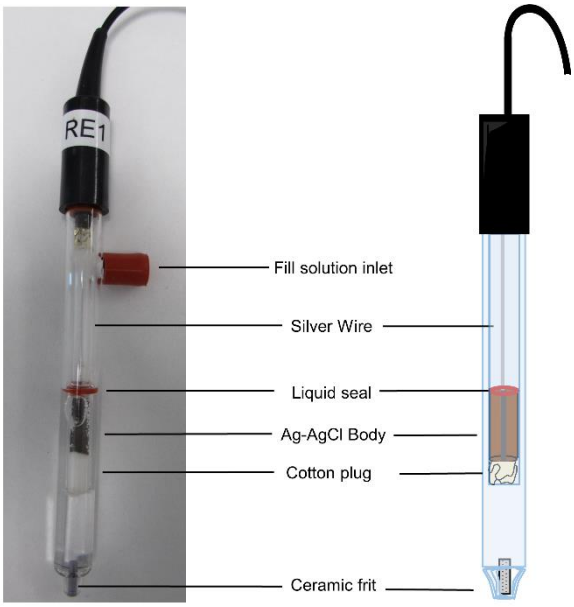

Figure 3.1 – Overview of a single junction, commercial, RE. The RE consists of an internal glass housing that has a silver wire drawn into a Ag-AgCl body which is prevented from falling down by a cotton plug. A liquid seal at the top of the Ag-AgCl body ensures no liquid can come in contact with the silver wire. The inner housing is placed in an outer glass housing which contains the filling solution. The ceramic frit is porous and forms the junction between the internal liquid and the external environment.

Ideally, this concept would be mimicked in an on-chip RE. Unfortunately, the use of a liquid electrolyte is challenging. Any liquids contained within the system pose problems for the mechanical strength of the device and increases the risk of leakage. Although non-toxic, the loss of electrolyte results in potential fluctuations. Therefore, research has been focussing on finding alternatives to the liquid electrolytes in the form of solid-state materials containing KCl. Three main aspects in the RE development can be identified: deposition of the underlying Ag, formation of the Ag-AgCl, development of the electrolyte.

3.1.1 Deposition of the underlying silver

To obtain a miniature Ag-AgCl RE, a Ag electrode first has to be formed. As discussed by *B.J. Polk*, the amount of Ag greatly influences the stability of the manufactured RE. As the size in a miniature RE decreases, the amount of Ag for conversion into AgCl is reduced. Furthermore, the grain structures and adhesion to the substrates have been found to be of influence on the reproducibility and stability of the AgCl layer (98, 99). As the amount of AgCl present on the electrode is the main factor influencing the stability and life-time, the amount and adhesive properties of the underlying Ag layer can be considered equally important. Hence, it is desirable to deposit thick-films, in the micrometre range (98, 100). Techniques used for fabricating Ag layers are:

1. Physical deposition: sputtering, chemical vapour deposition, pulsed laser deposition;
2. Screen-printing: printing of silver metal 'ink' onto a substrate;
3. Immersion plating: through ionic displacement silver is deposited on a less noble surface;
4. Electroplating: through electric current silver is deposited on a metal surface.

1. A photo-lithographic, pattern and etch process in which metal films are deposited onto a substrate containing patterned photoresist. The electrodes are fabricated by patterning and etching using standard clean-room processing techniques.

2. Metallic ink is printed onto substrates, which allows for the deposition of thick Ag films and can also be used to directly deposit Ag-AgCl layers. It is relatively easy to use and has been shown to provide stable layers suitable for RE development. Thicknesses of 5-10 µm can be achieved (93, 99, 101, 102)

3. Immersion plating is commonly employed in printed circuit board manufacturing. The technique relies on the displacement of less noble metal ions with more noble metal ions. The substrate is immersed in a bath containing Ag^{+} ions. When the entire surface of the target has been covered the reaction comes to a halt. This typically yields only thin layers of several nano meters thick (103-105).

4. In electroplating, a metal layer is formed by the application of a current. The metal ions are attracted to the cathodes surface. Depending on the time and applied current density, thick films can be achieved. In contrast to immersion plating, the reaction will continue as long as the current is flowing. The main advantage of this technique is the control of the deposition rate and the wide range of thicknesses of the deposits (103).

3.1.2 Formation of the silver-chloride

The formation of AgCl is schematically presented in Figure 3.2. As described by *de Mele et al.*, Ag-AgCl is formed in a cyclical manner. First chloride adsorbs to the available surface sites of the silver. Next, the AgCl dissolves into the bulk of the solution and forms a silver chloride complex ($AgCl_2^-$). The complex redeposits onto the surface forming nucleation sites for the build-up of consecutive Ag-AgCl layers (106). It should be noted that this process happens throughout the Ag layer.

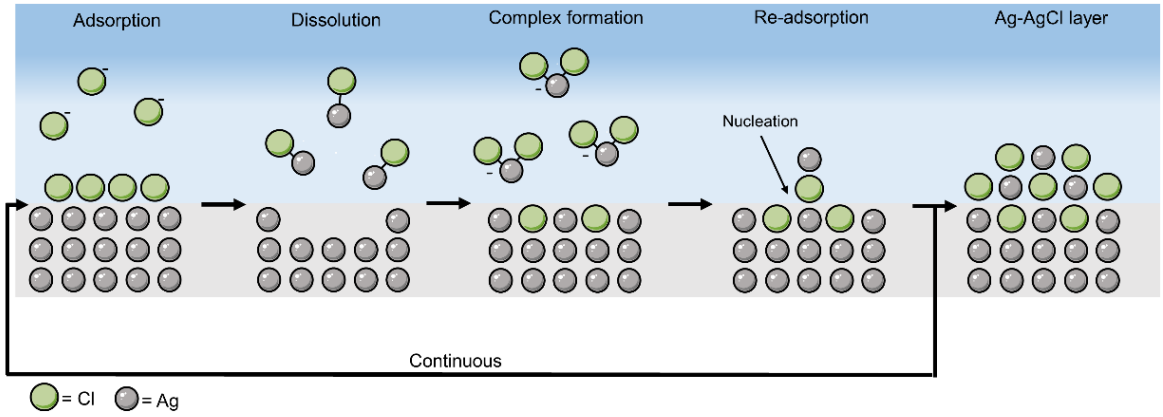

Figure 3.2 – Ag-AgCl formation on Ag during the application of a current. Chloride binds to the silver surface by adsorption followed by a dissolution into the bulk forming a silver chloride complex. The complex re-adsorbs on the surface forming a nucleation site. The process continues until the current flow is stopped. The process happens all throughout the silver layer (106).

The life-time and stability of the Ag-AgCl is one of the biggest issues in current RE design. Over time, a gradual dissolution of the AgCl occurs, causing instability and destruction of the electrode (91, 98, 107, 108). Especially in miniature electrodes, only a thin and limited amount of AgCl is available at the surface.

$$AgCl + Cl^- \rightarrow AgCl_2^- \qquad (eq.\,3.4.)$$

Dissolution of the available AgCl will thus have a significant effect on the potential stability and cripple its life-time. Dissolution of AgCl occurs due to non-negligible solubility of the AgCl in electrolytes with a high chloride concentrations (108-110). For this reason, commercial filling solutions contain trace amount of AgCl which limits the dissolution from the electrode surface into the electrolyte. Even though AgCl is poorly soluble, during prolonged exposure complex anions are formed as per the reaction shown in equation 3.4.

As stated in section 3.1.1, by increasing the amount of Ag available, the amount of Ag-AgCl which can be formed is increased. However, the relationship between silver and it salts is more complex. Interesting accounts have been made on the conversion ratio of Ag to AgCl by *Brewer et al.* A study amongst fourteen institution fabricating Ag-AgCl reference electrodes was conducted. Best results with regards to stability were observed with conversion percentages between 17 and 20% (111, 112).

3.1.3 Influence of the electrolyte

Fabrication of a fully miniature Ag-AgCl RE with long-term stability remains the 'holy grail' of research within the field. Although for many applications it is sufficient to use the RE in a pseudo-setup, it requires thorough knowledge of the chloride concentration within the analyte. To achieve a fully miniaturised RE, a separated environment has to be created for the Ag-AgCl layer, similar to a commercial Ag-AgCl RE. This is complicated by the fact that miniaturised REs are constricted in size and thus can only have a fraction of the electrolyte available compared to their commercial, macro-scale counterparts (95, 98, 108, 110).

Table 3.1 – Overview of the state-of-the-art for miniature reference electrodes.

	Deposition	**Thickness**	**Electrolyte**	**Drift**	**Life-time**	**Method**
D. Moshou (104)	Electro-less	2 µm	NA	<1 mV day^{-1}	20 day	Pseudo
E.T. da Silva (100)	Screen printed	NA	Liquid	<3 mV day^{-1}	15 days	Pseudo
I.Shitanda (113)	Screen printed	10 µm	PDMS	NA	70 days	Full
A.Simonis (96)	Evaporated	3 µm	Agar / PVC	<1 mV day^{-1}	70 days	Full/Pseudo
L.Tymecki (114)	Screen printed	NA µm	Paste	3 mV day^{-1}	10 days	Unclear
H.Suzuki (115)	Electrochemical	0.3 µm	Polyamide	<1 mV day^{-1}	4 days	Full
Mousavi (116)	NA	NA	PVAc	<0.5 mV	60 days	Full
T.Kim (117)	Sputtered	1 µm	Graphene	<2 mV day^{-1}	26 days	Unclear

Potential instability is worsened by a change in concentration at the interface of the RE as diffusion of Cl^- across the electrolyte-bulk interface causes desaturation of the electrolyte. Alterations in the concentration are also caused by loss of the solvent through evaporation, an inherent problem in miniature REs employing aqueous electrolytes (108). Efforts have been made to overcome these issues by replacing aqueous electrolytes by solid-state materials i.e. biological and synthetic polymers (118, 119). As described in the work by *Mousavi et al.* the use of solid-sate polymers can yield excellent performance over the course of two months with typical stability of ±0.5 mV when using Poly vinyl acetate (PVAc) in combination with Lithium acetate (LiOAc) (116). However, the latter is difficult to use *in vivo*. An interesting alternative is the use of porous glass as discussed in the work by *Cranny et al.* Here, the porous structure is used to contain the electrolyte, in effect mimicking the porous frit of a conventional macro-scale RE. Although long-term performance is lacking, its overall insensitivity to chloride changes over a wide range of concentrations shows it can be an interesting alternative to liquid electrolytes (120).

Of particular interest for this work is the use of biocompatible materials. A variety of materials have been investigated for this purpose including hydrogels such as agar and agarose, polyacrylamide (pAm) and chitosan (CS) (96, 121-123). The use of KCl hydrogels has the advantage of being applicable in biomedical processes and provides a more robust structure compared to liquid electrolytes. However, there are drawbacks.

First, a hydrogel is still susceptible to dehydration. Hence, the concentration in the electrolyte will be altered when stored. Typically, hydrogels need to be kept in solution to prevent dehydration. Second, the electrolyte cannot be replenished, so electrodes constructed in this manner will be disposable. Third, many of these materials are not readily biocompatible and their monomers are often toxic; care has to be taken to remove any residual toxic monomers from the gels and additional processing steps are needed to ensure biocompatibility is not compromised (92, 97). Solid state materials are of interest in harsh environments and include carbon pastes, silver chloride pastes and polyvinylchloride (PVC) membranes, all serve the same functional purpose of maintaining the chloride concentration around the RE (113, 124, 125).

3.1.4 Developments in the field of reference electrodes

As can be concluded from the previous sections, many aspects can be investigated and altered when constructing a miniaturised RE. For intrauterine sensing the most important aspects for the reference electrode are the following:

1. Life-time of at least one complete menstrual cycle (28 days);
2. Have a stable or predictable potential;
3. Fabrication needs to result in a biocompatible RE.

A summary of the literature on long-term REs is given in **Error! Not a valid bookmark self-reference.**. Mentioned are the fabrication methods, thicknesses achieved for the Ag-AgCl, electrolyte type, and drift. A wide variety of deposition methods have been used. It is also clear that thicknesses in the micro meter range are most common; the types of electrolytes range from hydrogels to solid pastes. However, their performance as a full RE remains compromised. *Shitanda et al*. have reported a good performing RE using polydimethylsiloxane (PDMS) membranes to form pockets of KCl saturated electrolyte around the RE surface. Unfortunately their data is limited with respect to their sample size and containment of the KCl (113). It is clear that there is still room for improvement on miniature RE performance. In none of the cases, is the yield of the devices given as a criteria. Something which is essential in this work for future use.

3.2 Materials and methods

REs were fabricated using sensors of Type-A, Type-B and Type-C, described in Chapter 2. Connection to the electrodes was established by soldering wires to the pads on the sensor die. *Araldite* rapid epoxy was applied in two stages in order to passivate and waterproof the connections. First, a small amount was deposited and left to cure overnight; this secures the contacts in place. Second, the sensor was strung through a pipette tip which was then filled with the epoxy mixture and left to cure. This ensures that no water can penetrate the epoxy or wires. An example of a finished, encapsulated sensor is depicted in Figure 3.3. Electrochemical deposition of Ag was chosen for its degree of control; a process which has been optimised in this work.

Figure 3.3 – Encapsulated sensor device prior to experimental use of sensor Type-C. The sensor and wires have been pulled through a pipette tip which is then filled with epoxy.

3.2.1 Silver-silver chloride formation

Platinum electrodes were Ag plated using a silver bath plating solution purchased from *Spa Plating ltd*. A Ag wire (0.5 mm^2 diameter) was used as the CE. Care was taken that the CE surrounded the plating target to achieve optimal current distribution. For the initial experiments, a power supply was used to supply a fixed potential. A resistor in series was used to limit the current through the electrode

to -1 mA cm^{-2} down to -0.5 mA cm^{-2} at -1 V. It should be noted that this is a non-ideal set-up, as the current fluctuates during Ag deposition. In later stages, the power supply set-up was replaced by a PalmSens3 potentiostat operating in chrono-potentiometry mode; the same two-electrode configuration was employed for deposition. Here, a fixed current was applied and the required voltage is automatically altered to sustain the current. This method yielded the most consistent results with respect to adhesion of the Ag to the Pt surface. A current density of -1 to -10 mA cm^{-2} was used for deposition.

Chloridisation was performed in two different ways: passively through immersion in sodium-hypochlorite; actively at anodic currents in aqueous solution of 3 M KCl with a Pt counter electrode. For the latter, the PalmSense3 set-up was used in a similar manner to the Ag plating. For Ag-AgCl formation, a positive current was supplied for ten minutes with a current density of 0.5 mA cm^{-2}. After chloridisation, the REs were left to anneal in an oven at 60 ^{0}C overnight as a minimum.

Ag-AgCl wires were fabricated using commercial Ag wire. Prior to conversion the electrodes were roughened and polished using coarse and fine sandpaper to remove any silver oxide and ensured an even formation of AgCl. The wires were immersed with a Pt CE in 3 M KCl. A power supply was connected directly, and the potential increased until the colour of the wire turned brown. The wire was left to chloridise for 2 minutes before being rinsed with DI and placed in an oven at 60 ^{0}C overnight.

3.2.2 Electrolyte formation

To fabricate and investigate the KCl containing polymer electrolyte two polymers were used: polyacrylamide and chitosan. Figure 3.4 shows an overview of the process for the deposition and formation of the polyacrylamide gels. Reference electrodes were fixed inside a 3D-printed mould and covered with a droplet of 3-(trimethoxysilyl)propyl-methacrylate (TMSPMA) mixture at half hour intervals, for two hours, to promote adhesion of the gel to the RE via salinization of the surface. Afterwards, samples were cleaned with methanol and dried using nitrogen gas. A droplet of the polymer mixture consisting of acrylamide - methylene bisacrylamide (40% w/v) with a 150 mM KCl concentration was deposited shortly after addition of the ammonium persulfate (APS, 5% w/v) and N,N,N',N'-tetramethylethane-1,2-diamine (TEMED) to the bulk solution. The mould was covered using a plastic petri dish. The gel was allowed to polymerise for two hours, resulting in a uniform, sticky hydrogel.

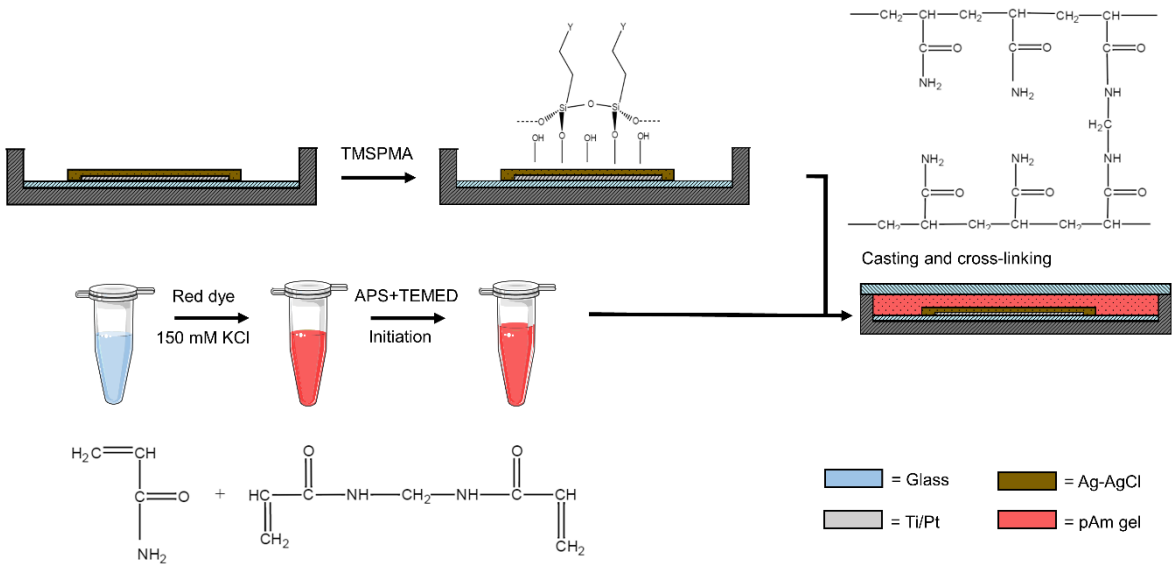

Figure 3.4 - Overview of the pAm casting process. The reference electrode is fixed in a 3D-printed holder. The surface is functionalised using TMSPMA. The acrylamide mixture is mixed inside an Eppendorf. APS and TEMED are added and mixed to the bulk polymer mixture containing KCl and food dye. Shortly after addition, the gel is cast on top of the RE and covered with a plastic cover. The gel is left to polymerise for two hours after which the cover is removed.

Chitosan gels were formed by dissolving CS flakes (2% w/v) derived from shrimp shells (80% deacetylation degree) in 2% v/v acetic acid in DI water containing 150 mM of KCl. The mixture was left to stir for 24 hours at room temperature. Next, the mixture was passed through a muslin cloth to filter out any undissolved CS flakes. The mixture was aliquoted for further use and stored at 7 ^{0}C.

To cross-link the CS mixture, 1 mg of Genipin (Gp) was dissolved in 1 mL of 99.98% ethanol. Gp is a natural cross-linker, with a lower toxicity compared to other synthetic cross-linkers. For a typical cross-linking 40-80 µL of the Gp-ethanol mixture was added to approximately 2 mL of CS stock. The mixture was stirred and left to polymerise for 72 hours. Polymerisation was considered complete when the mixture had turned blue. To reduce the acidity of the resulting gel neutralisation of the pH was performed either prior or after polymerisation. To achieve this, phosphate buffered saline (PBS, pH 7.4, 10 mM. 137 mM NaCl) solution was added to the mixture and left for 24 hours. For large samples, multiple flushes during consecutive days were performed. The resulting pH was measured using a *Hannah* instruments pH probe. When the pH exceeded pH 6 neutralisation was considered sufficient.

3.2.3 Reference electrode packaging

A polymethylmethacrylate (PMMA) package, shown in Figure 3.5 was micro-milled to hold the REs of Type-B via a slot incorporated in the package. An internal cavity, accessible via two side holes was used to contain the Gp-CS electrolyte. The polymerised, neutral pH, gel was injected into the packages using a syringe and needle tip. The injection holes were sealed using *Araldite*, fast-cure epoxy. Whilst curing, packaged REs were kept in a humid environment to prevent dehydration.

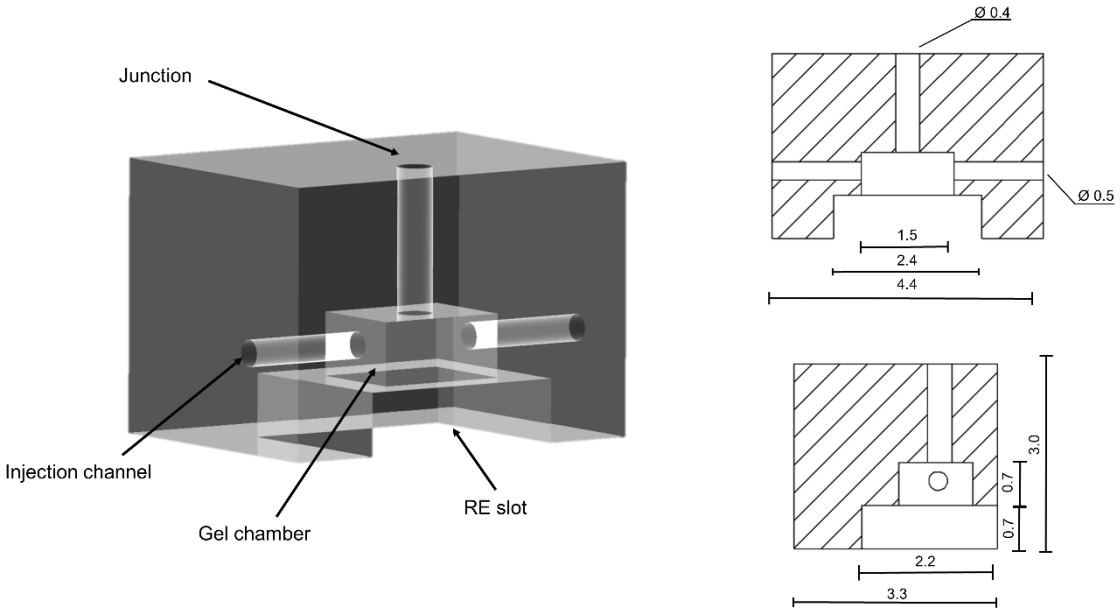

Figure 3.5 – Overview and cross-sectional views of the micro-milled PMMA package. REs of Type-B are slotted and fixed inside the package. The internal chamber is filled with the CS-Gp hydrogel through the injection channels which are then sealed. The junction ensures contact between the RE within the chamber and the external solution. Size in mm.

Membranes were cast from *Nafion*® 117 Solution (5% v/v in lower alcohols, *DuPont*). Best results were achieved by drop-casting, directly, on top of the PMMA packages, in one or two steps. A droplet of the *Nafion*® solution (10 µL) was deposited on the top surface, across the junction and transferred into an oven at 60 ^{0}C. The packages were left in the oven for 1 hour. The surface tension keeps the droplet in place across the junction. As the solvent evaporates, the *Nafion*® solidifies, forming the membrane. In some cases, the membrane did not form correctly, resulting in a hole or gap. An additional droplet was then cast across. In this case, the previous cast has turned the surface hydrophobic improving its coverage across the junction by forming a meniscus.

3.2.4 Measurement set-up

REs were tested using a differential measurement. For long-term experiments, a double junction commercial Ag-AgCl RE was used in order to prevent contamination of the internal filling solution over time[3]. The solutions used were prepared either using KCl or 1x PBS giving an ionic concentration of 150 mM or 137 mM, respectively. The volume was marked on the measurement vessel prior to each experiment. In order to limit evaporation, a PMMA lid was used to cover the vessel in addition to regular replenishments with DI water to keep the ionic concentration relatively constant throughout the long-term runs. The set-up was placed out of direct sunlight.

[3] All commercial REs used in experiments are checked on a regular basis versus a master double junction Ag-AgCl RE.

Measurements were performed at ambient temperature; typical fluctuations of 2.5 ^{0}C are experienced by the measurement set-up ranging between 19 and 21.5 ^{0}C. An USB6211-DAQ (16-bit, National instruments) running a *LabView* script was used to acquire the open circuit potential. A single reference point (the commercial RE) was used for all channels. Data was initially acquired at 1 s intervals and later selected at discrete ten minute or half hour intervals.

3.3 Results and discussion

Electroplating was chosen as the preferred method for the formation of the Ag electrodes. The reason for this is two-fold. First, the underlying substrate is a Pt electrode, hence techniques based on immersion plating are not possible due to the nobility of the Pt. Second, electroplating offers a higher degree of control as the current density determines the thickness of the deposit. At the start of this work, Ag plating was performed using a power supply. A resistor in series was used to create constant current conditions. Table 3.2 shows the results for the plating thickness for the stated current density and time for electrodes of Type-A. Thickness was assessed through surface profiling. Optical inspection and surface profiling was used to assess the uniformity. Each set consisted of three electrodes, plated individually; each surface profile was analysed at five points: one point at each edge and three points in the middle.

As shown by the results in Table 3.2, there is a significant edge when using electroplating. This effect is caused by the increased current density at the edges of the electrodes, which results in a build-up of Ag, forming a so-called 'dog bone' (103). The edge shields the middle part of the electrode retarding growth of the Ag in that area. AgCl formation was achieved through immersion of the electrode in sodium hypochlorite for ten minutes. Although the power supply and subsequent hypochlorite conversion resulted in usable electrodes for short term experiments, sample-to-sample variation was high and yield low, when considering long-term experiments. Hence, an alternative method using a potentiostat operating in chrono-potentiometry mode was investigated.

Table 3.2 – Plating results for electrodes of Type-A.

		Time	**Centre height**	**Edge height**	**Uniformity**
High current	Set 1	300 s	3.99 ± 1.0 µm	3.05 ± 1.1 µm	Medium
10 mA	Set 2	450 s	6.88 ± 1.9 µm	6.25 ± 0.9 µm	Medium
	Set 3	600 s	4.85 ± 0.4 µm	14.80 ± 6.8 µm	Poor

Because of the high degree of control established with the potentiostat, more reliable plating results can be obtained. Furthermore, the molecular weight (M_w), density (ρ) and surface area (A) can be used to compute the thickness, d, of the deposit. In practice, factors such as an uneven current

distribution, activity of the plating solutions, and surface roughness cause deviations from the calculated values obtained using equations 3.5 and 3.6.

$$m = \frac{Q}{nF} = \frac{It}{nF} \qquad (eq.3.5)$$

$$d = \frac{m\,M_w}{\rho A} \qquad (eq.3.6)$$

To assess the plating process, electrodes of type-C2 were plated using high current density (HCD) and low current density (LCD), with current values of -17 and -170 µA; equal to -1 and -10 mA cm^{-2}. Figure 3.6 shows the comparison between the calculated thickness, and the measured thickness of the silver layer. Measurements were taken using a surface profiler.

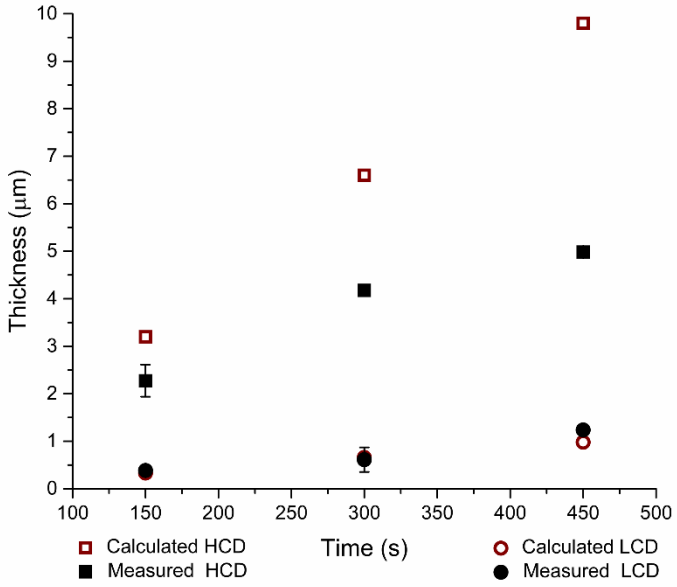

Figure 3.6 - Comparison of calculated with measured silver thickness on electrodes of Type-C2. Plating performed under non-convective conditions at HCD and LCD of 10 mA cm^{-2} and 1 mA cm^{-2}, respectively. Note: standard deviation smaller than symbol size.

For the LCD samples good agreement is found with the calculated values. However, the thickness of the deposit is thin compared to the HCD samples. Under HCD conditions the measured values do not match the calculated values. The reason for this discrepancy is that the solution is kept free of convection. Hence, without convection a diffusion limitation sets in, as can be denoted by the curvature across the time scale for the measured HCD samples. The thickness of the HCD at 300 s was chosen for further RE testing as this yielded thicknesses of several micro meters.

Figure 3.7 depicts the latest of the formed REs using electrodes of Type-C1 and Type-C2. Here, current densities of -10 mA cm^{-2} for Ag plating and 1 mA cm^{-2} for subsequent chloridisation were used. The results of the Ag plating on Type-C2 and Ag-AgCl on Type-C1 are presented in Figure 3.7 a and b, respectively.

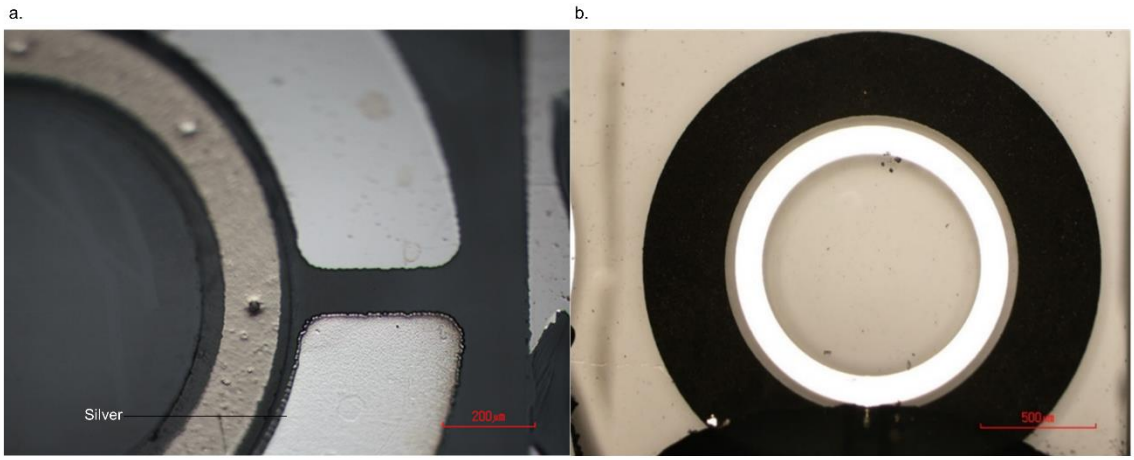

Figure 3.7 – a) Silver plated electrode of Type-C2. b) Formed Ag-AgCl reference electrode of Type-C1.

3.3.1 Pseudo reference tests

For the initial tests, the formed Ag-AgCl electrodes were used in a pseudo-reference setup. Here the REs were immersed directly in 150 mM KCl. The potential of the resulting cell, E_{cell}, can be described according to equation 3.7. The equation shows the miniature RE, described by the Nernst-equation subtracted by the commercial RE (3 M KCl, single-junction). Setting E^0 equal to +220 mV for the standard potential of the AgCl electrode at T equal to 293 K; and E_{ref} equal to +220 mV a cell potential of 48.6 mV is predicted for 150 mM sodium chloride (KCl) concentration.

However, in practice, the values for E^0 and E_{ref} are non-ideal. In fact, as the concentration of chloride ions is high, the value for $[Cl^-]$ given in equation 3.2, is more accurately described by the activity of the chloride ion a_{Cl} with activity coefficient α. If the activity coefficient is half, a potential of 24 mV is expected. The same applies to the potential of the commercial RE in saturated 3 M KCl described by E_{ref}; yielding a potential of +199 mV at normal temperature and pressure. Substituting this value into equation 3.7 results in a cell potential of 72 mV. Finally, variations between electrodes, both commercial and fabricated will result in slight differences in cell potential. In summary, a potential range between 24 to 72 mV is considered acceptable.

$$E_{cell} = (E^0 - 2.303\left(\frac{RT}{nF}\right)\log(a_{Cl})^{\alpha} - (E_{ref}) \qquad (eq.\,3.7)$$

Presented in Figure 3.8, are the data for a five day experiment, comparing the open circuit potential of: Ag-AgCl-wire; Ag-AgCl electrodes; miniature Ag electrodes. First, it can be noted that the potential offset for the Ag-AgCl wire is within the theoretical range determined by equation 3.7, with an average value of 44 ± 3 mV. The same applies to the potentials obtained with the miniature REs with values of 56 ± 1 mV vs. commercial Ag-AgCl. Second, it can be noted from the graph that at the initial start of the measurement (day 0 to 1) the potential of the Ag electrodes is close to the Ag-AgCl electrodes. As time progresses, the potential rapidly falls to negative values which has been

determined to be near the value of a Ag wire (data not shown, measured average equal to -140 ± 10 mV). It is unknown why this initial potential is present, but could be due to passive chloridisation from the Silver when immersed in solution. As this layer dissolves during the course of the measurement the potential drops and only the surface potential of Ag electrodes is observed.

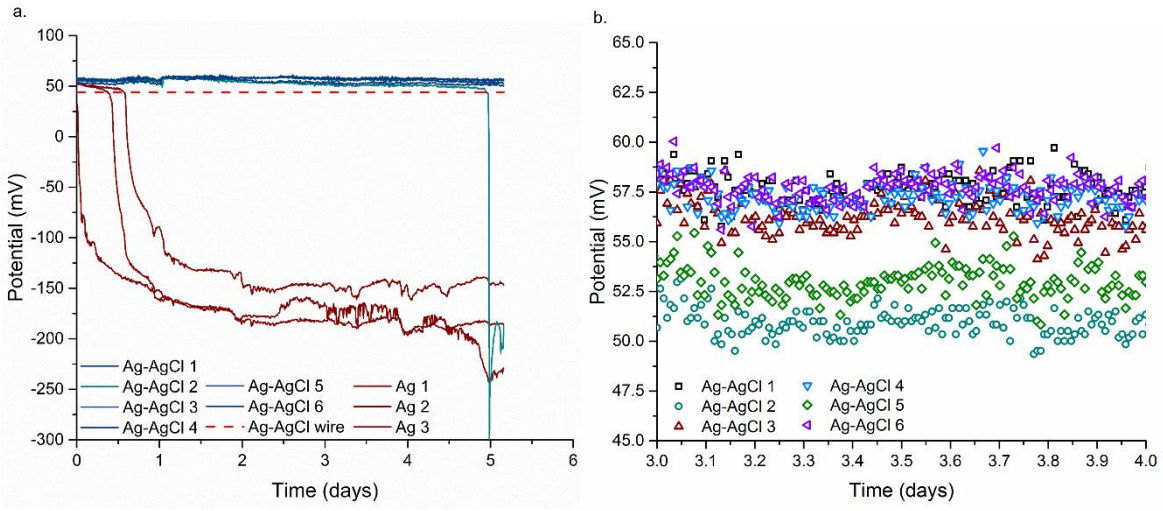

Figure 3.8 - a) Measurement of Ag and Ag-AgCl electrodes in 150 mM NaCl, pseudo-setup. All electrodes are referenced versus a single junction commercial RE with 3 M KCl internal filling solution. The initial drop towards negative values of the Ag samples shows the clear difference between correctly and incorrectly functioning REs. If failure occurs this, is noticeable by the drop in potential as registered by Ag-AgCl-2 on the fifth day. The purple dashed line shows the average values obtained from a separate measurement with a Ag-AgCl wire in 150 mM KCl. Note that all the REs are close to this reference line which is within the predicted theoretical range. b) Zoomed view of the fourth day.

Due to this observation, prior to each experiment, the formed miniature Ag-AgCl electrodes were immersed in 3 M KCl for up to two minutes. This allowed for a better distinction between correctly operating REs and electrodes containing only Ag. Correctly formed REs show values around 0 mV, whereas the Silver shows an immediate potential drop towards negative magnitudes due to the dissolution within the 3 M KCl solution. It should be noted here that electrodes should not be kept in the 3 M KCl solution for extended periods of time as prolonged immersion dissolves the formed Ag-AgCl over time. An added benefit of this initial check is, that poorly adhering Ag-AgCl structures fall off during this period. Hence, this brief check introduces a quality control mechanism. The effect of delamination of the AgCl due to improper Ag plating and ‘dog-bone’ effects, as illustrated by the drop-off for AgCl-2 in Figure 3.8.a.

A long-term plot of a RE batch formed using sensors of Type-C2 is presented in Figure 3.9. The measurement was setup for 40 days in 150 mM KCl. As shown, excellent performance and agreement with theory is observed for all samples. A negligible drift is observed with a value of 0.3 ± 0.1 mV day^{-1}; determined by the slope of the linear fits. It can be seen that around day 30 a drop in potential occurs. Although within the limits of the theoretical value potential and recovering after replenishment of the bulk solution, it is assumable that the electrodes are degrading as time progresses.

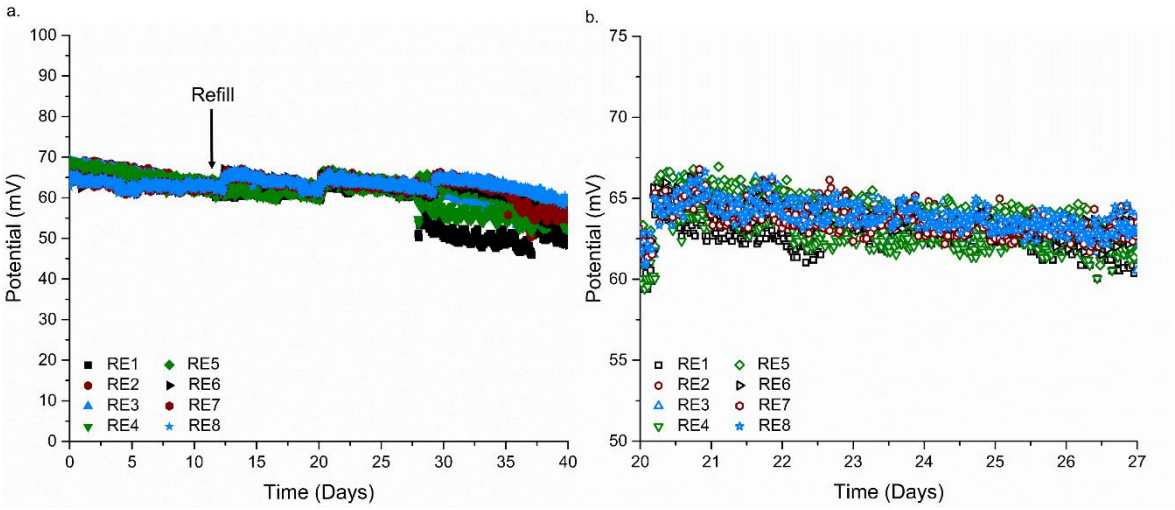

Figure 3.9 - Long term reference electrode of Type-C2 measured in 150 mM KCl for >40 days; n = 8. Indicated are the points in time at which a refill with DI occurred to keep the salt concentration at a constant level. Note that each point represents a discrete point from the full trace (1 sample per second) at half hour intervals. a) Full trace; b) Zoomed view of day 20 to 27. Note that drift is well below 1 mV day^{-1} indicating excellent performance.

Based on the long-term pseudo-setup data an estimate of yield can be made. The yield at four weeks when measured directly after fabrication includes samples that fail during measurements (data not shown) and equals 70% at the second week and 64.5% at the fourth week. However, if an initial quality control check is implement which consisting of an initial test of the miniature REs for 3 days in 150 mM KCl i.e. the start of the sample group at the 4th day, a yield of 90% is observed for the first two weeks (n = 24) and 80% across week three and four (n = 10)[4]. This three-day tests allows electrodes to be selected for long-term *in vivo* measurements, after fabrication and enhances the quality control.

3.3.2 Electrolyte development

In order for the RE to maintain stability in a variety of electrolytes, the use of hydrogels was investigated. Two gels were developed and used in the experiments. The first gel uses acrylamide and was developed in the early stages of this work; the second was made using genipin cross-linked chitosan. The results of both methods are discussed next.

3.3.3 Polyacrylamide based electrolyte

Polyacrylamide gels were prepared and deposited according to the methods described in section 3.2. For the experiment, RE samples of sensor Type-A were prepared at low current density and converted into Ag-AgCl using sodium hypochlorite. The gel was doped with 150 mM KCl. Red food dye was added to the monomer solution in order to see the correct deposition of the gel. As an example, Figure 3.10 shows the formed gels on top of bare Pt electrodes. Over time, the water within the gel

[4] Sample size represents experiments which ran for the designated period of time.

evaporates. Thus, it is critical that the devices containing hydrogels are kept in a humid environment or are immersed in solution after fabrication.

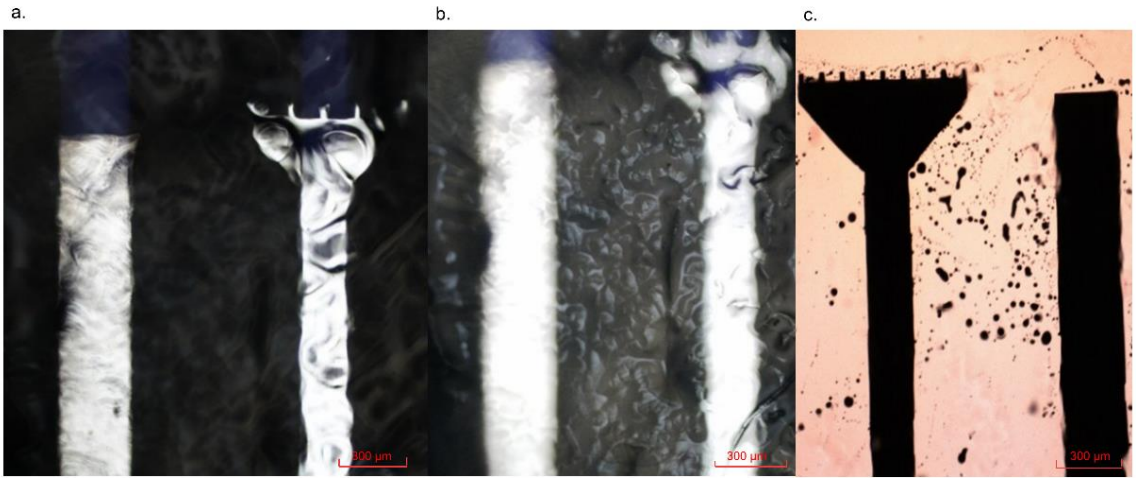

Figure 3.10 – Polyacrylamide gel on top of electrodes of Type-A. a) Hydrated; b) dehydrated; c) hydrated with red dye.

Figure 3.11 shows the resulting long-term plot for the formed reference electrodes of Type-A contained within the pAm electrolyte, with an external concentration of 3 M KCl. From the resulting plot it can be denoted that the RE maintains its function within a pseudo-type set-up (3M vs. 3M) for a period of eight days. The potential offset is near the expected offset potential for the commercial RE. After the eighth day, the electrode potential started to drift towards the negative potential value of Ag. This indicates a loss of Ag-AgCl into the electrolyte caused by the dissolution of the Ag-AgCl in the 3 M KCl electrolyte.

Further experiments were conducted with sensors of Type-B. However, during the fabrication a vulnerability was exposed: as the size of the electrode is half compared to Type-A, the amount of un-polymerised solution that can be deposited is significantly reduced. This resulted in un-polymerised solution. Oxygen is an inhibitor for the crosslinking of pAm (126). In large quantities it is easy to keep out oxygen from the bulk mixture. However, in the quantities used for the electrodes of Type-B (typically only 20 µL) it is impossible to achieve by casting. Alternatives like injection of the mixture into a package are possible, but will increase the risk of residual un-polymerised monomers and cross-linkers within the package. It cannot be guaranteed that the gel has polymerised without opening and destroying the package. As the components used for cross-linking and the monomer are highly toxic, carcinogenic and related to loss of fertility, the choice was made to investigate an alternative gel: Chitosan.

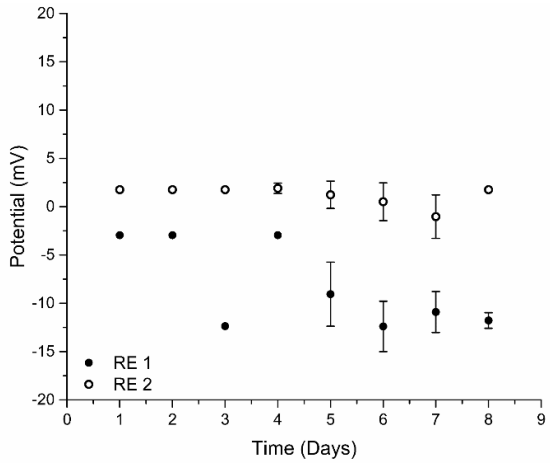

Figure 3.11 – Ag-AgCl reference electrodes of Type-A contained within a pAm gel electrolyte. Measurement performed in a pseudo set-up with 3 M KCl internal and external solution. Note that standard deviation is smaller than symbol size from day 0 to 4.

3.3.4 Chitosan based electrolyte

Chitosan dissolves in aqueous solution at low pH (pH 4 and below). To prevent swelling, the degree of protonation has to be reduced. This can be achieved by flushing with copious amounts of neutral solutions without disturbing or mixing the gel. For the CS gels described here flushing was performed with PBS (pH7.4, 10 mM, 137 mM NaCl). The benefit of this method is two-fold: first, the pH is neutralised to a value above pH 4 which reduces the swelling behaviour during measurements. Second, the concentration in the 1x PBS ensures the concentration remains constant.

Genipin was chosen as a cross-linker. This is a natural cross-linker which is less toxic then synthetic alternatives such as glutaraldehyde (127, 128). It takes 48-72 hours for the polymerisation to start, upon which the gel turns blue due to the linking of the amine-groups. During this time the gel has to be kept in a humid environment. The resulting gel is shown in Figure 3.12.a. Figure 3.12.b and c, show the bulk of a Gp-CS gel before and after immersion in PBS for one week. As can be seen from the figure, no swelling occurs within the matrix. However, the structure has opened to the aqueous surroundings indicating that liquid has penetrated into the gel and as such would result in a dilution of the internal salt concentration.

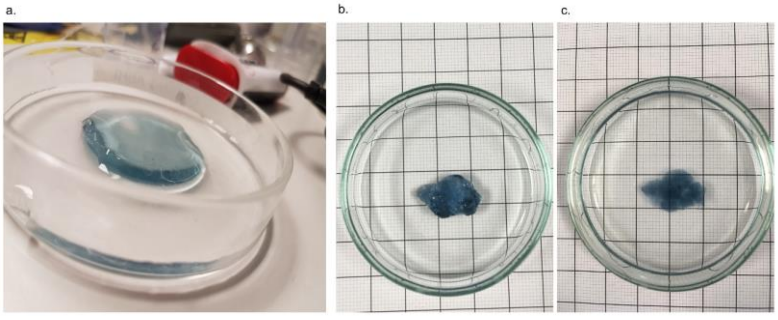

Figure 3.12 – Gp-CS hydrogel. a) Bulk sample in 1x PBS after neutralisation. b) Sample prior to immersion in 1x PBS. c) Sample after immersion in 1xPBS for 1 week. Squares equal 1x1 cm.

To test its function, the Gp-CS gel was injected with a syringe into a micro-milled package that houses the RE. Due to the blue colour of the gel, the filling of the cavity can be observed. An image of a sensor of Type-B encapsulated within the package, and the filling with the syringe is shown in Figure 3.13.a and b, respectively. Once filled, the injection channels are closed using fast-cure epoxy. Whilst curing, the packaged REs are kept in a humid environment to prevent dehydration of the gel.

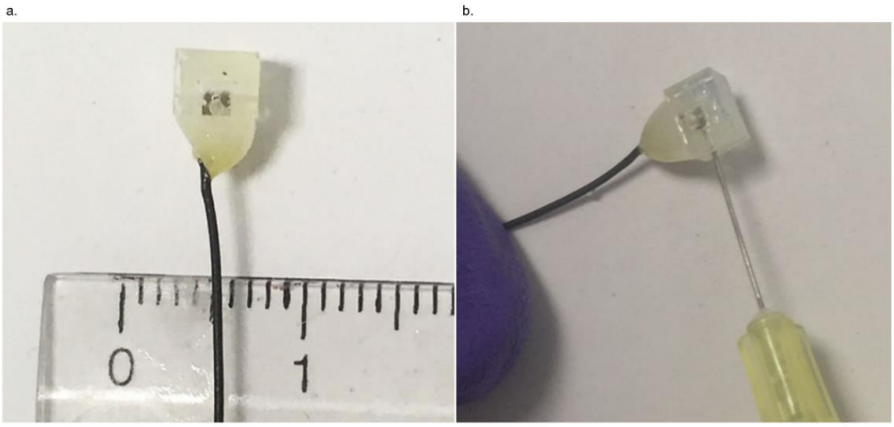

Figure 3.13 – RE of Type-B contained within a micro milled PMMA package. The injection channels on the side are used to fill the internal chamber with the Gp-CS gel electrolyte after which they are sealed with epoxy. Scale in cm.

Figure 3.14 shows the results from the packaged REs, Type-B, with a Gp-CS electrolyte gel immersed in an external solution of 150 mM KCl, pseudo setup. Figure 3.14.a shows the averaged value per day; **Error! Reference source not found.**.b shows a zoom of the continuous trace over a ten day period. Indicated is the maximum allowed error band of 6 mV which is approximately one-tenth of a Nernst slope; this is of importance to maintain the desired accuracy for the pH sensor, as discussed in Chapter 5. Comparing the data for the bare reference to the Gp-CS reference, there is no added advantage to the inclusion of the gel for full RE performance. This is also confirmed when looking at the differential drift of the mean as depicted in Figure 3.14.c.

An estimate of the error for the reference electrodes was made and is presented in Figure 3.14.d. Note that each count represents three times the standard deviation (σ) for each RE for the average of each day, with extreme outliers excluded. This is the worst-case error graph with a mean of 4.8 ± 1 mV; still within the error margin of one Nernst factor.

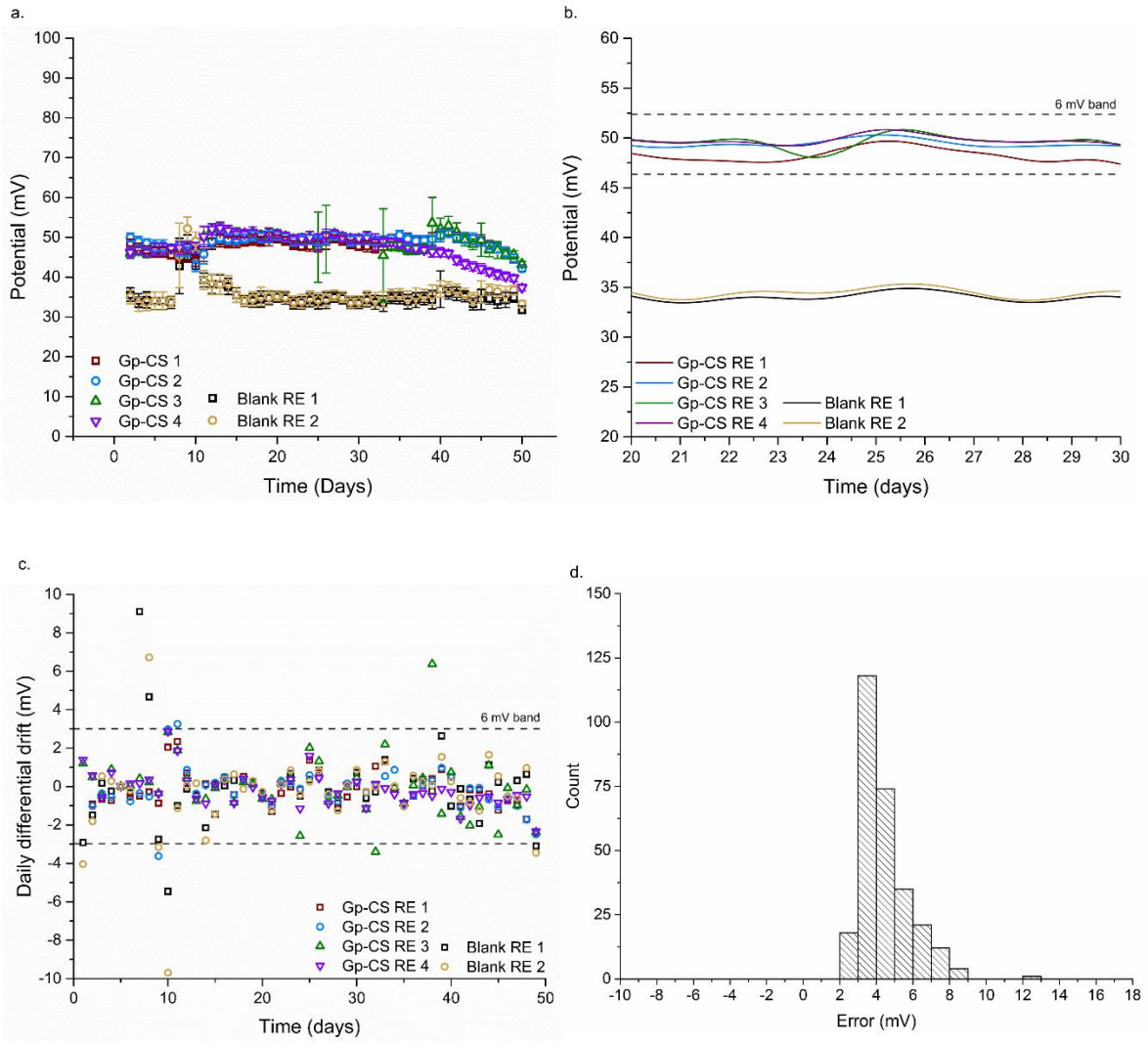

Figure 3.14 - Long-term experimental data for the Gp-CS hydrogel electrolyte REs in a PMMA package measured in 150 mM KCl. a) Average potential per day; b) Zoom of the continuous trace over the course of 10 days; c) Overview of the differential drift of the mean per day. d) Histogram of the worst-case (3x σ) for the error on the mean. Note that outliers have been excluded from the fit.

3.3.5 Full reference test

The REs are to be integrated into a single package containing the electrolyte (more details available in Chapter 6), so a *ComSol* simulation was developed to illustrate their effects. Details on the model are available in Appendix A2. Before discussing the results of the full reference tests a brief discussion on the underlying principle is required. In any situation where there is a concentration gradient between connected vessels, diffusion across the boundary will occur as described by Fick's Law (Chapter 1).

The time taken for the electrolyte to diffuse out of the gel dependents on the following:

1. Distance between the measured points;
2. Diffusional properties of the media;
3. Interfacial area of the connecting junction;

4. Concentration gradient;
5. Available volume.

The results are shown in Figure 3.15. The diffusion coefficient is constant and set to be that of chloride in water. The length of the junction is fixed. Figure 3.15 shows the variation of the Interfacial area, the concentration gradient and the available volume. Note that in Figure 3.15.b and d, the concentration has been converted into a cell potential using the Nernst-equation.

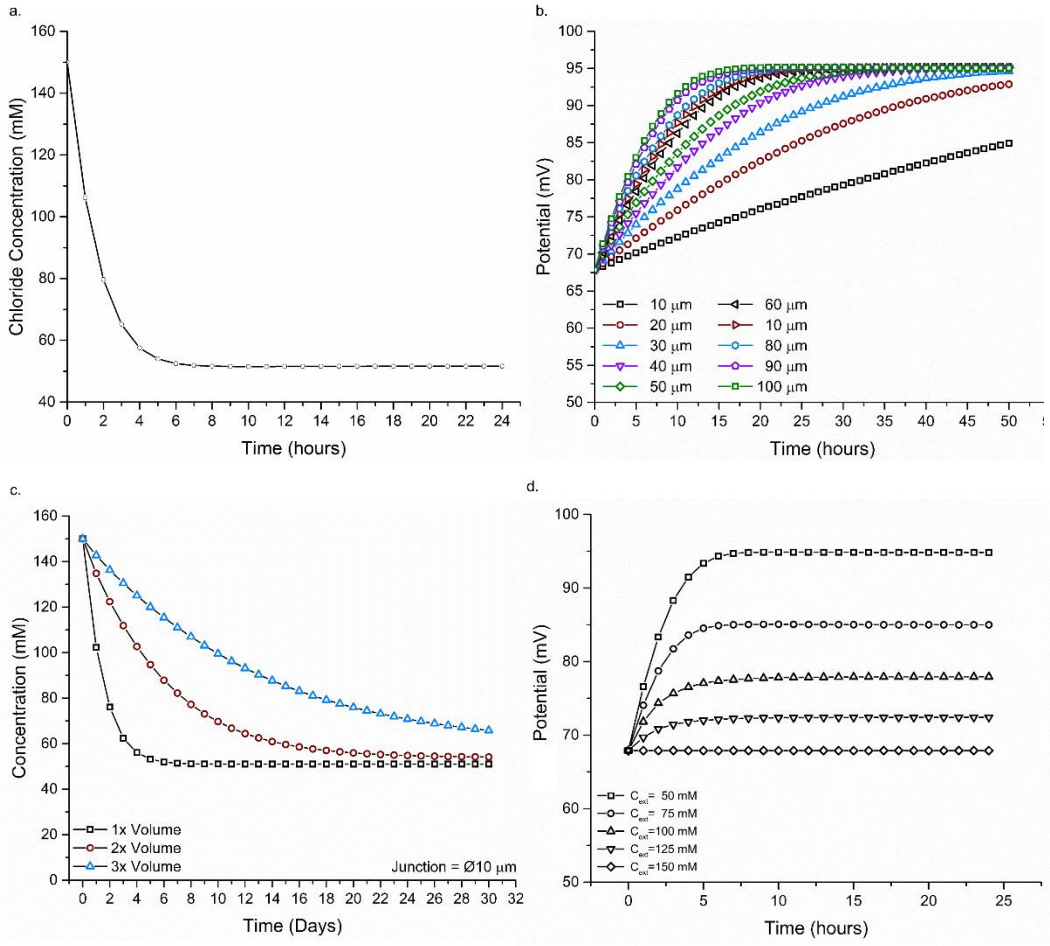

Figure 3.15 - Simulated diffusion profiles of chloride over time for a) the PMMA package; b) various junction diameters; c) chamber volume with a junction diameter of 10 µm; d) different external concentrations of chloride. Note that the potential for b and d is computed from the Nernst-equation.

The data in Figure 3.15.a shows the expected chloride concentration at the RE interface with an external concentration of 50 mM and a junction size of 400 µm in diameter. This represents the PMMA package. As seen, in this scenario the concentration will have equilibrated within eight hours. Figure 3.15.b shows the result when the size of the junction is decreased showing that a small-sized junction is preferred. Although it will not prevent complete loss of the chloride, it can be designed in such a way that a predictable drift over time is observed. *Zevenbergen et al.* reported on a similar concept for use in CMOS processed pH and chloride sensors. By creating a small channel inside a Silicon substrate, the diffusional loss of chloride from an internal chamber can be predicted and

compensated for (129). However, blockage of this pore by proteins can be a considerable issue during implantation.

Figure 3.15.c shows the result when the internal chamber volume is increased by a factor of 2 and 3, respectively. As can be seen, with a small junction and 3x the volume of the PMMA chamber a 30 day drift is observed which can be fitted to an exponential to predict the drift over time. Finally, Figure 3.15.d shows the effect of the concentration gradient on the loss of chloride. For the package used in this work, an approximate time of 7.5 hours is expected.

A comparison of the simulated data with the packaged REs is shown in Figure 3.16. It can be noted that the concentration is maintained slightly longer than expected with times of 10 hours and 15 hours for the bare and Gp-CS REs, respectively. This slight gain could be due to the difference in diffusion coefficient, but is more likely to be caused by misalignments within the package which increase the volume. It can be concluded that the Gp-CS has no influence on the diffusional characteristics compared to those of water. This result is to be expected as the diffusion coefficient is proportional to the hydrated radius of the ions. Although the viscosity within the polymer matrix is slightly higher, the chloride ion does not see a difference between CS and pure water.

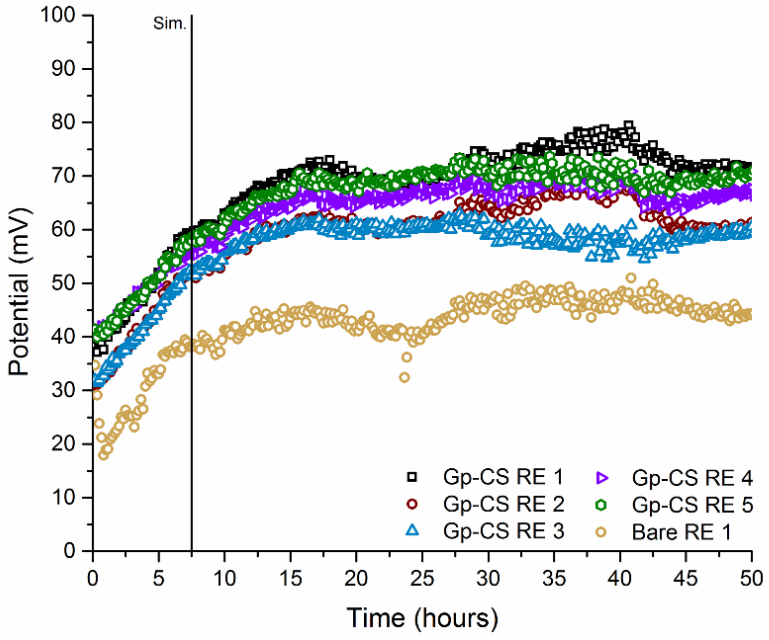

Figure 3.16 - Full reference test for Gp-CS inside a PMMA package and a bare 150 mM KCl filled control. The external concentration equals 50 mM NaCl. Indicated is the predicted equilibration time based on the simulation profile for the PMMA package.

To try and limit the diffusion of the chloride anion, an anion diffusion limiting membrane was incorporated on top of the junction formed with *Nafion*®, a fluoropolymer used throughout biology for its biocompatibility. Its internal channel structure allows for the contact between the electrolyte chamber and the external solution via its exchange capability for protons and water (130, 131). It is

easy to cast and sticks well to acrylate. An example of a formed *Nafion*® membrane across the package junction, viewed from the top and bottom, is shown in Figure 3.17.a and b, respectively.

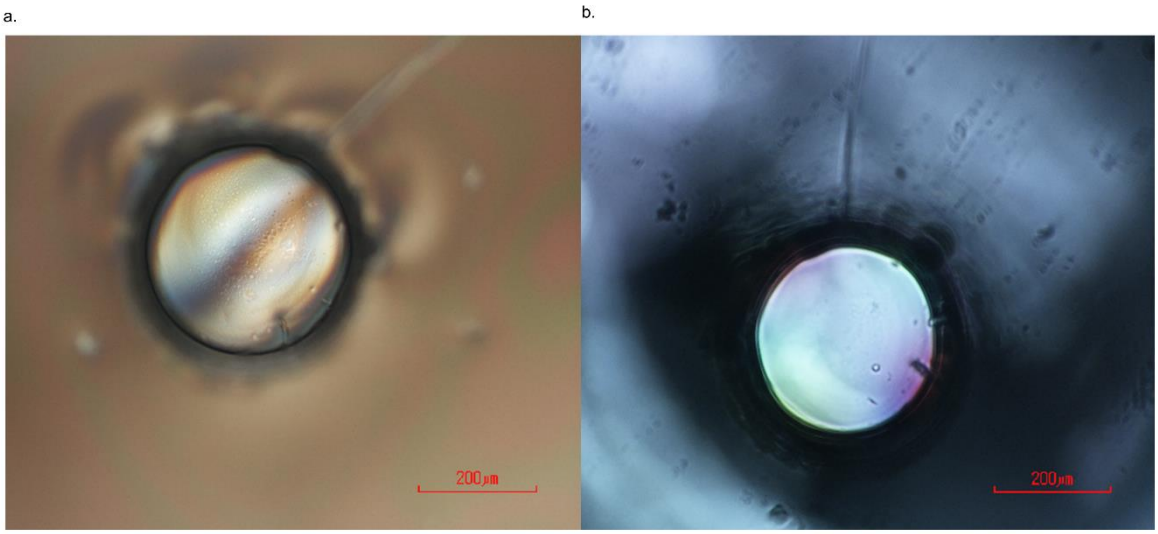

Figure 3.17 – Cast *Nafion*® membrane on PMMA package viewed from (a) top and (b) bottom.

Results from the Gp-CS REs with a *Nafion*® membrane are presented in Figure 3.18. The membrane was cast on top of the junction prior to filing with the electrolyte gel according to the methods described in section 3.2. Samples were pre-soaked in PBS before changing the external concentration to assess the performance of the REs. The REs were immersed in a solution changing from 1x PBS to 0.3x PBS. The linear times and drift are shown in Table 3.3.

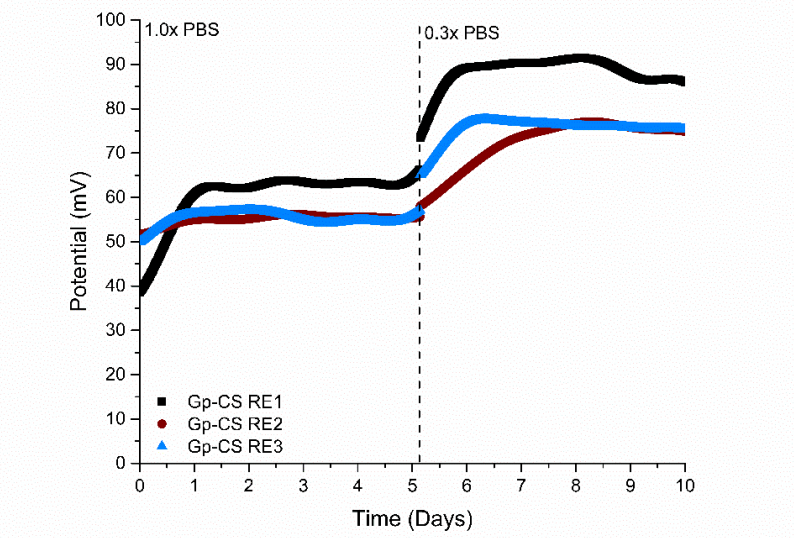

Figure 3.18 - Results from REs of Type-B with Gp-CS electrolyte and a cast *Nafion*® membrane with a PMMA package. The external concentration was changed from 1x PBS to 0.3 x PBS after a 5 day measurement period

Little benefit can be attributed to the addition of a *Nafion*® membrane. For the Gp-CS RE2 sample, in Figure 3.18 there is a drift of 2.5 days which is linear over the first 34 hours. However, the other samples show a similar diffusion time as the membrane-less samples discussed in Figure 3.16.

Table 3.3 – Extracted data values from the *Nafion*® Gp-CS full RE test.

	Linear Time	Slope	Average (PBS)	Average (0.3x PBS)
Sample 1	12 hours	26 mV hour^{-1}	60 ± 6 mV	88 ± 2 mV
Sample 2	34 hours	10 mV hour^{-1}	55 ± 1 mV	75 ± 1 mV
Sample 3	19 hours	14 mV hour^{-1}	55 ± 2 mV	76 ± 1 mV

Ostensibly, the PMMA packaging method with the hydrogel electrolyte cannot be expected to serve as full RE. To find a means to achieve a predictable behaviour, sensor Type-C was designed and fabricated. In this design, the open circle in the middle of the inner ring could be used to create a tiny aperture. Additionally, a sensor housing with as much volume inside the package (minimum of 3x the current volume i.e. 4.5 µL) should be used. However, creating straight holes with a diameter below 10 µm in a 600 µm glass substrate is challenging. This method and alternatives to obtain similar results are discussed in Chapter 7.

3.4 Summary

This chapter discussed the background, theory and state-of-the-art of current miniature RE developments. History has shown that there are no miniature full REs with low levels of drift. The REs presented in this work have shown excellent performance over the course of 50 days with a fabrication yield of 64.5% at 5 weeks. A method for preselecting REs based on initial measurements has been proposed and provides a reliability of 90%. The fabrication of the REs consisted of an electroplated Ag layer deposited onto Pt electrodes. The silver was converted into Ag-AgCl using electrochemical conversion in 3 M KCl. The worst-case error falls within the required range for the intrauterine application with drift levels below 1 mV day^{-1}

The use of hydrogel electrolytes was investigated. By employing a hydrogel the failure due to leakage of the electrolyte within the device package is limited. Both pAm and Gp-CS have proven their ability to function in pseudo-setups. However, their use for a full RE is questionable. As the diffusion models have shown and predicted, the loss of chloride is not limited by a hydrogel based polymer matrix. Nor does the inclusion of an additional flux limiting membrane in the form of *Nafion*® enhance its performance. The only feasible way to obtain a predictable drift with changing external concentration is the use of an aperture in the 10 µm scale with a large internal volume. A design for this type of setup has been made and is discussed in Chapter 6.

Chapter 4 - DO sensor development

This chapter describes the development of an implantable dissolved oxygen sensor. As discussed in Chapter 1, DO is a key parameter for the successful development and implantation of embryos. For the wireless implantable IUSD the power consumption should be kept to a minimum. A small footprint is required for future integration in the implantable device. With these constraints in mind, this chapter describes the development of a low-power miniature DO sensor. First, the history and state-of-the-art are discussed. Second, the electrochemical techniques and setups used to assess sensor performance are listed. Finally the development of the sensor based on theory and simulations is then discussed, followed by the results and discussion.

4.1 A brief history on dissolved oxygen sensing

The importance of dissolved oxygen, both in biology and environmental sciences, is widely recognised. The past century is marked by key milestones that have led to commercially available devices, as shown by the time line in Figure 4.1. The first person to devise a method to quantify oxygen levels in solution was *Winkler*. In 1888, the equally named Winkler titration was developed. In this method, manganese, manganese chloride and Iodide (Mn(II), $MnCl_2$, I^-) are added to the test sample. All components are added in excess in order to react with all the oxygen present in the sample. The oxygen oxidises the Mn(II) to Mn(IV), forming a brown precipitate of $MnO(OH)_2$. Upon the addition of excess acid (hydrochloric or sulfuric) the Iodide reacts with the $MnO(OH)_2$, resulting in the reduction of Mn(IV) back to Mn(II) and the oxidation of Iodine to triiodide. The latter causes a change in colour, proportional to the amount of dissolved oxygen present in the solution. (132-134). Unfortunately, this type of titration is not portable nor suitable for remote, and implantable use. More importantly, it is not able to perform a continuous determination of DO unless complex microfluidics is used.

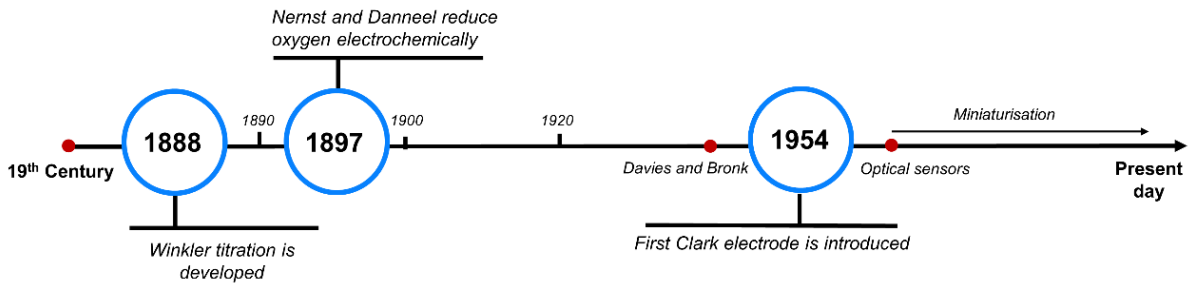

Figure 4.1- Time line of the developments in DO sensing from the late 19th century up to present day.

In the 1890's *Danneel* and *Nernst* discovered the electrochemical reduction of oxygen. Alongside their pioneering work in the field of electrochemistry this opened a world of applications. However it was not until the third decade of the twentieth century that practical sensing systems for use in

biology were developed (135, 136). Early measurements were made using DO sensors implanted into tissue, as performed by *Davies* and *Bronk* in the 1940's (137).

It was soon found that performing electrochemical measurements *in vivo* is challenging. Fouling and interferons have disastrous effects on the sensor performance. Additionally, the perturbing nature of the oxygen reduction reaction (ORR), in particular when large electrodes are used, makes it difficult to obtain accurate measurements for prolonged periods of time. In 1957, a break-through was made; *Clark* developed what is now known as the Clark electrode, depicted in Figure 4.2.a (135, 138). By employing voltammetry, the reduction of oxygen at a noble metal surface is controlled by sweeping the potential. The current related to the reduction of the species of interest is then measured via amperometric detection.

Unlike conventional amperometric sensors, Clark used a membrane, permeable to oxygen, in order to control the diffusional flux across the membrane into the internal electrolyte of the measurement cell. This limits the consumption of DO by creating a steady-state flux across the membrane, effectively creating a partial pressure difference across the membrane. It is this difference that is sensed in the Clark electrode. The addition of the membrane has the added benefit of keeping out any interferons from reaching the electrode surface. With the invention of the Clark electrode, the first intravenous monitoring of the pO_2 was achieved (139, 140).

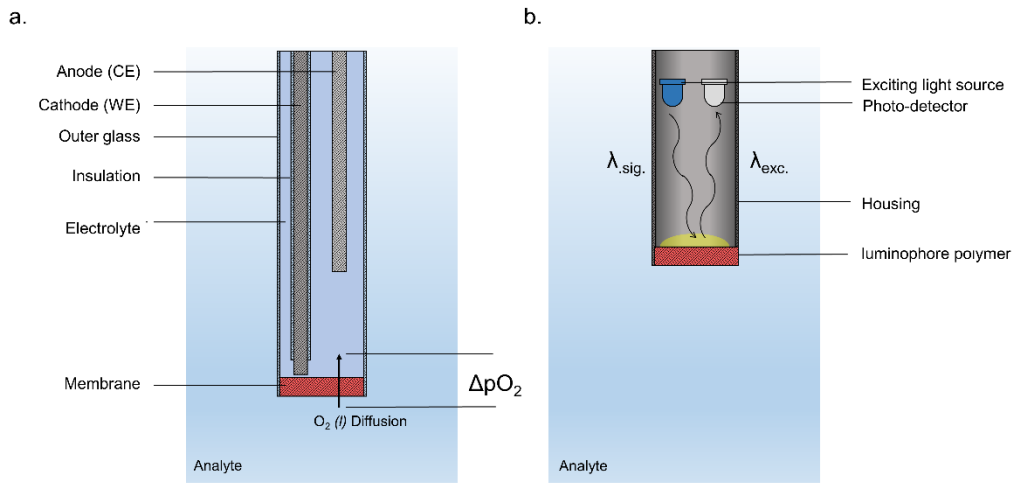

Figure 4.2 - a) Cross-section of a Clark electrode immersed in an analyte. Oxygen diffuses across the membrane into the internal electrolyte on the basis of a difference in partial pressure. The oxygen in the electrolyte is reduced at the cathode which is polarised at the oxygen reduction potential using the cathode. b) Cross-section of an optical dissolved oxygen probe. Oxygen reacts with the fluorophore inside the polymer cap. An exciting light wave is send from a light source which interacts with the fluorophore resulting in a quenching of the wave. The wave is detected using a photodetector.

Less invasive and less perturbing measurements of DO have been developed. This was achieved in the late 1960's by using optical methods to determine DO concentrations. With the development of luminescent dyes the road was paved for the development of oxygen sensitive luminophores. These luminophores are incorporated into a polymer-matrix forming a membrane in contact with the analyte

(141-144). When light is shone on the dye-matrix the luminophores are excited and in turn emit light. The excited light has an intensity or is quenched based on the amount of oxygen in the analyte. The light is detected using a photodetector. Due to the accurate tailoring of the oxygen sensitive dyes very high specificity is obtained. An overview of the optical sensing method is shown in Figure 4.2.b.

The greatest effort has gone in to miniaturisation of the sensor technologies making use of the advances in CMOS processes. Unsurprisingly, as the size of the system is scaled down vulnerabilities are exposed and a more thorough understanding of the mechanisms behind the sensing of DO is required.

4.2 Limitations of the current DO sensors

Of interest for this research is the difference between the developed electrochemical and a commercial optical sensing probe. It is important to establish what the limitations of these two methods are so as to form a complete view on what drives the application towards *in vivo* sensing.

The general advantage of the optical probes is their ability to sense a wider range of DOCs with very high specificity. This is possible due to their non-perturbing operating principle. As the dyes incorporated into the polymer matrix are specifically tailored towards their sensitivity to oxygen this can be achieved with great accuracy (145-147). Although great in function, the optical probes are in general bulky. Although progress has been made on reducing their footprint by using optical fibres they still require electronics with a relatively high power consumption compared to electrochemical sensors on the micro scale (51). For the optical probe two main subcategories exist based on their detection method: decay-time and intensity of the luminescent signal. The major advantage of the first is its prolonged life-time due to a reduction in photo bleaching of the oxygen sensitive dye. However, a more complex read-out is required as well as increased complexity in the signal-processing. For the later, the main advantage is its simplicity (148).

In general, any noble metal can be used to sense DO. By comparison, electrochemical sensors are easy to fabricate so it is easy to understand why most of the miniaturisation has focused on this type of sensor. Comparing the electrochemical sensors to the optical probes a faster response time is observed. This is especially important in applications where the DO concentrations fluctuate rapidly. Their main limitation is the lack of sensitivity in the lower end of the concentration range (near zero), due to the perturbation they impose on the measurement environment. The two sub-classifications are galvanic (self-polarising) or potentiostatic (external polarisation) (148). The first relies on the self-polarisation between cathode and anode made of different metals. For the later a stable RE is required which has been shown to be challenging and can cause poor reproducibility over time (149).

Looking more closely at the Clark electrode, the addition of a membrane differentiates it from conventional voltammetry based sensors. Many iterations and improvements have been made over

the past decades to optimise its use as an *in vivo* sensor. Issues related to miniaturisation provide the biggest challenge along with the stability of the RE. A closed system is prone to bubble formation inside the internal electrolyte. The inclusion of an internal electrolyte on a small sensor is difficult to achieve. Also, membrane deformation and non-uniformities can severely impact the sensors characteristics as they have an effect on the diffusion distance. This diffusion limitation of the membrane results in a longer response time compared to bare DO sensors, defined by the electrode-membrane distance and the composition of the membrane and the internal electrolyte. This results in a delayed response time (150).

4.3 Electrochemical measurement techniques

An electrochemical experiment is conducted using either a two- or three-electrode system. A two electrode system consists of a WE at which the reaction of interest occurs, and a RE/CE, single electrode, which supplies the current. In a two-electrode system the cell potential is measured as the potential difference between the WE and RE/CE. The major disadvantage of this configuration is that the current passes through the RE/CE causing an alteration in the cell potential, due to the reaction occurring at the interface. Especially in sensitive experiments where the active potential window of the reaction is small this can be problematic.

In DO sensing a three-electrode system is preferred. Here, the RE/CE is separated, ensuring the cell stays at a fixed reference potential provided by the RE. The reaction occurring at the CE then has no influence on the cell potential, and the resulting current is only attributable to the reaction at the WE. The potential at the WE is altered versus the RE. Consequently, the CE sources all the current required for the electrochemical reaction. In order to achieve this, the surface area of the CE has to be large compared to the surface area of the WE.

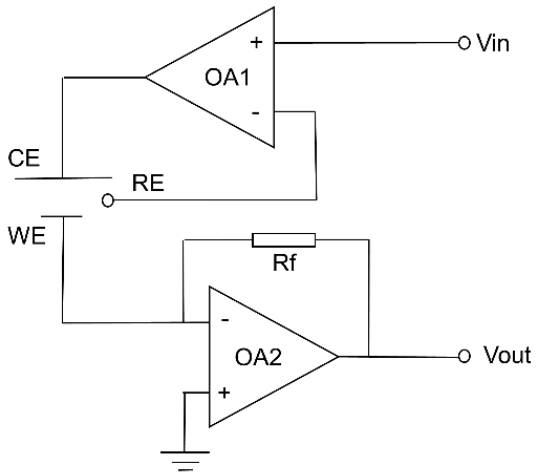

Figure 4.3 - Potentiostat schematic for a three-electrode configuration. OA1 controls the potential between the WE and RE based on the applied potential at the non-inverting input. As a result a current is sourced through the CE. The transimpedance amplifier formed by OA2 and the feedback resistor amplifies and converts the current through the WE into an output voltage.

The three electrode setup is controlled using a potentiostat, a diagram is shown in Figure 4.3. Its main function is to maintain the voltage between the WE and the RE. A current is sourced through CE by means of an operational amplifier (OA1), in order to keep the inputs equal. As the potential between WE and RE is altered, electrochemical reactions are initiated and a flow of electrons is ensued. The resulting current flowing through the WE is sensed by means of a transimpedance amplifier (151). A wide variety of measurements can be performed with a potentiostat as will be discussed next. The techniques of importance to the development of a DO sensor are discussed here.

4.3.1 Linear sweep voltammetry and cyclic voltammetry

In linear sweep voltammetry (LSV) the potential between the WE and RE is swept over time and the current from the electrochemical reaction is recorded. The LSV start potential is defined as one of two vertices set in the experimental conditions. The potential is swept at a constant scan rate ($V\ s^{-1}$) towards the second vertex where the measurement ends. In contrast to LSV, where the experiment ends after the potential has reached the second vertex, in cyclic voltammetry (CV), the direction of the sweep is reversed once this potential has been reached. Here, the starting potential can be defined anywhere within the range of the two vertices. The resulting current from the electrochemical reaction at the WE is plotted versus the potential. LSV and CV are powerful analytical tools which give insight into the electrochemical reactions occurring within the system. Valuable information that can be obtained via CV, relevant to the development of a DO sensor are:

1. Reversibility of the electrochemical species;
2. Steady-state current values;
3. Oxidation-reduction potential windows;
4. Stoichiometry of the electron transfer reaction;

Figure 4.4 shows a representation of the cyclic voltammogram for an ideally reversible couple. In the convention used in this thesis, negative current represents a reduction reaction; positive current represents an oxidation reaction. When the potential is swept towards the standard reduction potential of the reaction an increase in current at the WE is observed. Starting from *p1* in Figure 4.4 where the potential is swept more negative, an increase in current caused by reduction of the electro active species is observed. While the reaction takes place, the species near the electrode is consumed and depleted: an upper limit is reached represented by *p2*. At this point there is not enough of the active species present, and as a result the current falls until the rate of consumption equals the rate of mass transfer i.e. diffusion. This is referred to as the steady-state at *p3*.

As the direction of the sweep is reversed the same process occurs only now the reduced species is oxidised resulting in a positive current at *p4 (152)*. The magnitude of the peaks are equal when all the species, which had previously been reduced, are fully oxidised and the same amount of electrons

gained during the reduction are now lost in the oxidation process. The stoichiometry of the electrons transfer can be determined based on the magnitude of the peaks. An estimate of the standard reduction potential can be obtained by assessing the symmetry of the two peaks along the potential axis (152).

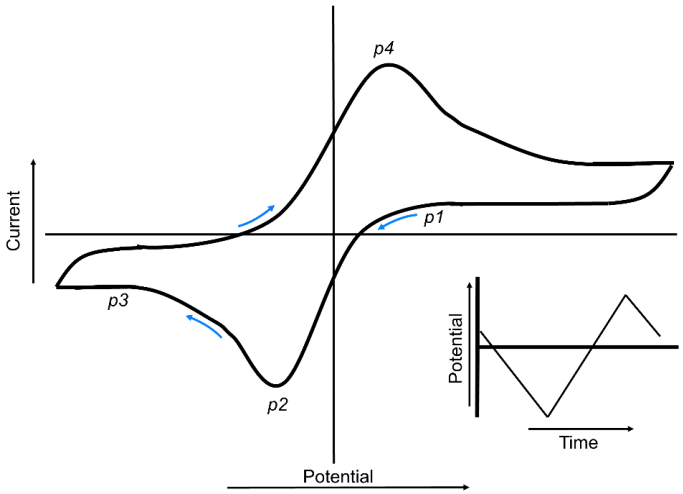

Figure 4.4 - Image of a CV for a reversible couple. As the potential is swept in the negative direction, the electroactive species are reduced at the WE (*p1*). As the sweep is continued the species near the surface are consumed and an upper limit is reached (*p2*). Because there is not enough of the species present in order to sustain the current, the current falls until the rate of mass transport equals the rate of consumption. Here a steady-state is reached (*p3*). As the direction of the sweep is reversed, the species previously reduced are now oxidised. The same key points are observed with an oxidation peak at *p4*.

4.3.2 Chrono-amperometry

During chrono-amperometry the potential at the WE is stepped rapidly. Similar to CV, a current flow is established dependent on the electrochemical reaction at the WE interface. Typically the chrono-amperometric measurement is of a shorter duration than CV measurements. Due to the rapid depletion of the species a mass-transport limitation sets in. A representation of the current vs. time curve obtained in this manner is shown in Figure 4.5. The current consists of two parts: an initial response in which the species is rapidly diminished (henceforth referred to as transient response); a later steady-state in which the rate of diffusion equals the rate of consumption.

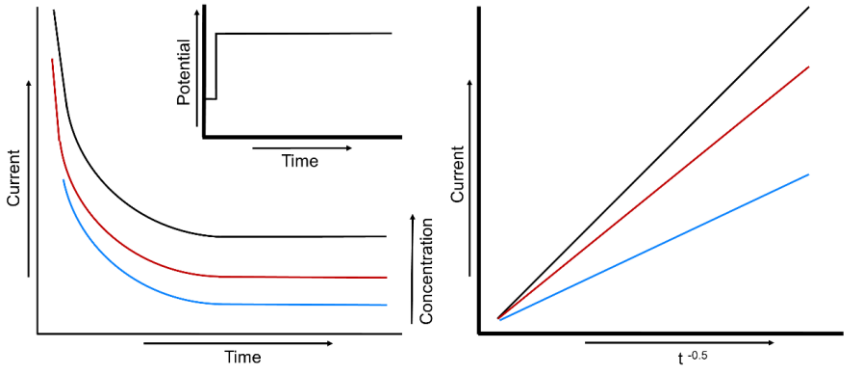

Figure 4.5 - Current versus time graph upon the application of a potential step. left) the resulting chrono-amperogram plotted versus time; right) the current plotted versus the reciprocal of the square root of time.

The first part of the curve is described by the Cottrell equation shown in equation 4.1. Here, *n* is the number of electrons involved in the reaction; *F* the Faraday constant, *A* the area of the WE; *C* the concentration; *D* the diffusion coefficient; *t* the time. Because the initial concentration at the WE is high, a large magnitude in current is observed. As the time progresses, the species is consumed and the current decays.

The transient response is highly dependent on the electrode geometry and the surface conditions. To obtain reproducible results it is therefore required that surface conditions are kept as identical as possible for each measurement (153). Assessment of the response is performed by plotting the current versus the reciprocal of the square root of time. If the Cottrell equation holds, a linear curve is observed. Additional effects, such as double layer charging and electrode polarisation are seen at very short time scales, limiting the linearity of the Cottrell equation to time points beyond the charging of these components. On the other end of the time scale, towards the steady-state, a deviation from the Cottrell equation occurs due to the three-dimensional diffusion profile.

Insight into the charging and diffusion profiles can be assessed further via integration of the Cottrell equation as shown in equation 4.2. In experimental terms this is referred to as chrono-coulometry. The resulting charge (*Q*) versus the square root of time graph is known as an Anson plot. The charging of the double-layer can be observed, as well as the presence of adsorbates, convective and diffusional effects.

$$I = nFAC\sqrt{\frac{D}{\pi t}} \qquad (eq.4.1)$$

$$Q = \frac{\sqrt{D}2nFAC\sqrt{t}}{\sqrt{\pi}} \qquad (eq.4.2)$$

4.4 The oxygen reduction reaction

The ORR is a complex process. It has been widely studied over the past decades and still is subject to investigation. The reason for its complexity is its multiple reduction pathways. In 1968, *Hoare* wrote an extensive work on the electrochemistry of oxygen (154). It covered the full range of anodic and cathodic oxygen electrochemistry up till then, as well as the formation of surface oxides on a wide variety of metal surfaces. In the sensor described here, the cathodic reduction of oxygen is investigated.

As shown in Table 4.1 oxygen reduction can proceed directly via a four electron pathway; indirectly with an intermediate species and two electrons in each pathway. These pathways have been found to be dependent on the pH of the bulk. Additionally, it has also been shown to be dependent on the type of material and the surface conditions (154).

Table 4.1 - Mechanisms for the reduction of oxygen in acidic and alkaline solutions.

	Acidic	Alkaline
Direct	$O_2 + 4H^+ + 4e^- \rightarrow 2H_2O$	$O_2 + 2H_2O + 4e^- \rightarrow 4OH^-$
Indirect	$O_2 + 2H^+ + 2e^- \rightarrow H_2O_2$	$O_2 + H_2O + 2e^- \rightarrow HO_2^- + OH^-$
	$H_2O_2 + 2H^+ + 2e^- \rightarrow 2H_2O$	$HO_2^- + H_2O + 2e^- \rightarrow 3OH^-$

Looking more closely at the way the oxygen molecule is reduced, a dissociative reduction is observed for the direct pathway. The indirect peroxide pathway is illustrated in Figure 4.6, here the adsorbed oxygen molecule gains an electron and recombines with a proton to form a hydroperoxyl radical. A second electron is gained and the hydroperoxide forms into hydrogen peroxide through the reaction with another incoming proton. In the case of Pt, which itself finds a use as a catalyst for the decomposition of hydrogen peroxide, it is to be expected that the second step in the pathway occurs on the basis of the decomposition of hydrogen peroxide into oxygen and water. In essence the loop is a duplex with the oxygen freed from the hydrogen peroxide being reduced in the second step, totalling the number of electrons to four (154-156).

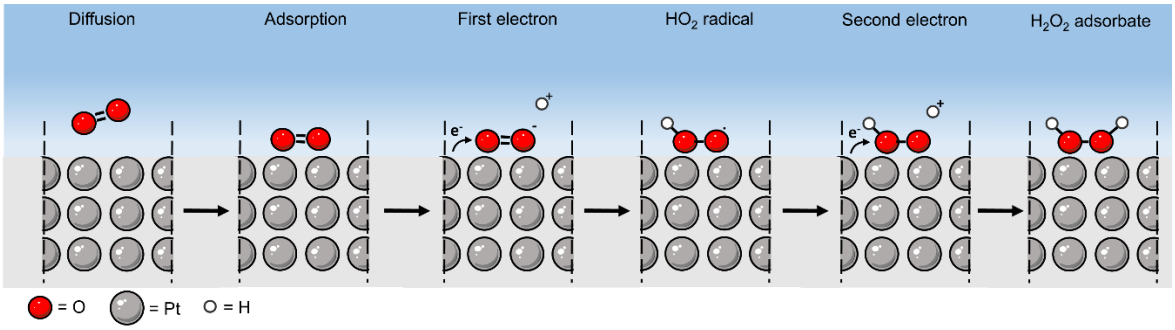

Figure 4.6 - Oxygen reduction mechanism for the indirect acidic pathway. Oxygen diffuses to and adsorbs on the Pt surface. An electron is gained and an incoming proton reacts with the negatively charged oxygen to form a hydroperoxide radical adsorbed on the surface. A second electron is gained and the hydroperoxide reacts with an incoming proton to form adsorbed hydrogen peroxide which can then be further reduced in to oxygen.

It is understandable that the direct pathways are preferred during the reduction of oxygen. Not only do they have a higher direct electron exchange, they also do not generate any intermediate species. Both hydroxide and hydrogen peroxide adsorb onto Pt and can alter the surface. As discussed by *Damjanovic et al.*, in alkaline conditions, the over-potential for the ORR is lower than observed in acidic conditions, most likely due to the fact that the peroxide is more stable in acidic than in alkaline conditions and adsorbs on the surface (156). Further complications arise due to local pH changes. In particular, the generation of hydroxide near the surface can shift the cell potential by -59 mV per pH.

It is important to note here that the reduction of the peroxides in both alkaline and acidic conditions is highly dependent on the surface conditions. What is important is that, hydrogen peroxide can be lost or produced during the reaction and have an impact on the accuracy of the DO measurement.

Measurements performed *in utero* are expected to be near neutral pH. In this situation all pathways have to be expected. It is therefore of critical importance to optimise the measurement procedures and sequences to allow any products and by-products to be moved away by mass-transport during the measurement in order to maintain optimal performance of the transient response.

4.4.1 Oxide formation and adsorbates

As stated, the reproducibility and performance of the ORR is highly dependent on the surface conditions of the electrode surface. During continuous use, even inert metals such as Platinum, experience surface changes. The highest impact on the ORR is caused by the formation of Pt oxides. *Lorenz* and *Hauser* reported on this "Oxide Theory" and showed that the surface potential at the electrode interface is dependent on the oxide-oxygen interaction, rather than the metal-oxygen interaction (157, 158) . This results in poor reproducibility in electrochemical oxygen sensing. More general, any adsorption or formation of oxide blocks the available sites for the reduction of oxygen. During ORR experiments this is caused by the following species: oxygen, hydrogen peroxide and hydroxide.

The mechanisms of Platinum oxide formation and its effects are still being investigated. Especially in the field of fuel-cell development it is important to understand the mechanism in order to obtain optimal performance, efficiency and life-time (159, 160). Controversy still exists, but less so compared to the early days of ORR research. It is now known that Platinum oxide forms through the adsorption of water on the surface. Water molecules chemisorb onto the formed hydroxide groups and dissociate, providing an electron to facilitate a place exchange: a Pt atom is displaced in the lattice. The vacancy left within the lattice is filled with oxygen forming the Platinum oxide. The process continues until all sites have been converted (161). This process is illustrated in Figure 4.7.

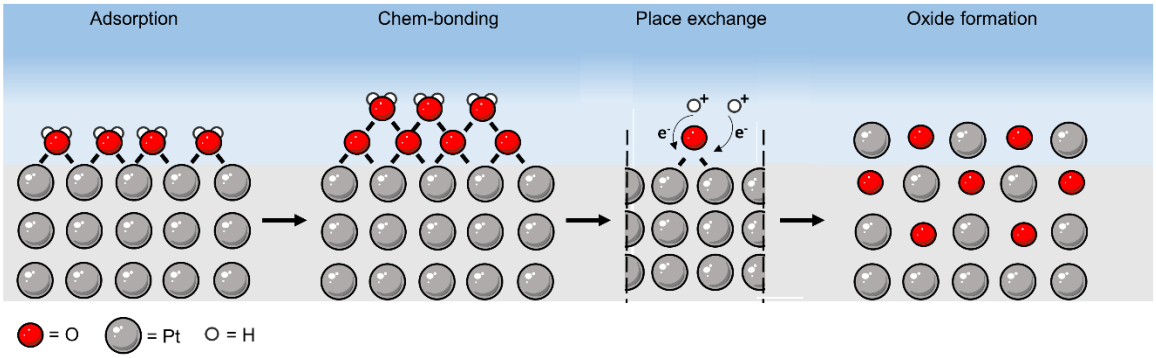

Figure 4.7 - The formation of oxide on a Pt surface. As water adsorbs on the surface a layer of oxide-water is formed. The hydrogen sites on the water molecule dissociate and provide energy to the oxide. This results in a place exchange in which an oxygen atom enters the Platinum lattice.

Formation of oxides and adsorption of hydroxide are a cause for discrepancies in ORR measurements. As discussed, the mechanism and effects are still subjected to investigation. *Bianchi*

has shown that an interfacial oxide layer on Pt can block the reduction of DO but enhance the reduction of hydrogen peroxide. This is caused by the negative dipoles present on the oxide layer which in turn facilitate the transfer of electrons reducing the adsorbed hydrogen peroxide (162).

It has further been shown that a reduced activity towards oxygen is observed when hydroxide is absorbed onto the platinum surface. The extent of which has been shown to be material dependent. As the potential of the WE is swept hydroxide adsorbs and forms an oxide layer. Positive potentials ranging from 0.4 and 0.9 V vs. SHE, have been reported (163-165). Therefore, care has to be taken to stay out of this potential window. A representation of a typical CV for the reduction of oxygen on Pt microelectrodes is depicted in Figure 4.8. Indicated are the regions of interest discussed in this work.

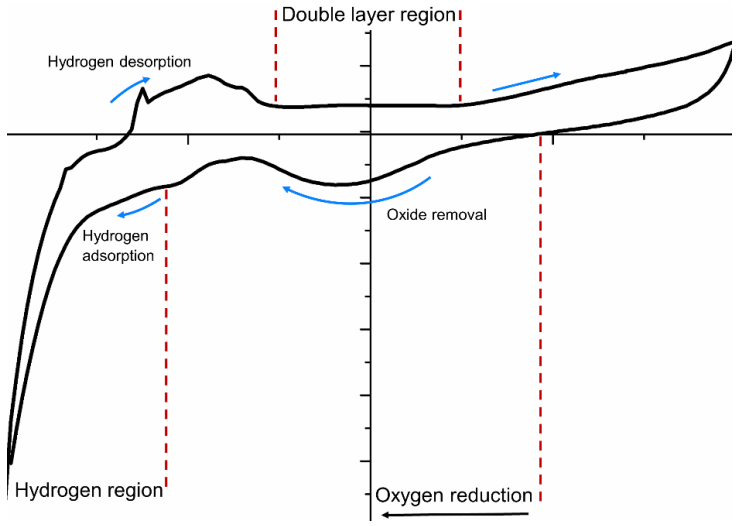

Figure 4.8 – Example of the ORR cyclic voltammogram for a Pt microelectrode in a deoxygenated bulk. Indicated are the regions of interest discussed within this work. At positive potentials, past the double layer region, Platinum oxide is formed. Any formed oxide is reduced in the return sweep within the oxygen reduction region. As the potential is swept more negatively hydrogen is adsorbed on the surface.

The transient response obtained by electrodes operated using chrono-amperometry is highly susceptible to alterations in surface conditions. In order to maintain the reproducibility and optimal sensitivity, the reactions occurring at the WE, the formation of oxides, and the build-up of local reaction products has to be controlled and optimised. One way of ensuring identical surface conditions is the use of a conditioning procedure prior to the measurement of DO. This procedure sweeps the potential between the hydroxide and hydrogen adsorption regions. By performing this type of sweep the thin, surface oxide layers can be removed and the available sites liberated, maintaining sensitivity over time (153, 166).

As reported by *Pletcher et al.* the same can be achieved by applying a conditioning pulse (CP). Here, instead of scanning across a potential range the potential is repeatedly stepped into the pre-determined regions (167). *Sosna et al.* have reported on using this method to create long-term stable DO sensors for maritime applications (153). In contrast to these systems, there is no convection *in*

utero. Therefor a non-convective system has to be assumed for the IUSD. In practice, this means that the only mechanism to clear any unwanted products from the surface and re-equilibration with the bulk is based on diffusion. This imposes a waiting time on the measurement system after the conditioning and measurement cycles have been completed.

During the removal of the oxide, especially in the case of oxide within the platinum lattice, a roughening of the surface occurs. As illustrated in Figure 4.9 the vacancies left by the removed oxide increase the interfacial area. The roughening of the surface can be observed as an increase in current as it alters the surface area.

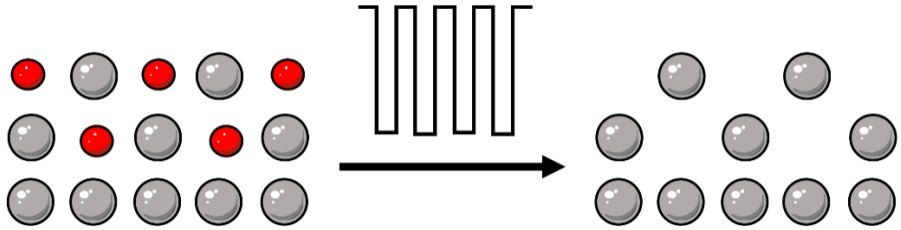

Figure 4.9 - Conditioning procedure and its effect on the Platinum lattice. As the oxide inside is removed under the application of a conditioning pulse vacancies are created. The vacancies cause a roughening of the surface increasing the surface area.

4.4.2 Macro- versus microelectrodes

Within electrochemistry the size of the electrode has great effect on the current associated with the reaction. In general the current scales with the area as can be denoted from the Cottrell equation. A wide variety of geometries can be used for the electrodes of which the most common are: rod-, disk- band-, sphere-, and hemispherical-shaped electrodes. Looking at the diffusion profile for a disk-shaped macroelectrode, represented in Figure 4.10, two phases can be defined: planar and hemispherical diffusion. The first occurs at short time intervals. Here, the diffusion is one-dimensional, towards the electrode surface.

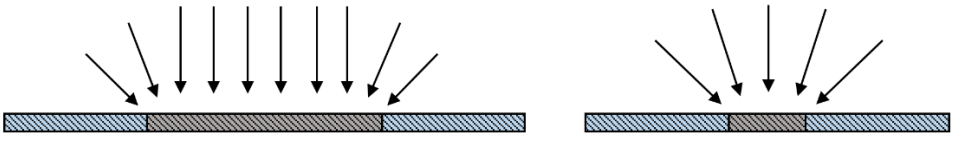

Figure 4.10: Diffusion profile for macro- (left) and micro- (right) electrodes. The small planar region of the microelectrodes facilitates a quick transition to three-dimensional diffusion from the bulk solution.

As the time extends, the one-dimensional diffusion boundary described by the Einstein equation shown in equation 4.3, progresses further into the bulk solution and the diffusion profile starts to resemble a hemisphere allowing mass-transport in three dimensions. In this situation the equation reforms to that for a hemisphere shown in equation 4.4. In both cases, δ is the distance of the diffusion boundary; D is the diffusion coefficient of the species of interest; and t is time.

One-Dimensional: $\partial = \sqrt{2Dt}$ $(eq. 4.3)$

Hemispherical: $\partial = \sqrt{\pi Dt}$ $(eq. 4.4)$

From cyclic voltammetry it is known that, as the reaction proceeds, a steady-state sets in i.e. the rate of consumption equals the rate of diffusion. Due to their large planar surface the diffusion profile of macro-electrodes takes a long time to reach a steady-state and is, in fact, hardly ever achieved. This diffusion limitation of macro-electrodes can be overcome by stirring the solution to ensure a constant replenishment of the active species allowing it to approach its steady-state. However, in applications such as implantable devices this forced convection cannot be achieved. It is also clear that the magnitude of the current is area dependent and thus, as the electrode size increases, the current that flows is increased. This poses a challenge for an implantable system operating within power constraints.

To overcome these limitations microelectrodes, defined by a critical radius smaller than 25 µm are employed (90). Here the diffusion profile is three-dimensional due to their aspect ratio, as shown in Figure 4.10. A steady-state is achieved quickly as the active species diffuses in from all directions taking away the associated diffusion limited peak in the CV. An additional advantage is its smaller size which results in an overall smaller current, allowing a two-electrode setup to be employed. Add to this the benefit of its small perturbation and it is understandable why microelectrodes are an attractive design for implantable devices. Other advantages include a reduced double layer charge time allowing faster measurements (90, 168, 169). There are complexities associated with the use of microelectrodes. Because of the reduced current associated with the smaller geometry it can be difficult to measure the low levels of current as the signal to noise ratio is reduced. This is especially true during steady-state conditions and at low DOC.

The time for a planar microelectrode employing a disk-shaped geometry to reach a steady-state is defined by equation 4.5. Here, t_{ss} is the time when the steady-state is reached; r_0 is the radius of the disk; D the diffusion coefficient. For a planar disk electrode with a radius of 10 µm and D equal to $2.1 \cdot 10^{-9}$ m^2 s^{-1}, a time of 7.7 s is calculated (170).

$$t_{ss} = 81\frac{(2r_0)^2}{D} \quad (eq. 4.5)$$

Further reduction of power without the loss of the enhanced signal to noise ratio can be achieved by measuring at short times i.e. within the one-dimensional diffusion regime. The difference in power consumption is clear, as the current needs to be supplied over a shorter period of time. The current for micro-disk electrodes operating in this regime is described by the Cottrell equation in equation 4.1. By using an array of microelectrodes the current can easily be scaled by factoring in the number of electrodes. The advantage of measuring this transient response is that: within the one-dimensional

diffusion regime the Cottrell equation predicts a linear relationship between the current and concentration. Moreover, it follows a $t^{-0.5}$ response having a large current magnitude at short times.

It should be noted here that there is a conundrum between reduced power consumption and the time scale at which measurements can be taken. As discussed, the reduced electrode size shortens the time for one-dimensional diffusion. In order to make use of the Cottrell equation this regime has to be extended without increasing the electrode size. To achieve this, disk microelectrodes recessed in a photoresist can be used.

4.5 Materials and methods

For the DO sensor two different electrode geometries were used: Type-B and Type-C. Electrodes were fabricated according to the process described in Chapter 2. Both electrode geometries consist of an array of Platinum disk microelectrodes recessed within wells, and an on-board counter electrode. Three different recess heights were used: 55, 25, 5 µm; formed in TMMF or SU-8. A commercial Ag-AgCl (3 M KCl) RE was used for the experiments. Data was acquired with a PalmSense3 potentiostat capable of performing CV and chrono-amperometry in a three-electrode configuration.

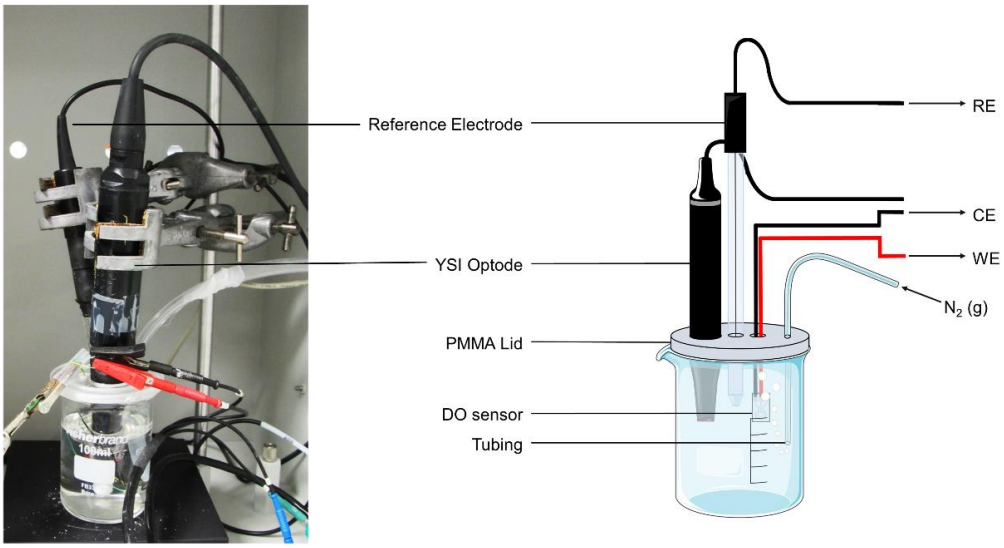

Figure 4.11 - Overview of the measurement set-up for the measurement of DO. The sensor, a commercial optical DO sensing probe, and a commercial RE are placed in a vessel containing 1x PBS covered by a PMMA lid. Nitrogen is flushed though the system to control the DOC. A PalmSense3 potentiostat, running in three-electrode mode is employed to perform the measurements.

Measurements were performed in 1x PBS, approximately 80 mL contained in a glass beaker. The volume was kept constant during long-term measurements by regular additions of DI water. The DO concentration was altered by purging nitrogen gas through the vessel. The nitrogen replaces oxygen within the solution resulting in a decrease in the DOC. A commercial Pro-ODO (optical probe, *YSI*) was used to obtain the reference DOC reading as well as temperature recordings. The probe was

calibrated monthly using a single-point calibration with a 100% air-saturation method. As stated by *YSI*, the probe has an accuracy of one decimal i.e. 0.1 mg L^{-1}, and a response time of 3 to 5 minutes. The measurements were conducted either on a bench or within a Faraday cage. An overview of the system set-up is shown in Figure 4.11.

Wafer tests were performed using a homemade probe set-up which consists of a needle electrode, placed in contact with the WE; an Ag-AgCl wire served as the RE and CE. A commercial Palmsense3 potentiostat operating in two-electrode mode was used to record the CVs. An overview of the measurement system and the probe setup is depicted in Figure 4.12. A droplet of 1x PBS was deposited on top of the WE in order to perform the measurement. After it was concluded that fabrication was successful, sensors were scribed into individual dies.

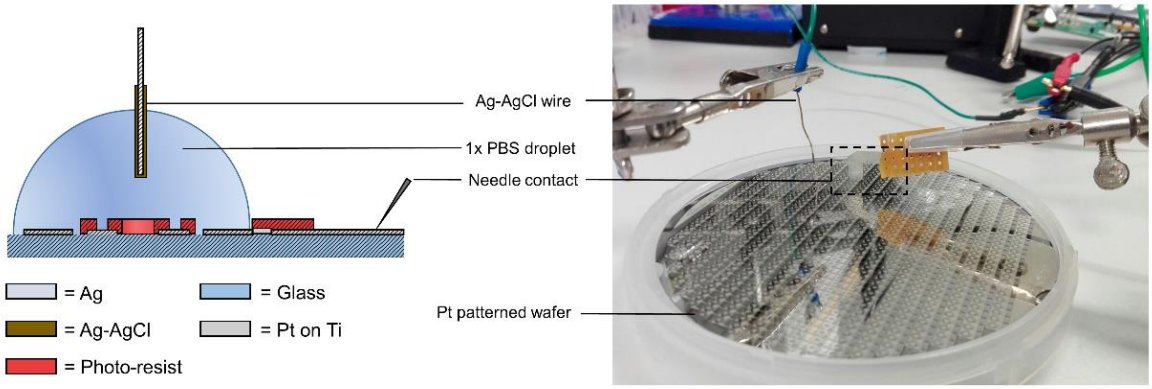

Figure 4.12 - left) Cross-section of sensor Type-C during on-wafer test in a 1x PBS droplet. The Ag-AgCl wire functions as the CE/RE; the needle is placed in contact with the WE contact pad on an individual sensor die. Right) Image of the lab set-up for the on-wafer test.

4.6 Results and discussion

This section discusses the results for the development of an implantable DO sensor for use *in utero*. Due to the complexity of the electrochemistry of microelectrodes recessed within a well, operating at short measurement times, a simulation model and its results are first discussed. These are then used as a reference for the experimental data obtained. The experimental data is separated into three parts: measurement procedure, sensor characterisation and long-term performance.

4.6.1 Diffusion of oxygen towards well recessed micro-disk electrodes

The DO related current at short time scales is dependent on the size, geometry and surface conditions of the WE. As discussed, the transient response described by the Cottrell equation is applicable when the diffusion occurs in one-dimension i.e. before the transition towards steady-state. In the case of planar microelectrodes this time is short due to their hemispherical diffusion profile. Although they can reach a steady-state quickly with a low current, there are limitations when considering their use in an implantable platform.

First, the oxygen reduction potential and its resulting current have to be supplied for the entire duration. This results in a high power demand by the sensor to reach steady-state. Second, the current at steady-state is typically very small in magnitude. Noise can thus have a significant impact. As the space on the IUSD is limited, pre-amplification of the signal is not possible. It is for this reason that an array of disk microelectrodes is used which can be manufactured using a lithographic process. Parameters which scale the current in steady-state are the radius of the micro-disk and the array size *N*; the first has an upper limit of 12.5 µm to maintain proper microelectrode functionality. Thus, the magnitude of the current, and consequently the power consumption of the DO sensor is determined by the array size. The equation for the steady-state current for a well-recessed disk microelectrode is shown in equation 4.6. Here, *n* is the number of electrons; *F* Faradays constant; *C* the concentration; r_0 the radius of the electrode; *H* the height of the recess. The time at which steady-state is reached for a recessed disk is described by *van Rossem et al.* and can be calculated using equation 4.7 (171).

$$I_{ss} = \frac{4\pi nFCDr_0^2}{4H + \pi r_0} \qquad (eq.4.6)$$

$$t_{ss} = \frac{(4H + \pi r_0)^2}{\pi D} \qquad (eq.4.7)$$

By recessing the disk microelectrode in a layer of photoresist, the linear time during which the Cottrell equation applies is extended due to prolonged one-dimensional diffusion. The transient current scales with both the area and the number of electrodes in the array which adds a multiplication factor *N* to equation 4.1. However, considering the small footprint of the sensor (2 x 4 mm) and minimum interelectrode spacing, *d*, required to prevent the overlap of diffusion boundaries (20x r_0) only limited space is available on the sensor die. For sensor Type-C the maximum amount of disks has been placed on the design with *N* equal to 8. Depicted in Figure 4.13 is a representation of the recessed disk array and its diffusion profiles. A simulation model was made to assess the diffusion within this type of sensor to gain insight into its response, time limits, current magnitudes, and steady-state conditions. Details of the model are available in Appendix B1.

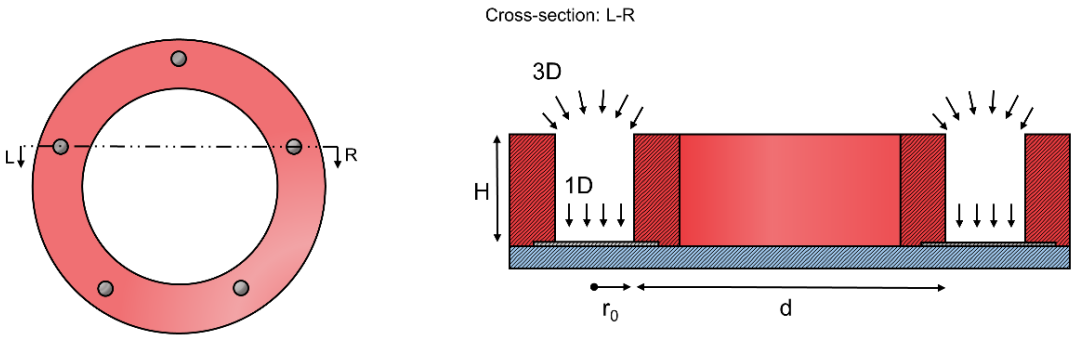

Figure 4.13 - left) Top view of sensor Type-C with *N* equal to 5. right) Cross-section L-R showing the diffusion profiles. Within the recess a one-dimensional profile is observed. At the top of the electrode hemispherical diffusion sets in.

Figure 4.14.a shows the progression of the oxygen consumption boundary over time when the concentration at the electrode surface is stepped down rapidly, as is the case during chrono-amperometric experiments. As depicted, a linear diffusion profile in one-dimension is maintained until the top of the recess is reached. The time at which this occurs is dependent on the height of the recess, *H*. It is clear that the higher the recess, the longer the one-dimensional diffusion. Figure 4.14.b shows the progression of the diffusion boundary into the bulk solution at three different time intervals for a 5 µm recess as the percentage of the bulk concentration at a given distance. As time continues, as shown by the 30 s curve, oxygen is consumed further away from the electrode surface. Calculating the time for the boundary to reach the top of the recess values of 720, 140 and 6 ms are determined for *H* equal to 55, 25 and 5µm, respectively; based on equation 4.3.

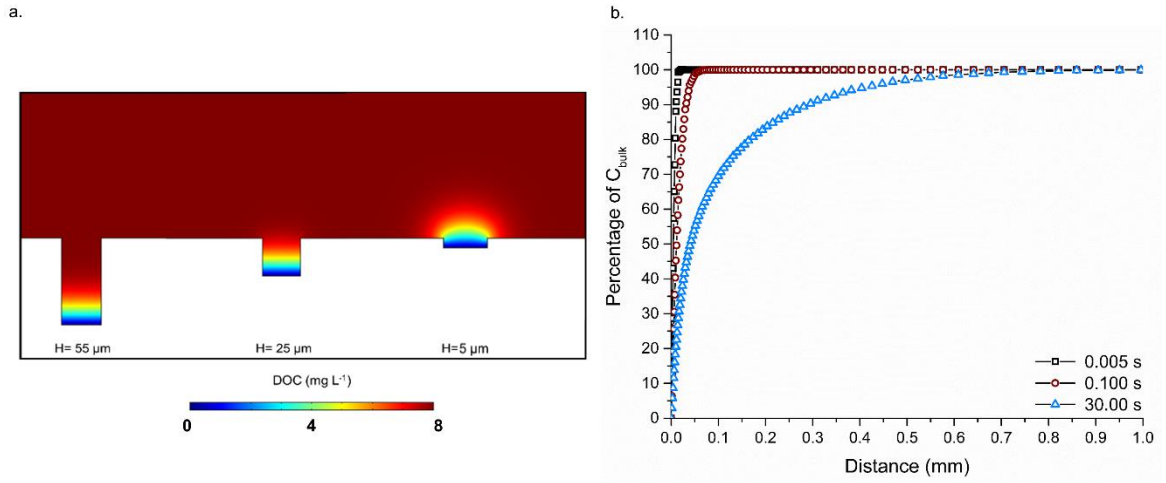

Figure 4.14 – a) DO consumption profile within recess upon the application of a reducing potential step at the electrode surface. Shown are diffusion profiles for different heights of the recess *H* at 5 ms. b) Progression of the boundary over time for the 5 µm recess presented as the percentage with respect to the bulk concentration. As time is increased more oxygen is consumed further away from the electrode surface.

Applying the Cottrell equation for a step down to 0 mg L^{-1} at the WE, an estimate of the expected current magnitude is obtained. Figure 4.15 depicts the transient current plotted versus the reciprocal of the square root of time for increasing DOC in the bulk solution; a magnitude of 10^{-7} is expected at short times. At t = 10 ms a calibration plot as depicted in Figure 4.16.a is expected. The current values for a steady-state measurement are shown in Figure 4.16.b, it is clear that very low currents are to be expected here. This is problematic in a system which has strict limitations on the discrete components that can be used to amplify the signal and filter noise.

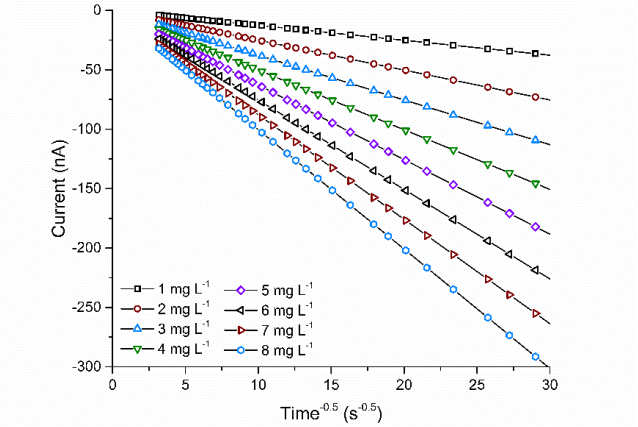

Figure 4.15 - Simulated Cottrell plot for different DOC when the concentration at WE is stepped down to 0 mg L^{-1}. Recess height equal to 5 um; *N* equals 5.

From the equations and model discussed, three parameters for the measurements are important: the steady-state time; the Cottrellian time limit i.e. one-dimensional diffusion profile within the recess; the discrete measurement time for the enhanced current response. The latter is chosen based on the trade-off between performance and reproducibility of the measurements. The values for three different recess heights are listed in Table ***4.2***. The value for the lower limit has been determined empirically and is discussed in section 4.3 in terms of the experimental results obtained in this work.

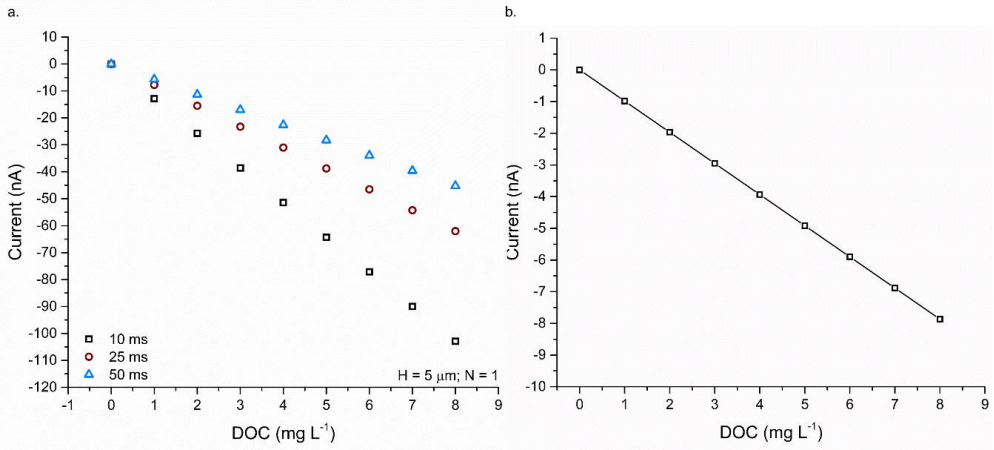

Figure 4.16 - Simulated calibration plots for (left) 10 ms value of the transient response; right) Steady-state current of a recessed disk with radius 12.5 µm and an array size of 5.

Table 4.2 - Important time points for the measurement of DO for a given recess height.

	t_{ss}	$t_{cott.}$	$t_{measure}$
5 µm	0.53 s	6 ms	50 ms
25 µm	2.93 s	140 ms	50 ms

55 µm	10.20 s	720 ms	50 ms

4.6.2 Dissolved oxygen sensor characterisation

Initial tests of the DO sensor were aimed at determining the functionality of the fabricated sensors. The performance was assessed both on-wafer prior to scribing, and on individual sensor dies. The former allowed for proper evaluation of the fabrication protocol, in particular to assess proper clearance of resist residues within the recesses. The latter to perform the actual measurements on individual sensor dies to be implemented into the future sensor platform. In order, the following was established:

1. Assessment of CV shapes and current values conform to theory;
2. Determination of proper measurement potential for transient response;
3. Assessment of the transient response for different DO concentrations.

The on-wafer test have been performed according to the methods described in section 4.5. The results of a CV taken with a 25 µm recessed electrode (*N* equals 5) is shown in Figure 4.17. As seen, a typical CV for oxygen reduction on a microelectrode is observed with its shape explained as follows:

Starting from 0.2 V, as the potential is swept more negatively into the oxygen reduction zone, an increase in redox current is observed. In accordance with theory, no diffusion limitation sets in i.e. no peak is observed. It is interesting to note that on these freshly made electrodes two cross-overs are observed. The first in the negative sweep at -0.46 V, close to the hydrogen adsorption region; the second on the positive sweep near 0.16 V. This matches the observations by *Sosna et al.* and the lower cross-over is considered a finger print for DO measurements on Platinum electrodes representing the limiting current for the microelectrode array with respect to DO (153).

Comparing the values of the current to the simulated values the same magnitude in current is observed. Near the steady-state at high DOC i.e. -0.4 to -0.5 V, a current of 6.6 nA is observed; this is close to the steady-state value from the simulation in Figure 4.16.b, which predicts a value of 6.8 nA at 7 mg L^{-1}. It is important to note here that, in some cases, the recesses had not properly filled when starting the measurement. This was noticeable by a reduced current compared to the expected value. As the recess fills over time, a sudden increase in current can be observed. Only once the CVs did not change in this manner it was decided that the wafer fabrication was successful. To test the individual dies, wires were soldered to the contact pads. The on-board CE was used for the experiments conducted. The contacts were encapsulated in fast-cure epoxy to ensure proper insulation. A similar process as for the RE was used.

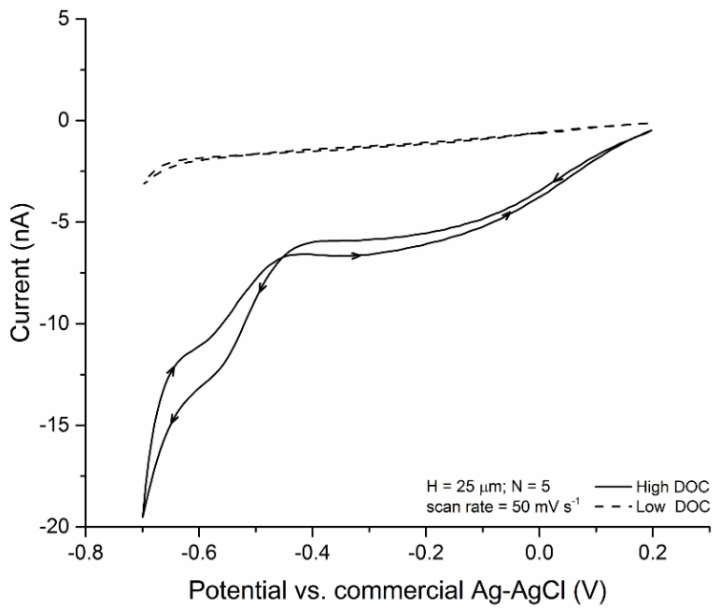

Figure 4.17: CV of a 25 µm recessed disk electrode with an array size of 5 at high and low DOC; High DOC equal to 7.3 mg L^{-1}. Indicated is the direction of the sweep. Note that there are two cross-overs related to the reduction of DO. The difference between high and low DOC can clearly be seen. Scan rate equal to 50 mV s^{-1}; measured versus Ag-AgCl.

Figure 4.18.a shows the results for sensor Type-B with array size equal to 12 and a diameter of ± 25 µm (variation across wells is common due to height of recess). The presented CVs, were taken at different points in time during a continuous experiment running from low DOC to high DOC; logged with the reference *YSI* probe. It can be seen that unlike the shape discussed in Figure 4.17, a regular shape, compared to that of a macro-electrode is observed. The cause for this is expected to be the inter-electrode spacing. In sensor Type-B the spacing equals 100 µm i.e. 8 times the critical radius. During the sweep the diffusion boundaries of the electrodes will therefore overlap and, instead of behaving as individual micro-electrodes, the electrodes behave as one.

A second observation which can be made from Figure 4.18.a is the formation of Platinum oxide. As the sweep extends into the oxide formation region near and beyond 0.2 V vs. Ag-AgCl, a layer of oxide forms. The reduction of the formed oxide can be seen in the return sweep at -0.05 V vs. Ag-AgCl. However, this does not completely remove the formed oxide. Thus, a gradual formation of Platinum oxide is observed which merges with the oxygen reduction peak observed at -0.3 V vs. Ag-AgCl in the sweep at 6.5 mg L^{-1}. It is clear that there were problems associated with sensor Type-B.

In sensor Type-C, care was taken to define the inter-electrode spacing. Here, *d* equals approximately 250 µm i.e. 23 times the radius. The resulting CVs at 6.85 mg L^{-1} DOC are presented in Figure 4.18.b; it is clear that microelectrode behaviour is observed for both array sizes. When factoring in the difference in array size, good agreement between the expected and measured current value for the limiting current at the cross-over point is observed.

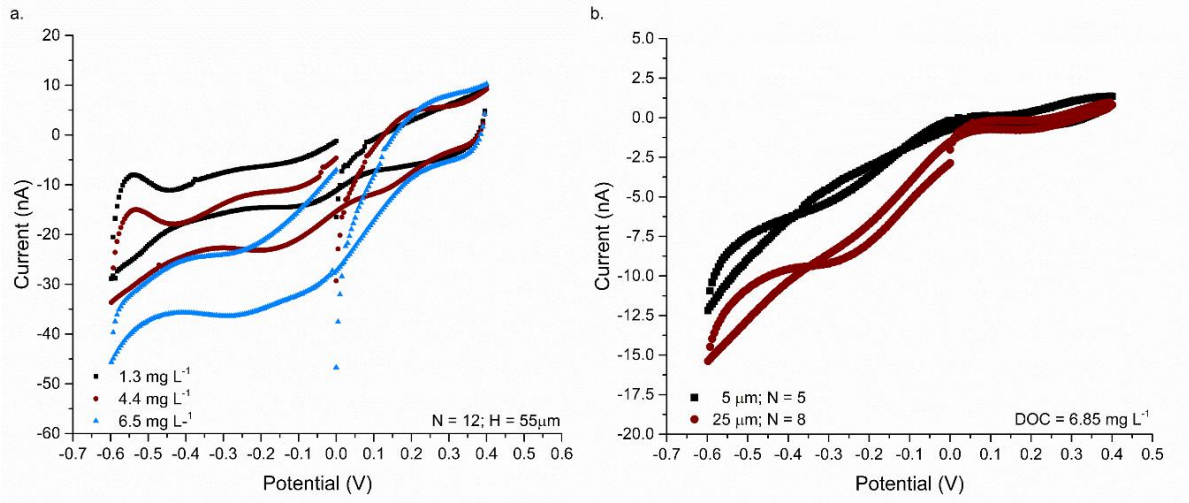

Figure 4.18 – a) CVs for sensor Type-B recessed in 55 µm TMMF, N = 12 and $r0$ = 32 µm. b) Comparison between sensors of Type-C1 recessed in 25 µm TMMF and 5 µm SU-8. N = 8 and 5, respectively. r_0 = 11 µm. Measured in 1x PBS versus Ag-AgCl.

From the discussed figures in this section, the measurement potential was defined and set just before the cross-over in the ORR region. Individual sensor dies were tested using CV and chrono-amperometry prior to long-term tests to define this point. In most cases a potential in the range of -0.4 to -0.5 V vs. Ag-AgCl was chosen. An added benefit is that the curve shows a shoulder at this point with a width of around 100 mV. This provides a margin of error caused by fluctuations in the potential of the RE.

4.6.3 Development of the measurement procedure

In order for the Pt electrodes to maintain proper function during transient measurements it is essential that surface conditions are kept consistent for each measurements. This is achieved by performing a conditioning procedure prior to the transient measurement. To investigate this, CVs were ran prior to the transient measurement. The window of the sweep was varied for each measurement to determine the upper limit at which oxide formation starts. To ensure no by-products from the sweep influence the results, and to re-equilibrate the recess with the bulk, a waiting time was incorporated in the measurement sequence. The wait time is based on the following:

1. Equilibration time of the DOC based on diffusion;
2. Simulation of the diffusion time for the reaction product i.e. hydroxide.

1. A quick estimate for the wait time can be made using the Einstein equation. Which gives the time for a species to cross a given distance, x in one-dimension. The time to run the CV at the defined scan rate of 250 mV s^{-1} for the potential window was used to compute the longest wait time. As an example: for a sweep between +0.4 V and -0.6 V vs Ag-AgCl, at a scan rate of 250 mV s^{-1}, the negative potential sweep lasts 4 s. In this time the boundary has progressed by approximately 185 µm according to equation 4.3. Thus, all the oxygen within the recess has been consumed. A wait

time of 30 s was set between cycles to ensure the concentration inside the recess had equilibrated with the bulk and can be shortened if an increased sampling rate is required.

Figure 4.19.a shows the results from the conditioning sweeps for a sensor of Type-B in a 25 µm recess made from TMMF, with *N* equal to 8. The upper vertex potential was swept more positively each cycle. The entire experiment comprised three cycles; the third cycle for each scan window is shown. As can be seen from the excerpt of the graph in Figure 4.19.b, a shoulder in the cathodic sweep starts to appear at vertex potentials exceeding 0.4 V vs. Ag-AgCl. The effect imposed on the current is of great effect across the oxygen reduction region. Hence, the upper vertex of the conditioning procedure is not swept beyond this potential and is chosen between 0.2 and 0.4 V vs. Ag-AgCl. It has to be noted here that it is important that the conditioning procedure ends in the positive direction; this to ensure the electrode is in an oxide free state.

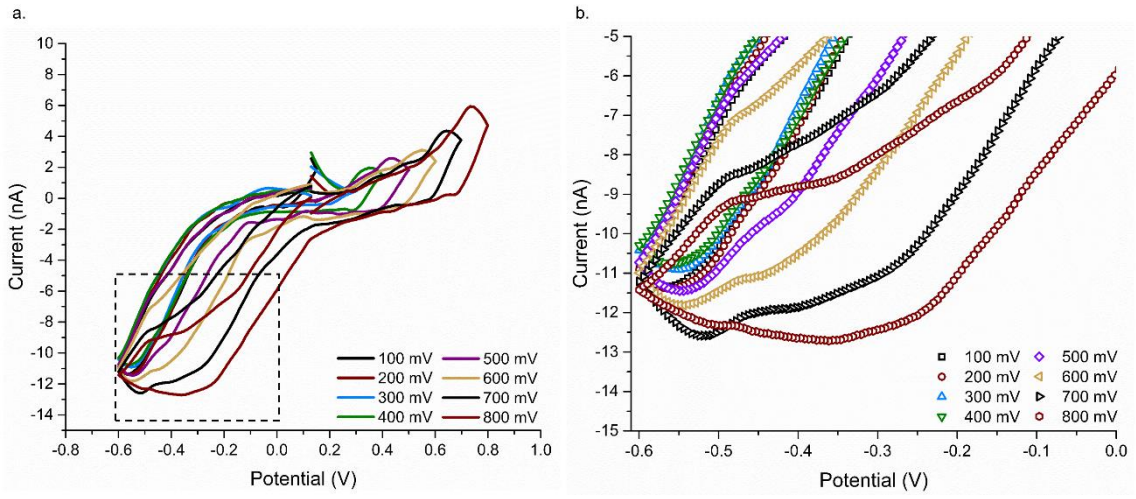

Figure 4.19 - Conditioning procedure characterisation for the upper vertex. a) The upper vertex of the potential window is increased step-wise each cycle. As the potential exceeds 0.4 V an oxide reduction peak related to the removal of formed Platinumoxide appears; b) Excerpt of the oxide peak and its effect at the potential.

2. During chrono-amperomteric measurements oxygen is consumed at the electrode surface. As discussed in section 4.3 all mechanisms for the reductions of oxygen are to be expected. To ensure minimal influence of the hydroxide species a diffusion model was created to determine the optimal period of rest after the conditioning procedure has been performed. In a worst-case, at maximum DOC, all of the oxygen is reduced to hydroxide. According to table 4.1 this results in four moles of hydroxide for each mole of DO. By computing the diffusion boundary length for the 100 ms transient measurement an estimated boundary distance of 39 µm is calculated. It is reasonable to expect that with the higher diffusivity of hydroxide compared to oxygen the current sample rate allows OH^- to diffuse away.

The complete measurement procedure has almost been fully mapped at this stage. What remains to be determined is what happens to the measurement cell during the measurement intervals. During the course of the development of the DO sensor it was found that best results were obtained by

keeping the cell in an electrically floating state during periods of inactivity. In literature it has been reported that the potential can be kept at a constant rest potential. This value is set at the zero-current x-axis intersect seen in the CVs (153, 172). Here, no current and thus no reduction occurs. However, there are two issues related to this method.

First, as the stability of the potential at the rest potential is determined by the RE, any instability will shift the potential, and consequently the rest potential. Although small in magnitude, this can cause DO to be reduced if the potential drifts in the ORR direction. Since the currents associated with the microelectrodes are small, this will impact the DO measurement. Second, during assessment of the conditioning procedure it was found that when a rest potential was used between measurements the response would reverse i.e. a decrease in current is observed with increasing oxygen. It is highly likely that this is related to the aforementioned issue with an unwanted reduction of DO. To summarise this section an overview of the developed measurement procedure is shown in Figure 4.20. This conditioning procedure precedes all data presented next in this chapter.

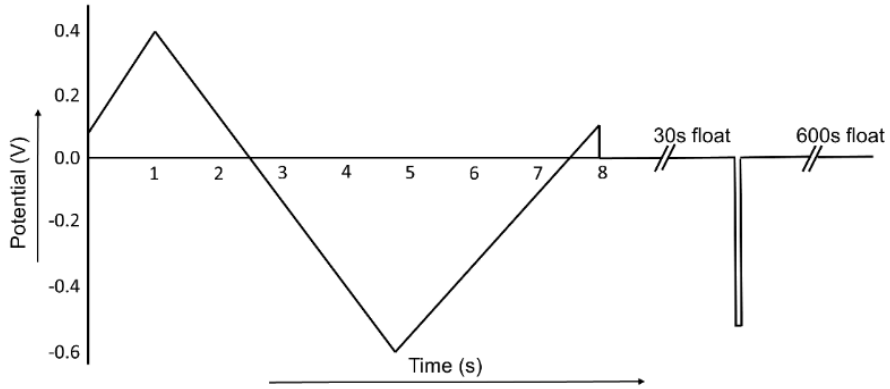

Figure 4.20 - The resulting conditioning procedure including the measurement pulse for the transient acquisition. The procedure consists of a CV sweep for 8 s at 250 mV s-1 scan rate between -0.6 V and 0.4 V ending on the positive sweep at 0.1 V. Between the conditioning procedure and after the measurement the cell is kept floating. The measurement is taken at -0.5 V for a 100 ms period.

4.6.4 Dissolved oxygen sensor short-term performance

The short-term tests described in this section were aimed at assessing the response of the sensors to DO. Figure 4.21 shows the results for sensors of Type-B and Type-C with varying array size and disk radius. The transient data was acquired by chrono-amperometric measurements at a cathodic potential of 0.5 V. The PalmSense3 acquires data in this mode of operation after an initial 64 ms period, thus recording has started from that time onwards. Multiple chrono-amperograms were obtained at a constant DOC of 6.9 ± 0.1 mg L^{-1}. A data filter was applied to remove the 50 Hz noise either using a high pass filter or through curve smoothing using adjacent averaging. Multiple transient measurements were taken and averaged at each time point. As shown, all sensors show a linear response for the set time as described by the Cottrell equation, with an increasing current for increased surface area due to the array size and radius.

Reasonable accordance with theory is observed when the current values are normalized for their respective array size and radius, as shown in Figure 4.21 - a) Cottrell plots for sensors of Type-B and Type-C with arrays and disk sizes indicated in the figure.b. The mismatch in value, although small in magnitude, is likely caused by inconsistencies in fabrication. Due to the poor resolution of the acetate mask, jagged edges and dots are observed across the resist layer which increases the surface area of the individual disk electrodes and total electrode area. Additionally, they influence the shape of the diffusion profile, as will be discussed further on in this section.

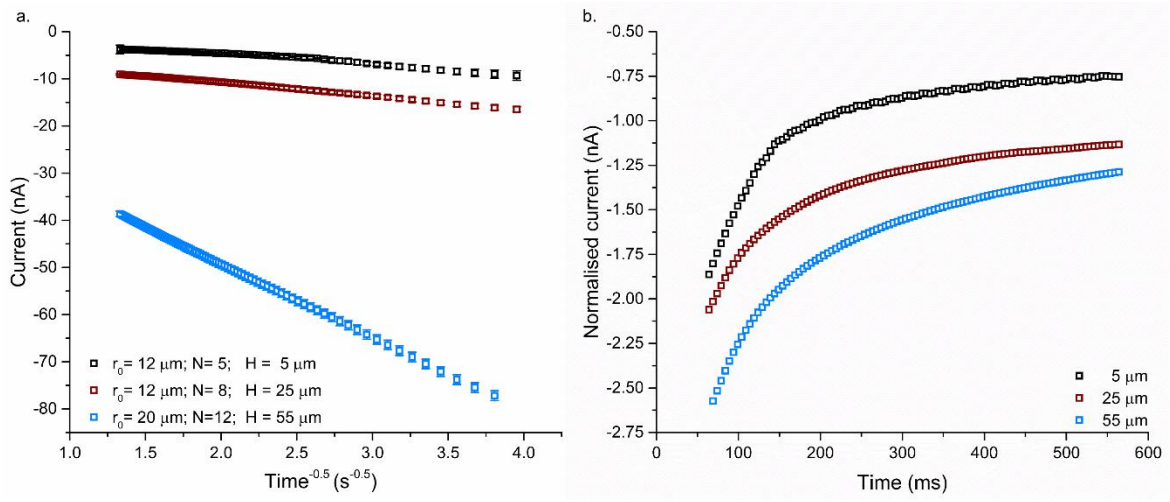

Figure 4.21 - a) Cottrell plots for sensors of Type-B and Type-C with arrays and disk sizes indicated in the figure. Data points are an average of 5 transient curves measured at a fixed DOC of 6.85 ± 0.1 mg L^{-1}, measured in 1x PBS at room temperature. b) Current normalised with respect to N = 1 and r_0 = 10 µm.

From the obtained transients the charging effects within the system have been determined. By integrating the Cottrell equation the charge curve is obtained, as shown in Figure 4.22. The data was fitted using an exponential decay fit i.e. for a capacitive element with R-squared values larger than 0.999 for all three fits. From this, the y-axis intersect was determined, which represents the initial charge in the system. This charge consists of three components:

1. Double layer capacitance;
2. Electrode polarisation;
3. Adsorbed surface species.

Because of the conditioning procedure applied prior to each measurement the adsorption of species on the surface is expected to be negligible. Moreover, the measured sensors were newly fabricated and have not been used prior to the experiments, so any formation of adsorbates on the surface over time is unlikely. The electrode polarisation will have an effect on the initial charge present in the system. After the conditioning pulse is applied the system is set to float. It is well known that Pt is a highly polarisable material with a long decay time. As the conditioning procedure ends in an upward direction to 0.1 V vs. Ag-AgCl the potential will gradually drift towards the surface potential of Pt

in 1x PBS. It is likely that some of this residual polarisation is still present when the potential is stepped down and causes the initial start position to be at a positive charge.

From Figure 4.22.a it can be denoted that the initial charge on the system for the equal sized radii sensors of 5 and 25 µm match closely, with values of 0.4 and 0.8 nC, respectively. A larger charge, explained by the increased double-layer at an electrode of larger size, is present on the 55 µm sensor, and equals 4.2 nC. Figure 4.22.b shows the Anson plot used to establish the diffusion profile within recess. At short times, a negative deviation indicates a lag in the sourced current by the potentiostat on the voltage step applied. This is associated with the potentiostat itself, and the uncompensated solution resistance. As the electrode spacing and current distribution is kept small and even within the design, this is minimal; neither the first nor the latter is observed.

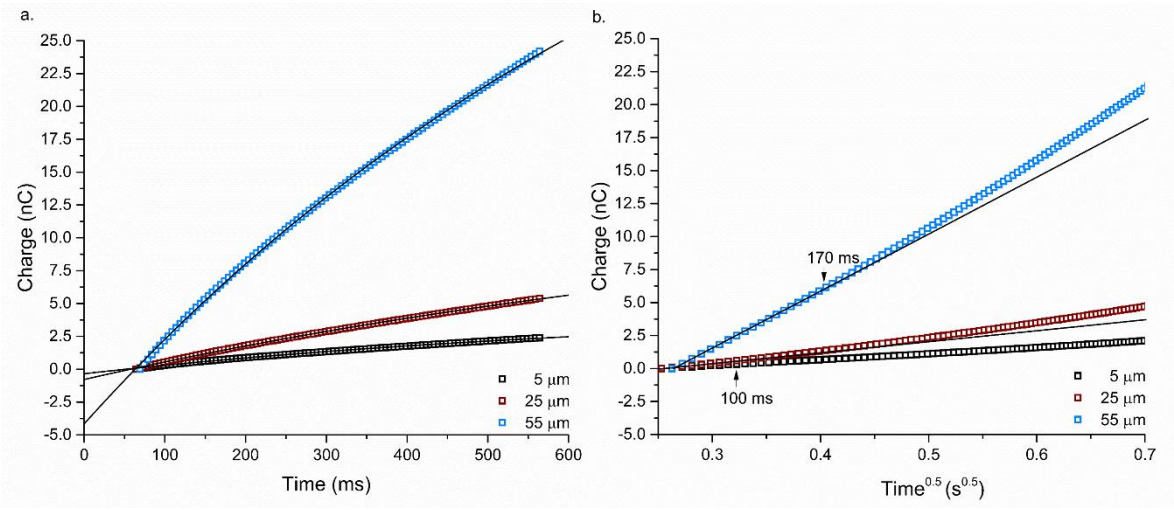

Figure 4.22 - a) Chrono-coulommogram for three different recess heights at 6.9 mg L^{-1} DOC in 1x PBS. The blue line represents the best fit (R-square > 0.999). The intercept with the y-axis shows the initial charge present in the system. b) Anson-plot for the chrono-coulommogram. The line indicates the linearity to the point where transition towards hemispherical diffusion occurs.

The positive deviation at extended time periods can be attributed either to convection in the system or the transition towards hemispherical diffusion. As the measurements described were taken in a convection-free system, the first is considered unlikely. Some small convective forces might be present due to human activity in the laboratory and natural convection due to evaporation, but this is considered to be minimal in the case of air saturated DOC measurement conditions. Thus, by drawing a linear fit through the initial part of the Anson plot an estimate on the progression of the diffusion boundary can be made. Indicated in the Figure 4.22.b is the point (in ms) at which deviation from the linear graph occurs. The transition in the 5 µm recess has occurred well before the time of measurement and is therefore not fitted. Comparing the values for the 25 µm and 55 µm recess to the values obtained in Table ***4.2*** a much shorter period of linearity for the 55 µm recess is observed. This is explained by fabrication problems due to the thickness of the photoresist.

Figure 4.23 depicts a microscope image at 10x magnification of a similar sensor used for the 55 µm experiments. The image on the left is focused on the top of the recess; the image on the right is focussed on the bottom of the recess. To maintain perfect one-dimensional diffusion the recess has to be straight. It is clear from the image that this is not the case. In fact, an average diameter of 34.3 ± 1.1 µm is observed for the top of the recess and an average of 24.4 ± 1.7 µm for the bottom. This is a 10 µm deviation through the 55 µm recess and indicates a large tapering of the walls. This tapering results in a quicker transition towards hemispherical diffusion as the opening becomes wider over time, effectively forming the bulk of the solution at a distance closer than expected.

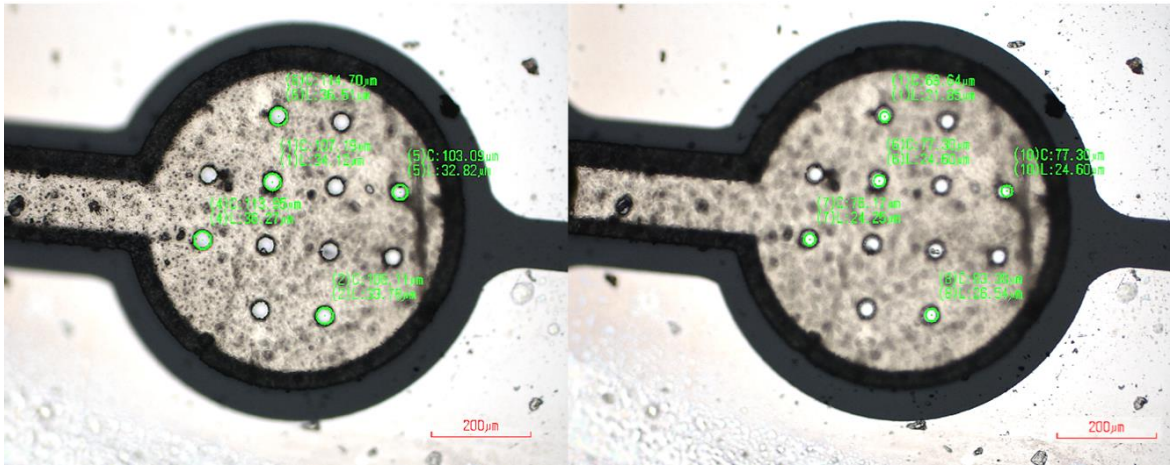

Figure 4.23 – Top view of sensor Type-B with array size 12, recessed within 55 µm TMMF. Focussed on: left) top of recess; right) bottom of recess. An average diameter of 34.1 ± 1.1 µm and 24.4 ± 1.7 µm is observed, respectively. This indicates a large tapering at the walls of the recess influencing the one-dimensional diffusion profile.

A second assessment of the double layer capacitance can be made. As described by *Huang*, the double layer capacitance, C_{dl}, can be estimated assuming a double-layer capacitance per area for Pt equal to (20 µF cm^{-2}) (172). The addition of a roughness factor of 3 times yields a value of 1.2 nF for an electrode with N equal to 5 and r_0 equal to 11 µm. This is within the margin determined from the chrono-coulommetry fit in Figure 4.22 which equals 6.25 nF.

By using the well-defined double layer region in the CVs of microelectrodes an experimental validation of the C_{dl} has been made. Figure 4.24.a shows the CVs at increasing scan rates for a Pt electrode with array size equal to 6. No conditioning procedure was performed prior to the experiment. It can be seen that the double layer increases with increasing scan rate. The slope of the current versus scan rate is equal to the double layer capacitance as depicted in Figure 4.24.b. Here a value of 10 nF was determined.

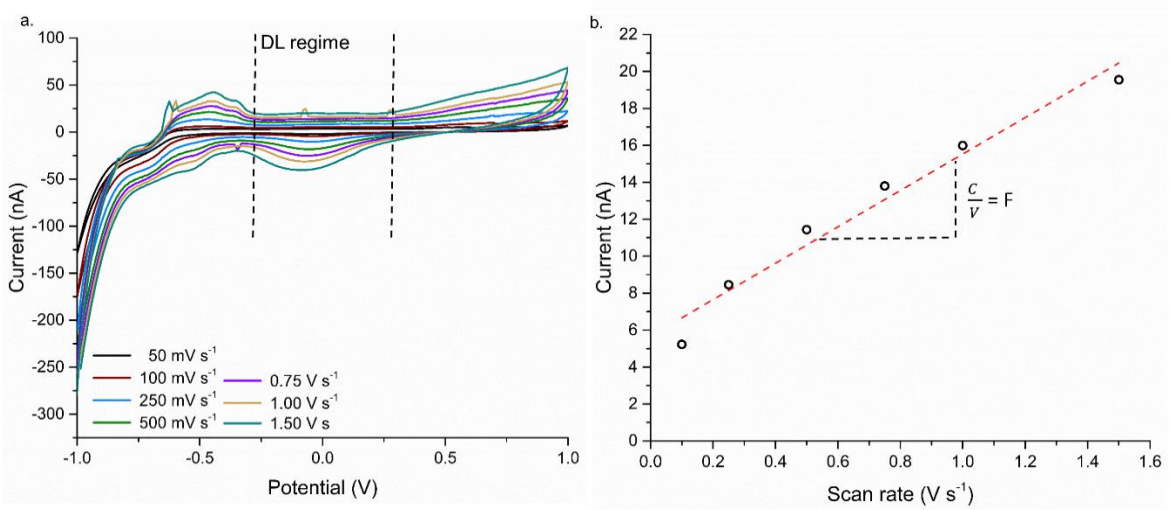

Figure 4.24 – Experimental validation for double layer capacitance of disk electrode with array size of 6. a) CVs recorded at different scan rates. Shown is the double layer regime from which the capacitive current is determined. B) Plot of capacitive current versus scan rate. The slope yields the value for the capacitance (R-squared > 0.98, 50 mV s^{-1} excluded). Measurements taken in 1x PBS, deoxygenated with nitrogen gas.

The minimum time for acquisition of the discrete data point, to be used for the DO calibration curves can be determined using equation 4.9. By determining the 97% charge time with the time constant τ, the minimum wait time after the ORR potential is applied can be determined. For the Pt disk electrode the resistivity i.e. charge transfer resistance R_{CT} is given by equation 4.10. With a conductivity (σ) for 1x PBS of 15 mS cm^{-1}, R_s equals 15.2 kΩ. Thus, 3 τ equals a time of 0.46 ms. Any discrete data point on the transient beyond this time can be taken.

$$I_{RC} = \frac{V}{R_s} e^{-\left(\frac{t}{\tau}\right)} \; with \; \tau = R_{CT}\, C_{dl} \qquad (eq.\,4.9)$$

$$\frac{1}{R_{CT}} = 4\,\sigma\, r_0 \qquad (eq.\,4.10)$$

Figure 4.25 shows the daily measured response of three DO sensors with varying array size and recess height. The left column depicts the transient graphs obtained at approximately 10.5 minute intervals. The right column shows the resulting calibration plots at three different, discrete time points on the transient. The reference DOC value was obtained with the *YSI* probe. As can be concluded from the figures, all sensors respond correctly to increasing DOC: as the concentration increases an increase in current is observed.

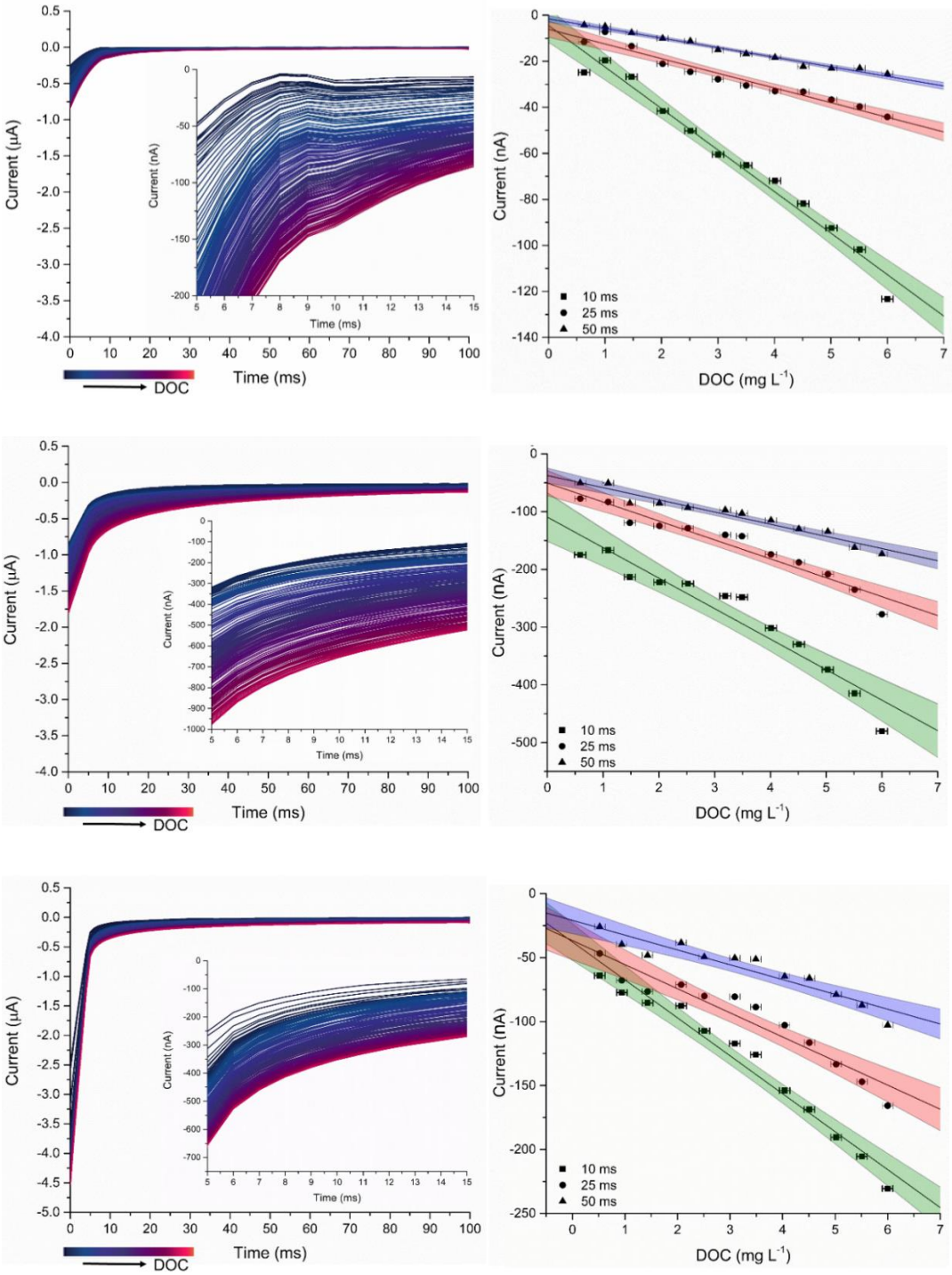

Figure 4.25 - left column) Transient response curves for three different recess heights and array sizes of 5, 25, 55 µm with *N* equal to 5, 8 ,12 from top to bottom, respectively. A proper response is observed for all samples. right column) Calibration plot obtained at discrete values with a 0.5 mg L-1 increment for different time points of the transient. Shown is the 95% confidence band. As the time is pushed further along, the confidence of the fit increases

At the start of the measurement the limitation of the systems setup can be observed. In all cases, the confidence of the fit decreases at low DOC. Two reasons give rise to this: first, DO is displaced by flushing the system with nitrogen gas. The residual convection at the start of the measurement from the nitrogen flush causes inaccuracies in current and registered DO values by the *YSI* probe at these initial measurement points; compared to the non-convective system at prolonged times. Second, both

the optical probe and the electrochemical sensor are least accurate at low DOC. Any residual nitrogen gas or DO on the surface of the membrane, surface of the electrode, or surface of the vessel will have a larger contribution on the error at low than at high DOC. It is also clear that, as the discrete time point at which the data point is taken is moved along the transient, a higher confidence of the fit is observed. Due to the nature of the transient, in which a large initial current is observed upon application of the potential step, any inconsistencies will be amplified. At later times i.e. towards the end of the curvature, a more stable state has been reached.

Comparing the results based on the height of the recess, it can be noted that the current values for a 25 µm recess are larger compared to the 55 and 5 µm heights. A problem in fabrication was shown to be the error. Over time, delamination of the TMMF insulator on the Platinum occurred. This causes an increase in current over time as more area of the Pt, in particular the parts at the contact pads gets exposed. Comparing the 5 µm recess versus the 55 µm, an overall better fit for the shallow recess is observed. Interestingly, the 55 µm recess shows a better fit at shorter time scales. This is most likely caused by the tapered geometry. From these results it was decided that the 5 µm recess i.e. shallow wells are to be used. It was further decided that the discrete time point should be taken at 50 ms, as determined in Table ***4.2***.

4.6.5 Long-term dissolved oxygen measurements

After the DO sensors were assessed on their short-term behaviour long-term measurements were performed. Due to issues in the fabrication, the TMMF based sensors could not be used for this purpose. Progress has been made on improving the fabrication and is discussed in more detail in this section. For the initial long-term measurements discussed next, only sensors of Type-C made with 5 µm SU-8 were used.

The steady-state response, repeated over the course of three different days is shown in Figure 4.26.a. The theoretical steady-state current response expected for a sensor of this type is indicated in the plot. As can be seen a good reproducibility is observed in the mid-DOC range. Overall, a lower response with regards to DO is observed for the sensors, compared to the theoretical value. From the steady-state current measurements the stoichiometry of the electrons was determined using equation 4.6. On average, n equals 2.6 ± 1 indicating an incomplete electron transfer process. This observation is not uncommon and has been reported by *Sosna et al.* (153). However, compared to their findings, the number of electrons in this study appears to be lower. The trend shows that there is an increased number of electrons transferred as the DOC increases, as shown in Figure 4.26.b.

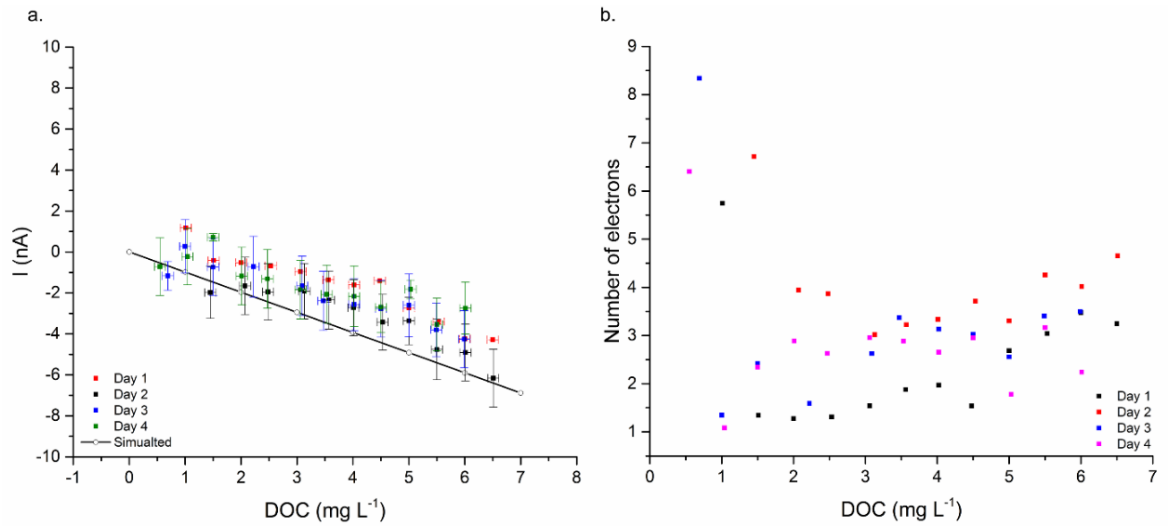

Figure 4.26 - a) Four day assessment of the steady-state current for sensor Type-C with an array size of 5 and compared to the theoretical steady-state current. Value taken as the average of the 28-29 seconds at 0.5 ms sampling rate. b) Calculated number of electrons at a given DOC.

The long-term response based on the transient measurement of DOC is shown in Figure 4.27. As a reference, the data is plotted as an absolute current value with the optical probe reading as a reference DOC. What can be noted from the figure is that as time progresses, a gradual drift is observed during the continuous measurements. This is likely related to the increase in electron transfer observed in the steady-state measurement and could be related to changes on the electrode surface over time. In fact, it is not unlikely that during the continuous conditioning the Platinum roughens and increases in surface area or contaminants on the surface, left over from fabrication, are removed. As explained in section 4.4.1, the removal of oxide from the Pt lattice produces vacancies.

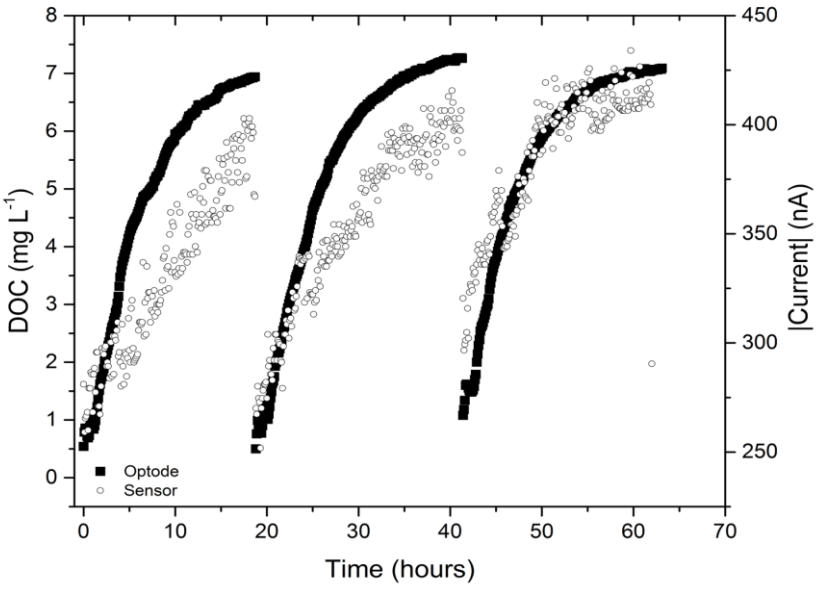

Figure 4.27 - DO measurement for a sensor of Type-C with an array size of 8. Measurements taken as discrete values at 50 ms of the transient response. The recorded DO values with the *YSI* probe are shown as a reference. A gradual drift in current is observed over the course of three days.

A more stringent problem was that in none of the cases could the life-time of the DO sensor be extended beyond a few days of consecutive measurements. During repeated measurements increases in current values beyond the µA scale were observed; this should be impossible as theory predicts a 100 nA current range. Interestingly, when measurements were taken at weekly intervals, the increase in current is not as drastic as seen before. Figure 4.28.a and .c show the long-term data taken over the course of three weeks for two different DO sensors using SU-8 as an insulator. Between measurements the sensors were stored in 1x PBS solution. Figure 4.28.b and d show the absolute error based on a linear calibration fit performed on the data from week one over the range of interest for intra-uterine DO sensing. As can be seen the error equals 0.8 ± 0.24 and 0.52 ± 0.2 mg L^{-1} for the top and bottom graphs, respectively.

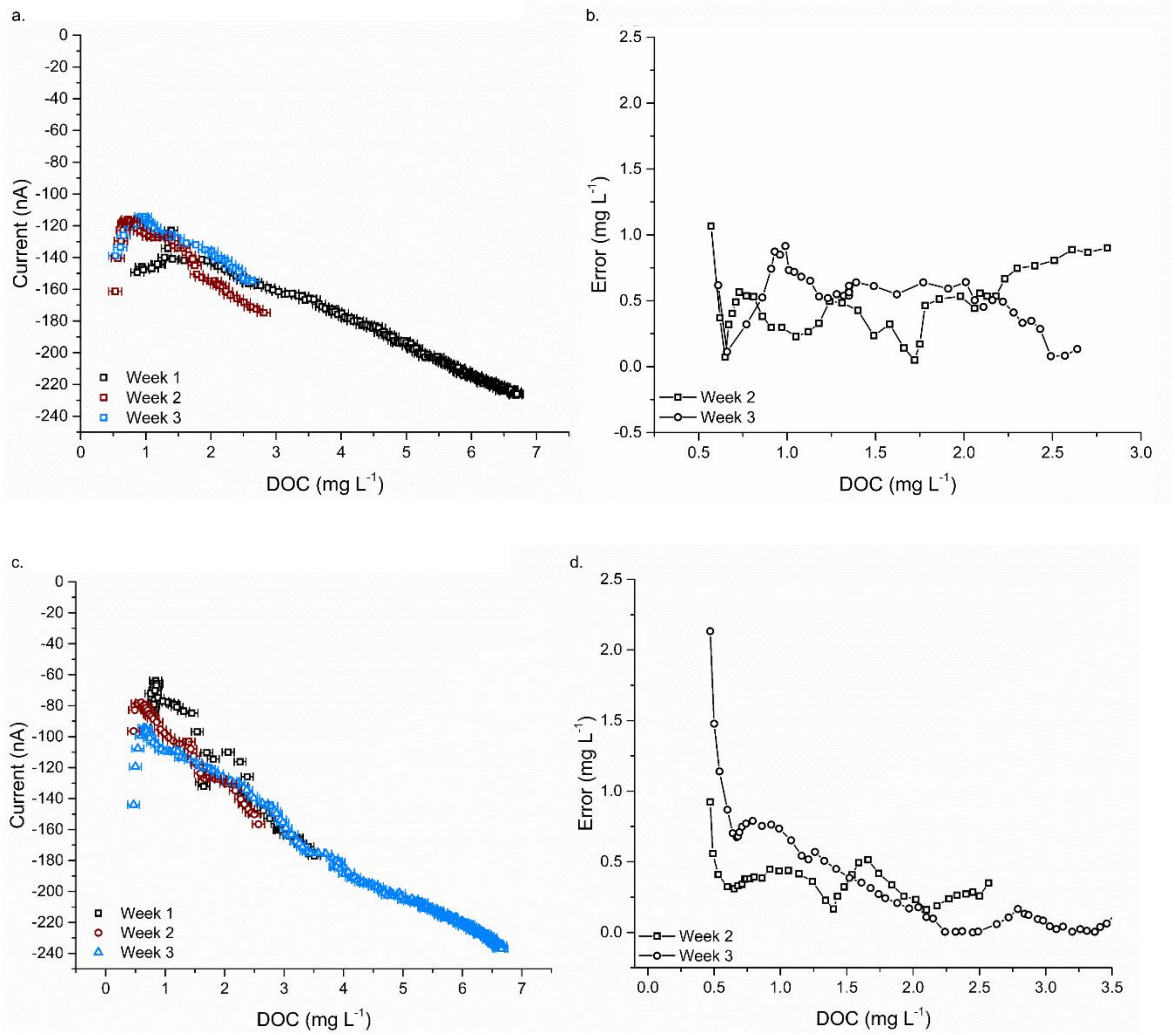

Figure 4.28 - Long term measurements for two DO sensors Type-C with an array size of 8. Figures (a) and (c) show the weekly measurements for the duration of three weeks. In between measurements sensors were kept in 1x PBS. Figures (b) and (d) show the relative error for the DOC based on the calibration plot from week 1. An average error of 0.8 ± 0.24 and 0.52 ± 0.2 mg L^{-1} for S1 and S2 is observed, respectively.

Despite the error, the experiment showed that there has to be a relationship between the measurement method and the observed increase in current. If the cause was regular delamination in solution, a current increase should still be observed due to storage conditions. However, optical inspection using a microscope provided no evidence of water ingress or delamination of the insulator. It was not until a long-term test was ran, exceeding four weeks, that an important observation was made: prolonged measurements cause degradation and lift-off of the insulator; in particular around the recessed disk. The image from which this find resulted is shown in Figure 4.29.

Figure 4.29 clearly shows that there is an effect over time on the photoresist. A clear distinguishable circular ring is seen around each of the recessed disk electrodes. Second, patches which resemble cracks are seen at regular intervals across the ring. It was hypothesised that the effect is caused by reaction products generated within the recesses. The products cause delamination and induce stress across the entire ring. A series of experiments were conducted with a wide variety of materials. The wafers types used consisted of:

1. Platinum with Silicon dioxide and SU-8;
2. Platinum with Silicon dioxide;
3. Titanium with SU-8.

As stated, the reaction products that can be expected to have an effect are: hydroxide and hydrogen peroxide. In order to mimic the prolonged measurement conditions sensors were exposed to anodic and cathodic currents for 30 to 60 s using chrono-potentiometry with fixed currents up to 10 µA. additionally, samples were immersed in solutions containing the reactant. It was found that hydroxide had no effect on the electrode surface so its effect was discarded. However, when samples were exposed to hydrogen peroxide (30% v/v) overnight the results in Figure 4.30 were obtained.

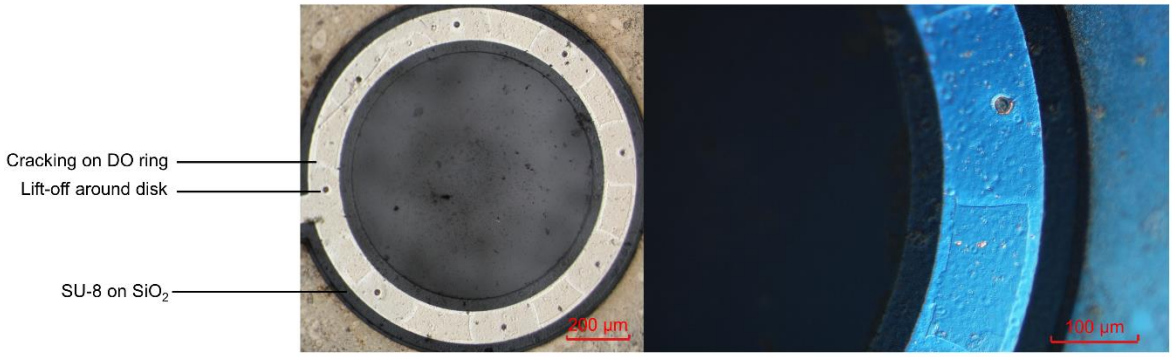

Figure 4.29 – Microscope image of SU-8 on SiO_2 on a Pt DO sensor immersed and measured continuously for 4 weeks. Measured in 1x PBS at room temperature at hourly intervals. A clear pattern of cracks has appeared around the Platinum ring. A lift-off of the insulator around the recessed disks can also be seen. left) bright field image; right) phase contrast image.

.

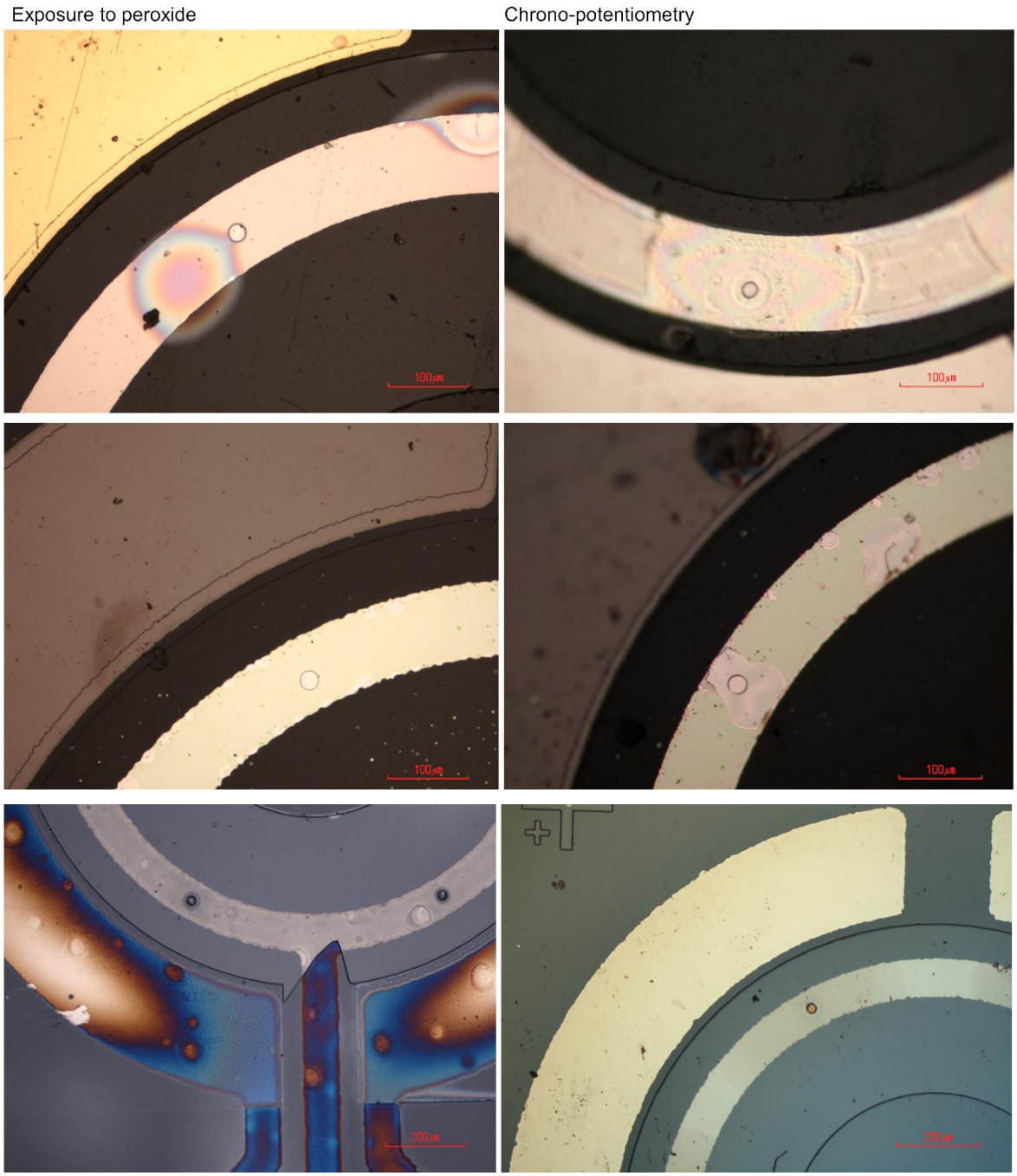

Figure 4.30 – Effect of reaction products on insulator adhesion. left) Sensors exposed to peroxide (30% v/v) overnight at room temperature. right) Sensor exposed to fixed negative current using chrono-potentiometry. Current sustained for 30 to 60 s. top to bottom) SU-8 on SiO_2 on Platinum electrodes; SiO_2 on platinum electrodes; SU-8 on Titanium electrodes. Similar effects are observed in all cases consisting of rainbow patterned fringes for the SU-8 with SiO_2; circular fringing and delamination of the SiO_2; note that pinholes within the deposited SiO_2 are clearly visible. Circular patterns around the recessed disks for SU-8 on Ti; note that the peroxide oxidises the Ti. This effect is also seen by the yellow colour of the disk electrode within the recess.

When comparing the sensors exposed to hydrogen peroxide with the sensor subjected to a negative current, high similarity between the two is observed. The SU-8 on SiO_2 shows a distinct rainbow coloured fringing at places where the peroxide has penetrated the insulator. The same colour pattern is seen with the sensor subjected to the negative current. A similar observation was made for the SiO_2

insulator. Here, fringing occurs at places where pinholes allow the peroxide to reach the Platinum surface. When the current is applied a complete destruction of the SiO_2 is noted at the pinholes and at the recessed disks. The sensor containing titanium shows a distinct ring around the recess in both cases. Additionally, oxidation of the Titanium is noted also during the chrono-potentiometry, noticeable by the colour of the electrode surface.

From these observations it is has been established that catylisation of the peroxide, which forms oxygen gas, is likely delaminating the insulator from the electrode surface. A similar situation is observed during the application of current. However, during this procedure hydrogen gas is produced at the Platinum electrode. It is possible that during the conditioning procedure in which the potential is swept to potentials of -0.6 V, into the hydrogen region, hydrogen gas is produced causing this lift-off. However the incomplete electron transfer in Figure 4.26, could also indicate the formation and catylisation of peroxide.

Although it cannot be ruled out entirely, it seems unlikely that the production of hydrogen gas is enough to cause this delamination. Mainly because the potential is only slightly and briefly stepped into the hydrogen region. In contrast, oxygen is reduced continuously throughout the sweep, generating peroxide in the process. In any case, a solution to this problem has to be found in order to create a long-term operable DO sensor. The only material which did not show any effect when exposed to hydrogen peroxide or subjected to negative currents, was Parylene-C

A long-term experiment was conducted with Parylene-C on SiO_2, the latter to improve adhesion. The results are listed in Figure 4.31.a. Indicated is the 0.5 mg L^{-1} error band. In order to reduce potential effects from the CP, the CV sweep was replaced with a pulsed CP consisting of 6 pulses of 100 ms. The rest of the CP was kept the same.

Two things can be noted. First, the sensitivity for the initial two days is lower than expected. The cause for this might lie in contamination of the electrode on the surface after fabrication or the conditioning of the electrode over time. After two days the repeatability is improved. Second, after 8 days a drastic increase in current is again observed. Optical inspection showed no effect of delamination, but from the previous experiments this has been shown to be an inaccurate assessment. It is assumable that delamination over time has occurred again during the continuous measurements limiting its life-time to a week. Figure 4.31.b depicts the comparison in DOC using the calibration curve obtained during the course of the third day. It can clearly be seen that readings below 1 mg L^{-1} are inaccurate and this value of DOC has to be considered as the lowest detectable limit of this type of DO sensor.

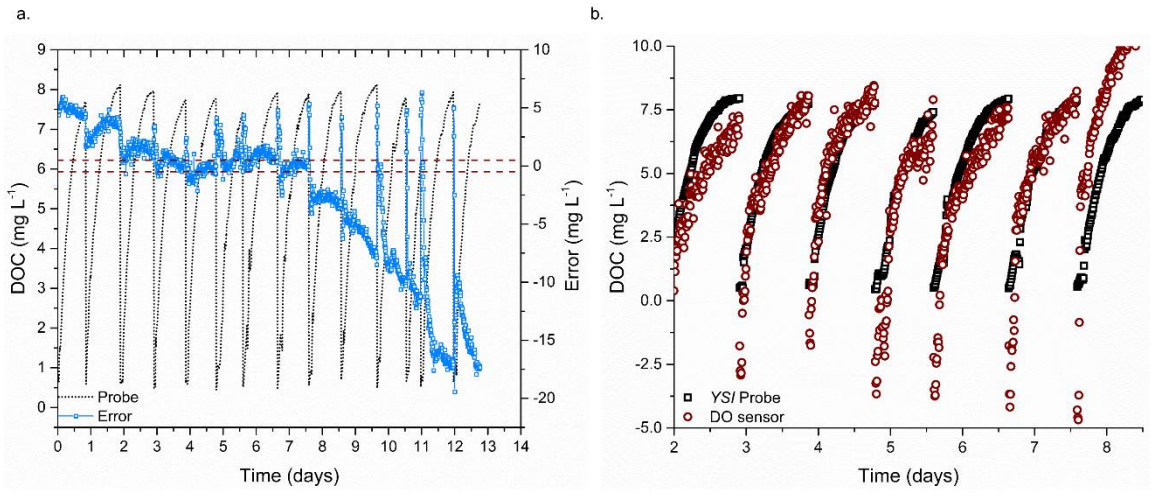

Figure 4.31 – Long-term DO measurement for sensor Type-C with Parylene-C on SiO_2 as insulating material. Array size equals 8 and recess height equals 2 µm. a) Plot of the error compared to the YSI probe reading. Indicated is the 0.5 mg L^{-1} error band. b) Excerpt of the long-term experiment from day 2 to 8. The calibration curve obtained from week 3 was used to compute the sensor DO reading.

The results shown in this work raise the question as to whether or not the use of recessed microelectrodes, in particular when microfabricated, can yield the desired performance over the aimed measurement period of 30 days. Unlike the results presented by *Sosna et al.*, in which disks microelectrodes were encapsulated in glass capillaries, the microfabrication indicates a variety of issues with respect to life-time (153). Similar fabrication issues have also been reported by *van Rossem et al*. with maximum measurement times in the same order as observed in this work (171).

The work by *Huang* claimed long-term performance exceeding 20 days, but reference readings from commercial DO probes are lacking. Additionally, they also observed an increase in DO current, which in the presented data, occurred to the extreme at day 4 (172). Looking at these reports and on the data obtained in this work an alternative method of DO measurement has to be developed in order to meet the biological requirements. A great benefit would be the removal of the recess defining structures. This could be achieved by using a ring-shaped microelectrode. Although the current attenuation is lost due to quick transfer from one- to three-dimensional diffusion, it is expected that the life-time can be extended. Alternatives are proposed in the future work in Chapter 7.

4.7 Summary

This chapter discussed the development of a miniature DO sensor for an IUSD. To meet the low-power requirements posed by the IUSD, arrays of disk microelectrodes were chosen as the WE. To attenuate the redox current associated with the reduction of oxygen on Pt, the disks were recessed in a photoresist. This extends the time of one-dimensional and increases the current as predicted by the Cottrell equation. The sensors were characterised based on short- and long-term performance. A simulation model was used as a reference for the experimentally obtained current magnitudes. A

conditioning procedure to maintain equal surface conditions between measurements was developed and optimised.

The results from the short-term experiments showed good agreement with the predicted current range as per Cottrell equation. For increasing array size and increased recess height a larger current magnitude was observed. It was found that as the recess height increased, the confidence of the linear regression fit with respect to DOC dropped. This was most likely caused by inconsistencies in fabrication. Especially in the case of a 55 µm recess, tapering of the sidewalls was observed.

During long-term measurements it was found that the life-time of the sensor could not be extended beyond 3 days. Interestingly, if measurements were taken on a weekly basis i.e. one day per week, failure was not observed. This led to the conclusion that the continuous measurement of DO must have an effect on the insulator. This was confirmed after a long-term test exceeding four week, where optical inspection showed fringing and cracking of the photoresist around the disk electrodes. It was hypothesised that the reaction products could have an effect on the insulators adhesion. Experiments were setup with a variety of recess materials to investigate the cause.

The experimental data showed that hydrogen peroxide, most likely, is catalysed on Pt areas through pinholes and defects, forming oxygen gas in the process. Chrono-potentiometric experiments showed similar effects under the influence of hydrogen gas. The only material which did not show any delamination was Parylene-C, so a long-term experiment was conducted. Although the life-time was extended, it seemed unlikely that these type of electrodes would last for the required measurement period. Although short-term monitoring of DOC is possible, a recalibration would be required to compensate for the drift due to increased surface area.

Chapter 5 -pH sensor development

As stated in Chapter 1, it is expected that the pH range of interest within the uterus lies between pH 6 and pH 8. This chapter discusses the background and theory of pH sensing; material and methods; and the results and discussion of the developed pH sensors. The main requirement for the pH sensor is to maintain a stable and accurate response whilst maintaining the biological relevancy throughout the course of the measurement period i.e. 30 days. The sensors are assessed against this criteria using the key sensor characteristics outlined in Chapter 1 which are: accuracy of 0.2 pH, long-term drift of less than 0.1 pH day^{-1}.

5.1 Background and theory on pH sensing

The acidity and alkalinity of solutions has been of great interest throughout history. Even before its mechanism was defined by *Arrhenius* in 1889, great names in the field of chemistry had investigated and proposed theories for the mechanism. As defined by Arrhenius[5]: the acidic behaviour is determined by the ability of the substance to interact with hydronium (hydrogen ion) and hydroxide. In simple terms, an acid is a substance capable of donating a proton.

Figure 5.1 shows a timeline for developments in the field of pH sensing. *Sørensen* in 1909, introduced the concept of representing the concentration of the hydronium ion as the negative log of the concentration resulting in the definition of pH as it is known today (173, 174). With electrical measurements within chemistry taking the fore-front in the early twentieth-century, the first glass pH probe was introduced by *Haber* and *Klemensiewicz*. Here, a glass membrane, sensitive to the hydrogen ion, was used to determine the hydrogen ion concentration within aqueous solutions. However, it was a non-practical device due to its large size and lack of portability (175).

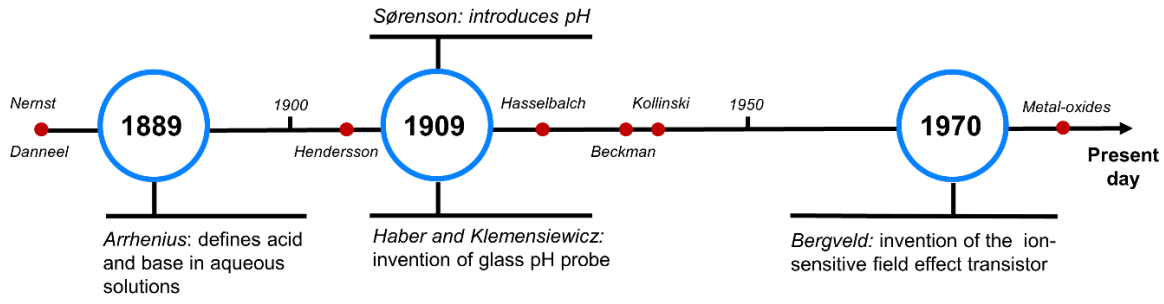

Figure 5.1 - Timeline showing the major development in the field of pH and pH sensing.

[5] Modified from hydrogen ion to hydronium ion as the hydrogen ion instantly forms hydronium in aqueous solutions.

5.1.1 The glass pH electrode

In 1935, *Beckham* extended the earlier work, and developed a portable, glass pH meter (176). As can be denoted from Figure 5.2, the glass pH meter consists of a two-electrode cell. The first electrode is located in a known buffer solution of known molarity. The second electrode, the RE, is situated in a filling solution of saturated KCl. The potential between the inner-electrode and the RE is monitored under the interaction of hydronium with the glass membrane's hydrated gel.

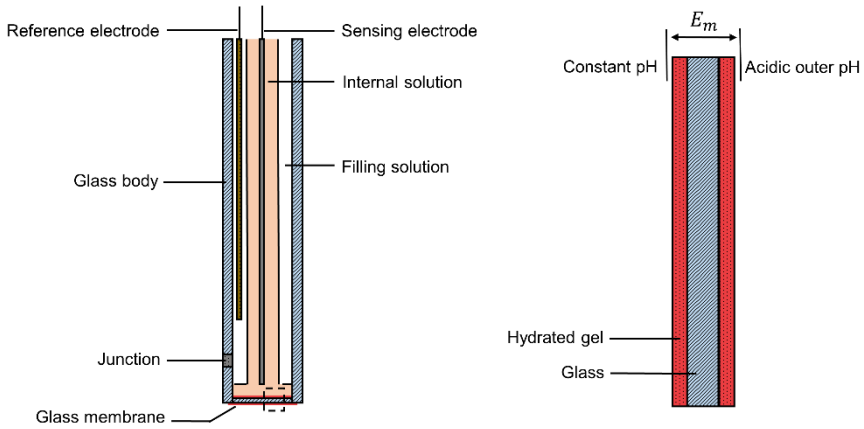

Figure 5.2 – Illustration of a glass pH electrode. The electrode consists of a glass body in which two electrodes are positioned. The sensing electrode is situated in a solution of known pH. The second electrode serves as the RE. A glass membrane with a hydrated gel responds to hydronium within the analyte establishing a potential difference across the membrane through an ion exchange reaction. The potential difference is measured as the potential at the sensing electrode and the RE.

Kolinski was the first to connect the ion exchange theorem as the underlying principle of this form of pH sensing (176). In general, hydronium interacts with the silicate matrix of the glass membrane and exchanges a metal ion, most commonly sodium or lithium. In acidic media this results in a positive charge at the outer membrane. The same applies for the inner membrane, which is kept at a constant pH. Thus an equilibrium reaction exists which is similar to the Nernst equation for the concentration of hydronium as shown in equation 5.1. Here, E represents the potential; E^0 the formal potential; R the gas constant; T the absolute temperature; F the Faraday constant; n the number of electrons; $[H_3O^+]$ the concentration of hydronium.

$$E = E^0 + 2.303\left(\frac{RT}{nF}\right)\log([H_3O^+]) \qquad (eq.\,5.1.)$$

The correct definition of this type of response as 'Nernstian' is debatable and is claimed part of a 'Nernst hiatus', in which the term is incorrectly associated with changes in pH. It is debatable as to whether this type of potential response can be called a Nernstian potential, as linearity for a glass electrode is not maintained across the complete logarithmic scale (177). Rather a general slope term should be used, related to the Boltzmann equation. In any case, it has become convention to refer to a pH response as Nernstian when the slope equals that of the Nernst factor of -59 mV pH^{-1} at T = 297 K; this convention is maintained in this work.

Glass electrodes can still be considered an impressive sensing tool, with an unmatched reliability and performance. However, it has clear limitations regarding its usability in miniaturised sensing systems. Firstly, it is sensitive to the following errors: dehydration, ageing and temperature effects (151). Therefore, prior to measurement, glass pH probes have to be calibrated and stored in solution (178, 179). Secondly, the glass membrane is sensitive to sodium error at high pH. Here, the amount of hydronium is minimum. As a metal ion is exchanged from the lattice competing ions in solution such as sodium can also be exchanged. Thus, at high pH, the glass probe could measure sodium rather than hydronium. Thirdly, and specific to the application described in this work, its large size and fragility make the glass pH probe unsuitable for use as an *in vivo* sensor.

5.1.2 Ion sensitive field effect transistors

Efforts have been made to use smaller, ion sensitive alternatives that are compatible with conventional microfabrication processes. The first break-through occurred in the nineteen-seventies in the form of the ISFET. As depicted in Figure 5.3, an ISFET is a field effect transistor in which the gate contact has been removed; exposing a pH sensitive oxide layer. The gate contact is replaced by a liquid bulk which interacts with the gate-oxide to establish an equilibrium potential (180, 181).

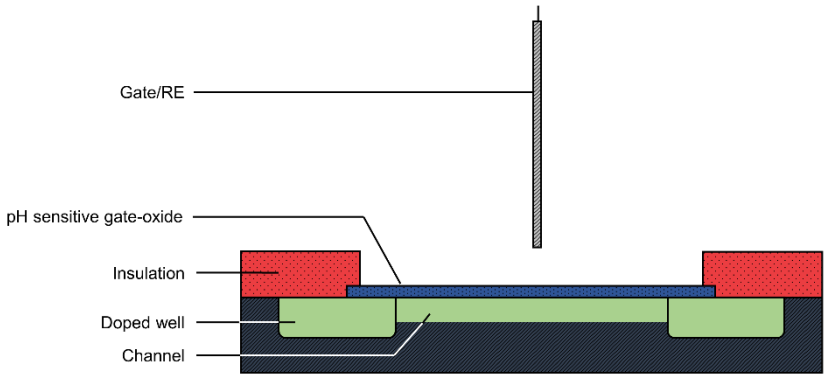

Figure 5.3 – Cross-section of an ion-sensitive field effect transistor. The transistor consists of doped wells in Silicon which create the drain and source contact and form the channel similar to conventional FETs. The gate-oxide is exposed and made of a pH sensitive material. As ions interact with the exposed gate-oxide the channel conductance is altered. A liquid gate in the form of a RE is placed in the same analyte.

Bergveld, in a 2003 conference paper, showed how the surface potential of the ISFET changes with pH. The change ($\delta\psi\ \delta pH^{-1}$) is given by equation 5.2 (182). In essence, the interaction between bulk and gate-oxide changes the conductance of the channel and influences the threshold voltage. In equation 5.2, α is defined as the sensitivity factor, defined by equation 5.3. Note that C_{dl} is the double layer capacitance at the interface; k is the Boltzmann constant; q is the charge, and β the buffer capacity of the gate-oxide. The latter is dependent on the material. To obtain a Nernstian response its value should equal unity. However, in most cases, its value is smaller than unity, resulting in a sub-Nernstian response typical for ISFETs. Materials used, in order of buffer capacity (low to high)

are: Silicon dioxide (SiO_2), Silicon nitride (Si_3N_4), Aluminium oxide (Al_2O_3) and Tantalum pentoxide (Ta_2O_5) (183, 184).

As for conventional glass pH probes and electrochemical sensors, a RE is still required to ensure changes in the potential are solely related to changes in surface events. This gives rise to the same limitation with respect to RE performance. Efforts have been made to incorporate a reference field effect transistor (REFET) manufactured during the same fabrication process. Here, the exposed gate is covered by an ion-insensitive membrane to provide a stable reference potential. Any changes in the solution pH will, in principle, only effect the ISFET and leave the REFET unaltered. Through differential electronic read-out the resulting potential difference can be related to the pH value. However, obtaining a completely ion-insensitive REFET has proven to be difficult (185).

$$\frac{\delta\psi}{\delta pH} = -2.3\frac{kT}{q}\alpha \qquad (eq.\,5.2)$$

$$\alpha = \left(\frac{2.3kTC_{DL}}{q^2\beta} + 1\right)^{-1} \qquad (eq.\,5.3)$$

Since their development ISFETs have been commercialised as a non-glass alternative. Their rigidness and safety compared to glass, and their non-susceptibility to dehydration make them more suitable for industrial and in-field applications (184). However, there are disadvantages. For instance, they exhibit a slow response, suffer from extreme long-term drift during continuous measurements and can be sensitive to light (179, 186). More importantly, the power consumption of an ISFET is an issue for an implantable system operating under power constraints. To be able to measure the change in channel conductance, a constant bias current is required.

5.1.3 Metal oxide based pH sensing

Metal-metal oxide pH sensors are considered to be the most promising type of electrodes for miniaturised pH sensors. It is difficult to pin down when their use for pH sensing was discovered but it is clear that the development of the ISFET has led to an increased interest (182, 184, 187, 188). Their measurement principle relies on the quasi reversible redox couple between two oxide states, which encompasses an electron transfer under the influence of incoming protons. When immersed in an aqueous solution, the pH sensitive metal oxides forms insoluble hydroxide groups. This formation allows for proton hopping to occur by exchanging protons between the hydroxylated sites and the solution. An illustration of this mechanism is presented in Figure 5.4.

The surface potential is defined by the Nernst-equation as shown in equation 5.4. Here, $E^{0'}$ represents the formal potential, defined by the material (as discussed later in this work). Over the past decades, numerous materials have been investigated for use in pH sensing applications. Materials include

oxides of: Antimony (Sb_2O_3), Platinum (PtO_2), Rubidium (RuO_2), Titanium (TiO_2), Iridium (IrO_x), Palladium (PdO_2) (184). Of particular interest for this study is IrO_x. This in fact is a metal oxide-metal oxide based system, in which the response is determined by the redox equilibrium reaction occurring between the two different oxidation states.

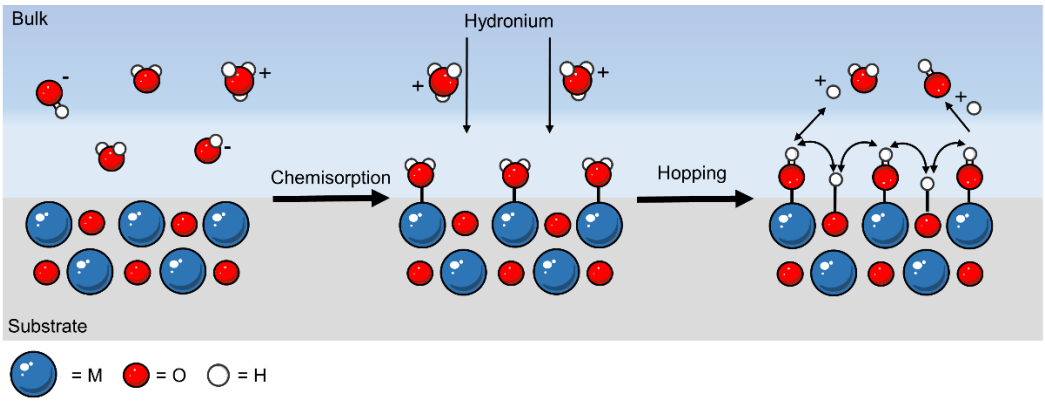

Figure 5.4 - Illustration of the proton exchange mechanism of the metal-metal oxide surface under the influence of pH. left to right) When immersed in an aqueous solution the metal-metal oxide forms hydroxyl groups through the chemisorption of water. The hydronium within the solution exchanges protons with the hydroxylated sites. In turn, the hydroxylated sites can exchange protons with the analyte. The process continues until an equilibrium is reached

$$E = E^{0\prime} + 2.303\frac{RT}{nF}\log([H_3O^+]) \qquad (eq.5.4)$$

Since their introduction mid twentieth century, Ir and its oxides have gained an increasing amount of attention for their use in electrochemical studies and application in pH sensing (189-191). The IrO_x pH sensor holds the following advantages: a linear response, low temperature coefficient, applicable in harsh environments, low impedance and low interference from competing ions (184, 191). Its simplicity of fabrication and biocompatibility make it a promising candidate for *in vivo* biomedical studies. Though all these efforts have shown promising results, the underlying pH sensing mechanism is of a complex nature and still poorly understood. Furthermore, studies that make claims on long-term stability and accuracy are highly suspect. This work aims to properly assess the IrO_x with well defined, long-term data.

The equilibrium reaction is reliant on the electron exchange reactions, as listed by *Pourbaix*, and shown in equation 5.5 - 5.7 (192). As shown, the reactions involve the Ir^{3+} and Ir^{4+} oxidation states. The Ir^{4+} oxide states are responsible for the adsorption of hydroxide from the solution through the dissociative adsorption of water. The resulting hydrated Iridium oxide is responsible for the pH sensitive properties, defined by equation 5.8.

$$Ir_2O_3 + 6H^+ + 6e^- \rightleftarrows 2Ir + 3H_2O \qquad (eq.5.5.)$$

$$IrO_2 + 4H^+ + 4e^- \rightleftarrows Ir + 2H_2O \qquad (eq.5.6.)$$

$$2IrO_2 + 2H^+ + 2e^- \rightleftarrows Ir_2O_3 + H_2O \qquad (eq.5.7.)$$

$$2[IrO_2(OH)_{2-x}\,(2+x)\cdot H_2O]^{(2-x)^-} + (3-2x)H^+ + 2e^- \rightleftarrows$$

$$[Ir_2O_3(OH)_3\cdot 3H_2O] + 3H_2O \qquad (eq.5.8)$$

As can be seen, a redox system consisting of the Ir^{3+} and Ir^{4+} is present. To cite *Hitchman* and *Ramanathan* in their 1989 paper on the pH dependence of hydrous Iridium oxide films:

"An increase in the number of Ir(IV) oxide sites will lead to a greater density of Lewis acid centres, which, in turn will lead to a greater OH adsorption and so enhance the proton exchange capability of the oxide surface."(191)

Note the Lewis acid centre takes the form of the first term in equation 5.8. More generally, this means that the amount of Ir^{4+} will determine the response of the fabricated sensor. The amount is influenced by the deposition method and can be influenced through electrode conditioning in dilute acids.

Reviewing the Nernst-equation, two factors would influence the stability of the pH sensor: sensitivity and formal potential. For a long term implantable system the potential needs to remain stable at fixed pH. Based on the redox reactions of the system previously described, the resulting potential from the IrO_x sensor can be rewritten in terms of the amount of the redox active species and the pH, as shown in equation 5.10. Note that $E^{0'}$ represents the standard potential for the IrO_x reaction. From here it can be noted that the complete formal potential consists of another Nernst factor related to the ratio of the Ir^{3+} and Ir^{4+} oxides. In fact, most of the current issues related to IrO_x sensors are due to drift of this formal potential, drifts as high as 104 mV have previously been reported (189). Thus, during the development of an implantable pH sensor, both sensitivity and formal potential stability need to be assessed. It should also be noted that a differential measurement versus a RE is required. As such, the same limitations as discussed in Chapter 3 apply.

$$E = \left(E^0 + 2.303\frac{RT}{nF}log\left(\frac{Ir^{4+}}{Ir^{3+}}\right)\right) - 2.303\frac{RT}{F}pH \qquad (eq.5.10.)$$

5.1.4 Formation of Iridium oxide pH sensitive layers

Deposition and formation of IrO_x on several metal surfaces is possible. Hitherto, a wide variety of fabrication methods exist each with their own advantages. Methods include:

1. Thermal oxidation of Iridium at high temperatures;
2. Electrochemical formation of IrO_x through cyclic voltammetry;
3. Sol-gel deposition through deposition from Ir_2Cl_4 suspensions.

1. Thermally prepared IrO_x can be formed on solid Iridium wires. By thermally oxidizing the Iridium metal at high temperatures an anhydrous layer of IrO_x is formed. Typically, near-Nernstian responses are obtained (193).

2. Of the aforementioned, the electrochemical formation of Iridium oxide has been studied extensively. One of its advantages is the resulting super-Nernstian response. During the cycling of the deposition potential using CV in dilute sulphuric acid (H_2SO_4), consecutive layers of hydrated oxy-hydrates are deposited (189, 191, 194). The oxide can either be formed directly on an iridium metal base or on a metal surface using a solution of Ir_2Cl_4 in oxalic acid; as described by *Yamanaka* (195).

3. Sol-gel deposition has recently been developed. Its advantage lies in ease of fabrication. Deposition of IrO_x is achieved through droplet deposition or spin-coating of an Ir_2Cl_4 acetate (sol-gel) solution on a metal substrate. The substrate is heated to temperatures between 300 – 400 ^{0}C, effectively burning of the acetate and leaving behind a film of Iridium. The Iridium film is then further oxidized into an anhydrous Iridium oxide film. Because there is little to no control over the type of oxide formed, responses can vary; typically a sub- to Nernstian response is achieved (196, 197).

To summarize, the state-of the art for IrO_x pH sensing, as shown in Table 5.1, is assessed with a focus on recent developments in the field. Listed are the method of deposition, sensitivities and life-times.

Table 5.1 – State of the art for IrOx pH sensors.

	Deposition	**Sensitivity**	**Life-time**
C.Nguyen (197)	Sol-gel	52-57 mV pH^{-1}	30 days
J. Chu (198)	Electrochemical	74.0 mV pH^{-1}	7 days
L.Kuo (199)	Sputtering	59.5 mV pH^{-1}	1 day
X.Huang (200)	Sputtering	58.7 mV pH^{-1}	NA
W.Huang (196)	Sol-gel	51.2 mV pH^{-1}	NA
S.Carroll (201)	Electrochemical	66.0 mV pH^{-1}	16 days
M.Wang (193)	Thermal	58.4 mV pH^{-1}	1.5 years

5.2 Materials and methods

For the development of the IrO_x pH sensor two different methods of fabrication were investigated: thermal Iridium oxide films (TIROF); electrodeposited Iridium oxide films (EIROF). Both methods

rely on a deposition solution proposed by *Yamanaka* in which a hydrate of Iridium-tetrachloride is dissolved in an acidic solution (195).

5.2.1 Iridium oxide formation

For the TIROF, sensors of Type-A were used. A lift-off process employing multi- or single-layer TMMF was developed. The deposition solution was prepared by dissolving 0.5 g of iridium-tetrachloride into a mixture of DI water, ethanol and acetic acid (10% v/v). The solution was stirred for 24 hours and stored in the fridge. Before use, the solution was stirred for at least one hour. Formation of the TIROF was achieved by deposition of droplets (10 - 20 µL) of the solution on top of the sensor die. The droplet was allowed to evaporate and deposition was repeated four times, after which the sensor dies were transferred to a hot-plate. The repeated deposition of droplets is required to achieve proper coverage within the TMMF structure used for defining the sensing area.

The hot plate was set to a temperature of 305 ± 5 ^{0}C; starting from room temperature. The sensors were left on the hot plate for 3.5 - 4 hours (optimised). Because of the variation between deposited droplets it is advisable that, starting from 3.5 hours, sensor samples are checked under the microscope to see if the IrO_x has formed properly. If the time is exceeded, cracking of the layer and peeling of the IrO_x is observed; resulting in destruction of the sensing layer. An overview of the deposition process is shown in Figure 5.5

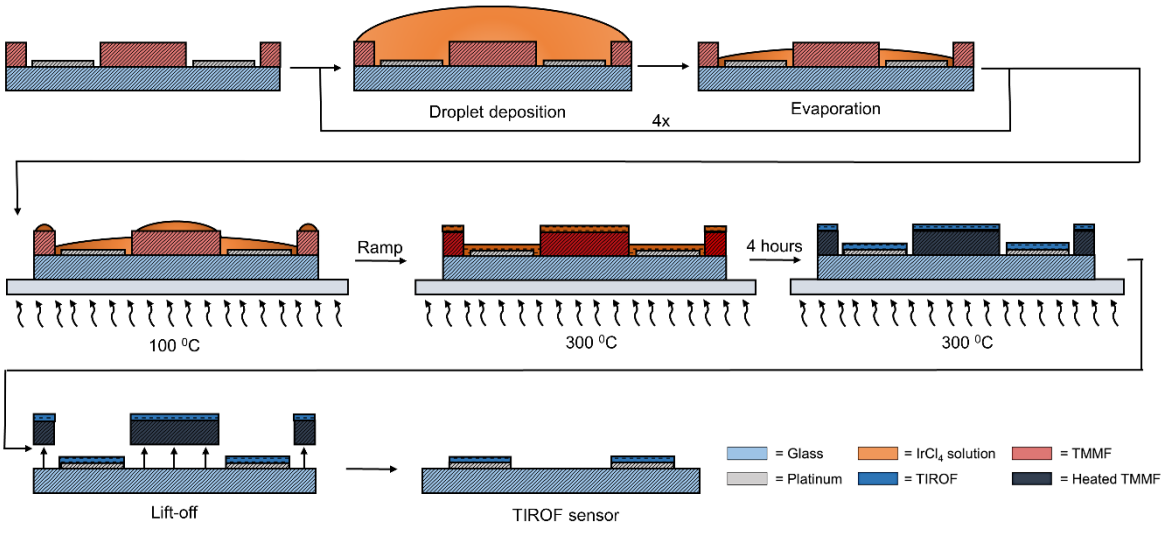

Figure 5.5 - Overview of the TIROF deposition and formation process using TMMF for lift-off. A droplet of the sol-gel solution is deposited in repeated cycles. The covered sensor die is transferred to a hot plate and left to oxidise for 3.5 to 4 hours. During this time the TMMF turns black and can be lifted off the surface. The result is a Pt electrode coated with and Iridium oxide film.

For the EIROF deposition sensors of Type-C were used. A deposition solution was prepared as follows: 0.5 g of Iridium tertrachloride was added to 100 mL of DI water and left to stir for thirty minutes. Next, 10 mL of hydrogen peroxide (30% v/v) was added and left to stir for 10 minutes.

Third, 0.5 g of oxalic acid dehydrate was added and the solution was left to stir for another 10 minutes. The pH of the solution was measured using a glass pH probe. Potassium-carbonate was added gradually to increase the pH to 10.5. The solution was left to stir at room temperature until the solution turned violet in colour. The solution was aliquoted and stored at 7 ^{0}C.

For electrochemical deposition a PalmSense3 potentiostat was used. Deposition was performed by means of CV. The potential of the WE is swept repeatedly, for 125 cycles, between +0.2 and +0.7 V vs. Ag-AgCl (3 M KCl) with a scan rate of 50 mV s^{-1}. Sensors were prepared and used immediately after fabrication. The EIROF deposition can be preceded by an additional gold layer. This promotes adhesion of the film, as will be discussed in section 5.3.4. For the deposition, gold bath plating solution from *Spa Plating Ltd*. was used. A PalmSense3 potentiostat running in chronopotentiometry mode was used for deposition. Gold was deposited for 5 minutes at -10 mA cm^{-2} current density (not optimised).

5.2.2 Calibration procedure

Calibration of the sensors was performed using commercial pH buffers. At the least, three different pH buffers of pH 4, 6, 7, 9 and 10 (*Reagecon*) were used for the calibrations with an error of 0.01 pH. Prior to measurement, buffers were checked using a calibrated *Hannah Instruments* glass pH probe with an accuracy of 0.05 pH, indicated as the x-error. Over the course of this work the systematic error, related to the calibration has been improved upon due to experience.

Open circuit potential measurements of the fabricated sensors versus commercial Ag-AgCl electrodes were performed using a Phidget interface board with a 1.5 TΩ input impedance and a minimum resolution of 1 mV which approximates to 0.02 pH. Electrodes were submersed in each buffer solution for at least half an hour in order to obtain a stable reading. Data analysis was performed using Origin. To obtain the calibration curve, the measured open circuit potential (OCP) was plotted versus the pH of the buffer solution. A linear regression fit was performed with a cut-off for the R-squared value below 0.98. The fit was performed on the average of the final, stable, part of the OCP measurement.

5.2.3 Long term measurement procedure

Long-term measurements were performed versus a commercial Ag-AgCl reference electrode in order to map the behaviour of the pH sensors. A Phidget pH/ORP interface board was used to measure the OCP. It was found highly important that the sensor contacts were encapsulated within large amounts of epoxy. To achieve this, a Pasteur pipette was slid across the sensor contacts and filled with fast-cure epoxy, similar to the method described in Chapter 3. By encapsulating the contact in a thick epoxy, device failure due to water absorption is kept to a minimum.

For the temperature controlled experiments, a temperature bath was used. Sensors were placed in a vessel containing 1x PBS with a PT100 thermistor; temperature was logged at 30 minute intervals. During the course of the long-term measurements, the 1x PBS solution was replenished with DI water to compensate for evaporation. Weekly measurements of the pH within the vessel were performed with a commercial pH probe. An overview of the long-term measurement setup is shown in Figure 5.6.

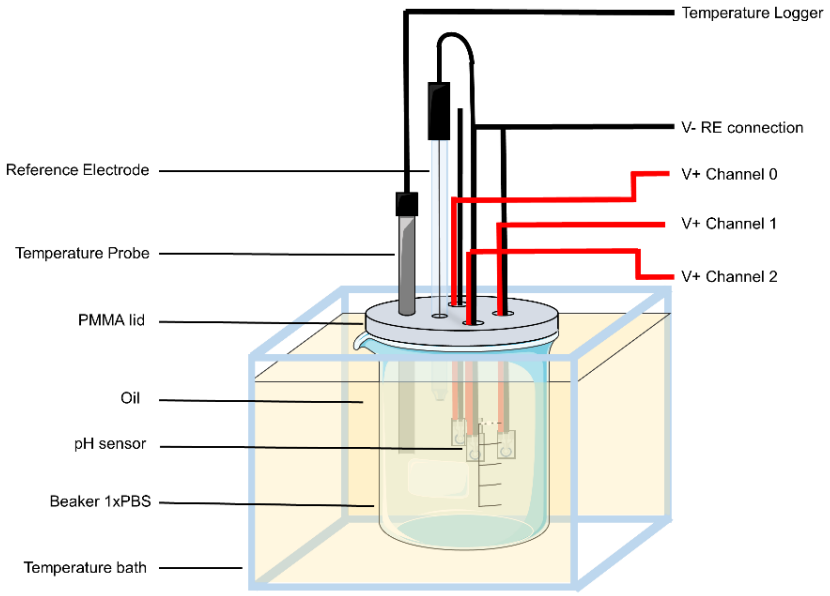

Figure 5.6 – Overview of the long-term pH measurement set-up in a temperature bath. The beaker contains the solution and the IrO_x pH sensors. The potential is monitored versus a commercial Ag-AgCl RE. A temperature probe is used to log the temperature within the beaker.

5.3 Results and discussion

This section covers the results and discussion for the IrO_x pH sensors. The performance of the TIROF and EIROF is discussed separately. A comparative summary between the different fabrication methods is obtained in this manner, in accordance with the criteria listed in Chapter 1. A comparison of performance to the literature is given, based on the experimental results.

5.3.1 Thermal Iridium oxide film sensor characterisation

The IrO_x is formed by the thermal treatment of the $IrCl_4$ solution deposited on top of the Platinum electrodes. During this process the acetate within the solution is burned off and the solid Iridium left behind; the Iridium is oxidised over the next hours. The time for the thermal treatment has been found to be important for the structural integrity and adhesion. The layer forms over time, indicated by the appearance of a blue-orange layer on top of the electrodes. It has been found that if the sensors are exposed to the elevated temperature for too long, cracking of the layer occurs due to induced stress within the film. For the lift-off process, the optimal time was found through trial-and-error and determined to be between 3.5 to 4 hours.

The thermal lift-off is a dirty process, during which the TMMF turns black. Additionally, deposition is performed by placing droplets on top of the entire sensor device for four cycles. As the acetate is burned off, shards of IrO_x are left across and around the edges of the photoresist walls, as shown in Figure 5.7.a. The shards can be cleared off easily through sonication in DI water and the result is a clean sensor as shown in Figure 5.7.b. One issue was that due to the height of the resist pattern which defined the pH electrode, edges of the Platinum were left uncovered, as shown in Figure 5.7.c. This has not been found to adversely affect the performance of the IrO_x sensor.

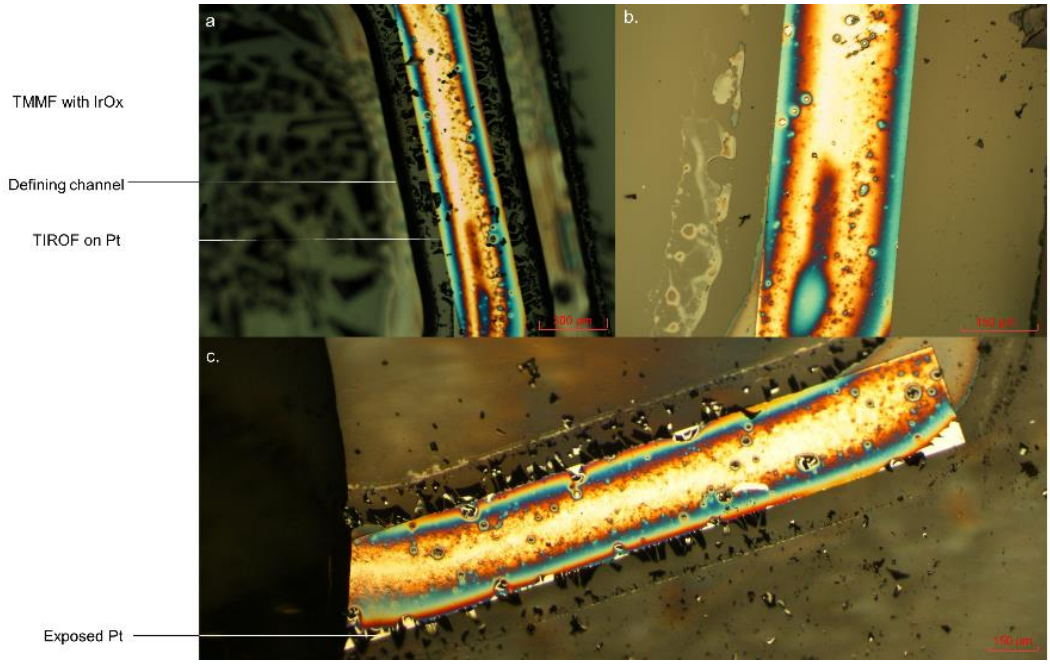

Figure 5.7 - Thermal IrO_x film deposited on Pt according to the lift-off process. a) TIROF on Pt within the TMMF used for lift-off. b) TIROF film after an ultra-sonic clean in DI water. c) TIROF film showing the exposed Pt edges present after lift-off.

Exemplar responses of three TIROF sensors during a calibration measurement are shown in Figure 5.8. As a control, and in order to show the exposed edges have no effect, the response of two bare Pt electrodes is shown. Based on these experiments, a cut-off between IrO_x and Pt sensitivity towards pH was determined. Sensitivities which were below 50 mV pH^{-1} were discarded and assumed to have failed. In other words, a near-Nernstian response for the TIROF and a sub-Nernstian response of the Pt electrodes is expected. This is in agreement with the studies from *Nguyen et al.* and *Huang et al.*, who report sensitivities ranging from 52 mV pH^{-1} to 58 mV pH^{-1} (196, 197).

An overview of the fitting results is shown in Table 5.2. From this, the limit of quantification can be determined based on the standard error of the linear regression fit, as well as the error of the residuals. In both cases the smallest detectable change is 0.06-0.07 pH with a 99.7% percent confidence. Note that the R-squared value for all fits is larger than 0.99. The response time of the TIROF samples is of the order of one minute for all samples and highly dependent on the hydration and pH change between buffers.

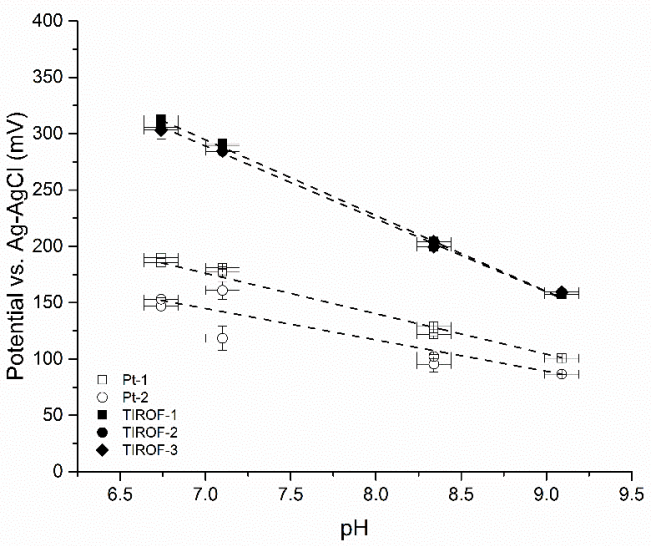

Figure 5.8 – Examples of three TIROF calibration curves compared to bare Pt electrode. A near-Nernstian sensitivity is observed for all samples compared a sub-Nernstian response for Pt-1 and -2. R-squared > 0.99.

It is well known that metal oxide films used in pH sensing require a hydroxylated surface, as explained in section 5.1.3. It is this hydrated surface that is responsible for the sensitivity towards pH changes. To illustrate the importance of hydration, a test of precision was performed for un-hydrated and hydrated samples. Figure 5.9 depicts the results for the precision of the TIROF sensor when used directly after fabrication, and after two days of hydration in 1x PBS. Calibrations were performed prior to the experiment. For the distribution plots, the bin size was set equal to a resolution of 0.05 pH; this is in accordance with the specifications for the application.

Table 5.2 - Calibration values obtained from the three TIROF curves.

	Slope	**Intercept**	**Standard error**	**Residuals**	**LOQ[6]**
TIROF-1	67.25	765.30 mV	1.41 mV	1.3 mV	0.06 pH
TIROF-2	64.74	742.24 mV	1.47 mV	1.5 mV	0.07 pH
TIROF-3	64.74	742.24 mV	1.47 mV	1.4 mV	0.06 pH

From Figure 5.9 it is clear that the precision of the sensor increases after hydration, in particular at high pH. Interestingly, accuracy is highest around the pH used for hydration i.e. pH 7. This illustrates an important aspect of pH sensing with IrO_x pH sensors: to obtain optimal performance hydration should be performed close to the pH of interest. This observation is explained by the fact that there

[6] Determined as three times the standard error divided by the sensitivity.

is a response time associated with the pH sensor, based on mass-transport within the porous IrO_x structure. A second data set is available in Appendix C1.

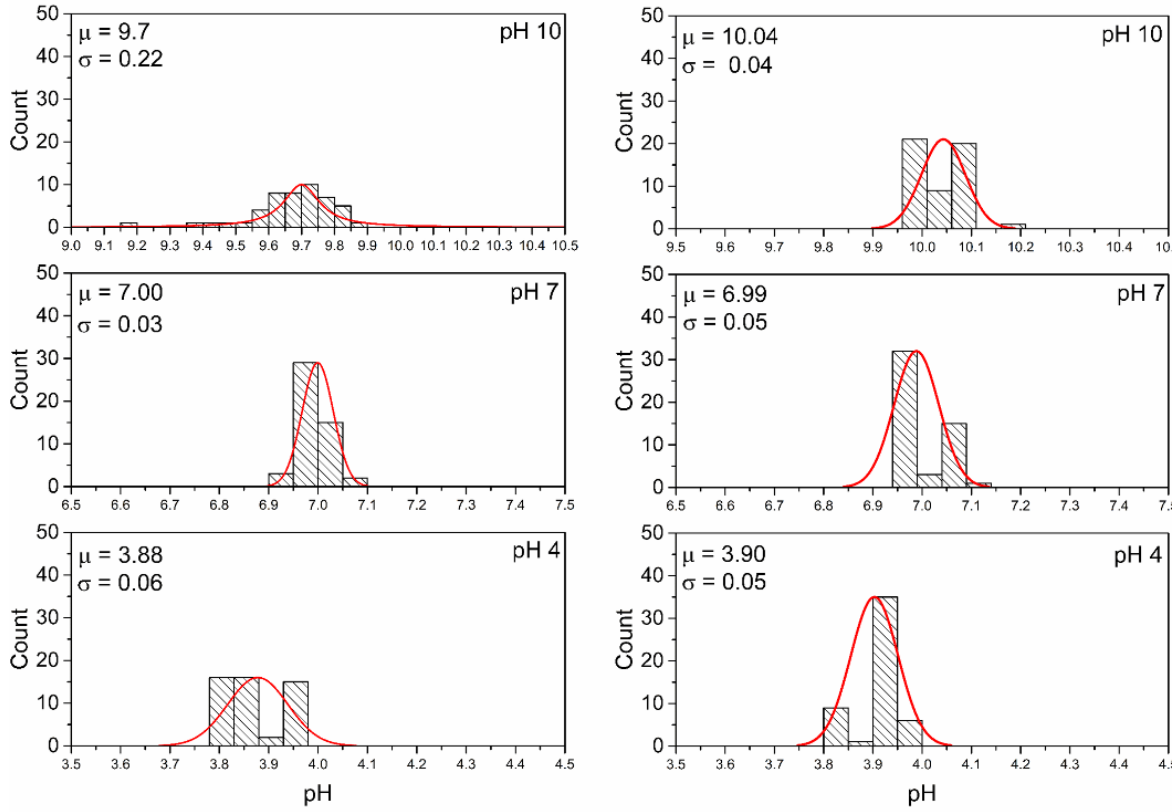

Figure 5.9 - Precision and accuracy test in (left) anhydrous and (right) hydrous state. Hydration performed in 1x PBS for two days. Precision values are: 35, 63 and 14% for the anhydrous and 70, 90, 63% for the hydrous in pH 4, 7, 10, respectively. As shown, both accuracy and precision increase drastically. T = 20.8 ^{0}C; n ≥ 40 per pH value.

Carroll et.al. and *Huang et al.* both recorded a similar behaviour on response time and precision once IrO_x samples were tested (196, 201); *Mazouk et al.*, reported a similar observation with respect to pH related accuracy for *Nafion*® coated samples. In general, it can be concluded from these claims and the experimental data that the closer the storage pH is to the measured pH the faster and the more accurate the response will be. The precision for the hydrated samples at pH 4, 7 and 10 equals 70%, 90% and 63%, respectively, compared to 35%, 63% and 14% for the anhydrous. This shows a significant improvement on the repeatability of the measured pH.

The effect of temperature on the TIROF sensors is presented in Figure 5.10 and summarised in Table 5.3. The effect is presented as a temperature coefficient and as calibration curves at different temperatures. According to the Nernst equation a temperature coefficient of 0.2 mV $^0C^{-1}$ should be observed. As can be denoted, the temperature coefficient is minimal and well below 1 mV $^0C^{-1}$. The effect on the sensitivity appears larger with a variation between 3 and 6 mV pH^{-1} being observed over a 20 ^{0}C change. The first can be explained by the fact that the predicted temperature coefficient is based on the Nernst equation.

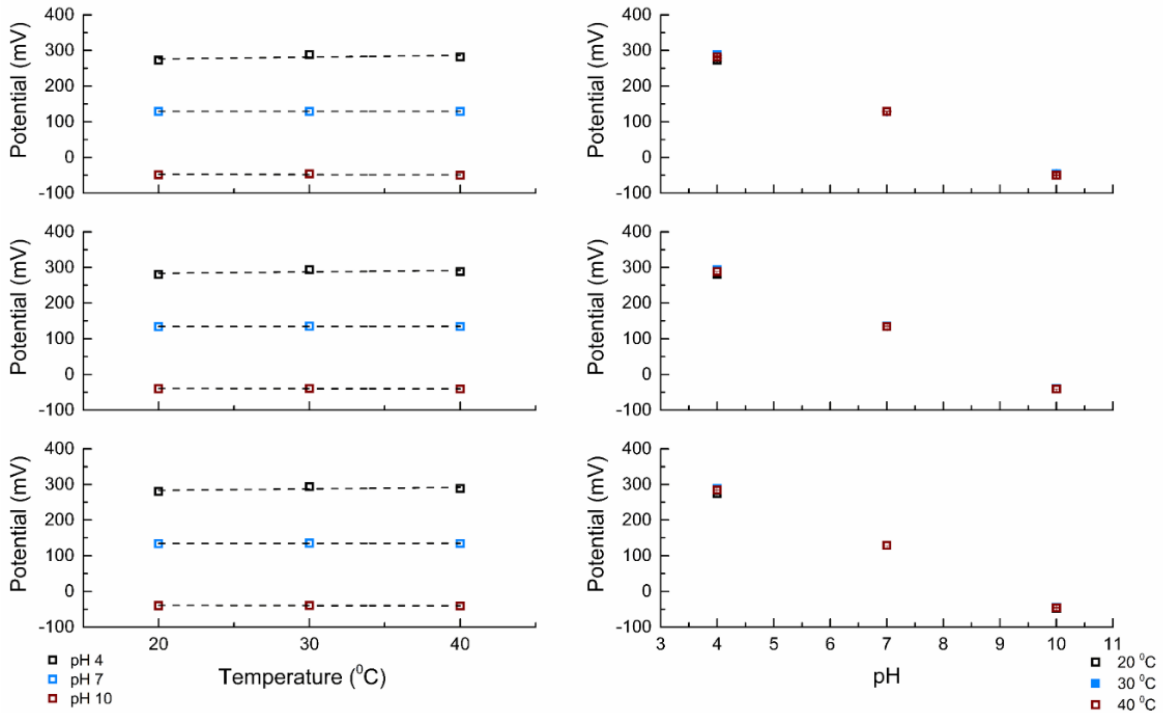

Figure 5.10 - The effect of temperature on three different TIROF sensors. left) Potential values for different pH buffers at different temperatures. right) Calibration curves at different temperature values.

It can easily be understood that this is a simplified representation of the metal oxide system. In practice, the formal potential will have a temperature coefficient associated with the Iridium oxidation states. Similar to the RE in Chapter 3, the approximation of the concentration might be better represented in the form of activity, reducing the expected value of the temperature coefficient. Second, the Nernst equation contains the universal gas constant, which applies to gas. However, in these experiments liquids are used. A deviation based on this discrepancy is likely. *Huang et al.* reported on an equally low temperature coefficient for their sol-gel based IrO_x films (196). From a practical perspective, the low temperature coefficient observed in this work is useful. As temperature fluctuations within the human body and uterus are minimal, temperature compensation *in vivo* might be omitted (38).

5.3.2 Thermal iridium oxide film long-term performance

The TIROF characterisation has served as a stepping stone for the long-term performance tests of the sensors. In particular its change in response during hydration is of key importance as this puts a time limit on the sensor applicability after fabrication. To further assess this aspect over prolonged periods of time, a weekly assessment of the calibration curves was performed. The two main variables in the calibration curves are the slope and intercept i.e. sensitivity and formal potential. It is vital that the sensitivity shows little to no variation over the measurement period. An experiment was setup to observe the change in these characteristic. Here, the TIROF sensors were calibrated on a weekly basis while immersed in 1x PBS solution in between calibrations. The results are shown in

Figure 5.11. Note that sensors were not hydrated prior to measurement. This effect can be observed in the difference in both sensitivity and formal potential between week 0 and week 1.

Table 5.3 – Summary of the temperature characteristics.

		Temperature coefficient	Sensitivity
TIROF-1	20 ^{0}C	pH 4: 0.43 ± 0.05 mV ^{0}C^{-1}	20 ^{0}C: 56 mV pH^{-1}
	30 ^{0}C	pH 7: -0.04 ± 0.06 mV ^{0}C^{-1}	30 ^{0}C: 56 mV pH^{-1}
	40 ^{0}C	pH 10: -0.03 ± 0.07 mV ^{0}C^{-1}	40 ^{0}C: 52 mV pH^{-1}
TIROF-2	20 ^{0}C	pH 4: 0.43 ± 0.05 mV ^{0}C^{-1}	20 ^{0}C: 55 mV pH^{-1}
	30 ^{0}C	pH 7: -0.04 ± 0.06 mV ^{0}C^{-1}	30 ^{0}C: 55 mV pH^{-1}
	40 ^{0}C	pH 10: - 0.03 ± 0.07 mV ^{0}C^{-1}	40 ^{0}C: 52 mV pH^{-1}
TIROF-3	20 ^{0}C	pH 4: 0.5 ± 0.6 mV ^{0}C^{-1}	20 ^{0}C: 54 mV pH^{-1}
	30 ^{0}C	pH 7: -0.0 ± 0.00 mV ^{0}C^{-1}	30 ^{0}C: 53 mV pH^{-1}
	40 ^{0}C	pH 10: -0.08 ± 0.2 mV ^{0}C^{-1}	40 ^{0}C: 59 mV pH^{-1}

Assessing the results, there is a good agreement with the previously established discrepancy between hydrated and un-hydrated samples as seen by the initial change in both sensitivity and formal potential within the first week. After this initial period there is little to no change in sensitivity, with the exception of the value at the 4th week. This was confirmed as due to a drift in the RE, causing a drop in potential across the entire set of samples. The filling solution of the reference electrode was replaced and the value returned to its original in the 5th week. In conclusion, the results show that changes in sensitivity are minimal for the required time period.

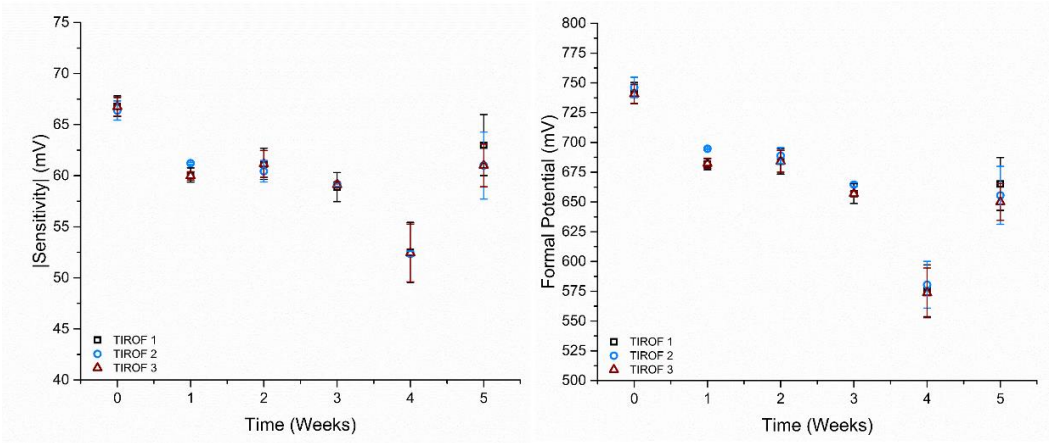

Figure 5.11 – Long-term assessment of sensitivity and formal potential for three different TIROF sensors in 1x PBS at room temperature. Between week 0 and week 1 the effect of hydration can be seen. After this period the sensitivity remains constant whereas the formal potential shows a large variation over time. Note that at week 4 the RE was replaced due to a malfunction.

The drift in formal potential is of a different nature. The formal potential consists of the ratio between Ir^{3+} and Ir^{4+} oxidation states. The resulting differences in formal potential should therefore be attributed to the oxidation states. The TIROF fabrication method does not allow for direct control over the ratio in which Ir^{3+} and Ir^{4+} are formed. Variations in deposition are common and will contribute to differences in formal potential (191, 194). This is a limiting factor compared to other methods such as electrochemical deposition.

In order to compensate for the drift in formal potential assessment over the measurement period has to be made. As calibration *in vivo* is not possible, these drift values have to be predictable across all sensors fabricated using the thermal oxidation method. Long-term measurements were set-up in 1x PBS to determine the drift over time over the course of 30 days and onwards. Figure 5.12 shows the results for three different TIROF sensors. It can be seen that drift values are minimal with an average below 0.01 pH day^{-1}. It can further be noted that the initial calibration curve accuracy is not optimal and shows the importance of the initial calibration in order to minimise the systemic error; the error equals 0.4 to 0.7 pH.

Figure 5.12.b shows the long-term traces for a set of four TIROF sensors in 1x PBS in a temperature controlled bath. A recalibration was performed after 1 day to enhance the accuracy at the elevated temperature. As can be seen the accuracy now falls within the 0.1 pH band required for this work. The entirety of the TIROF data sets for both characterisation and long-term performance is summarised in Table 5.4. Indicated is the sample size, average values and accuracy of the data set. For the long-term performance, the sample size implies those samples which were ran for the set course i.e. those aimed at running for thirty days and onwards, from which the yield has been established.

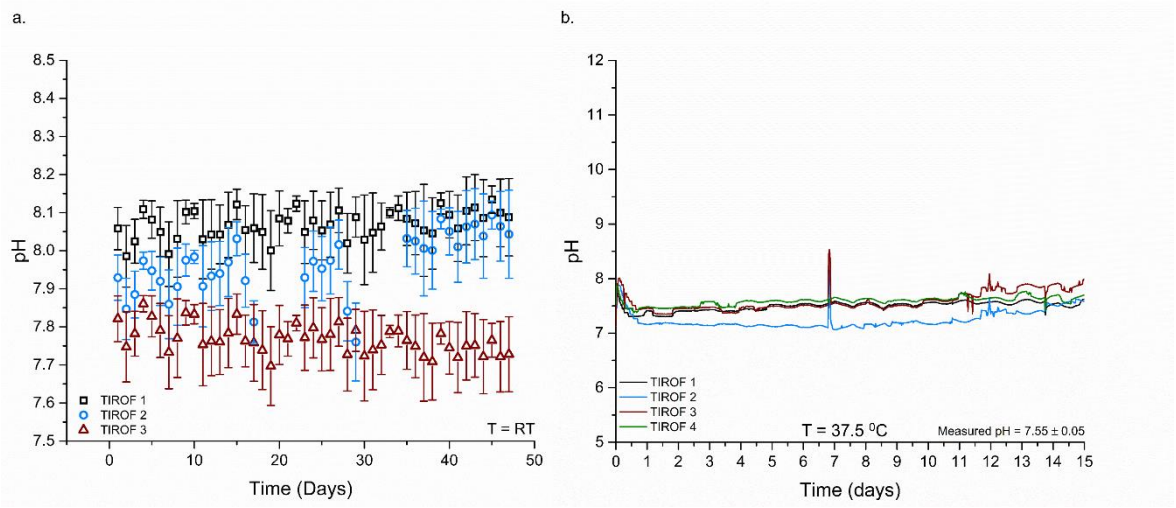

Figure 5.12 – Long-term plot for TIROF pH sensor in 1x PBS. a) At room temperature presented as the daily average. b) At body temperature presented as a continuous trace. Note each point taken at 30 minute discrete time intervals.

It can be concluded that, even when the systemic error is reduced, accuracy values appear to be no better than 0.24 pH. In part, this effect is attributed to the high reliability of the initial calibration curve. Even though little to no change in sensitivity has been observed over the time course, very slight variations can have a significant impact if 0.1 accuracy is to be achieved. Stability however, shows good performance with 0.017 ± 0.011 pH day^{-1} in drift. This indicates a high precision over the long-term course and would allow for the determination of a relative pH change within the stated biologically relevant range.

Table 5.4 – Overview of the TIROF data sets based on their characteristics and long-term performance.

Characteristics	**Sensitivity**	**E^0**	**Accuracy**	
n = 25	58.3 ± 0.3 mV pH^{-1}	600.6 ± 24.1 mV	0.24 ± 0.12 pH	
Long-term	**Drift (10^{-3})**	**Yield week 2**	**Yield week 4**	**Yield week ≥ 5**
n = 12	17 ± 11 pH day^{-1}	85%	67%	45%

5.3.3 Electrodeposited Iridium oxide performance

To enhance the accuracy of the pH sensor a second deposition method was investigated: electrochemical deposition. The electrodeposited Iridium oxide film (EIROF) can show a super-Nernstian response with sensitivities exceeding 70 mV pH^{-1}, providing a larger margin of error (191, 198). The electrodeposition was performed according to the method described in section 5.2. Figure 5.13 shows the calibration plots for the EIROF-on-Pt and EIROF-on-Au. Initially, the IrO_x was deposited directly onto the Pt electrodes. However, during long-term measurements it was found that the EIROF delaminated from the Pt. Therefore, an intermediate layer of Au was electrodeposited prior to EIROF deposition. Images of the formed EIROF sensors on Pt and Au are shown in Figure 5.14.a and b, respectively.

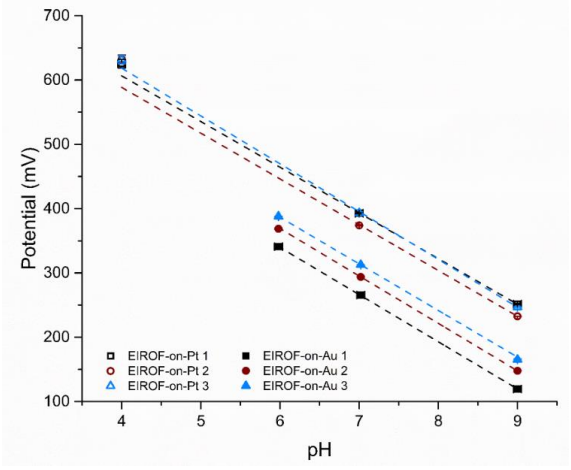

Figure 5.13 – Calibration plots for EIROF-on-Pt and EIROF-on-Au samples. A super-Nernstian response is observed for all samples. R-square >0.98 and > 0.99 for EIROF-on-Pt and EIROF-on-Au, respectively.

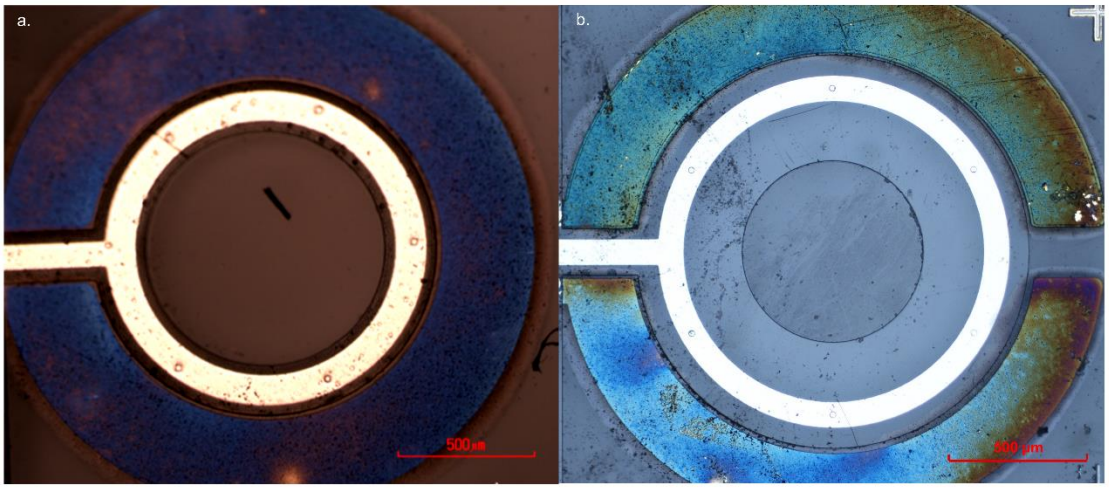

Figure 5.14 – EIROF deposition using CV. a) EIROF-on-Pt sensor Type-C1; b) EIROF-on-Au sensor Type-C2. Deposited for 125 cycles between +0.2 – 0.7 V; Scan rate equals 50 mV s^{-1}.

The parameters from the linear fit are listed in Table 5.5. As can be denoted a super-Nernstian response is observed for the samples. The limit of quantification is represented as three times the standard error of the fit and shows that high accuracy is obtainable. In particular, the fit for the EIROF-on-Au shows very good confidence across the pH range. Figure 5.15 shows short-term performance data for the EIROF-on-Pt. As can be concluded, high accuracy is achieved with the graph: over the entirety of the excerpt the pH reading falls within the 0.1 pH error band. However, during the course of the measurement, at times beyond six days, delamination of the layer resulted in device failure. It is unknown what governs this delamination from the Pt substrate, but it has been found to be independent of storage conditions and deposition method.

Table 5.5 - Linear fit parameters for EIROF-on-Pt and EIROF-on-Au.

	Slope	**Intercept**	**Standard error**	**LOQ**
EIROF-on-Pt 1	71.1 mV pH^{-1}	890.87 mV	1.67 mV	0.07 pH
EIROF-on-Pt 2	71.2 mV pH^{-1}	873.30 mV	2.11 mV	0.10 pH
EIROF-on-Pt 3	74.4 mV pH^{-1}	915.88 mV	1.68 mV	0.07 pH
EIROF-on-Au 1	73.4 mV pH^{-1}	779.67 mV	0.2 mV	0.01 pH
EIROF-on-Au 2	73.7 mV pH^{-1}	811.41 mV	< 0.01 mV	< 0.01 pH
EIROF-on-Au 3	72.5 mV pH^{-1}	821.26 mV	< 0.01 mV	< 0.01 pH

The inclusion of *Nafion*® membranes as reported by *O'Hare* has been investigated throughout the course of this work (194). However, in all cases the response time and sensitivity is retarded by the addition of this extra layer. This made it difficult to include such a containment membrane for this particular application in which long-term continuous monitoring is required. More work is needed to

assess the delamination phenomena. Due to the delamination long-term measurements with EIROF-on-Au were performed.

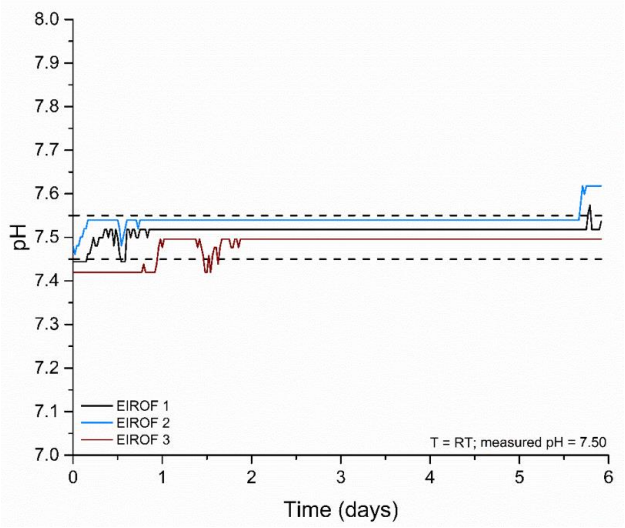

Figure 5.15 – Excerpt representing short-term performance of EIROF-on-Pt sensors. For the duration of 6 days, the error falls within the 0.1 pH error band. After the sixth day delamination causes a drop in potential i.e. towards high pH caused by delamination of the EIROF. Measured at room temperature in 1x PBS.

5.3.4 Electrodeposited Iridium oxide film long term performance

The long-term performance of the EIROF-on-Au electrodes was assessed in a similar manner as for the TIROF. Only one set consisting of three electrodes was tested so far. First, a weekly calibration measurement was performed over the course of 5 weeks. The results are presented in Figure 5.16. As can be denoted, the drift in sensitivity is again minimal for the devices with a peak-to-peak variation of 4 mV pH^{-1} as a maximum for EIROF-on-Au 2 and EIROF-on-Au 3. Examining the formal potential in Figure 5.16.b, a drift over time with values equal to 71.0 and 47.7 mV is observed for EIROF-on-Au 3 and 2, respectively. This is similar to the results of the TIROF sensors.

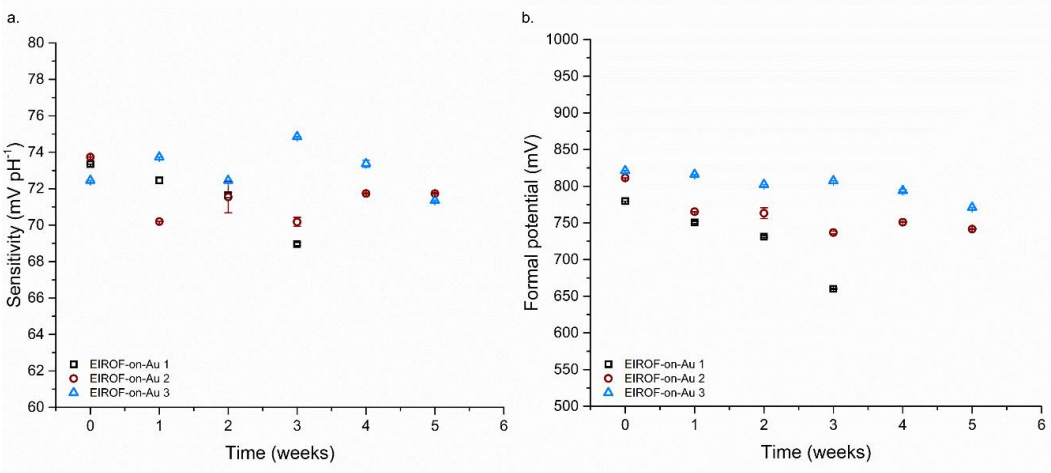

Figure 5.16 – Long-term calibration comparison for EIROF-on-Au sensors. a) Absolute sensitivity over the time period. b) Formal potential. A maximum peak-to-peak variation of 4 mV is observed for the sensitivity. A drift of 71.0 and 47.7 mV pH^{-1} is observed for the formal potential of EIROF-on-Au 2 and 3, respectively.

Presented in Figure 5.17 is the long-term performance of the EIROF-on-Au sensors from the weekly calibration batch discussed preciously. Figure 5.17.a depicts the continuous trace for all three sensor devices. Note that after two weeks EIROF-on-Au 1 fails. The drift analysis by means of linear regression is shown in Figure 5.17.b. As can be denoted, a low drift is observed with values of 1.53 and 1.02 mV day^{-1}. Figure 5.17.c depicts the continuous trace of EIROF-on-Au 2 and 3. Indicated is the 0.1 error band. The relative error based on the pH reading obtained with a commercial glass pH meter is shown in Figure 5.17.d. The error does not exceed 0.l pH showing good overall precision as required for this work.

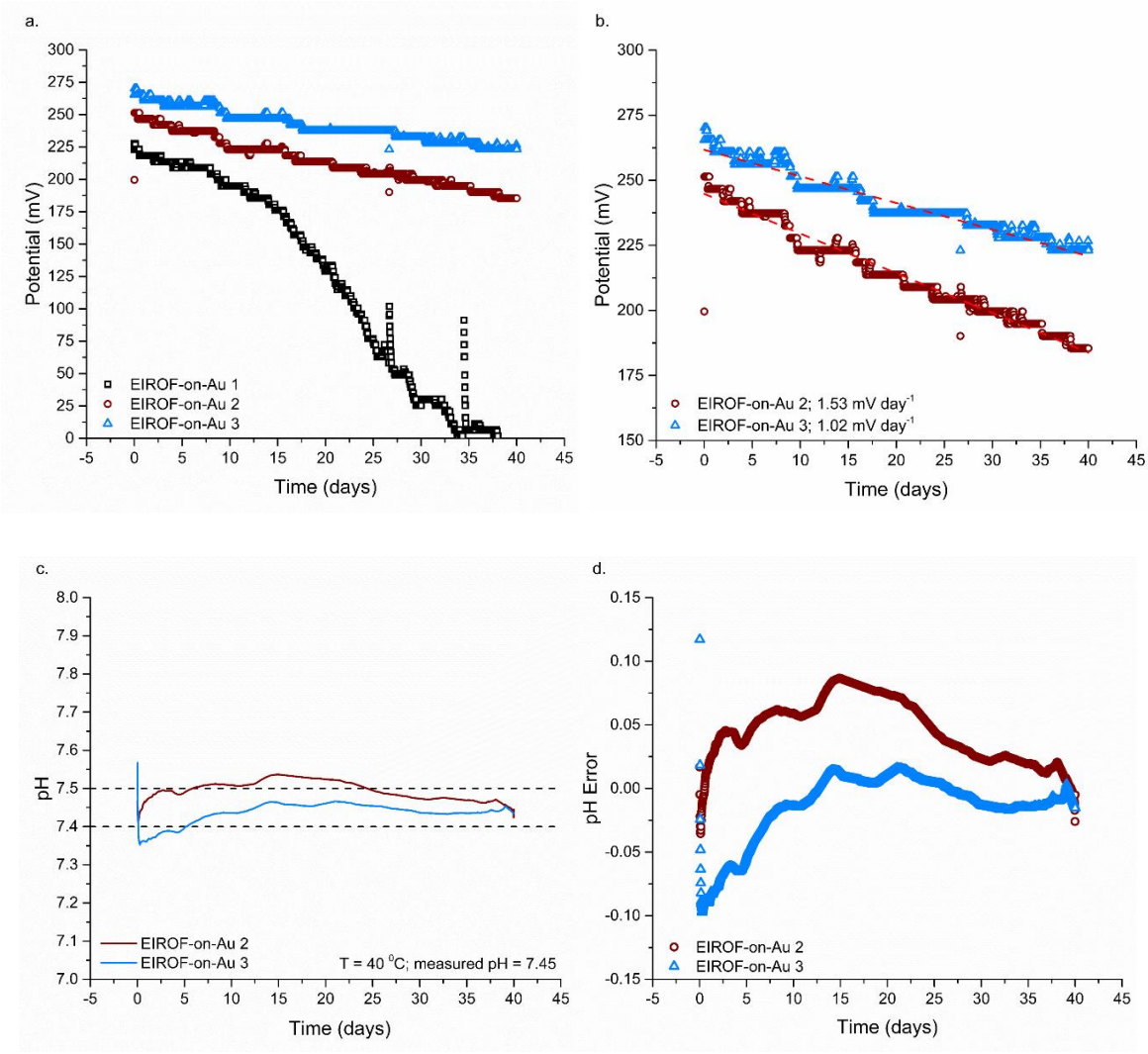

Figure 5.17 – Long-term performance of EIROF-on-Au sensors over a 40 day measurement period. a) Full long term trace for three different sensors. B) Linear regression fit for drift compensation for EIROF-on-Au 2 and 3. C) Drift compensated trace for EIROF-on-Au 2 and 3. Indicated is the 0.1 pH error band. D) Relative error with respect to glass pH probe average reading; average equals 0.02 ± 0.04 pH. Data points represent 30 minute discrete data points from the full trace.

When judging the EIROF sensor based on its performance it is clear that the measurement period is achievable. Furthermore, high accuracy and precision can be obtained. As stated, a required accuracy of 0.2 pH is required for the system and in the measured periods the EIROF-on-Au sensors fall within this range. The precision adheres to its required value, with a relative drift well below 0.1 pH day^{-1}. However, It should be noted that the sample size is small (n = 3) with a 4 week yield of 67%. A larger sample group needs to be established and future work will aim to achieve this. Of particular interest as well is the common fluctuation between the samples. This type of common signal drift can be further investigated as a means to compensate for drift using a differential measurement approach.

Similar inaccuracies with respect to the initial calibration were observed with EIROF samples. Because the hydration time period varies, and is at least 5-7 days, induced errors will be common. This puts a constraint on the calibration of the *in vivo* system. Furthermore, the error in the developed RE will contribute to the total error of the pH sensors. The propagation of the error including the reference electrode can be computed using equation 5.11. Note that this needs to be determined using the value for the error in potentials. For the TIROF this yields an error of: 0.25 pH using the values in table 5.5. For the EIROF we find an error of 0.07 pH using the error in figure 5.17.

$$Error = \sqrt{Error_{pH}^2 + Error_{RE}^2} \qquad (eq.5.11)$$

5.4 Summary

This chapter discussed the theory, background and results for the developed pH sensor. A variety of devices exist for commercial pH sensors. However, their use *in vivo* is complicated by size, power consumption and drift. In this work metal-metal oxide pH sensors utilising the pH sensitive properties of Iridium oxide have been fabricated. Two different fabrication methods have been developed and tested: thermal Iridium oxide films and electrochemical Iridium oxide films. Both methods have been assessed for their life-time, accuracy and stability suing the judgement criteria stated in Chapter 1. The TIROF has been formed using a lift-off process, forming the pH sensitive layer on the micro fabricated Pt electrodes. A near-Nernstian response is observed. Sensor life-time has exceeded the prerequisite period of 30 days with low drift values and high precision. However, accuracy of the TIROF has been shown to be difficult to reduce below 0.2 pH. The overall long-term yield equals 67%.The EIROF is formed on an intermediate layer of electroplated gold. A super-Nernstian response is observed. Although the sample size is small, a better accuracy is observed for the EIROF with values better than 0.1 pH. Long-term performance has shown that it is feasible to achieve the predetermined measurement period of 30 days with a current yield of 67%. However, to accurately assess the characteristics the sample size needs to be increased.

Chapter 6 - Sensor integration

The sensors discussed in the previous chapters of this work have shown good performance within the biologically relevant range. To combine the sensors into a single IUSD three key points have to be addressed: on-chip sensor check, biocompatibility and device packaging. All three are key for the development of a reliable device capable of measuring unobtrusively *in vivo* for prolonged periods of time. Each of the stated points will be discussed individually in this chapter.

The on-chip sensor check comprises a novel methodology (patent pending) for a re-calibration in vivo, after implantation of the device. The theory, working principle, materials and methods and results are discussed. The biocompatibility of the sensor components has been checked using a cytotoxicity assay in accordance with *ISO10993*. An overview of the packaging and encapsulation process, developed throughout the course of this work is given, followed by an overview of the complete device assembly.

6.1 On-chip sensor check

From the results in Chapters 3 and 5, it is clear that an inherent drift on both pH sensor and RE is inevitable. Albeit in a predictable nature, it requires an assumption on the performance of both, and a pre-determined drift rate. Variations in chloride ion concentration, sensitivity and formal potential can cause this to deviate, and result in inaccurate readings over time. Furthermore, as discussed in Chapter 5, the accuracy of the pH sensor is highly dependent on the initial calibration. This makes it complicated to acquire an accurate response for an unknown *in vivo* system. To try and overcome this conundrum, a self-check, which can serve as a recalibration, of the pH sensor on-chip has been investigated. Not only does this provide an up-to-date recording of the sensitivity of the electrodes, it also compensates for drift in the RE when external concentrations have changed drastically. In macro-scale devices recalibration and performance is assessed versus other macroscale components. The simplest example is recalibrating a pH sensor in known buffer solutions. Ostensibly, if different pH values can be created local to the sensors, the same effect is achieved. This section discusses the theory and principle of a novel on-chip sensor check and calibration method.

6.1.1 Self-calibration theory and mechanism

From the theory of buffers in Chapter 1, it is clear that the biological system present within the uterus will govern changes in pH. The question is, how can this be used as an advantage for a potential calibration during implantation? As discussed in Chapter 4, electrochemical reactions occurring at electrode surfaces can have an impact on the surrounding bulk, close to the electrode surface. In some cases, as with the peroxides decomposing on the DO sensor, this can have a significant impact on sensor performance. In most cases the by-products are an unwanted side-effect as it skews

measurement data, damages electrodes and puts a time constraint on the measurement interval. However, this technique can be used to locally generate an artificial bulk containing specific ionic reaction products, seen only by the sensing electrode. As the electrodes developed in this work are small, its effect on the bulk of the intrauterine environment is expected to be negligible.

Looking at the table of standard reduction potentials in Appendix A1, two reactions which would facilitates a change in pH can be found, and are part of the electrolysis reaction of water. Platinum is the most widely used material for generating these redox species as it can withstand the currents associated with the electrolysis. The sensor dies described in this work have Pt electrodes available and can be used for this purpose. As water is the main compound within the body, and present in abundance, electrolysis should be possible and relatively easy to achieve on-chip.

From Faraday's law, a direct relationship between the amount of coulombs injected into the electrochemical system and the generated products can be calculated using the stoichiometry of the reaction. As the ratio of electrons to protons is equal the amount of moles can be determined using equation 6.1. Here, *m* represents the generated amount of protons in moles; *I* the injected current; *t* the time; *F* the Faraday constant. Thus, if the injected current and the time is known, the amount of proton and hydroxide ions can be computed. However, the generation cannot be performed on the pH sensor itself as the IrO_x would not be able to withstand the injected current, thus an additional Platinum electrode is needed. In this case the electrode is available as the DO sensor.

$$m = \frac{It}{F} \qquad (eq.\,6.1)$$

The electrolytic cell proposed in this work consists of a two-electrode system. By applying a potential of +1.23 V versus SHE, water decomposes into its products, generating four protons. Conversely, applying a potential of -0.83 V vs. SHE, water is decomposed and four hydroxide anions are generated. Figure 6.1 shows an illustration for this type of set-up for sensor Type-C. The recessed disk electrodes, used in DO sensing form the first electrolysis electrode at which the pH change is generated the WE. As the sensor die is double sided it is possible to use the CE as the secondary electrode for the electrolysis reaction, generating the opposite pH change. It is clear that the polarisation of the electrodes can be changed resulting in an increase or decrease in pH at the WE.

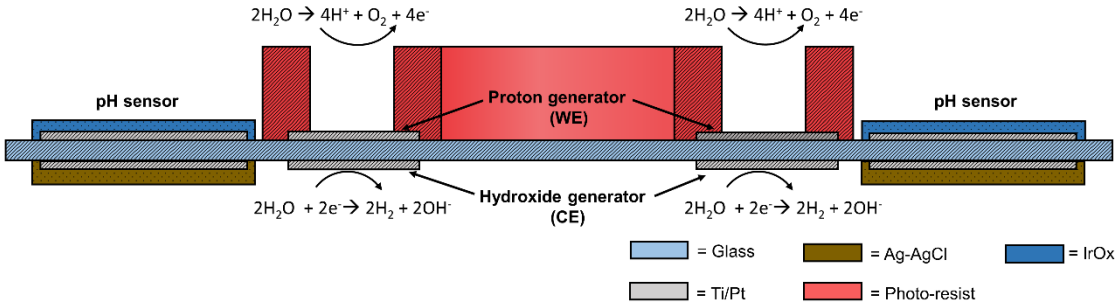

Figure 6.1 - Cross-sectional view of sensor Type-C1 used for on-chip calibration. The DO sensor recessed within the well is used to generate a local pH change extending across the IrO_x pH sensor by the generated protons during the electrolysis of water. The CE on the back is used as the second electrolysis electrode. The polarity can be reversed to achieve a decrease or increase in pH across the IrOx sensor.

The generated pH gradient will extend from the electrode surface according to the diffusion principles described in the previous chapters of this work. Briefly, as the pH is changed, a boundary extends outwards. This boundary interacts with the bulk. If the distance between the generating electrodes i.e. DO sensor and the pH electrode is known, the change in pH at a given time, as sensed by the IrO_x surface, can be predicted.

From the figure it is also clear that, in a similar manner, oxygen can be generated locally near the electrode surface. As described in the patents by *Bryan* and *Santoli et al.*, this local change in DO can be used to recalibrate DO sensor (202, 203). An implementation of this concept for the intrauterine sensing device is outlined in the future work in Chapter 7.

6.1.2 In situ calibration model

A *ComSol* model, either 2D (for recessed electrodes) or 2D revolved (for ring electrodes), was created to estimate the changes in pH upon the application of a current for a designated amount of time. Details on the model are given in appendix D1. The model follows a similar procedure as described by *Read et al.* in which a pH change generated near electrodes on boron doped diamond (BDD) was created to influence the electrochemical detection of Mercury (204). The model has been established as follows:

First, the electrode design and layout were sketched, consisting of the recessed disk electrodes for DO sensing and the pH sensitive IrO_x ring disposed at distance *d*. The bulk was modelled as a large block with an open boundary of dimensions much larger than the sensor chip to allow the diffusion boundary to progress. Second, the generation of protons is modelled by a flux *J* at the WE surface. Here, equation 6.2 is used to compute the amount of protons generated across the electrode area, *A*. The model proceeds by computing the diffusional flux extending outwards into the bulk and across the pH sensor using the regular diffusion equations for a non-convective system. The resulting pH gradient under the application of 50 µA of current is depicted in Figure 6.2 for an unbuffered solution at t = 1 s.

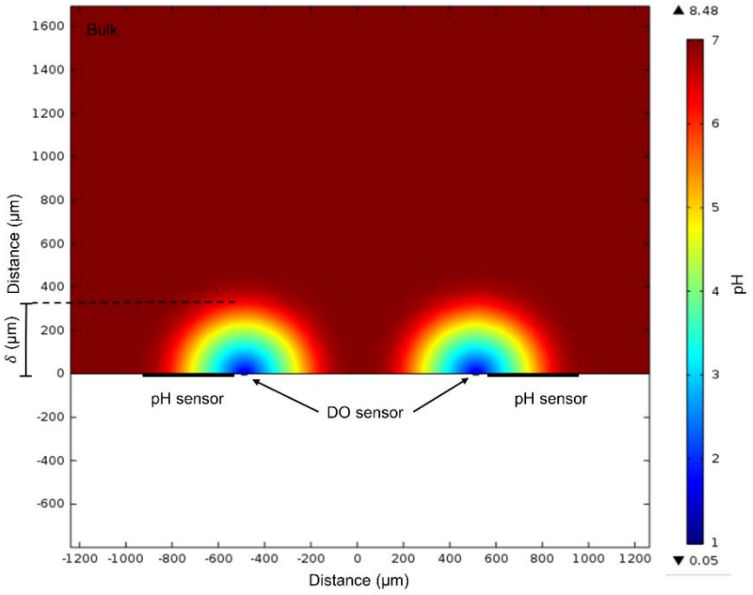

Figure 6.2 - Generated pH gradient for sensor Type-C1 at t = 1 s and I = 50 µA in an unbuffered solution. The influx of protons from the DO sensor causes a diffusion boundary to extend across the pH sensor surface over time. Indicated is the progression of the diffusion boundary δ.

$$J = \frac{I}{AF} \qquad (eq.6.2)$$

To obtain the pH value a line-average across the surface of the pH sensor is taken and plotted over time. The result is shown in Figure 6.3. The shape of the graph can be explained as follows: at t = 0 the pH is equal to the pH of the bulk. As the current is applied the boundary progresses and reaches across the pH sensor surface causing a drop in pH which continues as long as the current is applied. Over time a steady-state is reached; this state resembles the steady-state diffusion described in Chapter 4. Here, the pH will not change anymore unless the current is increased. A rough comparison of the pH change can be made by computing the volume of the formed hemisphere, using the boundary distance as the radius[7]. The generated amount of protons equals 5.2 10^{-10} moles, giving a pH of 3 within the hemisphere. This value is in close agreement with the value at t = 30 s in Figure 6.3.

The above situation describes the case for an unbuffered system. It is clear that if a buffer is present there will be an effect on the pH gradient. The initial influx of protons will still cause a drop in pH. However, as the boundary progresses, the protons become more diluted and the buffer starts to take effect. Thus, to achieve a more accurate model the buffer effect within the bulk has to be accounted for. As the CE is separated from the cell only one half-reaction has to be taken into account, i.e. no interaction between generated protons and hydroxides occurs. The buffer is included by implementing a continuous reaction within the bulk according to equation 6.3, where A^- represents

[7] Recess height is excluded; N equal to 1 disk.

the base, H^+ represents the proton and *HA* represents the conjugate acid. The pH can either be computed using the Henderson-Hasselbalch equation or the concentration of protons directly; both yield the same results.

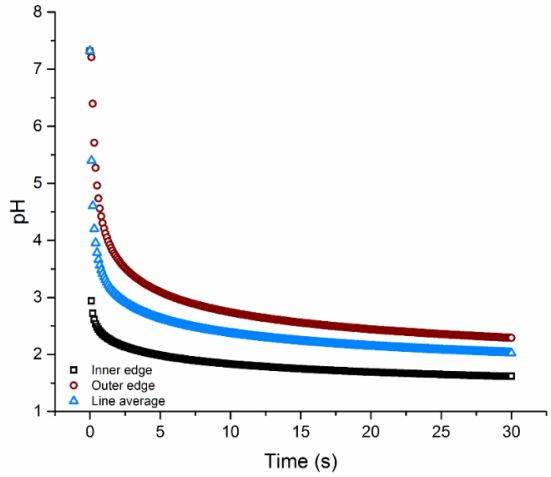

Figure 6.3 – Line-average of the pH across the pH sensor surface for the unbuffered solution. At t = 0 the pH is equal to the bulk pH. As the current is applied the generated protons create a drop in pH which extends outwards. Over time a stabilisation of the pH is observed similar to a diffusion limitation in an electrochemical sensor. Here the pH does not change any further and resembles a steady-state.

$$H^+ + A^- \rightleftarrows HA \qquad (eq.6.3)$$

Figure 6.4 shows the effect of the influx of protons on the inner edge of the pH sensitive ring electrode. As can be seen, with the influx of protons the concentration of the base decreases and the concentration of the conjugated acid increases. It should be noted here that the initial value of the pH is used as the initial concentration of protons. Additionally, the concentration of the buffer has been set equal to that of 1x PBS (see Appendix D1). These parameters have to be included in the model for it to compute the correct pH and thus some preliminary knowledge of the bulk solution is required.

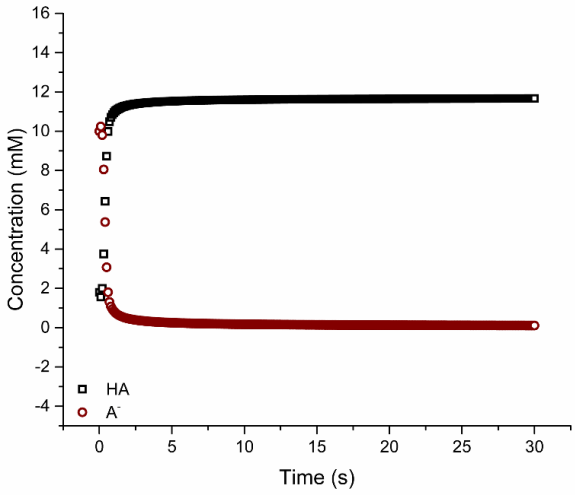

Figure 6.4 – Example of a simulation profile showing the buffer reaction within the bulk at the inner edge of the pH sensitive electrode. As protons are generated the amount of base (A^-) decreases and the amount of conjugated acid (*HA*) increases.

The model contains limitations which have to be resolved in the future work to obtain more accurate estimates of the pH, especially at short time scales. These limitations are:

1. Migration within the electric field;
2. pH limitation based on water and complex buffers;
3. Convective effects.

1. It is known that the application of an electric field has an effect on the ionic mobility as explained by proton hopping. The apparent diffusion coefficient is therefore likely to be higher than its normal value of $9.31 \cdot 10^{-9}$ m^2 s^{-1}. The effect of the electric field is not implemented in this model.

2. The model does not account for external, environmental factors such as the buffering effect of carbon dioxide in the air. These can be implemented in a similar manner as equation 6.3 but have not been included in this work.

3. Convective effects are ignored in the current model. In practice, convection occurs in many forms, most commonly due to movement. This has been observed whilst performing optical measurements on the generated pH change. Residual convection by changing of the cables, and placing the sensors in the vessels is also common.

It should also be stated that the effect of the CE is currently ignored and with it the electrochemical reaction occurring there. In practice, the current can only be sustained in a two-electrode system as long as the electrons lost are transferred to the CE i.e. the reaction at the generating electrode could be limited by the reaction at the CE. The current model does not take this effect into account. Further complications would arise from the fact that diffusion of hydroxide around the sensor will have an effect on the pH. This is currently ignored in both the model and experimental conditions. The latter is achieved by using a separated CE within the vessel of much larger size than the on-chip CE.

From the discussed model, two procedures for calibrating the pH sensor on-chip are proposed:

1. Steady-state calibration;
2. Differential pH calibration.

1. The most accurate and direct calibration method consist of injecting the current for the entirety of the time period until the mass-transport equilibrium of the boundary with the bulk has been reached, across the surface of the pH sensor. This will give a fixed pH for both the acidic and alkaline generation and will make sure the limitations of the model are of minimal effect.

2. From the simulation model a pH versus time diagram at a given distance is computed. In theory, for any given time a change in pH is obtained. A differential pH measurement between two time periods of generation can be used to estimate the sensitivity of the pH electrode. The disadvantage is

that inaccuracies in the model and experimental conditions will cause the two curves to differ. Furthermore, the initial pH and buffer capacity of the solution have to be well known in order to determine the change correctly.

6.1.3 Materials and methods

For the first experiments EIROF pH electrodes, sensor Type-C1, were fabricated according to the process described in Chapter 5. A power supply (*Alvatek*) was used to control the potential between the on-chip generating electrode and a separate Pt counter electrode, constructed from a platinised glass wafer piece. A commercial single junction RE was used for the experiments. The current through the system was controlled by means of a resistor is series, and recorded using a multi-meter (*TENMA*). The potential of the EIROF sensor was measured using a PalmSense3 potentiostat in OCP mode or a NI DAQ 6211.

For the optical mapping of the pH generation a solution of 0.01% w/v fluorescein was prepared in 1x PBS. A fluorescent microscope was used to record the intensity over time; image processing was performed using *ImageJ*. Note that all experiments were conducted without forced convection in the system during generation of the local pH change, as this would interfere with the diffusion boundary. Commercial buffers were used to obtain the EIROF calibration curves prior to the experiments.

6.1.4 Self-calibration results and discussion

To monitor the pH change, a disk electrode on-chip was fixed inside a Petri dish and the change in pH observed using a fluorescence microscope using a solution of fluorescein. Fluorescein is a pH sensitive fluorophore which shows a decrease in intensity with increasing acidity (205). **Error! Reference source not found.** depicts an exemplar image of the intensity of the fluorescence during a pH generation cycle at 1.5 V with 50 µA of current.

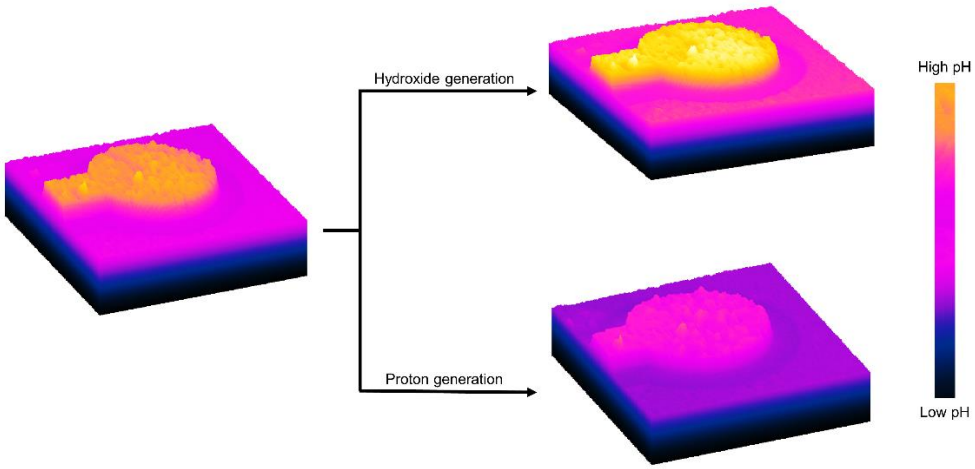

Figure 6.5 - Illustrative example of pH change toward more alkaline or acidic values through the generation of hydroxides or protons, respectively. Gradient represents the change in fluorescent intensity.

From the image it is clear that as the pH goes up an increase in intensity across the electrode surface is observed. Vice versa, a decrease is observed when the pH goes down. An accurate quantification was found to be problematic, due to the fact that the bulk also fluoresces, making it difficult to quantify different measurement cycles versus a calibration. Furthermore, as the microscope stage is moved convective waves are generated across the surface which flush away the generated pH; the same applies when hydrogen gas is generated on the electrode during the generation cycle. Bleaching is also an occurring phenomena and only allowed measurements of the intensity at 10 s intervals. Therefore these images serve an illustrative purpose to show that a change is being generated local to the electrode.

An electrically generated, local pH change was established in 1x PBS. The results are shown in Figure 6.6.a. Figure 6.6.b. shows a comparison based on the change in pH for three pulses compared to the line-average from the simulation. From the figures it is noticeable that the change in pH is highly reproducible over time. A slight drift from the initial generation is observed during consecutive cycles, but reduces as the process is repeated. However, the change is faster than predicated by the model. A possible explanation for this is that the current supplied by the power supply is not constant. As the system is a non-ideal current source, a fluctuating current is observed. Additionally, as the load in series is not constant (a reaction dependent electrochemical cell) the potential has to be continuously adjusted, increasing the current value beyond the aimed 25 µA for short periods of time. Second, the line average taken in the model might not be a true representation of the entire system, as discussed by the limitations in section 6.2. A further optimisation is needed to compensate for this difference. Towards the steady-state, at $t \geq 25$ s, the curves match and show a similar, relative pH (ΔpH) change as predicted by the model.

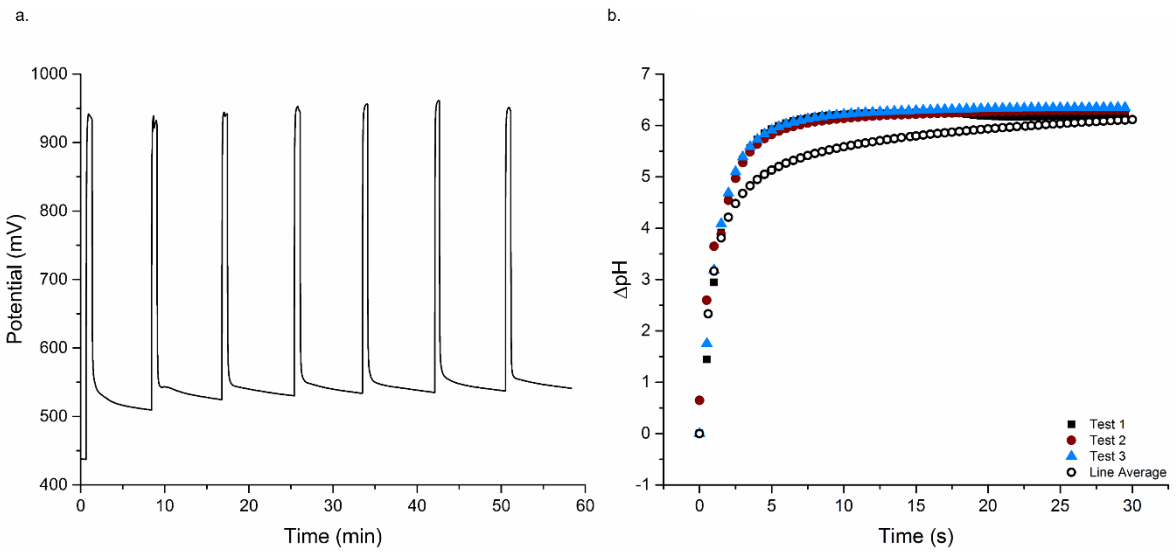

Figure 6.6 – Local pH change on electrode of Type-C1 with 25 µA of current injection in 1x PBS with pH = 7.7. Sensitivity determined prior to experiment as 74.1 mV pH^{-1}. a) Repeated changes in potential upon the injection of the current. b) Comparison between the generated and predicted pH change.

Due to the time difference between measured and simulated pH change it is difficult to perform a calibration on the transient part of the curve. However, the steady-state calibration values can be measured. To determine the sensitivity of the pH sensor pH gradients were generated in commercial buffers of pH 4, 7 and 9. As shown in Figure 6.7, the change in pH is highly reproducible over time. The resulting calibration plots of sensitivity (*S*), were obtained by taking the pH at steady-state as predicted by the model. In other words, the peak potentials are set as the predicted steady-state pH at t = 30 s. The initial pH value is chosen based on the pH measured using a commercial glass pH probe or by using the value of the commercial buffer solution. The results of the linear regression fit are listed in table Table ***6.1***.

Table 6.1 – Results of the linear fit for different buffers

	Sensitivity based on buffer	**Sensitivity based on pH probe**
pH 4	69.5 mV pH^{-1}	78.8 mV pH^{-1}
pH 7	70.2 mV pH^{-1}	68.6 mV pH^{-1}
pH 9	78.1 mV pH^{-1}	71.3 mV pH^{-1}

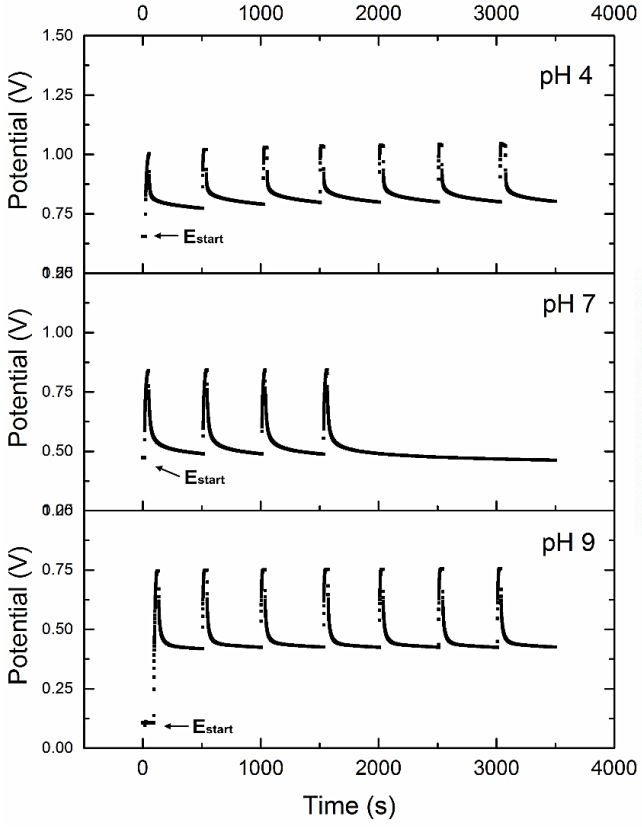

Figure 6.7 – Local change across pH sensor surface in three different commercial buffers. The calibration curve is based on the relative pH change in steady-state, taking either the commercial buffer value or the measured pH value using a glass pH probe.

Comparing these values to the predetermined sensitivity value of 74.7 mV pH^{-1} for the commercial buffer values and 67.8 mV pH^{-1} for the measured pH. It is clear that there is a degree of error, however the sensitivities registered using the on-chip calibration are within a similar range as those determined in Chapter 5. It is therefore potentially possible to use this method to derive an up-to-date value of the sensitivity.

Even though the sensitivity is predictable using an on-chip calibration, it is more important that the formal potential of the linear regression fit can be re-established. As explained in Chapter 5, the formal potential shows the largest variation over time. An interesting observation during the course of the experiments can be made both in Figure 6.6 and Figure 6.7. As seen in these figures, prior to each proton generating cycle there is a start potential (E_{start}). This potential is the value recorded prior to the experiment to determine the stability of the EIROF sensor during its hydration period.

Interestingly, when the generation of protons is halted and the system left to re-equilibrate and the potential allowed to decay back to that associated with the bulk pH, a different value is observed. This decay poses a problem for a potential on-chip calibration. As the return potential is not the same as E_{start}, the initial value cannot be taken as the start pH from which ΔpH is determined. However, it is observed that these decay curves show a high degree of reproducibility across the time frame. What is remarkable is that in all instances, in all buffer solutions, this observation holds. This raises an interesting question on the pH sensing properties of the EIROF used in this work. As the data indicates, there seems to be a reconditioning of the surface towards a fixed state upon the generation of a pH gradient across the IrO_x surface.

It can be hypothesised that, as the pH within the diffusion boundary is low, the hydroxyl groups within the metal oxide lattice become saturated. A stated in Chapter 5, the metal-metal oxide layer is porous, so it is likely that the surface becomes protonated throughout. It could even be hypothesised that the pH sensor is brought to its limit of detection from which it then decays towards the equilibrium state representing the bulk pH. In some degree, this is comparable to the initial hydration period required for the sensors to achieve optimal performance.

If this hypothesis is true, then if a boundary of high pH is created i.e. hydroxides, the surface should become more hydroxylated and attain a different equilibrium state. As shown in Figure 6.8.a, by changing the polarity across WE and CE, an alkaline pH change is generated. Indicated in the figure is the positive polarisation for proton generation and the negative polarisation for hydroxide generation. The resulting decay curves are presented in Figure 6.8.b. It is clear that when hydroxide is generated in abundance, a different equilibrium state is achieved. Starting from a low potential associated with that of alkaline pH values.

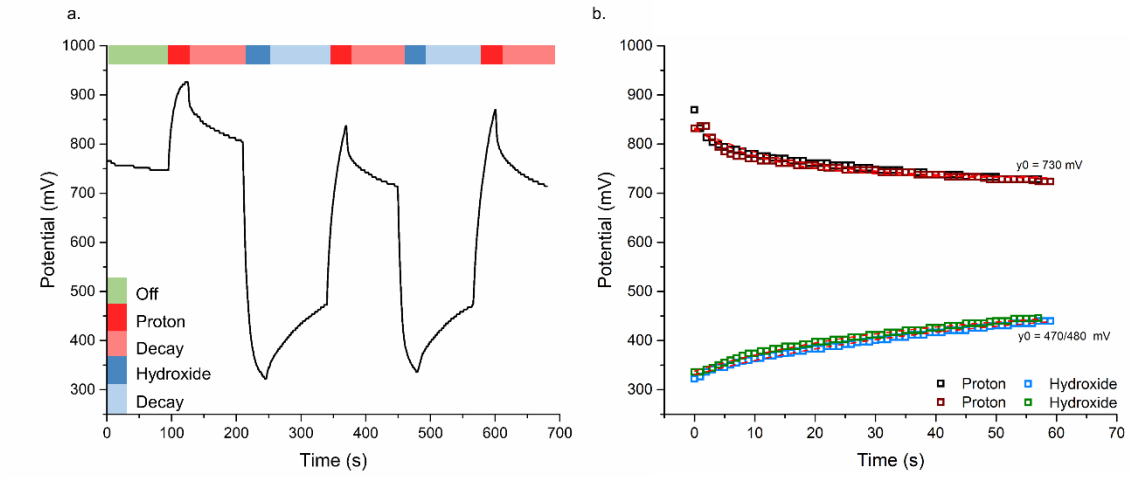

Figure 6.8 - Overview of the generation and decay of an influx of protons and hydrides across the IrO_x sensor surface. b) Selected decay curves (excluding first) fitted to a second order exponential. The value for the y-offset *y0* is indicated in the figure.

No accounts of this effect have been found in literature, however interesting accounts exist on the electrochemical activation of solid Iridium films. It is common to activate formed surfaces using solutions of H_2SO_4 (191, 206, 207). Although this is used to form the hydrous oxide, a parallel can be drawn between using these low pH conditions and the artificial bulk generated in this work. *Carroll et al.* reports on a similar form of reconditioning by applying a potential of 200 mV directly to the formed surface. It relies on the claim made by *Hitchman* that the application of a potential can recondition the surface by increasing its oxidation state from Ir^{3+} to Ir^{4+} (191, 201).

It could thus be postulated that: a fit based on the decay curve could predict the state that will be achieved, coming from a reproducible potential after conditioning in a low pH boundary. In contrast to the previously described method, this is independent on the value of E_{start}. This provides an unconventional means of recalibrating and even measuring pH using EIROF sensors. To prove this concept, a pH sensor as depicted in Figure 6.9 was constructed using a pH sensing EIROF-on-Au disk centred within a Platinum ring used as the proton generating electrode.

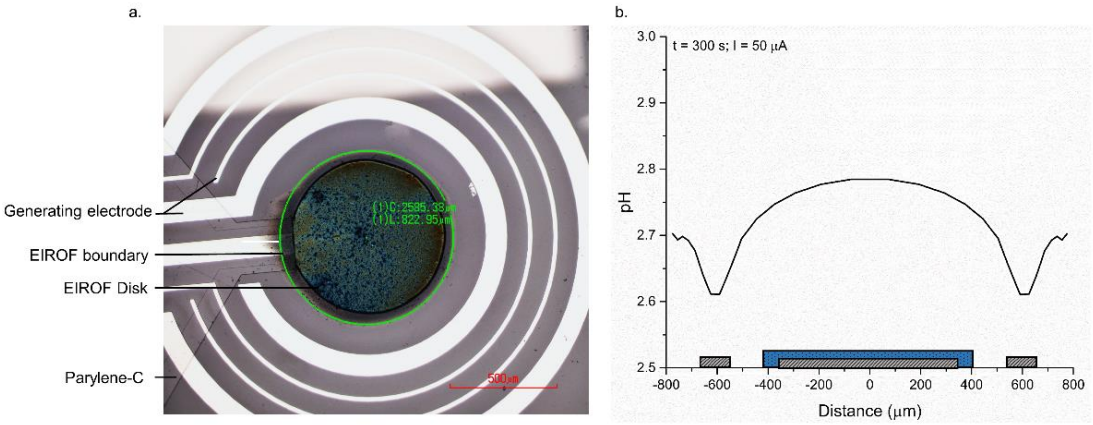

Figure 6.9 – a) Microscope image of the EIROF-on-Au disk centred within a Platinum generator electrode. b) Simulated curve at 300 s with 50 µA of current in 1x PBS.

Figure 6.10.a shows repeated proton generation with a sourced current of 50 µA in 1x PBS, pH 7.4. Figure 6.10.b shows the resulting decay curves from the individual pulses. As seen, they are highly reproducible. Figure 6.10.c depicts a single decay curve fitted with a second order exponential decay function. The shape of the curve and motivation behind this fitting could be explained using the pH sensing theory of IrO_x.

Starting from the steady-state it can be reasonably assumed that the main process which governs the drop in potential is caused by the diffusive and convective forces away from the surface of the pH sensing electrode. Additionally, the buffer within the bulk solution will diffuse towards the electrode surface contributing to the decay. The diffusional flux follows an exponential decay function as described by Fick's law of diffusion. The shape will follow similar diffusion equations as shown for one-dimension in equation 6.4. Where *C* is the concentration; *x* the distance; *D* the diffusion coefficient. Thus, the observed curvature should show a mass-transport limitation.

$$C\ (x,t) = C\ \mathrm{erf}\left(\frac{x}{2\sqrt{Dt}}\right) \qquad (eq.6.4)$$

From this point onwards, a slow diffusional process dominates which at prolonged time can be expected to turn into a linear drift, similar to that observed in the IrO_x sensors. Most likely, this has the characteristics of a second exponential decay, as illustrated by the hydration effect in Chapter 5.

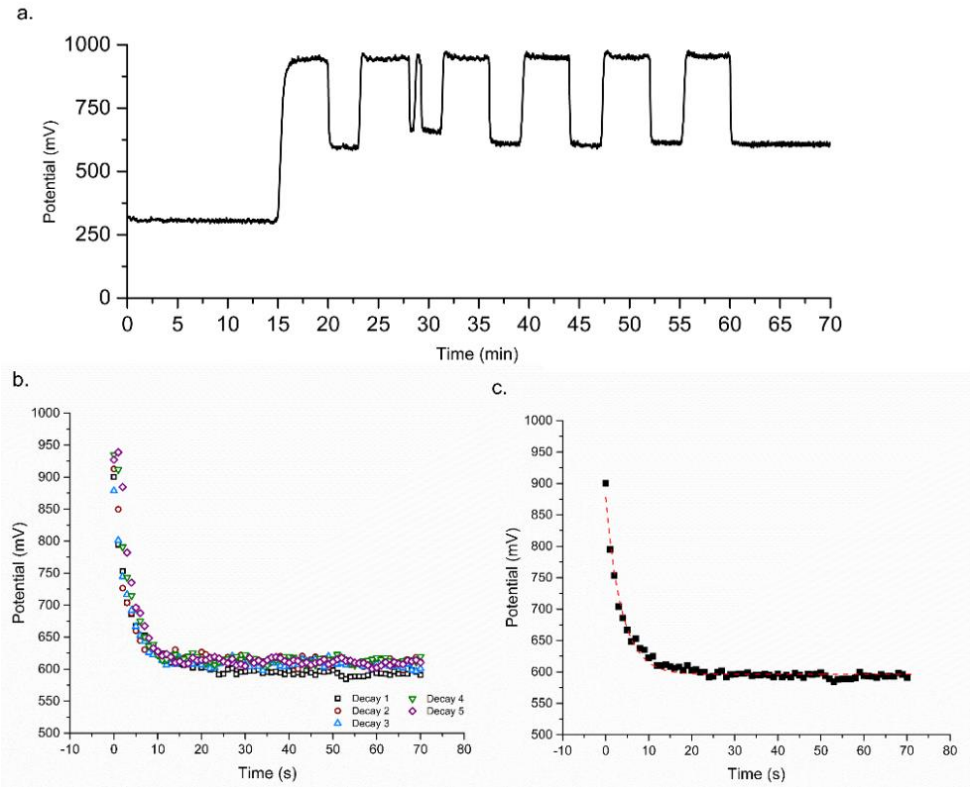

Figure 6.10 – a) Repeated generation of protons sensed across EIROF-on-Au disk. b) Decay curves for all pulses, excluding the second, starting from the steady-state potential after 30 s of sourced current. c) Example of a single decay curve fitted using a 2nd order exponential decay function.

Based on the profile of these decay curves, second order exponential fits were made and the potential of the asymptote, $y_{0,}$ was determined. The results are listed in Table 6.2. Also presented, is the value for the steady-state potential (E_{ss}). The sensitivity of the pH sensor was determined prior to the experiment and equalled 71.5 mV pH^{-1}. As discussed in Chapter 5, the sensitivity is relatively constant over the time period. As such, this value was used to determine the difference in pH (ΔpH) between E_{ss} and y_0. This difference in measured pH is then added to the steady-state pH value predicted by the simulation model for 1x PBS. As can be seen from the results in Table 6.2, an average pH of 7.50 ± 0.08 pH is obtained. Compared to the expected value for 1x PBS, a similar degree of accuracy is achieved, compared to the conventional EIROF calibration procedure.

Further confirmation is gained when Figure 6.6 is assessed in retrospect. The results are listed in Table 6.2. It has to be noted that since these experiments were not conducted for this purpose it is debatable how well they apply in this situation. However, it is clear that there is a high degree of reproducibility between E_{ss} and $y_{0.}$ Thus even though the pH value is not as accurate the precision is high.

Table 6.2 – On-chip calibration results based on decay curve method.

	y_0 (mV)	E_{ss} (mV)	ΔpH	pH_{sim}+ ΔpH	Error
Figure 6.10	596.0	943.1	4.85	7.55	0.14
	610.4	946.4	4.70	7.40	0.01
	602.9	949.5	4.85	7.55	0.14
	613.6	950.4	4.71	7.41	0.00
	607.3	955.3	4.87	7.57	0.16
Figure 6.6	554.3	941.9	5.19	7.95	0.18
	559.6	944.3	5.15	7.91	0.14
	562.5	955.4	5.26	8.02	0.25
	568.3	960.6	5.25	8.01	0.24
	561.2	947.1	5.17	7.92	0.16

Considering the same method yields similar results to those described in Chapter 5, especially with regard to reproducibility across different sensor geometries and pH values, it can be concluded that further investigation of this measurement principle is worthwhile. It could even be hypothesised that, if accurate models can be made for the decay curve, the buffer capacity of the solution could be determined using different generation currents. However, at the moment this is solely based on speculation. Long-term measurements employing this type of re-calibration and sensing will show whether the method is feasible for intrauterine use. Currently, the method cannot be implemented into the IUSD due to its high power consumption, required to source the current needed for the electrolysis reaction. In theory, the current could be reduced to achieve low power consumption and

the model adjusted accordingly. All of these aspects will have to be further investigated in the future work, as discussed in Chapter 7.

6.2 Biocompatibility

The biocompatibility of implantable medical devices is a major requirement to assess an implants' impact on the human body. In cases where the implanted device is in contact with the reproductive organs, extra care and assessment of cytotoxicity are required. When considering the complete IUSD, the human body is exposed to the implant in three ways: direct contact, diffusion, leakage. As stated in the ISO-10993 legislation documents on biocompatibility studies for medical devices:

"Biological evaluation of medical devices is performed to determine the acceptability of any potential adverse biological response resulting from contact of the component materials of the device with the body. The device materials should not, either directly (e.g., via surface-bound chemicals or physical properties) or through the release of their material constituents: (i) produce adverse local or systemic effects; (ii) be carcinogenic; or (iii) produce adverse reproductive and/or developmental effects, unless it can be determined that the benefits of the use of that material outweigh the risks associated with an adverse biological response" – ISO: 10993:5, *p.4* (208).

The direct contact area for the individual sensor dies is small. However, components of the sensor can leach out during the implantation period either through diffusion, effusion and device failure. By catching possible cytotoxic issues, at the sensor development level, problems during the legislation stage are prevented and safety measures can be put in place.

6.2.1 Biocompatibility assessment

As discussed within this work, the sensors contain a wide variety of components. During their development care has been taken to select materials which have been shown to exert limited cytotoxicity towards the human body. However, the cytotoxicity does not solely rely on the material but also on the materials and methods used to synthesise the components of the sensor device. The listed materials can be categorised into two subgroups: electrode materials and polymer-gels, respectively. The first consists of rare earth metals including Platinum, Silver and Iridium oxide and are used to achieve the sensors functionality. Because the polymers used within this work contain cross-linkers that are toxic in nature, as discussed in Chapter 3, proper assessment of their cytotoxic effect on organisms is needed.

Table 6.3 shows a summary of the sensor components. The toxicity of the components as found in literature is listed (note that references are given in text), as well as the biological application and duration of the test. Two main methods of assessing the cytotoxicity of materials are used: extraction and direct contact tests. For the first, material samples are incubated and left to extract for time

periods determined in *ISO 19033:5*. For long-term implantable devices (implantation times exceeding two weeks) a 72 hours extraction is required. During this period components leech into the media, which is then exposed to cells in culture. For the latter, the material sample is placed in direct contact with the cells in culture. As can denoted from Table 6.3, information on the cytotoxic effects on uterine cells is lacking and as such needs to be assessed in more detail. Therefore, the biocompatibility tests discussed here, have been performed on human endometrial epithelial cells.

Table 6.3 - List of components, their toxicity and purpose, used to fabricate the sensor device.

	Duration	**Method**	**Cell type**	**Toxicity**
Pt	72 hours	Extraction	Derma fibroblast	Biocompatible
IrO_x	-	Extraction	Neurons	Biocompatible
Ag	72 hours	-	Endometrial epithelial	Biocompatible[1]
Ag-Cl	2 hours	Direct contact	Vascular	Inconclusive
CS	24 hours	Direct contact	Uterus	Biocompatible
Gp	24 hours	Extraction	Osteoblasts; Hepatoma	Toxic[2]

6.2.2 Materials and methods

Human epithelial endometrial cells (HEC-1A, *ATCC*) originating from an adenocarcinoma from a 71 year-old female were used for the experiments. Culturing was performed using *McCoy's 5A* medium (30-2007, *ATCC*), specifically tailored for culturing the HEC-1A cell-line. The culture media is supplemented with 10% fetal bovine serum (FBS) and 1% penicillin-streptomycin (P4333, *Sigma-Aldrich*). Cells were maintained in culture for up to 20 passages, after which the cell-line was discarded and restarted form the frozen samples created from the second passage. Cells were incubated at 37 ^{0}C, under 5% carbon dioxide.

Samples were prepared according to *ISO 19033:5*. As shown in Table 6.4, the requirement for the componential testing is a surface-area dependent test that considers only the interfacing area of the device-under-test. The thickness of the individual sensor dies equals 600 µm; the device falls in second category and requires an area-to-volume ratio of 3 cm^2 mL^{-1}. To perform an extraction test in this manner fifteen sensors (sized 2.3 x 4.3 mm) were needed, as only the top of the electrodes is interfaced with the environment. To achieve an accurate representation of the sensor device the individual areas for each of the components on a single sensor die were determined i.e. the area of the parts containing Platinum, IrO_x, Ag-AgCl etc. In the case of Ag the same area was taken as for the AgCl to represent the scenario in which conversion fails, or the AgCl has been lost during measurement.

As the fabrication of 15 individual sensor dies is impractical and does not fit within a 1 mL volume, the area of each component was multiplied by the number of sensors *N*, equal to 15 with the inclusion of a safety factor, *SF*, set as 1.5. The total area can be determined according to equation 7.1. Platinised wafer pieces were used to create equally sized components through the deposition of the different materials using the methods discussed in the previous chapters. For the deposition of IrO_x, Ag and AgCl deposition times were extended until uniform coverage was achieved across the sample. Samples were autoclaved at 123 ^{0}C for 21 minutes and kept in aseptic conditions until used. The extract was created by immersing the samples into the predetermined volume of culture media. A serial dilution of 100, 50, 25, 12.5 and 6.25% v/v was created from each extract.

$$A_{tot.} = SF \cdot N \cdot A_{mat.} \text{ (eq. 7.1)}$$

Table 6.4 - Extraction ratio from *ISO19033:12* (208).

Thickness	Extraction ratio
≤ 0.5 mm	6.00 cm^2 mL^{-1}
≥ 0.5 mm	3.00 cm^2 mL^{-1}
< 1.0 mm	3.00 cm^2 mL^{-1}
> 1.0 mm	1.25 cm^2 mL^{-1}

6.2.3 Cytotoxicity assay

To test the biocompatibility a tetrazolium, 3-(4,5-dimethylthiozolyl-2)-2, 5-diphenyltertrazolium bromide (MTT) cell proliferation assay (30-1010K, *ATCC*) was used. The assay measures the proliferation rate of cells, which is indicative for cell viability and cytotoxicity. The MTT is reduced by metabolically active cells via the hydrogenase enzymes nicotinamide adenine dinucleotide (NADH and NADPH). The reductant is the insoluble formazan crystal, which is purple in colour and forms inside the active cells. The crystals can be re-dissolved and quantified using spectrophotometric means (209). An overview of the process is depicted in Figure 6.11.

For the assay, $1 \cdot 10^5$ cells (optimised) were cultured in a 96-well plate. For each step in the serial dilution triplicates were used. The negative control represents cells exposed only to normal culture media. The positive control represents cells exposed to 10% ethanol. An additional Cupper (Cu) extraction (12.5% v/v) was also included in the assay. By adding the Cu as a control, the proper operation of the assay can be checked as Cu is highly toxic to cells. Blank wells, containing only culture media were used to correct for background in the absorbance measurements.

The extracts were added on top of the cells, after removal of the culture medium. The well plate was returned to an incubator and left for 24 hours. After the exposure period, the extracts were removed

and a 100 µL of fresh medium was added. Next, 10 µL of the MTT reagent was added, followed by an incubation period of three hours. To re-dissolve the formazan crystals 100 µL of detergent was added, followed by an incubation period of four hours. After, the plate was read with a *Promega Glomax* plate reader at 550 and 780 nm wavelengths. The relative growth rate (RGR) was determined for all triplicates according to the following sequence:

1. Subtraction of the 560 nm reference reading per well;
2. Subtraction of the blank well average;
3. Division by the negative control average;
4. Average of the triplicates for each dilution in the series.

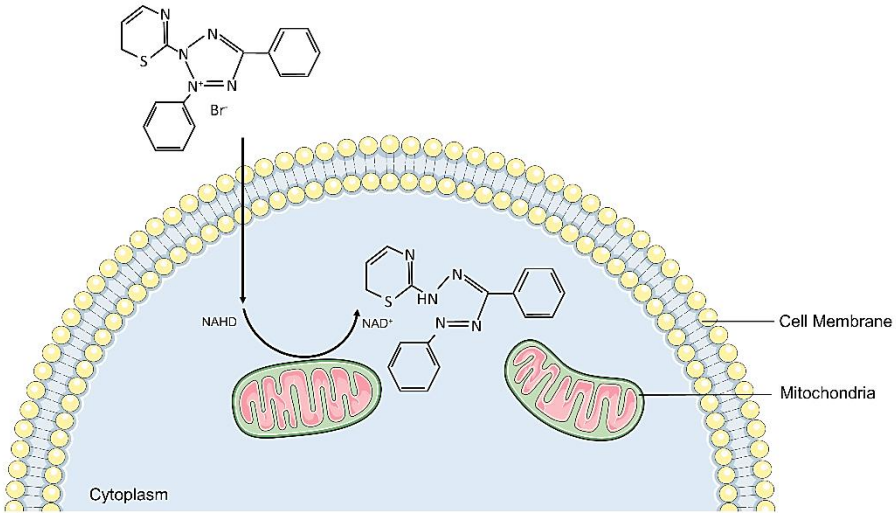

Figure 6.11 - Overview of the mitochondrial reductase of MTT into formazan. The active cells reduce the MTT through dehydrogenase enzymes, forming the formazan crystals within the cytoplasm.

6.2.4 Biocompatibility results and discussion

The cell proliferation has been performed for each of the sensor components. In most cases it relates to a combination of materials as present after the fabrication of the sensor. For all of the deposited metals a glass-substrate with a 20 nm Ti and 200 nm Pt layer was used. The electrolyte hydrogels were tested as individual components after cross-linking. The results from the assay are compared to the findings in Table 6.3.

Titanium-Platinum-IrOx

Geninatti et al. assessed the cytotoxicity of Platinum electrodes for adult derma fibroblasts (210). Extractions were performed with Pt electrodes for up to 72 hours. It was found that the proliferation rate of the human fibroblast cell line was not affected by the Pt extracts (n = 9 for all dilutions in the series). The results for the study on HEC-1A, as presented in Figure 6.12.a, are in good accordance

with this find. In all cases, no effect on the cell proliferation is observed, whereas both the Cu and positive control indicate cell death.

The biocompatibility of IrO_x has been assessed for *in situ* applications. IrO_x has a wide use as neuronal interface. Both *Tahnawala et al.* and *Goebbels et al.* grew neurons onto IrO_x films and assessed their viability (211, 212). In both cases, the viability of the cells was determined by visual means, based on cell count. Both studies concluded that there was no observably negative effect on the cell growth when the neurons were grown on IrO_x films. The extraction tests performed, as shown in Figure 6.12.b, shows that for all dilutions (n = 9) the RGR is higher than the negative control which indicates no cytotoxicity.

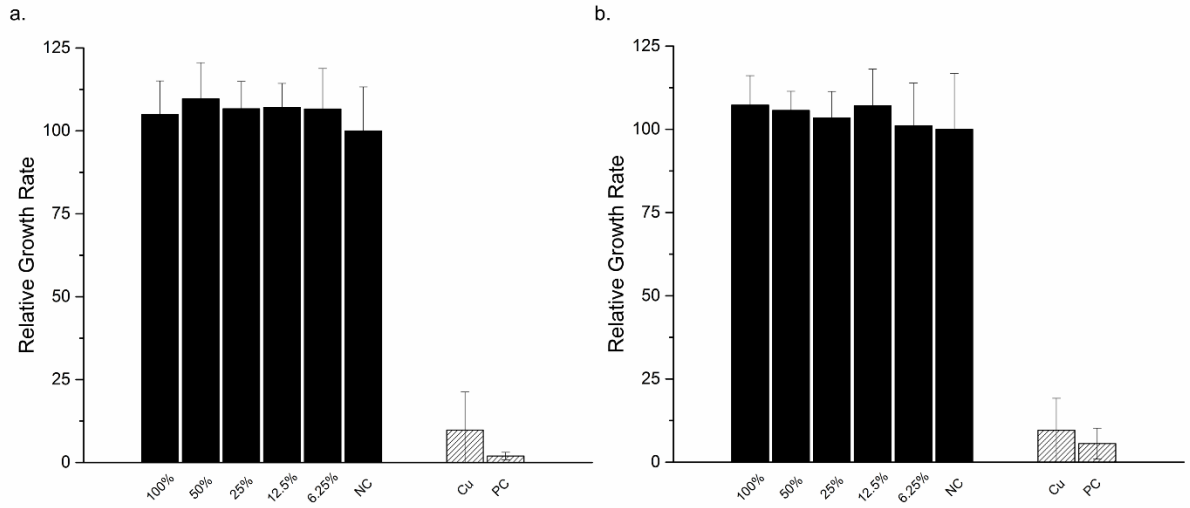

Figure 6.12 - Results from the extraction test (72 hours) using an MTT-assay for a) Ti-Pt and b) IrOx on Ti-Pt. No significant decrease in relative growth rate, which would indicate cytotoxicity, is observed for the cells exposed to the extracts; n=9 for all dilutions in the series.

Titanium-Platinum-Silver-Silver chloride

The cytotoxicity of silver has been shown to be concentration dependent. As discussed in the study by *Wu et al.* in which human endometrial epithelial cells were exposed to different extracts of silver (0 to 50 µM L^{-1} with 5 µM L^{-1} increments) for up to 72 hours (213). Concentrations exceeding 30 µM L^{-1} where found to effect cell viability drastically. *Hardes et al.* performed a direct contact study with osteosarcoma cell-lines. Silver powder in different quantities (5 to 25 mg with an increment of 5 mg) was exposed to the cells in culture for 48 hours. It was found that at low dosage i.e. 5 mg, the proliferation rate of the cells was above the cut-off with values of 77% and 87.7% (214).

For the Ag-AgCl, limited research has been performed on its cytotoxicity for *in vivo* applications. *Jackson et al.* tested its effects using direct contact between vascular smooth muscle and a Ag-AgCl RE. The exposed tissue was challenged at hourly intervals with a vasoactive stimulus. As a control,

exposure to Ag and AgCl wire was included in the test. It was found that cells exposed to components containing Ag lost responsiveness to the stimulant within two hours (215).

Figure 6.13.a shows the results for the HEC-1A cells exposed to silver extracts (n = 9 for all dilutions in the series). Overall, no cytotoxicity is observed in the quantities present on the sensor die. Figure 6.13.b shows the results for the Ag-AgCl (n = 9 for all dilutions in the series). Again, little to no effect on the growth rate is observed. Interestingly, the two graphs show similar trends with a slight increase in growth rate compared to 100% for the 50, 25 and 12.5% dilutions. The difference is approximately 1.3%. This confirms that the cytotoxicity, although of no significant impact, is related to the Ag present on the electrode.

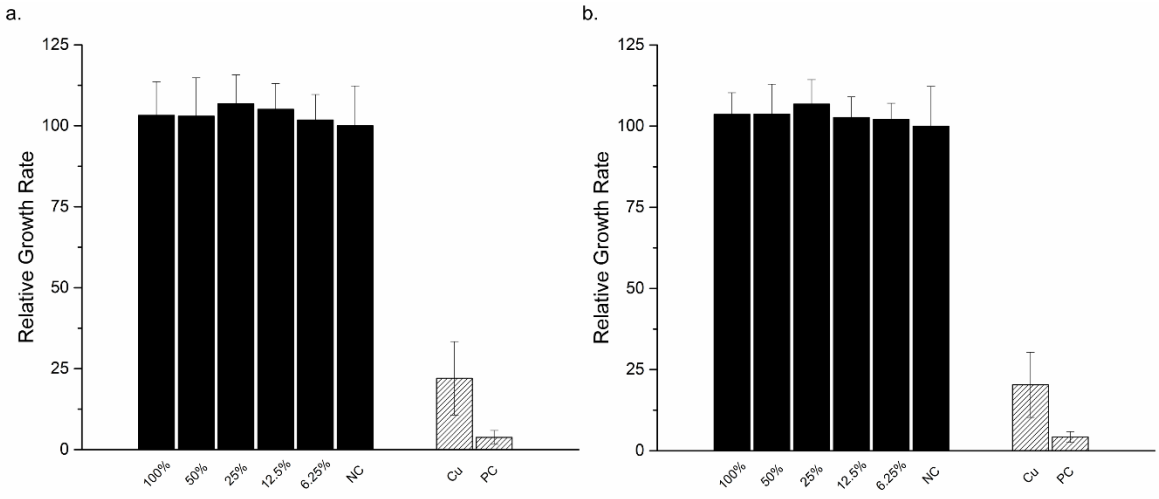

Figure 6.13 - Results from the extraction test (72 hours) using an MTT assay for a) Ag and b) Ag-AgCl on Ti-Pt. No significant decrease in relative growth rate, which would indicate cytotoxicity, is observed for the cells exposed to the extracts; n = 9 for all dilutions in the series. Note that there is a high degree of similarity between the graphs.

Genipin-Chitosan hydrogel

As discussed in Chapter 3, CS is a common material in biomedical applications. *Schmid et al.* investigated the use of chitosan-covered gause for intrauterine *post partum* haemorrhage in a clinical setting. Nineteen patients were treated with the gauze and in all but one, the bleeding was stopped. The gauze was left in utero for over 30 hours. Overall, no side effects due to the use of chitosan was found (216). Within the developed hydrogel, the most toxic component is the cross-linker. Although genipin is a natural cross-linker with a lower toxicity than other, non-natural cross-linkers, it can still be toxic in high dosage, as studied by *Wang et al.*, the effects of Gp on human fetal osteoblasts and primary chrondrocytes from porcine articular cartilage. Different concentration of Gp-media were prepared ranging from 0.5% - 0.0001%. It was found that there exists a dose dependent cytotoxic effect starting from concentrations exceeding 0.5 mM (217). Results obtained by *Kim et al.* also confirm these findings but here the cytotoxic effect were already observed at 200 µM (218).

Figure 6.14 depicts the results from the MTT-assay for a Gp-CS gel with a Gp concentration of approximately 200 µM. Although within the cut-off for being non-toxic, there is a significant effect of the gel on the HEC-1A cells for the 100% extraction. This is in good accordance with the findings discussed above. It should be noted that, due to the 1.5 safety factor, the cytotoxic effect within the actual sample size will be closer to the 50% dilution. In any case, the amount of cross-linker currently used, should not be exceeded.

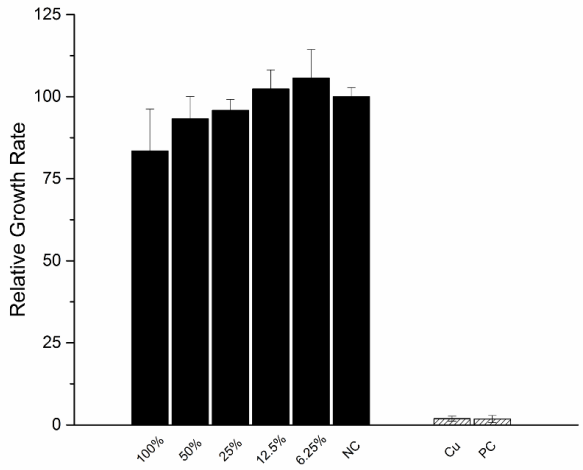

Figure 6.14 - Results from the extraction test (72 hours) using an MTT-assay for Gp cross-linked CS (200 µM). A decrease in relative growth rate is observed for the cells exposed to higher concentrations of the extracts; n = 6 for all dilutions in the series. The cytotoxic effect is above the 70% cut-off for all dilution in the series.

6.3 Device packaging

The packaging of implantable sensors is a challenge easily overlooked when considering research aspects of a sensor device. The sensing areas need to be interfaced with the *in vivo* environment via a window in the encapsulation of the IUSD. This poses a challenge for the manufacturing process, especially when the footprint of the sensor is small. The aim is to have a final device, similar to conventional intrauterine devices as the discussed in Chapter 1, with functioning sensors incorporated into the complete package.

An overview of the device components is shown in Figure 6.15. Here, the antenna for the communication and power transfer and the PCB with the electronics need to be interfaced with the sensor. Henceforth, the term ‘sensor package’ refers to the packaging of the individual sensor die; the term ‘encapsulation’ refers to the entirety of the IUSD including antenna, PCB and sensor head, which consists of the sensor package. The sensor package has been investigated separately. Discussed in this chapter is the development of a sensor package capable of maintaining its function with an on-board RE. The designs and data presented in this chapter are of a qualitative nature, relying on trial-and-error, rather than measurement data. The aim of the development process is: to develop a sensor packaging method which can be incorporated in the encapsulation and can be scaled towards a mass-manufacturing process.

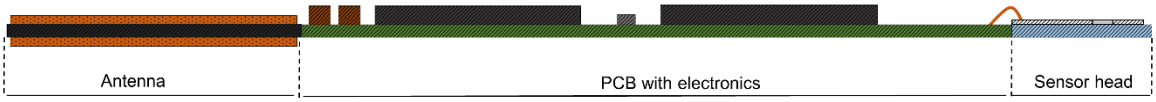

Figure 6.15 – Overview of the implantable platform and its major components. The sensor head needs to be packaged and connected to be incorporated in the encapsulation of the complete device, which contains the PCB with electronics and the antenna for data communication and power transfer.

6.3.1 Packaging time-line

The development of the sensor package has been a continuously evolving process throughout the course of this work. A wide variety of design iterations have been developed and tested. For the sensors the following critical functions, to be fulfilled by the sensor package, can be listed:

1. Hold both sensors and the RE;
2. Be able to connect to pads from the PCB;
3. Able to contain a hydrogel and keep it hydrated;
4. Electrolytic contact between sensors;
5. Scalable packaging process.

1, 2: The sensors are fabricated separately from the PCB. Therefore, an interconnect between sensor and PCB needs to be devised. Ideally, a modular approach to this problem is taken in which the sensors can be attached in a plug-and-play manner prior to an over-moulding process.

3, 4: As discussed in Chapter 3, the developed hydrogel has to be incorporated in the package. It is key that the internal concentration of chloride is maintained as long as possible. An injection of the electrolyte in one of the final steps of the fabrication process is considered most suitable. In addition to its function for the RE, the electrolyte forms the contact between the back and front side of the sensor die by means of a junction. It is therefore imperative that the formation of air pockets during injection is prevented.

The aspects discussed here formed the main guideline for the sensor package. An overview of the time-line of the sensor packages is shown in Figure 6.16; only the major design changes are shown.

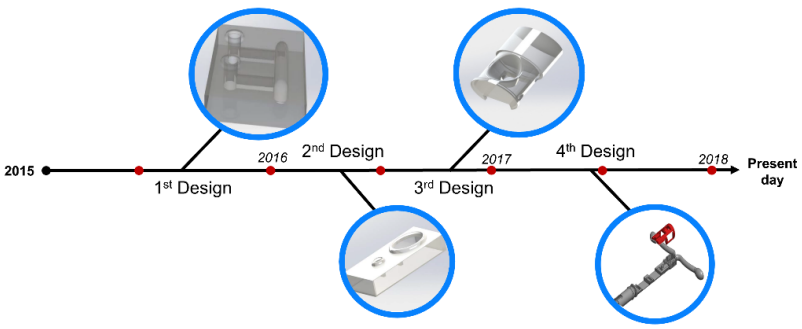

Figure 6.16 - Time-line of the sensor package development. Four major design milestones have occurred starting from individual sensor packages towards a fully encapsulated sensor package and system.

6.3.2 The first design

In the early stage of this research a single sided DO sensor of Type-A was considered first (size 4 x 8 mm). Here, the reference electrode is situated next to the CE as explained in Chapter 2. To contain the electrolyte, a PDMS channel was envisioned. The sensor package, illustrated in Figure 6.17, has an internal channel with an inlet and outlet, to be filled with the electrolyte. The key concept is the addition of an O-ring formed on top of the injection inlets. Employing the deformability of medical grade polydimethylsiloxane (MG-PDMS), pressure on the ring forms an anti-flashing seal during the encapsulation step.

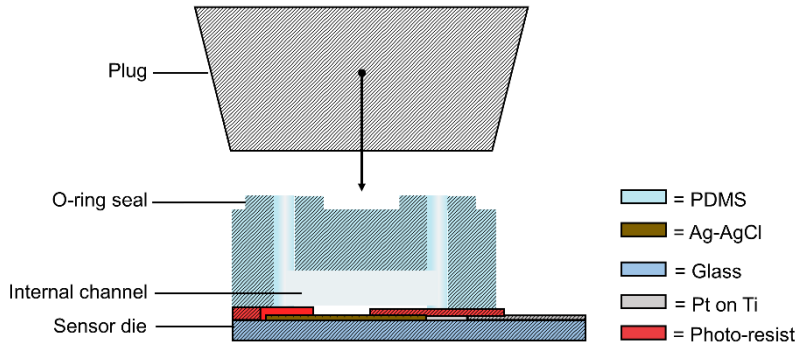

Figure 6.17 - First sensor package design. A medical grade PDMS piece is cast via moulding. An internal channel, accessible via an inlet and outlet channel is used to contain the electrolyte. The cast piece is bonded to the sensor die. The addition of a deformable O-ring structure on top of the inlet creates a seal during the encapsulation of the complete system by applying pressure to the plug in the encapsulation tool.

The channel structure and O-ring are formed through mould casting of MG-PDMS. The design model is depicted in Figure 6.18.a. The formed package was bonded to the sensor die using an oxygen plasma treatment of the PDMS and sensor prior to bonding. The contact pads were kept clear to connect the sensor to the PCB. The internal channel and salt-bridge were filled with the hydrogel after connection and encapsulation. This could be achieved because the O-ring kept the inlets clear of encapsulant. An image of the channel bonded to a glass substrate and filled with an agarose gel is shown in Figure 6.18.b. The advantage of this system is that, because the channel is internal, soft gels such as agarose and alginate can be used (not discussed in this work), as the electrolyte is protected by the MG-PDMS. The cytotoxicity of the Ag-AgCl is limited by the internal channel as no direct contact exists.

Experiments with the first design exposed two major problems: yield and scalability. The overall yield was poor due to bonding issues. The limited interfacial area for bonding onto the sensor die caused poor adhesion across the surface, which resulted in leaks. Further implementation of both sensors on a single chip was difficult to achieve with this type of package as even less of the area was available for bonding. This is problematic during the encapsulation of the complete IUSD as the forces during injection moulding would cause delamination. With the future down-scaling in mind,

these issues would make this type of package unfeasible. In summary, the list of criteria and the results from the experiments are listed in Table ***6.5***.

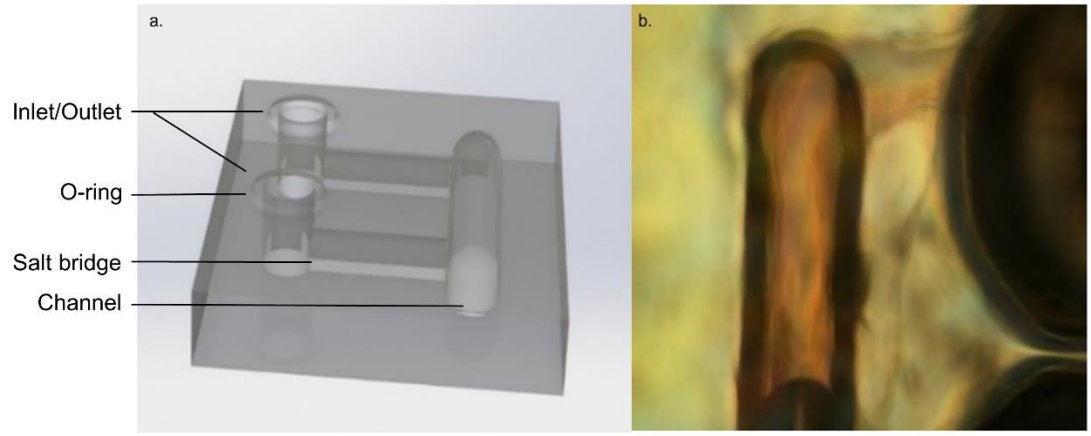

Figure 6.18 - a) Design drawing and (b) cast PDMS piece of the first design for the sensor package. Sensor package bonded to a glass slide and filled with agarose gel containing red food dye. The injection can be performed after full encapsulation of the system

Table 6.5 - List of criteria for the first sensor package.

Criteria	Rating
Hold both sensors	no
Be able to connect to pads from the PCB	yes
Able to contain hydrogel and keep it hydrated	yes
Electrolytic contact between sensors	yes
Scalable packaging process	no

6.3.3 The second design

The second design was based on a conventional integrated circuit package. A planar sensor package, in which the sensor was fixed, was developed. The design model is depicted in Figure 6.19.a. Here, a window has been opened above the electrodes in the lid. The electrolyte cavity is formed by the spacing between the top cover and the sensor. The un-polymerised solution can be added into the package either before encapsulation or after, by incorporating an injection inlet in the design. The addition of an O-ring in the lid served the same purpose as in the first design. An image of a sensor of Type-A, situated inside a 3D-printed package with inlet and outlet is shown in Figure 6.19.b and c.

The gel is directly interfaced with the environment, thus a higher strength hydrogel was required: pAm gel. Additional concerns regarding the cytotoxicity had to be considered in this case, as discussed in Chapter 3. The inclusion of a membrane, stretched across the window, could help in

limiting toxic components from reaching the intrauterine environment. However, it would be imperative that the membrane was uniformly stretched to prevent errors in the DO measurements through bubble formation and accumulation; this was found to be challenging.

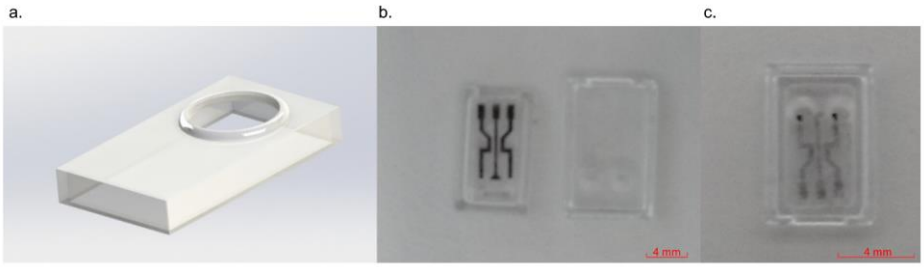

Figure 6.19 - a) Design model of the second design. An integrated circuit type sensor package consisting of a bottom piece which holds the sensor and a top lid. The window in the lid creates the contact between the sensor and the uterine environment. An O-ring surrounds the inlet to create an anti-flashing seal during encapsulation. b) Image of a sensor Type-A fixed inside a 3D-printed sensor package. c) Image of a sensor of Type-A contained within the sensor package. Two inlets for injection of the electrolyte are created in the lid.

Although the fabrication of this type of package was easy and less prone to alignment errors, it was discovered during the scaling towards sensor Type-B that the pAm gel would not be able to set as the volume decreases during further scaling. As discussed, this is caused by the reduced amount of polymer solution. Moreover, the 3D-printed material was not impermeable to oxygen. For the scalability of the process, a custom design in which the sensors is wire-bonded within an epoxy-type package would be needed, which is costly for the first versions of the IUSD device. Because of the box-type structure the footprint of the sensor increased with the width of the side walls which was problematic when the diameter of the IUSD was to be kept within the range of conventional IUDs. In summary, the list of criteria and the results from the experiments are listed in Table 6.6.

6.3.4 The third design

For the third design the shape of the package was altered to a coherent, tubular shape with respect to the rest of the encapsulant. As illustrated in Figure 6.20.a, the sensors were fixed inside a sensor package which could attached to the PCB. The sensor dies were stuck together with fast cure epoxy and slid inside the package with the contact pads extending outside the package in order to achieve the interconnect. The dead-space around the top was used to contain the electrolyte required for the RE, which is also situated on the top. A membrane could then be fixed at the top of the package to prevent leaking of the gel into its surroundings and limit cytotoxicity.

During its development it was found that the increased diffusion distance with the electrolyte positioned at the top of the electrode interferes with the sampling time. As the volume of the gel, situated on top of the sensor, and more importantly the height of it was increased a time delay is imposed on the sensor response. Similar to Clark electrodes, the time delay is caused by the increase in diffusional length related to the height of the package. A variety of iterations were performed to

overcome the time-delay issues by reducing this distance. An example iteration is shown in Figure 6.20.b. Here, the sides of the top package were tapered down towards the WE. Hence, a shorter sample interval can be achieved at the cost of the internal volume of the cavity. An example of a fully packaged sensor of Type-B is shown in Figure 6.21.a-c.

Table 6.6 - List of criteria for the second sensor package.

Criteria	Rating
Hold both sensors	no
Be able to connect to pads from the PCB	yes
Able to contain hydrogel and keep it hydrated	yes
Have electrical contact between sensors	yes
Scalable packaging process	partially

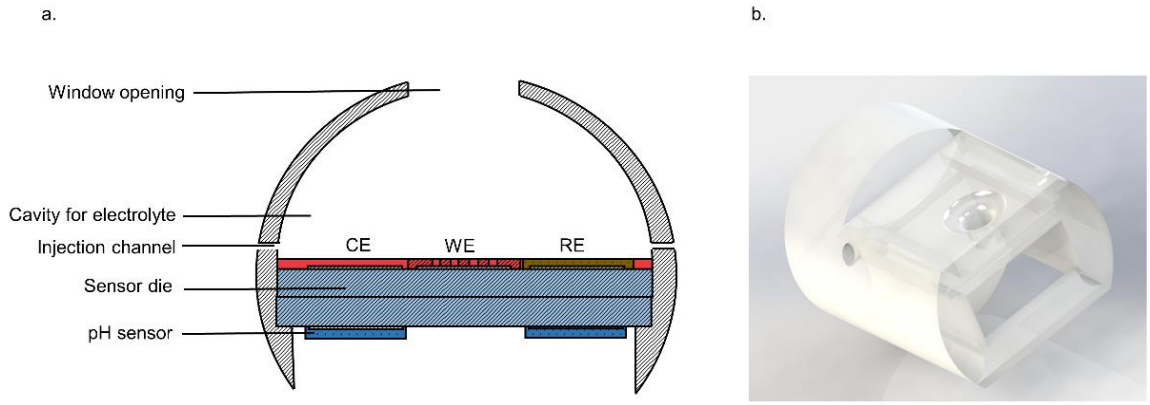

Figure 6.20 - a) Cross-section of the third design containing two sensor dies stuck together and slid inside the sensor package. The empty space on top of the DO sensor, consisting of a CE, WE and RE, is filled with the electrolyte via the injection channels. These are later sealed during the encapsulation process. The pH sensor is situated on the bottom of the package. b) Tapered iteration of the third design where the diffusion distance towards the WE is reduced by sloping the side walls down to the electrode surface.

In practice, it was found difficult to maintain accurate spacing and inclusion of a membrane was near impossible. For the encapsulation, the sensor package would be over-moulded in a later processing step. This required the electrolyte to be injected before encapsulation, which made it difficult to keep the hydrogel hydrated. In summary, the list of criteria and the results from the experiments are listed in Table 6.7.

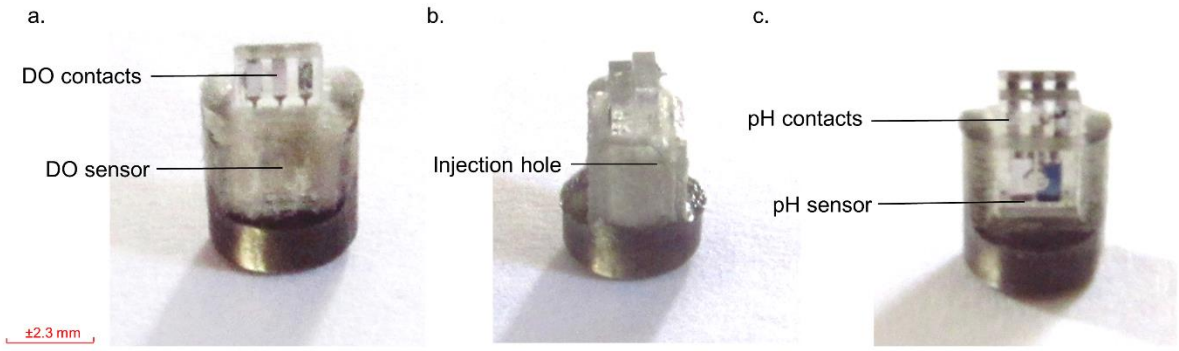

Figure 6.21 - a) Top side image, b) side image, c) bottom side image of a dual function DO and pH sensor fixed inside a 3D-printed sensor package based on the third design. The contacts for both DO and pH sensor extend outside of the package for the connection to the PCB. The internal cavity is filled via the injection hole located on the side.

Table 6.7 - List of criteria for the third sensor package.

Criteria	Rating
Hold both sensors	yes
Be able to connect to pads from the PCB	yes
Able to contain hydrogel and keep it hydrated	no
Electrolytic contact between sensors	yes
Scalable packaging process	partially

6.3.5 The fourth design

Based on the findings of both sensor research and packaging development, a complete redesign of the sensor system was proposed. Based on the initial findings of the biocompatibility research, the diffusion modelling and membrane fabrication problems, it was chosen to discard the inclusion of a membrane. As discussed, there has been no indication of any cytotoxic effects on the surrounding cells. The sensor design itself was also altered. Instead of fabricating all sensors on a single-sided wafer, a double-sided design was proposed: sensor Type-C. Here, the RE and CE were situated on the back side. The electrolyte would be injected into the cavity via an inlets and outlet, which were to be closed during the encapsulation process. An illustration of the design is depicted in Figure 6.22.a. By relocating the RE, the time delay associated with the electrolyte on top of the electrode was removed. Furthermore, the dead space on the back-side of the sensor package was used to store the electrolyte, creating a larger volume. A junction inside the glass substrate was envisioned to slow down the loss of chloride into the uterine environment allowing for drift prediction on the RE potential.

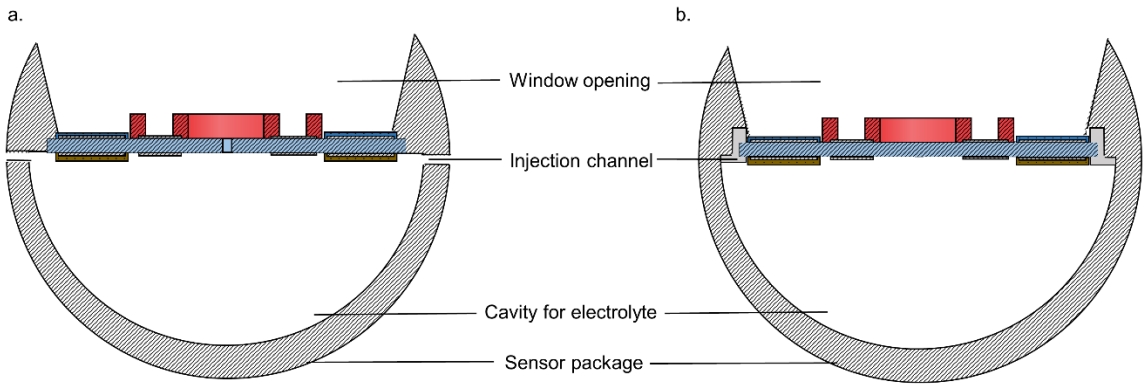

Figure 6.22 - Cross-section of the fourth sensor package design containing a double-sided sensor chip. The RE is located on the back side of the chip which removes the time delay present in the previous designs. a) Connection between the back and front is made via an aperture in the glass substrate. b) Connection between the front and back is made via two channels located at the sides of the sensor die.

As discussed in chapter 3, the volume and size of the aperture is critical to maintain a constant drift over time. The challenge here was to create the small aperture inside a thick glass substrate. Although efforts were been made in creating such a through-hole, no successes have been booked yet. A compromise design was developed in which the junction is formed at the sides of the sensor die. The injection of the gel is performed through inlets from the top side of the sensor package. An illustration is shown in Figure 6.22.b. Here, the junction is of larger size which results in pseudo-setup behaviour. This has to be taken into account during the long-term measurements *in utero*. Shown in Table 6.8 are the criteria as met by the fourth design.

Table 6.8 - List of criteria for the fourth sensor package.

Criteria	**Rating**
Hold both sensors	yes
Be able to connect to pads from the PCB	yes
Able to contain hydrogel and keep it hydrated	yes
Electrolytic contact between sensors	yes
Scalable packaging process	yes

The fourth design had been shown feasible and reproducible enough for further optimisation. The compromised design has led to the development of a proper encapsulation process in collaboration with *Vivoplex* to reach a fully functional prototype. The sensor package of design four has been redesigned as a clip-on frame as illustrated in Figure 6.23.

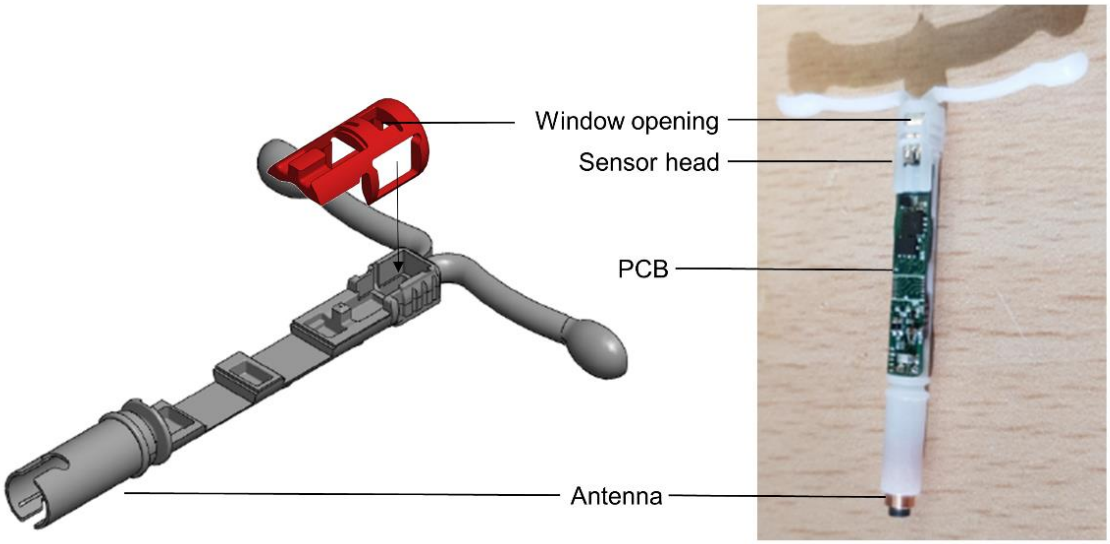

Figure 6.23 - Design model as developed by *Vivoplex ltd.* based on the fourth design. A frame is used to position the antenna, PCB and sensor dies. A clip-on structure is used to create the window on top of the electrode. The cavity for the electrolyte is defined within the structure of the sensor head.

The resulting final device, encapsulated in medical grade PDMS is depicted in Figure 6.24. The injection moulding has been performed by *Vivoplex* and is achieved via an optimised injection moulding process. The integrated sensor head contains the sensors developed in this work assembled into the pocket and chassis. The internal pocket of the sensor chip is filled with the electrolyte gel prior to implantation. The complete device shown here is currently being used in animal studies and will proceed into the legislative testing and certification, allowing the device to be used as a new diagnostic tool for sub-fertility.

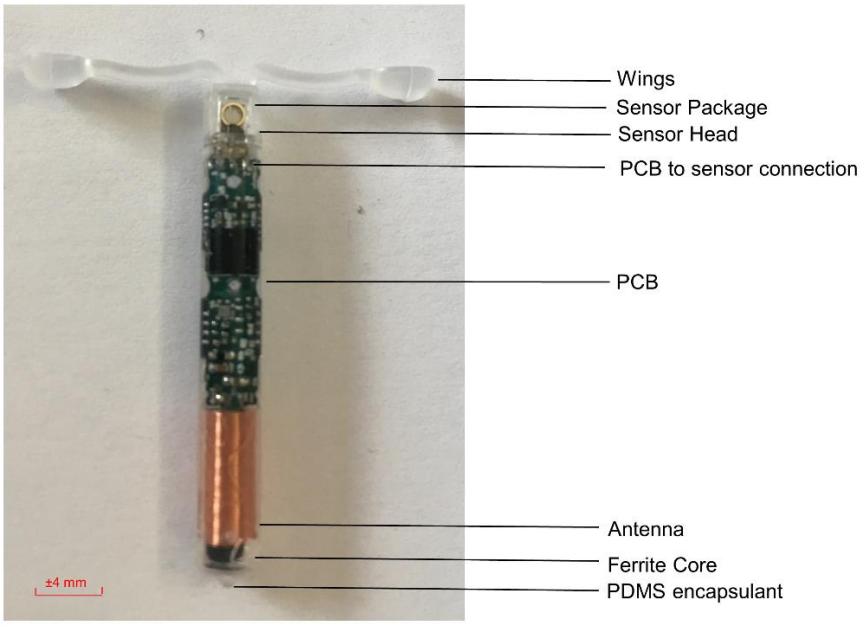

Figure 6.24 – Final encapsulated IUSD in medical grade PDMS for animal trials. Consisting of sensor package with added wing for positioning of the device *in utero*. The PCB contains the electronics for the analogue front-end and the data communication link. An antenna with Ferrite core is used to achieve the wireless data and power transmission.

6.4 Summary

This chapter discussed the theory and practice of a novel on-chip calibration method to improve the accuracy of the metal oxide pH sensor during the course of the implantation period. By utilising the generated by-products during the electrolysis of water local pH changes are generated. The pH boundary generated in this manner extends outwards according to the diffusion principles. A *ComSol* model has been developed and tested, taking into account the buffer capacity of the bulk solution. The obtained pH versus time plots at a set current and for a given geometry can be computed in this manner. It has been shown that the sensed change in pH follows an exponential decay curve reaching a steady-state over time. The pre-determined pH value at this point can be used to obtain a new calibration curve for the given sensor.

Repeated observations of a fixed, limiting pH value, have led to an unconventional method of recalibration in which the decay of the potential versus time diagram is used to obtain the difference in pH. Both the steady-state potential and decay curves show high reproducibility. It has been hypothesised that this consistency is caused by the high degree of protonation and hydroxylation within the Iridium oxide surface, effectively reconditioning its sensing properties. Results indicate that it is feasible to obtain a similar degree of accuracy as established with conventional pH sensing methods proposed in this work.

The biocompatibility of the sensor components has been assessed. Each of the individual components were tested for cytotoxicity according to *ISO 19033:5*. Human endometrial cells were cultured and exposed to a serial dilutions of extracts obtained from the sensor components. From the list of materials none of the components showed cytotoxic effects. In all cases, the cut-off (viability below 70%) was never reached. Only in the case of 100%, undiluted extract of the Gp-CS hydrogel, was a decrease in cell viability observed.

Throughout the course of this work a sensor package for future device integration into the IUSD has been developed in parallel. Four major designs have been fabricated and tested for their potential use. The designs were prototyped and assessed based on key criteria which included: connection to the PCB, inclusion of a hydrogel, ionic conductivity between sensors and RE, scalability. From the experience gained during the sensor development process, a final design consisting of a double sided sensor die contained within a tubular package was proposed. Here, the internal space within the package is used to contain the electrolyte for the RE. A future implementation of an aperture, in order to limit the efflux of chloride, can be implemented in the design to achieve full RE performance. The design has been further developed by *Vivoplex*.

Chapter 7 -Conclusions and future work

7.1 Conclusion

This report discussed the need for and development of a novel *in vivo* sensing platform for intrauterine studies and subfertility diagnostics. Couples are increasingly being confronted with subfertility issues without a clearly established reason. It is therefore of great importance to find a method to determine the underlying cause. As current diagnostic tools are unable to provide in depth information on the female reproductive system and in particular the uterus, new means are required. It is thought that, the intrauterine environment and within it the endometrium, is of influence on the success rate in female conception. Studies have shown that physiological parameters such as dissolved oxygen and pH greatly influence the process of implantation and development of the embryo. Empirical data from *in vitro* fertilisation studies confirms that embryo development is influenced by variations in DO concentrations. Lower concentrations providing the best environment for embryonic development. The pH of the media has also been shown to be of influence, and is estimated to be optimal in a range of pH 6 and 8. It is hypothesised that, the subfertility issues stated, are caused by abnormalities in these physiological parameter in the intrauterine environment. However, to-date no means exist to confirm these claims.

As the endometrium experiences cyclical changes i.e. menstrual cycle, a diagnostics tool capable of providing data continuously during this cycle (30 days) would be of great benefit. An ideal platform to perform such a task is an implantable sensor system. This thesis described the development of a multi-parameter sensor system, capable of measuring DO and pH unobtrusively for prolonged periods of time. The sensors have been developed in conjunction with an on-board miniature RE. All have been assessed on their performance for both the sort- and long-term. The hypothesis in this work has tried to show that it is feasible to develop a DO and pH sensor capable of acquiring biologically relevant data, unobtrusively, for long time periods. The system is to be implemented in an IUSD, previously developed at the UoS.

For both pH and DO sensing, an on-board miniature RE had to be developed and implemented. It should provide a stable potential during the 30 day period. A miniature Ag-AgCl RE has been developed in this work which meets the size and biocompatibility requirements. A layer of Ag was deposited by means of electroplating in an optimised process. The Ag was converted into Ag-AgCl using constant current conditions in 3 M KCl. Its performance has been assessed versus a commercial RE. Long-term pseudo-setup measurements have shown excellent performance with long-term drift values below 1 mV day^{-1} for a large sample size. The overall yield of the fabrication method equals 64.5%. By implementing a quality control check for long-term performance over a 40 day course the yield is increased to 90%.

In order to create a full RE, insensitive to external changes of the chloride concentration, hydrogels were investigated. First, pAm hydrogels were tested for their applicability. Although good performance was initially observed, the smaller footprint of the second iteration of sensors made it difficult to ensure cross-linking. This impaired the biocompatibility requirement of the RE. A less toxic gel in the form of Gp-CS was developed and tested. Although the gel performed well in a pseudo-setup, no added benefit in regards to the loss of chloride was observed. This also applied to the addition of a *Nafion*® membrane. Results from simulation models showed that the most likely way to obtain a full RE was through the clever design of the sensor and its package. Proposed in this work is a double sided sensor die in which a small aperture is created. The aperture (10 µm) ensures that a predictable drift can be maintained over the measurement period.

For the DO sensor, arrays of Platinum disk microelectrodes recessed within a layer of photoresist were fabricated and tested. By using microelectrodes to measure the DOC the low power constraint posed by the IUSD is met. Furthermore, it reduces the degree of perturbation within the uterus. By implementing the recessed electrode structures one-dimensional diffusion is maintained. This allows read-out at the 50 ms scale without the need for signal amplification. A simulation model was used to obtain estimates on the expected current values and calibration curves. Three recess heights have been tested and compared: 5, 25, 55 µm. A conditioning procedure to maintain a reproducible electrode surface state was developed and implemented. Overall, a good agreement with the model was observed. For the 55 µm recess, tapering of the walls was observed causing non-linearity in the diffusion profile. However, all sensors still showed proper response to DO.

Long-term measurements were shown to be problematic. During prolonged measurement periods delamination of the photoresists was observed; noticeable by fringes and rings around the disks. It was found that similar failures occurred when sensors were exposed to hydrogen peroxide overnight. Additionally, the application of a negative current, generating hydrogen gas at the WE surface, caused the same effect. It has been postulated that the continuous measurement of DO, in which hydrogen peroxide is formed as an intermediate, caused delamination of the photoresist. A variety of photoresists were tested to see if adhesion could be improved. Only Parylene-C showed no delamination under these extreme test conditions. A long-term test was conducted with this type of electrode. Although the life-time was extended, similar observations were made for measurement periods beyond one week. It is clear from this work that the use of this type of electrode for long-term measurements is not ideal. However, the performance of the DO sensor did show that values of 0.5 mg L^{-1} can be distinguished. Although this is slightly higher than the 0.4 mg L^{-1} required, it is acceptable considering no other means exist to assess DO *in utero*.

For the pH sensor metal-metal oxide electrodes were created using the Pt electrodes as a substrate. IrO_x was deposited thermally forming TIROF, or electrochemically forming (EIROF). Short-term experiments with the TIROF electrodes showed good performance in agreement with literature. Nernstian sensitivities were obtained with an accuracy of 0.24 pH. The long-term experiments showed good performance. The sensitivity showed little to no variation over the course of 4 weeks. Drift values below 0.02 pH day^{-1} over the course of 40 days were observed. In contrast, the EIROF pH sensor showed a super-Nernstian response. Short-term performance indicated a higher accuracy compared to TIROF due to the increased sensitivity. Long-term performance showed negligible drift on the sensitivity. Drift values were determined as 1 - 1.5 mV day^{-1}. The sample size for the EIROF sensors is still small, so estimates on yield have not been made.

Form the results obtained during the pH sensor development it was clear that the accuracy is determined by the initial calibration taken prior to long-term use. In order to limit the degree of inaccuracy a novel on-chip calibration method was developed. Here, the pH change generated at electrode surfaces during the electrolysis of water was employed. By applying a positive current an influx of protons could be created locally. The diffusion gradient established in this manner, could be sensed with the EIROF pH sensor. A model was made to predict the change in pH under the application of a current. By estimating the pH over time, the current state of the pH sensor could be obtained. An interesting proposal was made for an unconventional approach to this form self-calibration. Based on the experimental data, it could be concluded that once the pH conditions were generated a stable, highly reproducible decay was observed. As was shown in this work, this state could be predicted and used to derive the pH of the bulk solution with a similar accuracy as normal pH sensing.

The materials used to manufacture the sensors were tested for their biocompatibility. For an implantable device, biocompatibility is the key criterion. HEC-1A cells were exposed to extract of the materials and their viability was determined after a 24 hour exposure period. None of the materials used showed signs of cytotoxic effects. In parallel to the sensor development designs and prototypes of sensor packages had been made. The sensor package holds the sensors and the electrolyte for the RE. Four main designs were manufactured and tested in the course of this work. The final design has been presented and includes the future implementation of the RE aperture to achieve full RE performance.

In conclusion, this work has shown that a single sensor die, sized 2.3 x 4.3 mm containing a pH sensor, DO sensor and miniature RE can be developed. Although improvements on the DO sensor are needed, the pH sensor and RE have shown excellent performance. With the knowledge gained during the DO development new concepts for long-term monitoring *in utero* have already been devised. As the sensor development has continuously kept the future device packaging, integration

and biocompatibility in mind, it can be said confidently that the sensors presented here will be used to help couples achieve their dream.

7.2 Future work

Although the results obtained in this work have shown the feasibility of creating miniature sensors capable of measuring unobtrusively *in utero* for long periods of time, there are still challenges that have to be overcome. First, the RE developed in this work has shown excellent performance in a pseudo-setup. However, its performance as a full RE has not been obtained. The investigation of a hydrogel electrolyte has shown that it is not possible to maintain a constant concentration of chloride for prolonged periods of time. Therefore, it can be stated that further investigation into these types of polymers, for this purpose, is not advisable. More feasible is the investigation of solid electrolytes as outlined in the literature search in Chapter 4.

Other alternative methods have been proposed. It can safely be said that for an RE operated in an unknown intrauterine environment knowledge on the potential drift is required. One possible way to achieve this is to incorporate a small aperture. The sensors of Type-C developed in this work have been designed for this purpose. However, a method has to be devised to create these apertures in a glass substrate. Alternatively, the substrate material can be changed to polyamide. This flexible material has been used in sensor development. Alternatives to the proposed aperture are possible. One of the most likely alternatives is to create a tortuous path. As the loss of chloride is directly related to the length of the diffusional path, a thin and long junction could maintain the concentration for the required time period. This path can take the form of paper microfluidics, patterned photoresist channels, and hollow glass fibres. Key is that it can be implemented into the sensor package. Parts of these concepts have already been investigated during the course of this work and are feasible, however, more work is needed.

The implementation of a conductivity sensor to elucidate the conductivity of the uterine environment is also beneficial. Considering that intrauterine conductivity is an ‘unknown’ and governs RE performance its value is considered high. A design for this additional sensor has already been made and fabricated, as shown during the on-chip calibration. The electronics for this sensors have to be developed with the low-power requirements in mind. It can be reasonably stated that the resulting RE will be combination of all the aforementioned aspects in which a trade-off between complexity, size and performance will have to be made.

For the DO sensor a new approach to the problem has to be found. Although this work has aimed to create a very specific type of DO sensor, it can be stated that from a practical perspective better performance can be obtained with a simpler design, less prone to fabrication and delamination error. The data has indicated that the use of recessed micro-electrodes is difficult to achieve and is not

worth pursuing considering the limited advantage the extended Cottrell time yields on performance. At the time of writing initial tests with a ring microelectrode have already been performed. Additionally, this thin ring design can serve as the generator electrode for on-chip calibration and as electrodes for a four-point conductivity measurement. A self-calibration method for DO can be incorporated on-chip. Here, oxygen is consumed and generated near its surface in a similar manner to the pH. This principle is easier than the pH calibration as it does not require accurate knowledge of the bulk. Instead, it creates upper and lower DOC limits, based on the conventional ORR.

The pH sensor has shown good performance throughout this work. However, the sample size for the EIROF has to be increased to gain confidence on the predictability of the drift and fabrication yield. An interesting aspect of research would be the investigation of the influence of the substrate materials on the adhesion and performance of the IrO_x sensors. It can be reasonably expected that there has to be an underlying principle that governs the adhesion, and as such the life-time and shelf-life of these devices. An alternative metal-metal oxide based sensor has already been fabricated and tested. This sensor is based on Ruthenium oxide. Its advantage is its shelf-life. A similar characterisation method as employed in this work can be used to determine its performance.

A novel aspect in this work has been the development of an on-chip calibration method. As shown, interesting finds have been made including an unconventional approach to this form of self-calibration. By optimising the model, performing experiments and comparing the two, it could be possible to calibrate the pH sensor. More work is needed to investigate the observed protonation and hydroxylation of the surface. A patent has already been filed for the on-chip calibration method. By improving the model a higher degree of accuracy is expected. For this method to be implemented into the IUSD a reduction in current is needed.

At the time of writing parts of the encapsulation and sensor packaging have been outsourced to external manufacturing companies. By using professional injection moulding tools progress towards an implantable IUSD has been made. The first animal trials on rabbits have taken place as part of a fact finding study. Currently, 6 rabbits have been implanted with an IUSD containing dummy sensors to test encapsulation, and functioning DO sensors and REs. These fact finding studies are critical to properly assess the following aspects:

1. Biofouling during prolonged implantation;
2. RE performance *in utero*;
3. Electrolytic contact from the front to the back side of the sensor die;
4. Toxicity and inflammation caused by the entire implant.

Because the intrauterine environment is unknown, the only means to obtain accurate data on performance is through animal studies. Although short-term animal trials performed in previous with

the IUSD have not shown no indication of biofouling, the results from this work have indicated that short-term performance is not a guarantee for long-term success.

Part of this work and future work will be published in scientific journals in the near future. In particular, the individual chapters on the sensor development of DO and pH will be published. A comparative study between the performances of the recessed disk micro-electrodes can be given in detail which includes comparisons to theory using the established *ComSol* models presented in this work. For the pH sensor a performance evaluation based on long-term data is envisioned including a comparison to the Ruthenium oxide sensor discussed in this section. Finally, the on-chip calibration method (patent pending) will be published once its performance has been assessed in more detail.

References

1. Disposable medical sensor market analysis by product, technology, application and segment forecast to 2020. Grand View Research, 2014 Contract No.: ISBN: 978-1-68038-256-3.

2. Pawar S. Emerging Trends in Medical Diagnosis: A Thrust on Nanotechnology. 2014 21610444 Contract No.: 4.

3. Vashist SK, Venkatesh, A. G., Zengerle, R. Nanotechnology-Based Biosensors and Diagnostics: Technology Push versus Industrial/Healthcare Requirements. BioNanoScience. 2012;2(3):115-26.

4. Beyette FR, Kost, G. J., Weigl, B. H. Point-of-Care Technologies for Health Care. IEEE Transactions Biomedical Engineering. 2011;58(3):732-5.

5. Riesgo T, Juanola-Feliu, E., de la Torre-Arnanz, E. Challenges facing academic research in commercializing event-detector implantable devices for an in-vivo biomedical subcutaneous device for biomedical analysis. 2011;8067:80670P-P-10.

6. Xiayu X, Akay, A., Huilin, W., ShuQi, W. Advances in Smartphone-Based Point-of-Care Diagnostics. Proceedings of the IEEE. 2015;103(2):236-47.

7. Karsten SL, Tarhan, M.C., Kudo, L.C., Collard, D., Fujita, H. Point-of-care (POC) devices by means of advanced MEMS. Talanta. 2015.

8. Goode JA, Rushworth, J. V., Millner, P. A., . Biosensor Regeneration: A Review of Common Techniques and Outcomes. Langmuir : the ACS journal of surfaces and colloids. 2015;31(23):6267-76.

9. Meng E, Sheybani, R. Insight: implantable medical devices. Lab on a chip. 2014;14(17):3233-40.

10. Juanola-Feliu E, Colomer-Farrarons, J., Miribel-Català, P.Samitier, J., Valls-Pasola, J. Market challenges facing academic research in commercializing nano-enabled implantable devices for in-vivo biomedical analysis. Technovation. 2012;32(3-4):193-204.

11. Patel S, Park, H., Bonato, P., Chan, L. Rodgers, M. A review of wearable sensors and systems with application in rehabilitation. Journal of neuroengineering and rehabilitation. 2012;9:21.

12. Black RD. Recent Advances in Translational Work on Implantable Sensors. Sensors Journal, IEEE. 2011;11(12):3171-82.

13. Qi S, Hao L, Hongyi L, Yunsheng Y, editors. Miniature pH sensor for capsule endoscopy with composite diagnosis. Sensors, 2014 IEEE; 2014 2-5 Nov. 2014.

14. Yan Q, Major TC, Bartlett RH, Meyerhoff ME. Intravascular glucose/lactate sensors prepared with nitric oxide releasing poly(lactide-co-glycolide)-based coatings for enhanced biocompatibility. Biosensors & bioelectronics. 2011;26(11):4276-82.

15. Eckert MA, Vu, P. Q., Zhang, K., Kang, D., Ali, M. M., Xu, C., Zhao, W. Novel molecular and nanosensors for in vivo sensing. Theranostics. 2013;3(8):583-94.

16. Bazaka K, Jacob M. Implantable Devices: Issues and Challenges. Electronics. 2012;2(1):1-34.

17. Yazdandoost KY, Kohno R, editors. Wireless Communications for Body Implanted Medical Device. Microwave Conference, 2007 APMC 2007 Asia-Pacific; 2007 11-14 Dec. 2007.

18. Shields D, Patil R. World In Vitro Fertilization (IVF) Market - Opportunities and Forecasts, 2013 - 2020. Alied Market Research, 2014 ME 14124.

19. Lu S. A Multi-parameter In-vivo Sensing Platform for Intra-uterine Environment Monitoring. Southampton: University of Southampton; 2015.

20. Fertility: Assessment and treatment for poeple with fertility problems. National Institute for Health and Care Excellence, 2013 Contract No.: CG156.

21. Fertility Treatment in 2013: Trends and Figures. Human Fertilisation Embryo Authority, 2013.

22. Inhorn MC, Patrizio P. Infertility around the globe: new thinking on gender, reproductive technologies and global movements in the 21st century. Human Reproduction Update. 2015;21(n4).

23. Crawford NM, Steiner AZ. Age-related Infertility. Obstetrics and Gynecology Clinics of North America. 2015;42(1):15-25.

24. Burns LH. Psychiatric Aspects of Infertility and Infertility Treatments. Psychiatric Clinics of North America. 2007;30(4):689-716.

25. Cousineau TM, Domar AD. Psychological impact of infertility. Best practice & research Clinical obstetrics & gynaecology. 2007;21(2):293-308.

26. Evers JLH. Female subfertility. The Lancet. 2002;360(9327):151-9.

27. Brandes M, Hamilton CJ, van der Steen JO, de Bruin JP, Bots RS, Nelen WL, et al. Unexplained infertility: overall ongoing pregnancy rate and mode of conception. Human reproduction. 2011;26(2):360-8.

28. Papaioannou S, Aslam M, Al Wattar BH, Milnes RC, Knowles TG. User's acceptability of OvuSense: a novel vaginal temperature sensor for prediction of the fertile period. Journal of obstetrics and gynaecology : the journal of the Institute of Obstetrics and Gynaecology. 2013;33(7):705-9.

29. Keshwani N, McLean L. State of the art review: Intravaginal probes for recording electromyography from the pelvic floor muscles. Neurourology and urodynamics. 2015;34(2):104-12.

30. Hemalatha R, Ramalaxmi, B., Swetha, E., Balakrishna, N., Mastromarino, P. Evaluation of vaginal pH for detection of bacterial vaginosis. The Indian Journal of Medical Research. 2013;138(3):354-9.

31. PHILIPS, inventorIntrauterine Sensor-Tip Press for Catheter Fetal monitoring with disposable sensor-tip Netherlands.

32. Jauniaux E WA, Ozturk O, Quick D, Burton G. In-vivo measurement of intrauterine gases and acid-base values early in human pregnancy. Hum Reprod 1999 (Nov; 14(11):):2901-4.

33. Causes of infertility. Complete fertility Centre Southampton.

34. Strowitzki T, Germeyer A, Popovici R, von Wolff M. The human endometrium as a fertility-determining factor. Hum Reprod Update. 2006;12(5):617-30.

35. Revel A. Defective endometrial receptivity. Fertility and sterility. 2012;97(5):1028-32.

36. Zhang S, Lin H, Kong S, Wang S, Wang H, Wang H, et al. Physiological and molecular determinants of embryo implantation. Molecular aspects of medicine. 2013;34(5):939-80.

37. Silverthorn DU. Human Physiology: An Integrated Approach. Fifth Edition ed. San Fransico: Pearson Benjamin Cummings; 2010. p. 844-51.

38. Ng KYB, Mingels R, Morgan H, Macklon N, Cheong Y. In vivo oxygen, temperature and pH dynamics in the female reproductive tract and their importance in human conception: a systematic review. Human Reproduction Update. 2018;24(1):15-34.

39. Silverthorn DU. Human Physiology: An Integrated Approach. Fifth Edition ed. San Fransico: Pearson Benjamin Cummings; 2010. p. 598-601.

40. Nejat EJ, Zapantis G, Rybak EA, Meier UT. It's time to pay attention to the endometrium, including the nucleolar channel system. Fertility and sterility.96(6):e165.

41. Isaacs JD, Jr., Wells CS, Williams DB, Odem RR, Gast MJ, Strickler RC. Endometrial thickness is a valid monitoring parameter in cycles of ovulation induction with menotropins alone. Fertility and sterility. 1996;65(2):262-6.

42. Casper RF. It's time to pay attention to the endometrium. Fertility and sterility. 2011;96(3):519-21.

43. Gonen Y, Casper RF. Prediction of implantation by the sonographic appearance of the endometrium during controlled ovarian stimulation for in vitro fertilization (IVF). Journal of in vitro fertilization and embryo transfer : IVF. 1990;7(3):146-52.

44. Yedwab GA, Paz G, Homonnai TZ, David MP, Kraicer PF. The temperature, pH, and partial pressure of oxygen in the cervix and uterus of women and uterus of rats during the cycle. Fertility and sterility. 1976;27(3):304-9.

45. Garris DR, Mitchell JA. Intrauterine oxygen tension during the estrous cycle in the guinea pig: its relation to uterine blood volume and plasma estrogen and progesterone levels. Biology of reproduction. 1979;21(1):149-59.

46. Mitchell JA, Yochim JM. Intrauterine oxygen tension during the estrous cycle in the rat: its relation to uterine respiration and vascular activity. Endocrinology. 1968;83(4):701-5.

47. Kaufman DL, Mitchell JA. Intrauterine oxygen tension during the oestrous cycle in the hamster: patterns of change. Comparative biochemistry and physiology Comparative physiology. 1994;107(4):673-8.

48. Mastroianni L, Jones R. Oxygen Tension Within The Rabbit Falopian Tube. Journal of Reproduction and Fertility. 1965;9(1):99-102.

49. Kigawa J. Studies on the levels of pO2 and pCO2 in the uterine cavity and uterine tissue. 1981;33(10):1646-54.

50. Fischer B, Bavister BD. Oxygen tension in the oviduct and uterus of rhesus monkeys, hamsters and rabbits. J Reprod Fertil. 1993;99(2):673-9.

51. Ottosen LD, Hindkaer J, Husth M, Petersen DE, Kirk J, Ingerslev HJ. Observations on intrauterine oxygen tension measured by fibre-optic microsensors. Reproductive biomedicine online. 2006;13(3):380-5.

52. Bettelheim FA. General, Organic and Biochemistry. Eighth Edition ed. Canada: Thomson Brooks Cole; 2007. p. 251-79.

53. Mather EC. "In vivo" uterine lumen pH values of the bovine. Theriogenology. 1975;3(3):113-9.

54. Eggert-Kruse W, Kohler A, Rohr G, Runnebaum B. The pH as an important determinant of sperm-mucus interaction. Fertility and sterility. 1993;59(3):617-28.

55. Macdonald RR, Lumley IB. Endocervical pH measured in vivo through the normal menstrual cycle. Obstetrics and gynecology. 1970;35(2):202-6.

56. Brabin L, Roberts SA, Fairbrother E, Mandal D, Higgins SP, Chandiok S, et al. Factors affecting vaginal pH levels among female adolescents attending genitourinary medicine clinics. Sexually transmitted infections. 2005;81(6):483-7.

57. Peeters F, Snauwaert R, Segers J, van Cutsem J, Amery W. Observations on candidal vaginitis. American Journal of Obstetrics & Gynecology.112(1):80-6.

58. Pereira Da Silva D, Martinez De Oliveira J, Negreiro F. Observational study of vaginal pH in healthy Portuguese women. Minerva ginecologica. 2011;63(2):203-12.

59. Menezo Y, Guerin P. The mammalian oviduct: biochemistry and physiology. European Journal of Obstetrics & Gynecology and Reproductive Biology. 1997;73(1):99-104.

60. Iritani A, Nishikawa Y, Gomes WR, VanDemark NL. Secretion rates and chemical composition of oviduct and uterine fluids in rabbits. Journal of animal science. 1971;33(4):829-35.

61. McLachlan JA, Sieber SM, Cowherd CM, Straw JA, Fabro S. The pH values of the uterine secretions and preimplantation blastocyst of the rabbit. Fertility and sterility. 1970;21(1):84-7.

62. Kwak-Kim J, Han AR, Gilman-Sachs A, Fishel S, Leong M, Shoham Z. Current trends of reproductive immunology practices in in vitro fertilization (IVF) - a first world survey using IVF-Worldwide.com. American journal of reproductive immunology. 2013;69(1):12-20.

63. Nelissen EC, Van Montfoort AP, Smits LJ, Menheere PP, Evers JL, Coonen E, et al. IVF culture medium affects human intrauterine growth as early as the second trimester of pregnancy. Human reproduction. 2013;28(8):2067-74.

64. Mantikou E, Youssef MA, van Wely M, van der Veen F, Al-Inany HG, Repping S, et al. Embryo culture media and IVF/ICSI success rates: a systematic review. Hum Reprod Update. 2013;19(3):210-20.

65. Chronopoulou E, Harper JC. IVF culture media: past, present and future. Hum Reprod Update. 2015;21(1):39-55.

66. Mantikou E, Bontekoe S, van Wely M, Seshadri S, Repping S, Mastenbroek S. Low oxygen concentrations for embryo culture in assisted reproductive technologies. Hum Reprod Update. 2013;19(3):209.

67. Trounson AO, Gardner D. Embryo Culture Systems. Handbook of In Vitro Fertilization. Second Edition: CRC Press; 2000.

68. Swain JE. Is there an optimal pH for culture media used in clinical IVF? Human Reproduction Update. 2012;18(3):333-9.

69. Bayer. Mirena IUD [cited 2017]. Available from: https://www.mirena-us.com.

70. inc. C. ParaGard IUD [cited 2017]. Available from: https://www.paragard.com.

71. Barron ML, Fehring RJ. Basal body temperature assessment: is it useful to couples seeking pregnancy? MCN The American journal of maternal child nursing. 2005;30(5):290-6; quiz 7-8.

72. OvaCue. OvaCue Fertility Monitor [cited 2017]. Available from: http://www.ovacue.com.

73. Fehring Richard J, Schneider M, Raviele K, Barron Mary L. Efficacy of Cervical Mucus Observations Plus Electronic Hormonal Fertility Monitoring as a Method of Natural Family Planning. Journal of Obstetric, Gynecologic, & Neonatal Nursing. 2007;36(2):152-60.

74. Diagnostics SP. ClearBlue Fertility Monitor [cited 2017]. Available from: http://uk.clearblue.com.

75. Sediame S, Zerah-Lancner F, d'Ortho MP, Adnot S, Harf A. Accuracy of the i-STAT bedside blood gas analyser. The European respiratory journal. 1999;14(1):214-7.

76. Medica. EasyBloodGas Brochure. MedicaCorp; 2010.

77. SphereMedical. Proxima Technical Specification United Kingdom2017.

78. Lauks IR, inventor; iStat Corporation, assignee. Disposable Sensing Device For Real Time Fluid Analysis. United States of America1992.

79. Harter TS, Shartau RB, Brauner CJ, Farrell AP. Validation of the i-STAT system for the analysis of blood parameters in fish. Conservation Physiology. 2014;2(1):cou037-cou.

80. Lauks IR, inventor; iStat Corporation, assignee. Metal oxide Electrodes. United States of America1991.

81. Davis G, inventor; iStat Corporation, assignee. Method for Measuring Gas Concentrations and Microfabricated Sensing Device for Practicing Same. United States of America1996.

82. EasyStat 510(k) Substantial Equivalence Determination decision summary assay and instrument combination template In: Administration USFaD, editor.

83. Tong Boon T, Johannessen EA, Lei W, Astaras A, Ahmadian M, Murray AF, et al. Toward a miniature wireless integrated multisensor microsystem for industrial and biomedical applications. Sensors Journal, IEEE. 2002;2(6):628-35.

84. Koulaouzidis A, Iakovidis DK, Karargyris A, Rondonotti E. Wireless endoscopy in 2020: Will it still be a capsule? World J Gastroenterol. 2015;21(17):5119-30.

85. Cao H, Rao S, Tang S-j, Tibbals HF, Spechler S, Chiao JC. Batteryless implantable dual-sensor capsule for esophageal reflux monitoring. Gastrointestinal Endoscopy. 2013;77(4):649-53.

86. Fontana R, Mulana F, Cavallotti C, Tortora G, Vigliar M, Vatteroni M, et al. An Innovative Wireless Endoscopic Capsule With Spherical Shape. IEEE Transactions on Biomedical Circuits and Systems. 2016;PP(99):1-10.

87. Ye CA, Gao YJ, Ge ZZ, Dai J, Li XB, Xue HB, et al. PillCam colon capsule endoscopy versus conventional colonoscopy for the detection of severity and extent of ulcerative colitis. Journal of digestive diseases. 2013;14(3):117-24.

88. Xu F, Yan G, Wang Z, Jiang P. Continuous accurate pH measurements of human GI tract using a digital pH-ISFET sensor inside a wireless capsule. Measurement. 2015;64:49-56.

89. Cao H, Landge V, Tata U, Seo YS, Rao S, Tang SJ, et al. An Implantable, Batteryless, and Wireless Capsule With Integrated Impedance and pH Sensors for Gastroesophageal Reflux Monitoring. IEEE Transactions on Biomedical Engineering. 2012;59(11):3131-9.

90. Aoki K. Theory of ultramicroelectrodes. Electroanalysis. 1993;5(8):627-39.

91. Idegami K, Chikae M, Nagatani N, Tamiya E, Takamura Y. Fabrication and Characterization of Planar Screen-Printed Ag/AgCl Reference Electrode for Disposable Sensor Strip. Japanese Journal of Applied Physics. 2010;49(9):097003.

92. Inzelt G, Lewenstam, A., Scholz, F. Handbook of Reference Electrodes: Springer; 2013.

93. Cranny AWJ, Atkinson JK. Thick film silver-silver chloride reference electrodes. Measurement Science and Technology. 1998;9(9):1557.

94. Fernandes JCB, Heinke EV. Alternative strategy for manufacturing of all-solid-state reference electrodes for potentiometry. Journal of Sensors and Sensor Systems. 2015;4(1):53-61.

95. Madou MJ. Fundamentals of Microfabrication and Nanotechnology. Volume 1. Third Edition ed: CRC Press; 2012. p. 550-7.

96. Simonis A, Lüth H, Wang J, Schöning MJ. New concepts of miniaturised reference electrodes in silicon technology for potentiometric sensor systems. Sensors and Actuators B: Chemical. 2004;103(1-2):429-35.

97. Guth U, Gerlach F, Decker M, Oelßner W, Vonau W. Solid-state reference electrodes for potentiometric sensors. Journal of Solid State Electrochemistry. 2008;13(1):27-39.

98. Polk BJ, Stelzenmuller A, Mijares G, MacCrehan W, Gaitan M. Ag/AgCl microelectrodes with improved stability for microfluidics. Sensors and Actuators B: Chemical. 2006;114(1):239-47.

99. Glanc M, Sophocleous, M., Atkinson, J. K., Garcia-Breijo, E. The effect on performance of fabrication parameter variations of thick-film screen printed silver/silver chloride potentiometric reference electrodes. Sensors and Actuators. 2013;197:1-8.

100. da Silva ET, Miserere S, Kubota LT, Merkoci A. Simple on-plastic/paper inkjet-printed solid-state Ag/AgCl pseudoreference electrode. Analytical chemistry. 2014;86(21):10531-4.

101. Atkinson JK, Glanc, M., Prakorbjanya, M., Sophocleous, M., Sion, R. P., Garcia-Breijo, E. Thick film screen printed environmental and chemical sensor array reference electrodes suitable for subterranean and subaqueous deployments. Microelectronics International. 2013;30(2):92-8.

102. Sun X, Wang M. Fabrication and characterization of planar reference electrode for on-chip electroanalysis. Electrochimica Acta. 2006;52(2):427-33.

103. M.Schlesinger MP. Modern Electroplating. Fourth edition ed. Canada: John Wiley & Sons; 2000.

104. Moschou D, Trantidou T, Regoutz A, Carta D, Morgan H, Prodromakis T. Surface and Electrical Characterization of Ag/AgCl Pseudo-Reference Electrodes Manufactured with Commercially Available PCB Technologies. Sensors. 2015;15(8):18102-13.

105. Abbott AP, Griffith J, Nandhra S, O'Connor C, Postlethwaite S, Ryder KS, et al. Sustained electroless deposition of metallic silver from a choline chloride-based ionic liquid. Surface and Coatings Technology. 2008;202(10):2033-9.

106. de Mele MFL, Salvarezza RC, Vasquez Moll VD, Videla HA, Arvia AJ. Kinetics and Mechanism of Silver Chloride Electroformation during the Localized Electrodissolution of Silver in Solutions Containing Sodium Chloride. Journal of The Electrochemical Society. 1986;133(4):746-52.

107. Shinwari MW, Zhitomirsky D, Deen IA, Selvaganapathy PR, Deen MJ, Landheer D. Microfabricated reference electrodes and their biosensing applications. Sensors. 2010;10(3):1679-715.

108. Suzuki H, Hiratsuka A, Sasaki S, Karube I. Problems associated with the thin-film Ag/AgCl reference electrode and a novel structure with improved durability. Sensors and Actuators B: Chemical. 1998;46(2):104-13.

109. Forbes GS. The solubility of silver chloride in chloride Solutions and the exsistence of complex argentichloride ions. Journal of the American Chemical Society. 1911;33(12):1937-46.

110. Fritz JJ. Thermodynamic properties of chloro-complexes of silver chloride in aqueous solution. Journal of Solution Chemistry. 1985;14(12):865-79.

111. Brewer PJ, Brown RJ. Effect of Structural Design of Silver/Silver Chloride Electrodes on Stability and Response Time and the Implications for Improved Accuracy in pH Measurement. Sensors. 2009;9(1):118-30.

112. Brewer PJ, Stoica D, Brown RJC. Sensitivities of Key Parameters in the Preparation of Silver/Silver Chloride Electrodes Used in Harned Cell Measurements of pH. Sensors (Basel, Switzerland). 2011;11(8):8072-84.

113. Shitanda I, Kiryu H, Itagaki M. Improvement in the long-term stability of screen-printed planar type solid-state Ag/AgCl reference electrode by introducing poly(dimethylsiloxane) liquid junction. Electrochimica Acta. 2011;58:528-31.

114. Tymecki Ł, Zwierkowska E, Koncki R. Screen-printed reference electrodes for potentiometric measurements. Analytica Chimica Acta. 2004;526(1):3-11.

115. Suzuki H, Shiroishi H, Sasaki S, Karube I. Microfabricated Liquid Junction Ag/AgCl Reference Electrode and Its Application to a One-Chip Potentiometric Sensor. Analytical chemistry. 1999;71(22):5069-75.

116. Mousavi Z, Granholm K, Sokalski T, Lewenstam A. An analytical quality solid-state composite reference electrode. Analyst. 2013;138(18):5216-20.

117. Kim TY, Hong SA, Yang S. A solid-state thin-film Ag/AgCl reference electrode coated with graphene oxide and its use in a pH sensor. Sensors. 2015;15(3):6469-82.

118. Huang IY, Huang R-S, Lo L-H. Improvement of integrated Ag/AgCl thin-film electrodes by KCl-gel coating for ISFET applications. Sensors and Actuators B: Chemical. 2003;94(1):53-64.

119. Lee JS, Lee SD, Cui G, Lee HJ, Shin JH, Cha GS, et al. Hydrophilic Polyurethane Coated Silver/Silver Chloride Electrode for the Determination of Chloride in Blood. Electroanalysis. 1999;11(4):260-7.

120. Cranny A, Harris NR, White NM. Screen-printable porous glass: a new material for electrochemical sensors. Journal of Materials Science: Materials in Electronics. 2015;26(7):4557-64.

121. Michalska A. All-Solid-State Ion Selective and All-Solid-State Reference Electrodes. Electroanalysis. 2012;24(6):1253-65.

122. Guinovart T, Crespo GA, Rius FX, Andrade FJ. A reference electrode based on polyvinyl butyral (PVB) polymer for decentralized chemical measurements. Anal Chim Acta. 2014;821:72-80.

123. Bhattarai N, Gunn J, Zhang M. Chitosan-based hydrogels for controlled, localized drug delivery. Advanced drug delivery reviews. 2010;62(1):83-99.

124. Francis Moussy DJH. Prevention of the Rapid Degradation of Subcutaneously Implanted Ag/AgCI Reference Electrodes Using Polymer Coatings. Analytical chemistry. 1994;66:674-9.

125. Hlavatá L, Vyskočil V, Beníková K, Borbélyová M, Labuda J. DNA-based biosensors with external Nafion and chitosan membranes for the evaluation of the antioxidant activity of beer, coffee, and tea. Central European Journal of Chemistry. 2014;12(5):604-11.

126. A. K. Bohwmick HS. Handbook of Elastomers. Second Edition ed2000.

127. Xi-xun Y, Fei L, Yuan-ting X, Chang-xiu W. In vitro study in the endothelial cell compatibility and endothelialization of genipin-crosslinked biological tissues for tissue-engineered vascular scaffolds. Journal of materials science Materials in medicine. 2010;21(2):777-85.

128. Yoo JS, Kim YJ, Kim SH, Choi SH. Study on genipin: a new alternative natural crosslinking agent for fixing heterograft tissue. The Korean journal of thoracic and cardiovascular surgery. 2011;44(3):197-207.

129. Zevenbergen M, Altena G, Dam VA, Goedbloed M, Bembnowicz P, McGuinness P, et al. Solid state pH and chloride sensor with microfluidic reference electrode2016. 26.1.1-.1.4 p.

130. Hashemi P, Walsh PL, Guillot TS, Gras-Najjar J, Takmakov P, Crews FT, et al. Chronically Implanted, Nafion-Coated Ag/AgCl Reference Electrodes for Neurochemical Applications. ACS Chemical Neuroscience. 2011;2(11):658-66.

131. Schmidt-Rohr K, Chen Q. Parallel cylindrical water nanochannels in Nafion fuel-cell membranes. Nature materials. 2008;7(1):75-83.

132. Bryan JR, Rlley JP, Williams PJL. A winkler procedure for making precise measurements of oxygen concentration for productivity and related studies. Journal of Experimental Marine Biology and Ecology. 1976;21(3):191-7.

133. Wheatland AB, Smith LJ. Gasometric determination of dissolved oxygen in pure and saline water as a check of titrimetric methods. Journal of Applied Chemistry. 1955;5(3):144-8.

134. Carpenter JH. The accuracy of the Winkler method for dissolved oxygen gas analysis. Limnology and Oceanography. 1965;10(1):135-40.

135. Severinghaus JW, Astrup PB. History of blood gas analysis. IV. Leland Clark's oxygen electrode. Journal of Clinical Monitoring. 1986;2(2):125-39.

136. Severinghaus JW, Astrup PB. History of blood gas analysis. V. Oxygen measurement. Journal of clinical monitoring. 1986;2(3):174-89.

137. Davies Pw Fau - Bronk DW, Bronk DW. Oxygen tension in mammalian brain. (0014-9446).

138. Clark, L. Electrolytic sensor with anodic depolarization. Google Patents; 1968.

139. Clark LC, Wolf R, Granger D, Taylor Z. Continuous Recording of Blood Oxygen Tensions by Polarography. Journal of Applied Physiology. 1953;6(3):189-93.

140. Clark LC, Gollan F, Gupta VB. The Oxygenation of Blood by Gas Dispersion. Science. 1950;111(2874):85.

141. Amao Y. Probes and Polymers for Optical Sensing of Oxygen. Microchimica Acta. 2003;143(1):1-12.

142. Quaranta M, Borisov SM, Klimant I. Indicators for optical oxygen sensors. Bioanalytical Reviews. 2012;4(2-4):115-57.

143. Park EJ, Reid KR, Tang W, Kennedy RT, Kopelman R. Ratiometric fiber optic sensors for the detection of inter- and intra-cellular dissolved oxygen. Journal of Materials Chemistry. 2005;15(27-28):2913-9.

144. Dunphy I, Vinogradov SA, Wilson DF. Oxyphor R2 and G2: phosphors for measuring oxygen by oxygen-dependent quenching of phosphorescence. Analytical Biochemistry. 2002;310(2):191-8.

145. Wang X-D, Wolfbeis OS. Fiber-Optic Chemical Sensors and Biosensors (2008–2012). Analytical chemistry. 2013;85(2):487-508.

146. Wolfbeis OS. Luminescent sensing and imaging of oxygen: fierce competition to the Clark electrode. (1521-1878 (Electronic)).

147. Wang X-d, Wolfbeis OS. Optical methods for sensing and imaging oxygen: materials, spectroscopies and applications. Chemical Society Reviews. 2014;43(10):3666-761.

148. YSI. The Dissolved Oxygen Handbook: a practical guide to dissolved oxygen measurements.

149. Eminaga Y, Brischwein M, Wiest J, Clauss J, Becker S, Wolf B. Self calibration of a planar dissolved oxygen sensor. Sensors and Actuators B: Chemical. 2013;177:785-91.

150. Miniaev MV, Belyakova MB, Kostiuk NV, Leshchenko DV, Fedotova TA. Non-obvious Problems in Clark Electrode Application at Elevated Temperature and Ways of Their Elimination. Journal of Analytical Methods in Chemistry. 2013;2013:8.

151. Pethig RR, Smith, S. Introductory Bioelectronics: for Engineers and Physical Scientists Wiley; 2012. p. 446.

152. Mabbott GA. An introduction to cyclic voltammetry. Journal of Chemical Education. 1983;60(9):697.

153. Sosna M, Denuault G, Pascal RW, Prien RD, Mowlem M. Development of a reliable microelectrode dissolved oxygen sensor. Sensors and Actuators B: Chemical. 2007;123(1):344-51.

154. Hoare JP. The Electrochemistry of Oxygen. United States of America: John Wiley & Sons, Inc.; 1968.

155. Gerischer RaG, H. . Über die katalytische Zersetzung von Wasserstoffperoxid an metallischem Platin. Joutnal of Physical Chemsitry. 1956(6):178.

156. Damjanovic A, Dey A, Bockris JOM. Kinetics of oxygen evolution and dissolution on platinum electrodes. Electrochimica Acta. 1966;11(7):791-814.

157. Lorenz R. Die Oxydtheorie der Sauerstoffelektrode. Zeitschrift für Elektrochemie und angewandte physikalische Chemie. 1908;14(48):781-3.

158. Lorenz R, Hauser H. Zur Oxydtheorie der Knallgaskette. Zeitschrift für anorganische Chemie. 1906;51(1):81-95.

159. Rinaldo SG, Lee W, Stumper J, Eikerling M. Mechanistic Principles of Platinum Oxide Formation and Reduction. Electrocatalysis. 2014;5(3):262-72.

160. Baroody HA, Jerkiewicz G, Eikerling MH. Modelling oxide formation and growth on platinum. The Journal of Chemical Physics. 2017;146(14):144102.

161. Thanh Tung Pham X, Thi Thanh Tuyen L, Phu Duy T, Binh Van P, Duy Hien T, Mau Chien D. Oxidation of a platinum microwire surface applied in glucose detection. Advances in Natural Sciences: Nanoscience and Nanotechnology. 2010;1(2):025013.

162. Hall SB, Khudaish EA, Hart AL. Electrochemical oxidation of hydrogen peroxide at platinum electrodes. Part 1. An adsorption-controlled mechanism. Electrochimica Acta. 1998;43(5):579-88.

163. McCrum IT, Janik MJ. Effect of pH and Alkali Cations on Hydroxide Adsorption on Ir, Pt, and Au (111). Meeting Abstracts. 2017;MA2017-01(38):1791-.

164. Markovic N, Gasteiger H, Ross PN. Kinetics of Oxygen Reduction on Pt(hkl) Electrodes: Implications for the Crystallite Size Effect with Supported Pt Electrocatalysts. Journal of The Electrochemical Society. 1997;144(5):1591-7.

165. Pletcher D, Sotiropoulos S. Hydrogen adsorption-desorption and oxide formation-reduction on polycrystalline platinum in unbuffered aqueous solutions. Journal of the Chemical Society, Faraday Transactions. 1994;90(24):3663-8.

166. Perry SC, Denuault G. Transient study of the oxygen reduction reaction on reduced Pt and Pt alloys microelectrodes: evidence for the reduction of pre-adsorbed oxygen species linked to dissolved oxygen. Physical Chemistry Chemical Physics. 2015;17(44):30005-12.

167. Pletcher D, Sotiropoulos S. Towards a microelectrode sensor for the determination of oxygen in waters. Analytica Chimica Acta. 1996;322(1):83-90.

168. Scharifker BR. Microelectrode Techniques in Electrochemistry. In: Bockris JOM, Conway BE, White RE, editors. Modern Aspects of Electrochemistry. Boston, MA: Springer US; 1992. p. 467-519.

169. Rajendran L, Sangaranarayanan MV. Diffusion at Ultramicro Disk Electrodes: Chronoamperometric Current for Steady-State Ec‘ Reaction Using Scattering Analogue Techniques. The Journal of Physical Chemistry B. 1999;103(9):1518-24.

170. Ferrell RT, Himmelblau DM. Diffusion coefficients of nitrogen and oxygen in water. Journal of Chemical & Engineering Data. 1967;12(1):111-5.

171. van Rossem F, Bomer JG, de Boer HL, Abbas Y, de Weerd E, van den Berg A, et al. Sensing oxygen at the millisecond time-scale using an ultra-microelectrode array (UMEA). Sensors and Actuators B: Chemical. 2017;238(Supplement C):1008-16.

172. Huang X. In-Situ conductivity, temperature, and dissolved oxygen (VT-DO) sensor system for marine measurement: University of Southampton; 2012.

173. Myers RJ. One-Hundred Years of pH. Journal of Chemical Education. 2010;87(1):30-2.

174. Szabadvary F, Oesper RE. Development of the pH concept: A historical survey. Journal of Chemical Education. 1964;41(2):105.

175. Marczewska B, Marczewski K. First Glass Electrode and its Creators F. Haber and Z. Klemensiewicz – On 100th Anniversary. Zeitschrift für Physikalische Chemie2010. p. 795.

176. Graham DJ, Jaselskis B, Moore CE. Development of the Glass Electrode and the pH Response. Journal of Chemical Education. 2013;90(3):345-51.

177. Cheng KL. Explanation of Misleading Nernst Slope by Boltzmann Equation. Microchemical Journal. 1998;59(3):457-61.

178. S.A. RA. pH Theory and Pratice. 2001.

179. Pethig RR, Smith, S. Introductory Bioelectronics: for Engineers and Physical Scientists. Wiley; 2012. p. 446.

180. Bergveld P. Thirty years of ISFETOLOGY: What happened in the past 30 years and what may happen in the next 30 years. Sensors and Actuators B: Chemical. 2003;88(1):1-20.

181. Bergveld P. Development of an Ion-Sensitive Solid-State Device for Neurophysiological Measurements. Biomedical Engineering, IEEE Transactions on. 1970;BME-17(1):70-1.

182. Bergveld P. ISFET Theory and Practice. IEEE Sensor Conference; Toronto2003.

183. Abe H, Esashi M, Matsuo T. ISFET's using inorganic gate thin films. Electron Devices, IEEE Transactions on. 1979;26(12):1939-44.

184. Kurzweil P. Metal Oxides and Ion-Exchanging Surfaces as pH Sensors in Liquids: State-of-the-Art and Outlook. Sensors. 2009;9(6):4955-85.

185. Lai C-S, Lue C-E, Yang C-M, Dawgul M, Pijanowska GD. Optimization of a PVC Membrane for Reference Field Effect Transistors. Sensors. 2009;9(3).

186. Kühnhold R, Ryssel H. Modeling the pH response of silicon nitride ISFET devices. Sensors and Actuators B: Chemical. 2000;68(1–3):307-12.

187. Yu-Ren Li S-HC, Wan-Lin Tsai, Chia-Tsung Chang,, Kuang-Yu Wang P-YY, and Huang-Chung Cheng. Highly Sensitive pH Sensors of Extended-Gate Field-Effect Transistor With the Oxygen-Functionalized Reduced Graphene Oxide Films on Reverse Pyramid Substrates. Electronics Device Letters. 2015;36(11).

188. Vonau W, Guth U. pH Monitoring: a review. Journal of Solid State Electrochemistry. 2006;10(9):746-52.

189. Steegstra P, Ahlberg, E. Influence of oxidation state on the pH dependence of hydrous iridium oxide films. Electrochimica Acta. 2012;76:26-33.

190. Steegstra P, Busch M, Panas I, Ahlberg E. Revisiting the Redox Properties of Hydrous Iridium Oxide Films in the Context of Oxygen Evolution. The Journal of Physical Chemistry C. 2013;117(40):20975-81.

191. Hitchman ML, Ramanathan S. Considerations of the pH dependence of hydrous oxide films formed on iridium by voltammetric cycling. Electroanalysis. 1992;4(3):291-7.

192. Pourbaix M. Atlas of Electrochemical Equilibria. Houstan, Texas: National Association of Corrosion Engineers; 1974. p. 397.

193. Wang M, Yao S, Madou M. A long-term stable iridium oxide pH electrode. Sensors and Actuators B: Chemical. 2002;81(2–3):313-5.

194. Ng SR, O'Hare D. An iridium oxide microelectrode for monitoring acute local pH changes of endothelial cells. Analyst. 2015;140(12):4224-31.

195. Yamanaka K. HJournal of Applied Physics. 1989;28(4):632-7.

196. Huang W-D, Cao H, Deb S, Chiao M, Chiao JC. A flexible pH sensor based on the iridium oxide sensing film. Sensors and Actuators A: Physical. 2011;169(1):1-11.

197. Nguyen CM, Rao S, Yang X, Dubey S, Mays J, Cao H, et al. Sol-gel deposition of iridium oxide for biomedical micro-devices. Sensors. 2015;15(2):4212-28.

198. Chu J, Zhao Y, Li S-H, Yu H-Q, Liu G, Tian Y-C. An Integrated Solid-State pH Microelectrode Prepared Using Microfabrication. Electrochimica Acta. 2015;152:6-12.

199. Kuo L-M, Chou Y-C, Chen K-N, Lu C-C, Chao S. A precise pH microsensor using RF-sputtering IrO2 and Ta2O5 films on Pt-electrode. Sensors and Actuators B: Chemical. 2014;193:687-91.

200. Huang X-r, Ren Q-q, Yuan X-j, Wen W, Chen W, Zhan D-p. Iridium oxide based coaxial pH ultramicroelectrode. Electrochemistry Communications. 2014;40:35-7.

201. Carroll S, Baldwin RP. Self-Calibrating Microfabricated Iridium Oxide pH Electrode Array for Remote Monitoring. Analytical chemistry. 2010;82(3):878-85.

202. A.I. Bryan MRC, inventorDissolved oxygen sensor calibration, monitoring and reporting system1988.

203. E. Santoli PR, J. Gobet, R. Pfandler, P. Bitsche, inventor; ZUELLIG AG, Adamant Technologies SA, assignee. Method for Use of an Electrochemical Sensor and Electrodes Forming Said Sensor2005.

204. Read TL, Bitziou E, Joseph MB, Macpherson JV. In Situ Control of Local pH Using a Boron Doped Diamond Ring Disk Electrode: Optimizing Heavy Metal (Mercury) Detection. Analytical chemistry. 2014;86(1):367-71.

205. Zhu H, Derksen R, Krause C, Fox R, Brazee R, Ozkan H. Fluorescent Intensity of Dye Solutions under Different pH Conditions. 2005.

206. Blau A, Ziegler C, Heyer M, Endres F, Schwitzgebel G, Matthies T, et al. Characterization and optimization of microelectrode arrays for in vivo nerve signal recording and stimulation1Paper presented at WPB '96, Bangkok, May 1996.1. Biosensors and Bioelectronics. 1997;12(9):883-92.

207. Marzouk SAM, Ufer S, Buck RP, Johnson TA, Dunlap LA, Cascio WE. Electrodeposited Iridium Oxide pH Electrode for Measurement of Extracellular Myocardial Acidosis during Acute Ischemia. Analytical chemistry. 1998;70(23):5054-61.

208. ISO19033 . Biological evaluation of medical devices. 2009.

209. MTT Cell Proliferation Assay. In: ATCC, editor. United States: ATCC.

210. Geninatti T, Bruno G, Barile B, Hood RL, Farina M, Schmulen J, et al. Impedance characterization, degradation, and in vitro biocompatibility for platinum electrodes on BioMEMS. Biomedical microdevices. 2015;17(1):24-.

211. Thanawala S, Palyvoda O, Georgiev DG, Khan SP, Al-Homoudi IA, Newaz G, et al. A neural cell culture study on thin film electrode materials. Journal of Materials Science: Materials in Medicine. 2007;18(9):1745-52.

212. Göbbels K, Kuenzel T, van Ooyen A, Baumgartner W, Schnakenberg U, Bräunig P. Neuronal cell growth on iridium oxide. Biomaterials. 2010;31(6):1055-67.

213. Wu J, Wang L, He J, Zhu C. In vitro cytotoxicity of Cu2+, Zn2+, Ag+ and their mixtures on primary human endometrial epithelial cells. Contraception. 2012;85(5):509-18.

214. Hardes J, Streitburger A, Ahrens H, Nusselt T, Gebert C, Winkelmann W, et al. The Influence of Elementary Silver Versus Titanium on Osteoblasts Behaviour In Vitro Using Human Osteosarcoma Cell Lines. Sarcoma. 2007;2007:26539.

215. Jackson WF, Duling BR. Toxic effects of silver-silver chloride electrodes on vascular smooth muscle. Circulation Research. 1983;53(1):105.

216. Schmid BC, Rezniczek GA, Rolf N, Saade G, Gebauer G, Maul H. Uterine packing with chitosan-covered gauze for control of postpartum hemorrhage. American Journal of Obstetrics and Gynecology. 2013;209(3):225.e1-.e5.

217. Wang C, Lau Ting T, Loh Wei L, Su K, Wang DA. Cytocompatibility study of a natural biomaterial crosslinker—Genipin with therapeutic model cells. Journal of Biomedical Materials Research Part B: Applied Biomaterials. 2011;97B(1):58-65.

218. Kim B-C, Kim H-G, Lee S-A, Lim S, Park E-H, Kim S-J, et al. Genipin-induced apoptosis in hepatoma cells is mediated by reactive oxygen species/c-Jun NH2-terminal kinase-dependent activation of mitochondrial pathway. Biochemical Pharmacology. 2005;70(9):1398-407.

A1 – Standard reduction potentials

Measured at 298 K in aqueous solutions.

Half-reaction	Potential *vs. SHE*	Potential vs. *Ag-AgCl*
O_2 (g) + 4 H^+ (aq) + 4 e^- → 2 H_2O	+ 1.23 V	+1.031 V
Ag^+ (aq) + e^- → Ag (s)	+ 0.8 V	+0.6 V
O_2 (g) + 2 H^+ (aq) + 2 e^- → H_2O_2 (aq)	+ 0.6 V	+0.4 V
O_2(g) + 2 H_2O (l) + 4 e^- → 4 OH^- (aq)	+ 0.4 V	+ 0.2 V
AgCl (s) + e^- → Ag (s) + Cl^- (aq)	+0.222 V	0 V
2 H^+ (aq) + 2 e^- → H_2 (g)	+ 0.00 V	-0.2 V
2 H_2O (l) + 2 e^- → H_2 (g) + 2 OH^- (aq)	- 0.83 V	-1.03 V

A2 – Simulation model for full reference experiments

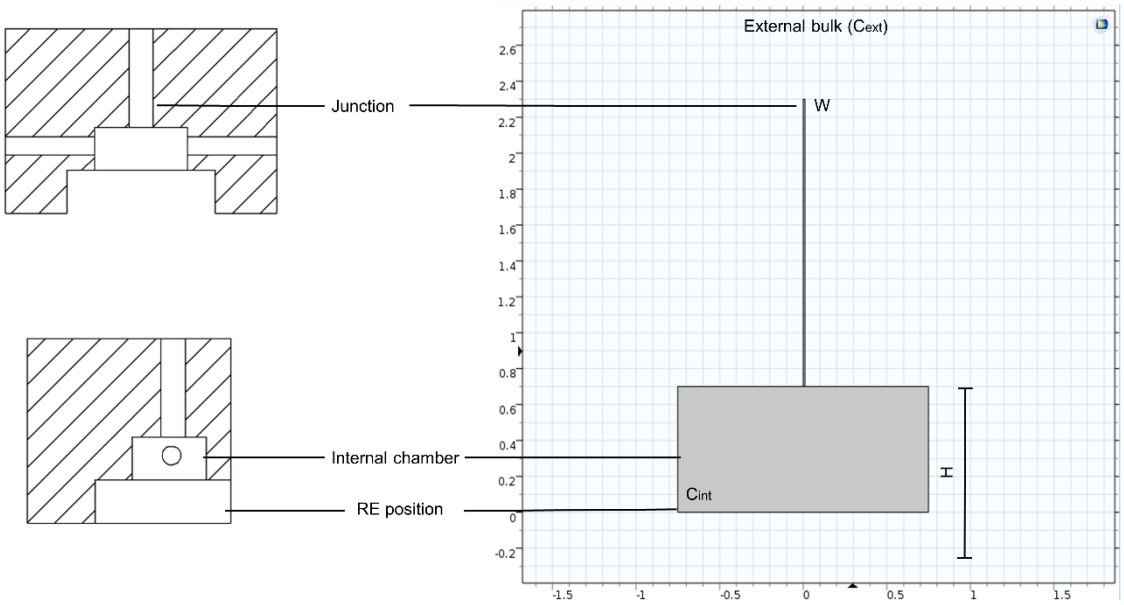

Model: transport of diluted species; solved for concentration of chloride, c; Scale in mm.

Nernst equation: $E = E^0 - 2.303\frac{RT}{F}\log[c]$

Constants	Definition	Value	Units
D	Diffusion coefficient of chloride in water	1.38 10-9	m^2 s
R	Gas constant	8.314	J K^{-1} mol^{-1}
T	Absolute temperature	293	K
F	Faraday's constant	96485	C mol^{-1}
E^0	Formal potential Ag-AgCl	220	mV
C_{int}	Internal chloride concentration	150	mM

Variables	Definition	Value	Units
C_{ext}	External chloride concentration	-	mM
W	Diameter of junction	-	mm
H	Height of internal chamber	-	mm

B1 – Dissolved oxygen simulation model

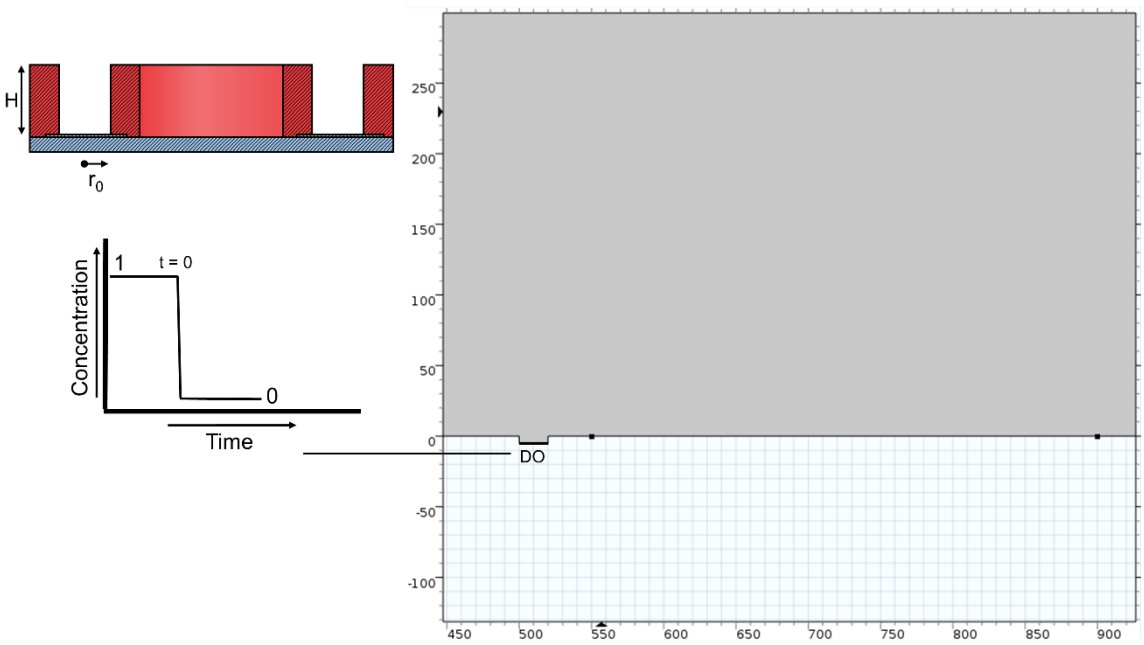

Model: transport of diluted species; 2D. Solved for concentration of DO, c over time when concentration is rapidly stepped down to 0. Scale in µm.

Cottrell equation: $$I = N\left(nFAC\sqrt{\frac{D}{\pi t}}\right)$$

Steady-sate equation: $$I_{ss} = N\left(\frac{4\pi nFCDr_0^2}{4H+\pi r_0}\right)$$

Constants	Definition	Value	Units
D	Diffusion coefficient of oxygen in water	$2.1\ 10^{-9}$	$m^2\ s$
F	Faraday's constant	96485	$C\ mol^{-1}$
C	Bulk DO concentration	7	$mg\ L^{-1}$
Variables	**Definition**	**Value**	**Units**
r_0	Disk radius	-	µM
H	Recess height	-	µm
N	Array size	-	-
A	WE area	-	$µm^2$

C1 – Precision test for TIROF sensor

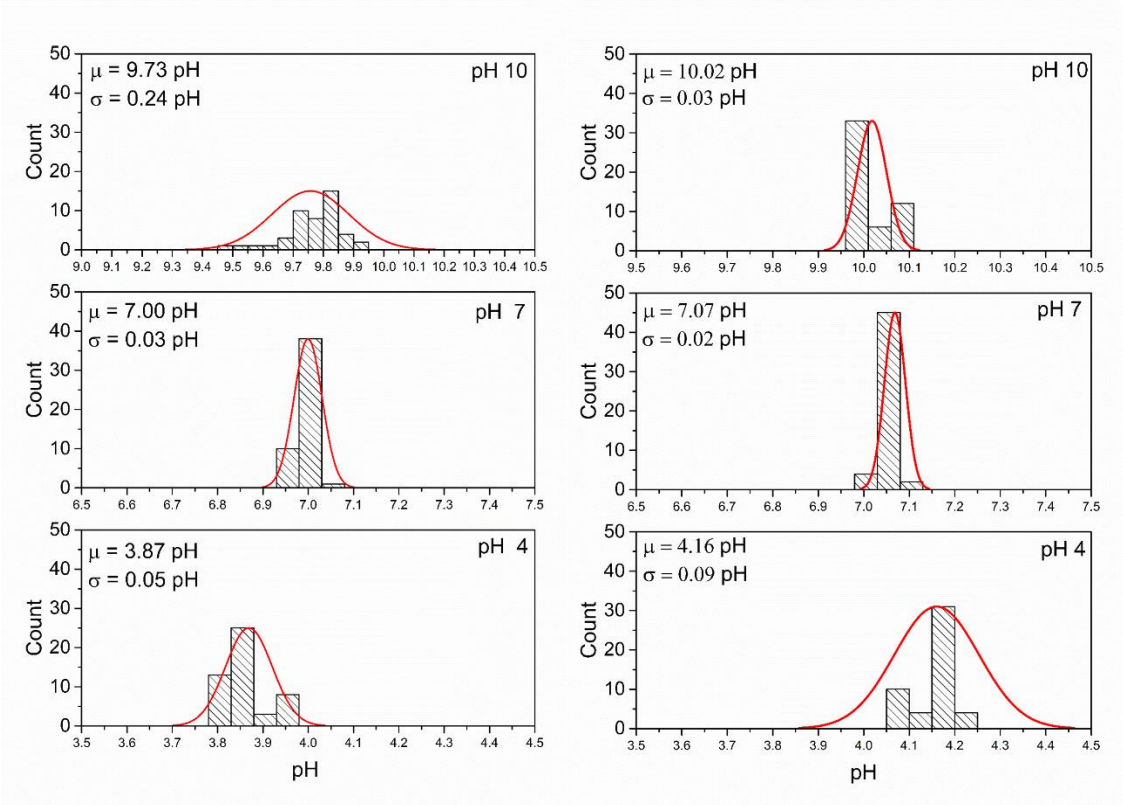

D1 – On-chip Calibration Model

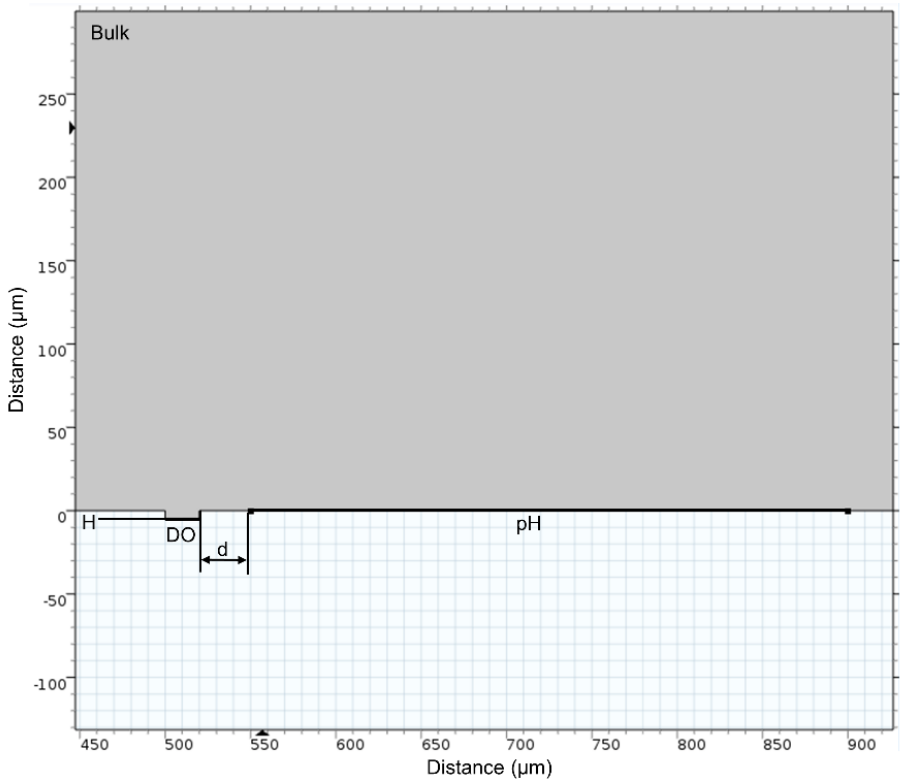

Model: transport of diluted species; Chemical reactions. 2D or 2D-revolved. Solved for concentration of protons (cH); concentration of base (cBase); concentration of acid (cAcid). Scale in µm.

Boundary flux at 'DO': $Flux = \frac{I}{AF}$

Equilibrium in 'Bulk': $A^- + H^+ \rightleftarrows HA$

Concentration to pH[8]: $-log10(cH) = -log10\left(\frac{cH*cAcid}{cBase}\right) - log10\left(\frac{cAcid}{cBase}\right)$

Constants	Definition	Value	Units
Dh	Diffusion coefficient of proton	$9.31\ 10^{-8}$	$m^2\ s^{-1}$
Da	Diffusion coefficient of HPO_4	$7.59\ 10^{-10}$	$m^2\ s^{-1}$
Dha	Diffusion coefficient of H_2PO_4	$9.59\ 10^{-10}$	$m^2\ s^{-1}$
H	Recess height	5	µm
F	Faraday's constant	96485	$C\ mol^{-1}$

[8] Computed in mol L^{-1}.

Variables	Definition	Value	Units
I	Sourced current	-	µA
cAcid	Concentration of acid	-	Mol L^{-1}
cBase	Concentration of base	-	Mol L^{-1}
cH	Concentration of protons	10^{-pH}	Mol L^{-1}
d	Distance between electrode and sensor	-	µm
A	Electrode area	-	μm^2
t	Time	-	s